ABSTRACT

Title of Dissertation: ON-RESISTANCE VERSUS BREAKDOWN VOLTAGE CAPABILITIES OF EMERGING SEMICONDUCTORS FOR OPTO- AND POWER ELECTRONICS

Franklin Lowa Lowe Nouketcha
Doctor of Philosophy, 2022

Dissertation Directed by: Professor Neil Goldsman
Department of Electrical and Computer Engineering

Compared to silicon, wide-bandgap (WBG) and ultrawide-bandgap (UWBG) semiconductors exhibit high internal electric critical fields, low intrinsic carrier concentration, and higher saturation velocities. Those properties make them suitable for electric vehicles, radio frequency electronics, solar-blind ultraviolet photodetectors, and power conditioning to name a few. As those new materials emerge for modern electronics, an accurate assessment of their capabilities is necessary for informed material selection and device designs. For power electronics, the Baliga figure-of-merit (BFoM) is the metric commonly used to assess the trade-offs between the on-resistance and the breakdown voltage; however, the effects of underlying physics on material parameters are often not accounted for, leading to unrealistic performance predictions. This work improves devices' performance predictions by investigating dopants' incomplete activation and ionization and using impact ionization coefficients for breakdown voltage calculations. In addi-

tion to silicon, this study is carried out on WBG (4H-SiC and GaN) and UWBG ($Al_xGa_{1-x}N$, β-Ga_2O_3, and Diamond) semiconductors.

The work first investigates the on-resistance part of the BFoM. Poisson's equation is used to evaluate the steady-state concentration of ionized dopants. Challenges related to dopants activation and ionization are addressed. Capacitance-voltage-temperature characteristics measured on 4H-SiC $p-i-n$ diodes provide a baseline for validating the model of incomplete ionization on WBG semiconductors. The work shows that for UWBG semiconductors with high ionization energy, failure to account for incomplete ionization may result in an estimated on-resistance 1000 times lower than their practical values. In the second part of the dissertation, the breakdown voltage is evaluated using the reduced ionization integral. A modified Thornber expression, calibrated with impact ionization coefficients surveyed from the literature, measured breakdown voltages, and measured multiplication, is proposed for a temperature-dependent model of impact ionization coefficients. Results show that an emphasis should be placed on the minimum doping (background doping) concentration of materials as it determines their maximum blocking capabilities. Impact ionization coefficients are essential for modeling power- and opto-electronic devices; they need to be quantified more accurately, as processed data suggest that they are doping-dependent.

4H-SiC $p-i-n$ diodes are used to measure the photo-multiplication and for the experimental extraction of impact ionization coefficients. For a better understanding of the diode performance, deep-level transient spectroscopy (DLTS) characterization is used to extract the density of generation-recombination centers and address the source of the dark current. Because the diodes are opto-electronics devices, insight is gained into the carrier multiplication process by measuring their responsivity, quantum efficiency, dark count, and single-photon detection efficiency. The calculations of this work help understand the operation of avalanche photodiodes

by establishing how calculated field profiles drive multiplication processes. Calculated breakdown voltages and on-resistances allow the assessment of the efficiency and power density of the investigated materials through modeling of conduction and switching losses. This work led to the development of a 1D-simulator that predicts the performance of power electronic devices based on their geometry, the doping concentration of their constituent layers, and the material selected for their fabrication. The results of this work provide parameters essential for technology computer-aided design (TCAD) modeling of power electronic devices, including vertical power devices.

ON-RESISTANCE VERSUS BREAKDOWN VOLTAGE LIMITS OF EMERGING SEMICONDUCTORS FOR OPTO- AND POWER ELECTRONICS

by

Franklin Lowa Lowe Nouketcha

Dissertation submitted to the Faculty of the Graduate School of the
University of Maryland, College Park in partial fulfillment
of the requirements for the degree of
Doctor of Philosophy
2022

Advisory Committee:
Professor Neil Goldsman, Chair/Advisor
Professor Kevin Daniels
Professor Pamela Abshire
Professor Timothy Horiuchi
Professor Patrick F. McCluskey

© Copyright by
Franklin Lowa Lowe Nouketcha
2022

Acknowledgments

I wish to thank everyone who has supported me through my academic journey. I acknowledge my parents for their unconditional love. I thank my dad, Jean Nouketcha, for raising my siblings and me as a single parent. I am grateful to my mother, Euphrasie Keutchamegne, for arranging our move to the United States. Lionel Nouketcha, Sandra Nouketcha, and Cedric Nouketcha, I am thankful for our childhood experience. Thank you to Florenza Nouketcha, Lionel Nouketcha II, and Milann Tchantchou for making me feel like a great uncle. To Sonia Jouonang, Natacha Jouonang and Kevine Tchantchou thank you for making family moments great. I also want to acknowledge the Yomba family for their support.

To **my second father, Dr. Neil Goldsman**, thank you for the great pieces of advice and also for referring me to ARL. I am grateful for the skillset I have developed under your mentorship. **Dr. Ronald Green**, words are not enough to thank you for your active contribution to my success.

Thank you to my teachers in Cameroon for my early education, Particularly Mr. Calvin Tchatat Njanja and Dr. Omer Destin Kuimi Tatchou. My education in the U.S. would not have been possible without the help of great teachers and mentors that I have met along the way. I thank all my professors and mentors at Montgomery college. Some of them are Satrom Heather, Miriam Zemen, Dr. Kam F. Yee, Dr. Lan Xiang, Dr. Chienann Alex Hou, Dr. Thomas Gleim, Micheal Mehalick, and Patricia Lopez. I am grateful to the STEM program and Kendall's family for supporting me financially during my transfer years as an undergraduate at the University

of Maryland, College Park. Moving to the University of Maryland, I thank friends from the MERIT 2011 Summer REU internship for the great experience that we have shared. I am also grateful to all my teachers for all of our interactions. I am particularly thankful to Dr. Abshire for advising me during the MERIT internship and during my undergraduate studies. The early stage of my graduate studies was challenging, and I am grateful to Steward Heather from the graduate office for helping me stay in school. I am thankful to the department of electrical and computer engineering for letting me serve on the committee for diversity, equity, and inclusion; being part of such a committee has contributed to my professional growth. Big shout-out to Prof. Timothy Horiuchi (for hooding me) and Prof. Patrick F. McCluskey for their availability.

I want to acknowledge my teammates at the University of Maryland, Dr. Christopher Darmody, Dr. Yumeng Cui, Dr. Xiyang Xiao, Alex Mazonni, and Ittai Baum. I have learned so much from you. I am grateful to ECEGSA and its board members for all the good times we shared as graduate students. Dr. Helene Nguewou, thank you for being so supportive. To Sana Awan and Priyanka Kaswan, thank you for your friendship.

I also want to thank the people I met at the national institute of standards and technology (NIST) in the physical measurement lab during my stay as a SURF summer intern. Thanks to Dr. Jason Campbell for the discussion on pursuing graduate studies. I also want to acknowledge the help of my co-workers at the Army Research Laboratory, Timothy Griffin, Daniel Habersat, Jeremy Smith, Micheal Derenge, Dr. Mary Gelanko, Dr. Owen Vail, Dr. Adam Wilson, Dr. Jonathan Schuster, and Dr. Stephen Kelly. I am grateful for the help of senior mentors, Dr. Randy Tompkins, Dr. Kenneth Jones, Dr. Gregory Garrett, Dr. Barbara Nichols, Dr. Aivars Lelis, Dr. Anand Sampath, and Dr. Conn family. There are many that I couldn't acknowledge; please know that our interactions meant a lot to me.

Table of Contents

Acknowledgements ii

Table of Contents iv

List of Tables viii

List of Figures ix

List of Symbols and Abbreviations xiii

Chapter 1: Introduction 1

1.1 Device Physics and Power Electronics . . . 2

1.1.1 Developing Electronics to Address the World's Biggest Challenges . . . 2

1.1.2 The Ideal Characteristics for Power Electronics Devices . . . 4

1.2 Emerging Materials for Opto- and Power Electronics Devices . . . 5

1.2.1 Wide-Bandgap Semiconductors . . . 6

1.2.2 Ultrawide-Bandgap Semiconductors . . . 7

1.3 Advantages of Wide- and Ultrawide-Bandgap Semiconductors . . . 10

1.3.1 Advantages due to Material Properties . . . 10

1.3.2 Application Space for Wide- and Ultrawide-Bandgap Semiconductors . . . 13

1.4 Assessing the Power Capabilities of Materials . . . 13

1.4.1 The Baliga Figure-of-Merit: A Metric Commonly Improperly Evaluated . 13

1.4.2 Avalanche Breakdown: An Alternative for the Evaluation of the On-resistance Versus Breakdown Voltage Limits of Semiconductors . . . 16

1.5 Literature Review and Scope . . . 17

1.5.1 Literature Review . . . 17

1.5.2 Scope of the Dissertation . . . 19

Chapter 2: Study of Incomplete Ionization as a Function of Electric Field and Temperature for a More Accurate Assessment of the Resistance 22

2.1 Depletion Approximation and Full Ionization Assumptions . . . 24

2.1.1 Triangular Field Profile in $p-i-n$ Diodes . . . 25

2.1.2 Trapezoidal Field Profile in $p-i-n$ Diodes . . . 26

2.2 Incomplete Activation of Dopants: A factor that Increases Resistance . . . 29

2.2.1 Definition and Modeling of Incomplete Activation . . . 29

2.2.2 Dopants Incomplete Activation in p-type Doped 4H-SiC . . . 31

2.3 Incomplete Ionization in the Bulk of Wide- and Ultrawide-Bandgap Semiconductors 34
2.3.1 Ionization Energy of Wide-Bandgap and Ultrawide-Bandgap Semiconductors . . . 34
2.3.2 Modeling of Incomplete Ionization with the Poisson Equation . . . 35
2.3.3 Accounting for Incomplete Ionization in the Charge Neutrality Equation . 38
2.4 Incomplete Ionization in Junctions . . . 44
2.4.1 The Finite Difference Method for the Calculation of the Potential and the Concentration of Ionized Dopants . . . 44
2.4.2 Effects of Temperature on the Incomplete Ionization of Dopants in $p-i-n$ Diodes at Zero Bias . . . 48
2.4.3 Electric Potential, Electric Field, and Incomplete Ionization in Reverse Biased $p-i-n$ Diodes . . . 52
2.4.4 Background Currents in Devices Fabricated with Wide- and Ultrawide-Bandgap Semiconductors . . . 57
2.5 Validation of Incomplete Ionization with Capacitance-Voltage-Temperature Measurements . . . 61

Chapter 3: Characterization of 4H-SiC $p-i-n$ diodes for the Validation of Incomplete Ionization and the Calculation of Impact Ionization Coefficients 67
3.1 Effects of Incomplete Ionization on Measured Resistance . . . 68
3.1.1 Effect of the Temperature on the Total Resistance of the $p-i-n$ Diodes 70
3.1.2 Extraction of the Series Resistance . . . 74
3.2 Deep-Level Transient Spectroscopy Analysis for the Study of the Dark Current, the Multiplication, and Impact Ionization Coefficients . . . 78
3.2.1 Generation-Recombination Centers and their Impact on Devices Performance . . . 79
3.2.2 Modeling the Transient of Generation-Recombination Centers Occupied by Electrons . . . 81
3.2.3 Experimental Setup for Deep-Level Transient Spectroscopy Measurements 84
3.3 Baseline for the Dark Current in Wide-Bandgap Semiconductors from DLTS Characterization of 4H-SiC $p-i-n$ Diodes . . . 89
3.3.1 Measured Capacitance as a Function of the Temperature for Extracting the Characteristics of Deep-Level Centers in 4H-SiC . . . 90
3.3.2 Extracted Density of Deep Traps, Temperature Dependence of the Emission Time Constant, and Implication on the Dark Current . . . 92
3.4 Extraction of the Multiplication from Reverse I-V Measurements . . . 98
3.4.1 Modeling The Photo Current of $p-i-n$ Diodes . . . 98
3.4.2 Dark and Photo Measurements for the Experimental Evaluation of the Multiplication and the Establishment of the $p-i-n$ Diode Equivalent Circuit Model . . . 102
3.4.3 Extraction of the Unity-Gain Dark Current . . . 104

Chapter 4: Survey of the Literature and Use of Experimental Data for the Calibration of Impact Ionization Coefficients Needed for Breakdown Voltage Calculations 108

4.1 Modeling the Avalanche Process with Impact Ionization Coefficients 109
4.1.1 The Multiplication Process in The Depletion Region of Semiconductors . 110
4.1.2 The Ionization Integral for the Breakdown Voltage Condition 113
4.2 Key Differences Between $p-i-n$ and $n-i-p$ Structures 116
4.2.1 The Ionization Integral for $p-i-n$ Structures 116
4.2.2 The Ionization Integral for $n-i-p$ Structures 117
4.2.3 Impact of the Injection Method on the Multiplication 118
4.3 History of Impact Ionization Coefficients and Proposed Model 121
4.3.1 History of Impact Ionization Coefficients 123
4.3.2 Proposed Model for the Temperature Dependence of Impact Ionization Coefficients 125
4.4 Establishing the Value of Impact Ionization Coefficients by Accounting for both Measured Multiplication and Impact Ionization Coefficients Reported in the Literature 127
4.4.1 Measured Breakdown Voltage for the Calibration of Impact ionization Coefficients 129
4.4.2 Survey of the Literature for the Values of Impact Ionization Coefficients . 133
4.4.3 Established Models for the Impact Ionization Coefficients of Wide- and Ultrawide-Bandgap Semiconductors 135

Chapter 5: Using Calibrated Impact Ionization Coefficients to Establish more Accurate On-resistance versus Breakdown Voltage Limits of Wide- and Ultrawide-Bandgap Semiconductors for Power Electronics 141
5.1 Calculation of the Breakdown Voltage Using Calibrated Impact Ionization Coefficients 141
5.1.1 Proposed Method for the Calculation of the Avalanche Breakdown Voltage in Semiconductors 141
5.1.2 The Optimum Structure for the On-resistance Versus Breakdown Voltage Limits 145
5.1.3 Breakdown Voltage Calculations in WBG and UWBG Semiconductors . 149
5.2 The Critical Field: a By-product of Breakdown Voltage Calculations 153
5.2.1 Extraction of the Critical Field from Breakdown Voltage Calculations . . 153
5.2.2 Modeling of the Critical Field Calculated Using Impact Ionization Coefficients 156
5.3 Improved On-resistance versus Breakdown Voltage Figure-of-Merit for Wide- and Ultrawide-Bandgap Semiconductors as a Function of the Temperature 158
5.3.1 Impact of the Temperature on the Breakdown Voltage 158
5.3.2 Impact of the Temperature on the On-Resistance 159
5.3.3 Improved On-Resistance Versus Breakdown Voltage of Wide- and Ultrawide-Bandgap Semiconductors 161

Chapter 6: Application and Conclusion 168
6.1 Use of Calculated Breakdown Voltage and On-Resistance to Assess the Efficiency of Power Electronics Devices 168
6.2 Impact Ionization Coefficients and the Performance of Avalanche Photodiodes . . 175

6.2.1 Characterization of Avalanche Photodiodes in Linear Mode 175
6.2.2 Characterization of Opto-electronics Devices with Impact Ionization Coefficients: Geiger Mode Operation 181
6.3 Impact Ionization Coefficients and the Drift-Diffusion Equations 185
6.4 Conclusion, Key Contributions and Future Work 187
6.4.1 Contributions 188
6.4.2 Future Work 192

Appendix A: Equations for Trapezoidal Field Profile of Punch Through $p-i-n$ Diodes **194**

Bibliography **197**

List of Tables

1.1 Maturity of some materials for electronics. For a given material, the checkmark indicates materials with somewhat established properties, and the cross mark indicates properties that are not so well defined. For entries with two marks, the first is for electrons and the second for holes. 19

2.1 Mathematical equations to model the electric field (triangular profile) and the potential in $p-i-n$ structures. 26
2.2 Reported dopants ionization energy for wide- and ultrawide-bandgap semiconductors. 34
2.3 Proposed parameters of the Pearson-Barden model for the doping dependence of the ionization energy. 35
2.4 Measured and calculated effective doping concentration. 65

3.1 Extracted resistances of the 4H-SiC $p-i-n$ diodes described in Section 2.5. . . 76
3.2 Possible states of generation recombination centers. 80
3.4 Change in charges due to change in G-R center occupancy in a p-type substrate. . 85
3.5 Predicted changes in capacitance due to changes in generation-recombination centers occupancy. 87

4.1 Device characteristics and measured breakdown voltage as a function of the temperature for the calibration of impact ionization coefficients in 4H-SiC. 133
4.2 Calibrated parameters for the impact ionization coefficients of wide- and ultrawide-bandgap semiconductors. 139

5.1 Thicknesses and doping concentrations of the 4H-SiC $p-i-n$ simulated for theoretical multiplication studies. 142
5.2 Critical electric field parameters. 157

6.1 Calculated optimum thickness ($W(V_{BR})$) and on-resistance (R_{ON}) for a targeted breakdown voltage of 6.5 kV in wide- and ultrawide-bandgap semiconductors. . . 171

List of Figures

1.1 Main components of an electric vehicle. 3
1.2 Schematic of a typical boost converter used in power electronics. 3
1.3 Typical structure of a GaN HEMT. 8
1.4 Intrinsic carriers' concentration of wide- and ultrawide-bandgap semiconductors as a function of the temperature. 12
1.5 Triangular field profile for the derivation of the Baliga figure-of-merit. 14
1.6 Calculated and reported BFoM for Si, WBG, and UWBG materials. 15
1.7 Breakdown evolution in semiconductors. 17

2.1 Triangular field profile within a $p-i-n$ structure. 25
2.2 Trapezoidal field profile within a $p-i-n$ structure. 27
2.3 Illustration of incomplete activation. 29
2.4 Hall mobility in p-type doped 4H-SiC. 33
2.5 Resistivity of p-type doped 4H-SiC substrates. 33
2.6 Graphical method for the calculation of ionized dopants concentration. 39
2.7 Temperature dependence of the Fermi level in n-doped 4H-SiC substrates. 40
2.8 Temperature dependence of the Fermi level in p-doped 4H-SiC substrates. 41
2.9 Ionized dopants fraction in n-type 4H-SiC as a function of the temperature. . . . 42
2.10 Ionized dopants fraction in p-type doped 4H-SiC as a function of the temperature. 42
2.11 Incomplete ionization in p-type doped 4H-SiC (Aluminum). 43
2.12 Impact of temperature on bulk incomplete ionization in WBG and UWBG semiconductors. 44
2.13 Non-uniform mesh for the calculation of the potential using finite difference. . . . 45
2.14 Simulated electric potential, free and ionized dopants concentration, and field in a $p-i-n$ diode. 49
2.15 Temperature dependence of the electric potential profile. 50
2.16 Temperature dependence of the electric field at 0 V. 51
2.17 Profile of ionized dopants as a function of the temperature at 0 V. 52
2.18 Quasi Fermi level position for reverse-biased diodes. 53
2.19 Temperature dependence of the electric potential in reverse-biased $p-i-n$ diodes. 55
2.20 Temperature dependence of the electric field profile in reverse biases junctions. . 55
2.21 Temperature dependence of the concentration of ionized dopants in a reverse-biased $p-i-n$ structure. 56
2.22 Profile for the concentration of free carriers as a function of the temperature. . . . 56
2.23 Measured dark count rate in 4H-SiC avalanche photodiodes. 58
2.24 Calculated reverse saturation current in 4H-SiC as function of the temperature. . . 59

2.25 Potential energy of free carriers drifting back to the cladding layer due to the effect of the electric field. 61
2.26 Schematic of the diode used for capacitance measurements. 62
2.27 Top view of the $p-i-n$ diode (From CoolCAD Electronics) used for C-V measurements. 62
2.28 Calculated and measured C-V-T. 64

3.1 A uniformly doped semiconductor bar for the evaluation of the resistance. 69
3.2 Schematic of the double-diffuse MOSFET (DMOS). 70
3.3 Forward I-Vs measured on a 4H-SiC $p-i-n$ diode at several temperatures. . . 71
3.4 Measured forward I-Vs characteristics of $p-i-n$ diodes plotted on the logarithmic scale for function of the temperature. 73
3.5 Natural logarithmic of the diode current for the extraction of the non-ideality factor. 73
3.6 Regions of a forward biased $p-n$ junction. 74
3.7 Extraction of the series resistance. 76
3.8 A generation-recombination center under the occupancy of an electron and a hole. 80
3.9 Reported deep traps in 4H-SiC 81
3.10 Dynamic of the band diagram of semiconductors for DLTS analysis. 82
3.11 Predicted peak in the function $f(\tau_e)$ =e$^{-t_1/\tau_e}$−e$^{-t_2/\tau_e}$. 87
3.12 DLTS measurement setup. 88
3.13 Illustrative diagram for DLTS measurements. 89
3.14 Measured capacitance transient as a function of the temperature in 4H-SiC $p-i-n$ diodes for DLTS analysis. 91
3.15 Capacitance versus temperature measured after a wait time following the filling pulse. 91
3.16 Capacitance versus the post-filling time. 92
3.17 DLTS spectra for different gate windows. 94
3.18 DLTS spectra calculated for several gate windows. 95
3.19 Extracted energy for the generation-recombination centers. 96
3.20 Extracted emission time constant. 97
3.21 Calculated lifetime in 4H-SiC $p-i-n$ diodes. 100
3.22 Equivalent model for the $p-i-n$ diode. 102
3.23 Measured dark- and photo-current in 4H-SiC $p-i-n$ diodes for the extraction of impact ionization coefficients. 103
3.24 Bias dependent measured photo-multiplication in 4H-SiC $p-i-n$ diodes. . . . 104
3.25 Extraction of the unity-gain dark current using the $\log(M)$ versus $\log(I_{dark})$ method. 106

4.1 Illustration of current injection and charge multiplication in the depletion region. . 111
4.2 Electric field profiles in $p-i-n$ structures. 117
4.3 Electric field profiles in $n-i-p$ structures. 118
4.4 Comparison of the multiplication initiated by electrons and holes injection in a $p-i-n$ diode. 120
4.5 Comparison of multiplication with holes injection in a 4H-SiC $p-i-n$ diodes with an n-doped i-layer and a p-doped i-layer. 120

4.6 Predicted temperature dependence of the breakdown voltage based on impact ionization coefficients surveyed from the literature. 122
4.7 Establishing values for impact ionization coefficients by accounting for measured multiplication, measured breakdown voltages, and reports from the literature. . . 128
4.8 Illustration of the solution space for the eight-parameters proposed model of impact ionization coefficients. 129
4.9 Measured reverse I-V characteristics of 4H-SiC $p-i-n$ diodes as a function of the temperature. 130
4.10 Current-voltage characteristics of a 4H-SiC $p-i-n$ diode in the avalanche regime. 131
4.11 Temperature dependence of the breakdown voltage in a 4H-SiC $p-i-n$ diode. . 131
4.12 Impact ionization coefficients reported in the literature for silicon at room temperature. 134
4.13 Impact ionization coefficients reported in the literature for 4H-SiC at room temperature. 134
4.14 Block diagram explaining the calibration process of impact ionization coefficients. 137
4.15 Modeled multiplication using calibrated impact ionization coefficients. 138
4.16 Measured and modeled temperature dependence of the breakdown voltage in 4H-SiC. 139

5.1 Process used for calculating the avalanche breakdown voltage. 142
5.2 Calculated field profile in 4H-SiC $p-i-n$ diode to evaluate the ionization integral. 143
5.3 Impact ionization coefficients calculated from the electric field profile of 4H-SiC $p-i-n$ diodes. 144
5.4 Illustration of the iterative approach for solving the ionization integral. 145
5.5 Variation of the breakdown voltage as a function of the i-layer thickness. 146
5.6 Calculated i-layer resistance of a 4H-SiC $p-i-n$ diode as a function of device thickness. 148
5.7 On-resistance versus breakdown voltage of a 4H-SiC $p-i-n$ diodes with an i-layer doping concentration of 2×10^{17} cm^{-3}. 149
5.8 Calculated breakdown voltage as a function of the i-layer thickness for several doping concentrations in 4H-SiC. 150
5.9 Calculated breakdown voltage as a function of the i-layer thickness for several doping concentrations in AlN. 150
5.10 4H-SiC $p-i-n$ structures: designing for a targeted breakdown voltage 151
5.11 Calculated field profile at breakdown voltage for 4H-SiC $p-i-n$ diodes with different i-layer thicknesses. 153
5.12 Thickness dependence of the critical field in 4H-SiC $p-i-n$ diode at room temperature. 154
5.13 Calculated critical field in 4H-SiC $p-i-n$ diodes as a function of the i-layer thickness for several doping concentrations. 155
5.14 Calculated critical field in AlN as a function of the i-layer thickness for several doping concentrations. 155
5.15 Extracted doping dependence of the critical field in wide- and ultrawide-bandgap semiconductors. 157
5.16 Calculated temperature-dependence of the breakdown voltage in 4H-SiC. 159

5.17 Temperature dependence of the i-layer resistance of 4H-SiC. The resistance is observed to increase with the temperature. 160
5.18 Temperature dependence of the i-layer resistance in an n-type doped diamond. The i-layer resistance decreases significantly when the temperature rises. 160
5.19 On-resistance versus breakdown voltage calculated as a function of drift-layer doping. 162
5.20 Rotating the R_{ON} versus V_{BR} curves to obtain the optimum limits. Rotating by an angle of $5\pi/8$ radians makes the optimum points maximums easily extractable. . . 163
5.21 Calculated on-resistance versus breakdown voltage along with the limits given by the optimized structures (black line). 164
5.22 On-Resistance versus breakdown voltage limits at 300 K. 165
5.23 On-Resistance versus breakdown voltage limits at 400 K. 165
5.24 On-Resistance versus breakdown voltage limits at 800 K. 166

6.1 Calculated area dependence of the conduction, switching, and total loss for a 4H-SiC in a switching application. 172
6.2 Calculated power losses in wide- and ultra-wide bandgap semiconductors devices during switching application. 173
6.3 Effect of the temperature on the power losses of 4H-SiC power switches. 174
6.4 Effects of the temperature on the power losses in Diamond. 174
6.5 Setup for linear mode testing. 176
6.6 Measured photo-current in 4H-SiC avalanche photodiodes as a function of the optical wavelength. 177
6.7 Measured responsivity in 4H-SiC avalanche photodiodes. 180
6.8 Illustrative diagram for scanning Geiger mode experiments. 181
6.9 Dark and photo counts measured on 4H-SiC avalanche photodiodes as a function of the applied bias. 182
6.10 Calculated single-photon detection efficiency of a 4H-SiC avalanche photodiode. 183
6.11 Spatial dependence of the photo-current in 4H-SiC avalanche photodiodes. 184
6.12 Measured and modeled with impact ionization coefficients current-voltage characteristic of a 4H-SiC $p-i-n$ diode. 187

A.1 Quadratic equation for the trapezoidal field profile. 194

List of Symbols and Abbreviations

Symbol	Description	Unit
A	The surface area of the device	cm^2
α	Impact ionization coefficients for electrons	cm^{-1}
α_{op}	The absorption coefficients	cm^{-1}
β	Impact ionization coefficients for holes	cm^{-1}
d_e	The electron dead space	μm
d_h	The hole dead space	μm
D_n	The diffusion constant for electrons	cm^2/s
D_p	The diffusion length for holes	cm^2/s
ΔE_A	Acceptors activation energy	eV
ΔE_D	Donors activation energy	eV
ξ	The electric field	V/cm
ξ_C	The critical electric field	V/cm
ϵ	The permittivity	F/cm
E_g	The bandgap	eV
E_C	The conduction band energy (w.r.t valence band)	eV
E_F	The Fermi energy level	eV
E_V	The valence band energy (w.r.t valence band)	eV
g_A	Spin and band degeneracy factor for holes	
g_D	Spin and band degeneracy factor for electrons	
G_n	Electrons generation rate	$cm^{-3}s^{-1}$
G_p	Holes generation rate	$cm^{-3}s^{-1}$
I	The current	A
I_n	The light's intensity	W/m^2
I_{n0}	The light's intensity at the top surface	W/m^2
I_{SW}	The side wall leakage current	A
$\hbar$	The Plank's constant (6.626×10^{-34})	J·s
J	The current density	A/cm^2
k	The Boltzmann's constant (1.38×10^{-23})	J/K
K_A	Nouketcha's acceptors factor for incomplete ionization	
K_D	Nouketcha's donors factor for incomplete ionization	
λ_e	Mean free path for electrons	μm
λ_h	Mean free path for holes	μm

λ_{op}	The optical wavelength	nm
L_n	The diffusion length for electrons	cm
L_p	The diffusion length for holes	cm
M	The multiplication factor	
μ_{Hall}	The hall mobility	$\mathrm{cm^2V^{-1}s^{-1}}$
n	Concentration of electrons in the conduction band	$\mathrm{cm^{-3}}$
N_A	Concentration of active p-type dopants	$\mathrm{cm^{-3}}$
$N_A^{'}$	Concentration of added p-type dopants	$\mathrm{cm^{-3}}$
N_A^0	Concentration of active non-ionized p-type dopants	$\mathrm{cm^{-3}}$
N_A^-	Concentration of ionized p-type dopants	$\mathrm{cm^{-3}}$
N_D	Concentration of active n-type dopants	$\mathrm{cm^{-3}}$
$N_D^{'}$	Concentration of added n-type dopants	$\mathrm{cm^{-3}}$
N_D^0	Concentration of active non-ionized n-type dopants	$\mathrm{cm^{-3}}$
N_D^+	Concentration of ionized n-type dopants	$\mathrm{cm^{-3}}$
n_i	Intrinsic free electron concentration	$\mathrm{cm^{-3}}$
$\aleph$	The quantum efficiency	
p	Concentration of holes in the valence band	$\mathrm{cm^{-3}}$
P_{op}	The optical power	W
P_b	Photon initiated avalanche probability	
q	The electronic charge 1.602×10^{-19}	C
$\Re$	The responsivity	A/W
r	The Hall factor	
ρ_c	The specific contact resistivity	$\Omega\cdot \mathrm{cm^2}$
ρ_m	The resistivity of the material	$\Omega\cdot$ cm
t	Time	s
Υ_A	Fraction of incorporated acceptors that are active	
Υ_D	Fraction of incorporated donors that are active	
T	Temperature	K
W	Width of the depletion region	μm

Chapter 1: Introduction

Arguably, the rapid development of semiconductors observed in the second half of the twentieth century was fueled by intellectual rivalries between John Bardeen, Walter Brattain, and William Shockley. Although the three Bell Lab researchers were awarded the 1956 Physics Nobel Prize for the invention of the point-contact transistors in 1947 [1, 2], it is reported that the trio disagreed on sharing the credits of their discovery. Eventually, the Nobel Prize winners parted ways, and William Shockley, on his own, was credited with the invention of the bipolar transistors in 1948 [3]. Whether friendly or competitively, the work of semiconductor pioneers has revolutionized the world, changing the way humans run their daily activities and interact with each other.

Transistors have infested the world; they are present in miniature systems for nanotechnologies and larger platforms such as power converters for electric vehicles and energy distribution. The rapid pace at which the electronic world has grown in the decades following the invention of the point-contact transistors is intriguing. A perfect example is the evolution of computers, which, once gigantic complex machines such as the Atanasoff-Berry computer (1942) and the ENIAC (1945), are now pants pocket objects. A modern pico pi has the size of a medical band-aid, costs less than $5, and has spectacular computing capabilities. Further improvement of electronics platforms is a challenge; however, considering new materials can unleash new capabilities.

1.1 Device Physics and Power Electronics

Progress in electronics has not just been reflected in the miniaturization of computers. One of the key heritages of electronics pioneers is the body of knowledge relevant to understanding electronics systems. Laws of classical physics, in conjunction with those of quantum mechanics, provide a framework for capturing the macroscopic performance of electronic systems by looking at the atomic scale microscopic behaviors. Such a framework helps evaluate the performance of electronic devices.

1.1.1 Developing Electronics to Address the World's Biggest Challenges

Current societal trends require electronic systems to be faster, more powerful, and more efficient. Overcoming environmental changes requires replacing fossil-fuel-powered systems with greener technologies to suppress greenhouse gas emissions. Although generating electricity could be a complex process, energy is best used in the electric form as prompted by the growing number of electrical systems (electric vehicles, for example). Electricity is needed to energize more powerful platforms such as boats, planes, and even tanks for military applications. The growing number of electric vehicles already reflects this need. For a reference for the type of electrical systems needed in a carbon-free world, Fig. 1.1 shows an electric vehicle with its main components [4]. Among those components are the DC/DC converters, the onboard charger, and the power electronics controller, which convert and control energy between the battery pack and the electric motor.

Like electric vehicles, most electronic platforms use power conversion systems that convert electricity from one form to another, proper for load components. As such, ac-to-ac, ac-to-dc, dc-

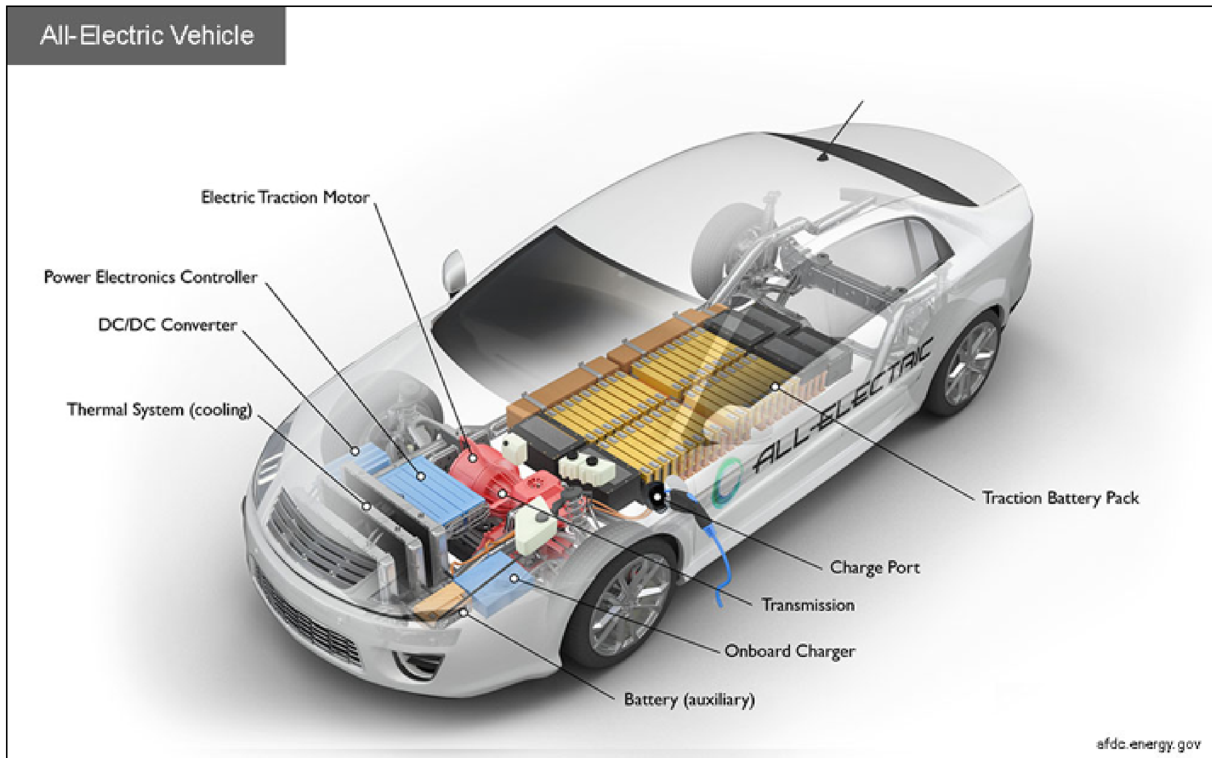

Figure 1.1: A typical electric vehicle and its main components. Power switching and conditioning are essential parts of the system.

to-ac, and dc-to-dc converters are used to adjust voltages and currents for specific applications. Fig. 1.2 shows a typical boost converter that takes in an input voltage V_{in} and outputs a higher voltage at the load terminals. At the heart of the boost-converter is a power switch, M_1, that controls the operation. Improving the switch M_1 is a priority because it results in more efficient conversion and system compactness.

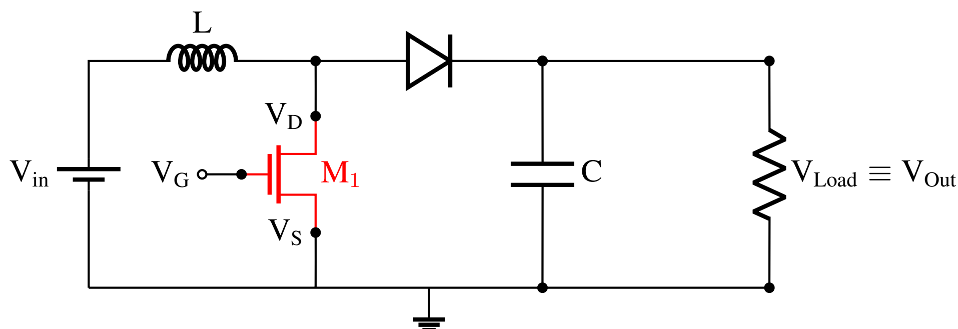

Figure 1.2: Schematic of a typical boost converter used in power electronics.

1.1.2 The Ideal Characteristics for Power Electronics Devices

To further improve the robustness, speed, and efficiency of power conversion systems, it is necessary to develop power switches approaching ideal characteristics given by:

- **Zero gate leakage** ($\mathbf{I_G = 0\ A}$): Suppressing the gate leakage ensures that there is no power on the gate terminal used to control the switch ($P_G = V_G \times I_G$).
- **Capability to withstand infinite voltages**: Transistors may be subjected to high biases depending on their use within a circuit; a device that can handle infinite voltages without breaking down is robust for any application.
- **Zero off-state leakage** ($\mathbf{I_{D\text{-}off} = 0\ A}$): In the off-state, the device may be subjected to high drain biases. Zero off-state leakage ensures that no energy is lost in the blocking state.
- **Zero on-resistance**: It is desired to have transistors that operate like superconductors in the on-state so that no energy gets lost due to Joule heating. This property also eliminates the need for sophisticated cooling systems.
- **Infinite frequency (instantaneous switching)**: Eliminating inductive and capacitive parasitic are the keys to enhancing operational frequencies and increasing circuit speed. In the case of boost converters, for example, driving transistors at high frequencies diminishes the voltage they have to block in the off-state.
- **Zero switching losses**: Transistors operate by toggling between the on-state and the off-state. The energy loss due to switching can become significant at high frequencies and cause self-heating.

- **Infinite lifetime and zero degradation**: Having a switch that can last eternally removes worries about repairs and consequences due to unexpected failures.
- **Stability**: During its operation, a switch may experience harsh environmental conditions such as exposure to radiation and extreme temperature variations. An ideal switch preserves its characteristics after being exposed to extreme conditions.
- **Zero footprints and zero mass**: Devices that are as small as possible are desired to enhance the power density of electronic systems.

1.2 Emerging Materials for Opto- and Power Electronics Devices

In reality, having a transistor with all the above characteristics is impossible. Indeed, there are trade-offs between the metrics used to assess those properties. Devices that handle high power tend to operate at low frequencies; vice versa, switches meant for radio frequency (RF) circuits operate at high speed but have much lower breakdown voltages. Devices cannot achieve ideal properties, but the performance of power devices can be improved by increasing their breakdown voltage (power), speed (frequency), or efficiency. It is often the case that the improvement of one metric comes with the deterioration of other performance metrics.

Following the appearance of semiconductor devices in the middle of the twentieth century, silicon has dominated the fabrication of electronic components. As the primary material for device fabrication, silicon has been well studied and is currently approaching intrinsic limitations; in other words, it is increasingly complicated to improve the performance of electronic devices further when using silicon as the base material. As silicon nears its performance optimization points, it fails to meet the emerging requirements of electronic systems. With a bandgap of just

1.12 eV, silicon is not controllable at temperatures above 200 C because of the large concentration of intrinsic carriers.

The downscaling of electronics devices results in higher speed and reduced weight; however, it also leads to increased internal electric fields, which cause major reliability concerns. Improving the performance of transistors is challenging, but it remains an urgent need in a world that, more than ever, needs independence from fossil fuels due to rising environmental concerns. As an alternative to silicon, wide and ultrawide-bandgap semiconductors are attractive because their properties show the potential to fabricate high-power devices with reduced size and weight suitable for power electronics.

1.2.1 Wide-Bandgap Semiconductors

The primary wide-bandgap materials investigated in this work are 4H-SiC and Gallium nitride. Devices fabricated with these materials are already commercially available.

1.2.1.1 4H-Silicon Carbide

SiC is a material with a wide bandgap (3.26 eV at room temperature) and a large critical field; its ability to easily grow a thermal oxide is a plus for device fabrication [5]. It is a prominent material for its superior radiation hardness, large thermal conductivity, and resistance to chemical attack. There are multiple polytypes of SiC; the more prominent ones are the hexagonal 4H- and 6H-SiC [6]. 4H-SiC is preferred over 6H-SiC for its higher and more isotropic bulk mobility; 4H-SiC is also known to have the largest bulk bandgap and drift velocity [6]. One advantage that 6H-SiC has over 4H-SiC is its higher band offset with SiO_2, a characteristic desired for the

fabrication of MOSFETs [7].

1.2.1.2 Gallium Nitride

GaN is a semiconductor with a bandgap slightly larger than SiC (3.4 eV) and stands out because of its piezoelectric property. Once a challenge, the ability to dope GaN p-type [8] expands the space of devices fabricable with gallium nitride. GaN is receiving a lot of attention because of its capability to house the 2-dimensional electron gas (2DEG) which simultaneously has a high concentration and a high mobility (up to 1×10^{13} cm^{-2} and 2000 cm^2/V·s). Figure 1.3 shows a typical GaN high electron mobility transistor (HEMT) with its different epilayers and the location of the two-dimensional electron gas. The 2-DEG finds its origin in the difference in polarization between the GaN buffer layer and the AlGaN barrier layer subjected to tensile stress. The higher the alloy composition of the barrier layer is, the larger the electron's concentration in the 2-DEG, but extremely high alloy composition (>0.8) results in unstable structures. GaN and SiC substrates are the most desired for improved lattice matching and thermal performance, but those substrates are also the most expensive. In addition to the HEMT structures, the GaN MOSHEMTs [9] is considered for normally off devices.

1.2.2 Ultrawide-Bandgap Semiconductors

Wide-bandgap semiconductors (GaN and SiC) have successfully demonstrated their capabilities to expand the operational range of power electronic devices. Owing to the belief that the bandgap significantly boosts the Baliga figure-of-merit (BFoM) [10], ultrawide-bandgap semiconductors are currently under study for even higher power operational ranges. Other materials

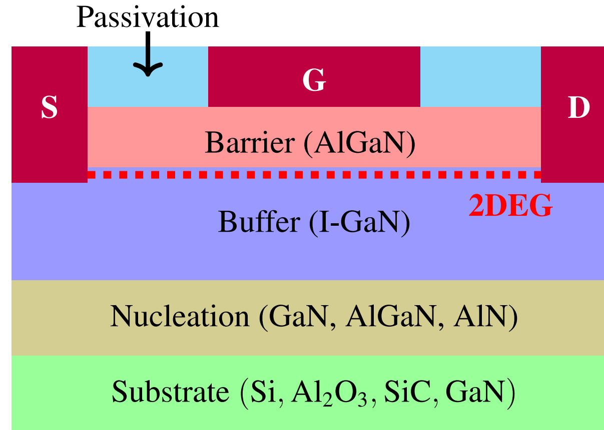

Figure 1.3: Typical structure of a GaN HEMT.

are also emerging as ultrawide-bandgap semiconductors ($MgGa_2O_4$, Al_2O_3, $ZnSiN_2$, $MgSiN_2$, and BN) [11], but the most prominent are diamond, β-Ga_2O_3, and AlGaN/AlN; this work investigates them.

1.2.2.1 Diamond

Diamond is an indirect bandgap material with its conduction band minimum at the X-point and its valence band maximum at the Γ-point. Atoms in diamonds are arranged following the face-centered cubic lattice configuration. In addition to its large bandgap (5.5 eV), diamond is known to have the highest thermal conductivity (2.2 kW mK^{-1} [12]) of all materials, a property tremendously advantageous for the thermal management of electronic devices. In diamond, both the electron and hole mobilities are higher than 2000 $cm^2V^{-1}s^{-1}$. Similar to silicon, diamond has six equivalent conduction band minima [13]. P-type doping of diamond with boron atoms using ion implantation is possible, but n-type doping by ion implantation results in crystal defects that are unrecoverable [14]. One of diamond's main drawbacks is its dopants' high ionization energy. Katamune et al. have reported n-type doping of diamond with phosphorous; they also mentioned

nitrogen as an alternate dopant with a much deeper level (1.7 eV) [14], which is challenging to ionize at room temperature.

1.2.2.2 $\beta-Ga_2O_3$

Ga_2O_3 (4.8 eV) is another promising ultrawide-bandgap semiconductor. It exists in five crystalline phases (α, β, γ, δ, and ϵ) with β-Ga_2O_3 being the most stable phase. While p-type doping remains a challenge in gallium oxide, n-type doping can be well modulated in the range of 10^{15}-10^{19} cm^{-3} [11]. Because it has a corundum crystal structure, high-quality β-gallium oxide crystals can be grown. Significant breakthroughs in the growth of Ga_2O_3 have been reported from the 1990s to the 2000s. The methods used to grow high-quality Ga_2O_3 include edge film-fed growth (EFG) [15–17] and homoepitaxial growth techniques such as halide vapor phase epitaxy (HVPE) [18–24]. It is also reported that β-Ga_2O_3 has a direct bandgap of 4.87 eV and a smaller indirect bandgap of 4.83 eV [25]. It is reported that holes in Ga_2O_3 have a large effective mass of 10 m_e, relating to the practical difficulty of achieving high hole mobility. As an oxide semiconductor, gallium oxide is inherently stable against oxidation.

1.2.2.3 $Al_xGa_{1-x}N$

A third promising ultrawide-bandgap material for electronics is $Al_xGa_{1-x}N$. When the alloy composition, x, is significant, the $Al_xGa_{1-x}N$ ternary is another ultra-wide bandgap material of interest for high-power opto-electronic applications. The direct bandgap of this class of materials ranges from 3.4 to 6.0 eV. While moderate n-type doping is achievable in $Al_xGa_{1-x}N$, p-type doping is poor. Just as for GaN, the growth of $Al_xGa_{1-x}N$ ternaries is challenging because of

the absence of single-crystal substrates with the quality necessary for epitaxial growth [11]. Aluminum gallium nitride is essential for optoelectronics because it enables the fabrication of deep ultraviolet photodetectors.

1.3 Advantages of Wide- and Ultrawide-Bandgap Semiconductors

Wide- and ultrawide-bandgap materials are desired to fabricate power electronics devices because their properties allow them to sustain operating conditions not achievable with silicon.

1.3.1 Advantages due to Material Properties

Better stability at elevated temperatures is one of the primary advantages of wide and ultrawide-bandgap semiconductors over silicon. At high temperatures (above 500 K), the intrinsic carrier concentration in silicon becomes so large that it starts to overshadow carriers added through the doping processes. The intrinsic carriers concentration for a given material is given by

$$n_i = \sqrt{N_C N_V} \exp^{(-Eg/2kT)}, \tag{1.1}$$

N_C and N_V are the density of states in the conduction and valence band, respectively. k is the Boltzmann's constant, and T is the temperature. The intrinsic carriers concentration is plotted in Fig. 1.4 for Si and selected WBG and UWBG semiconductors. Fig. 1.4(a) shows that the intrinsic carrier concentration of silicon is much higher than that of WBG and UWBG materials. As seen in Fig. 1.4(b), the intrinsic carrier concentration in silicon at 500 K is about 10^{14} cm^{-3} while it is still below 10000 cm^{-3} for WBG and UWBG materials.

WBG and UWBG materials can operate for a wide range of temperatures. Directly related

to the low concentration of intrinsic carriers, another advantage of Wide- and ultrawide- bandgap materials is that they exhibit low leakage current in the off-state. In theory, the diode reverse-saturation current could be as low as 10^{-45} Amps at room temperature as in the case of 4H-SiC; in practice, it is so low that it is below the resolution limits of most modern days measuring instruments. Low off-state leakage current implies the possibility of fabricating devices with a large area, allowing a boost of the on-state current drive capability of the devices while maintaining its off-state current insignificant.

WBG and UWBG materials can withstand high internal electric fields; when the bandgap is large, more energy is required to excite an electron from the valence band into the conduction band. Much higher electric fields are needed to trigger breakdown for materials with a larger bandgap. WBG and UWBG materials can handle large voltages within thinner layers, for they can support high internal electric fields. Because devices fabricated with WBG and UWBG materials can be made thin, high-frequency operations are possible because carriers have less travel distance. Having a semi-insulating substrate is advantageous for reducing parasitic capacitances, enabling high-frequency operations. Thin devices also imply low on-resistance and, consequently, less from joule heating and higher efficiency in terms of energy. Less joule heating could also alleviate the need for cooling requirements. In the boost converter shown in Fig. 1.2, if the switch M1 can operate faster, the passive components (inductors and capacitors) can be made smaller. Electronic systems that use devices fabricated with wide- and ultrawide-bandgap can be made significantly smaller due to the possibility of reducing the size of passive components (capacitors and inductors). Using wide- or ultrawide-bandgap materials to fabricate electronic systems results in simultaneously powerful and compact platforms, adding the convenience of portability and easy integration.

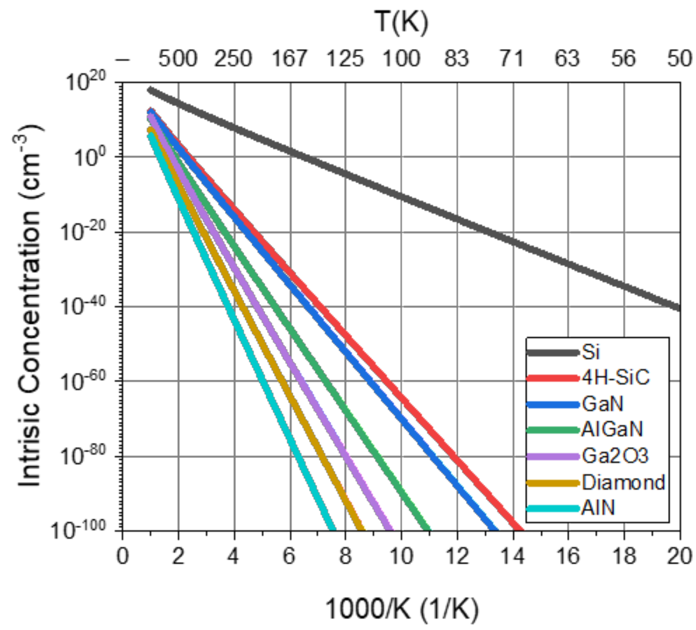

(a)

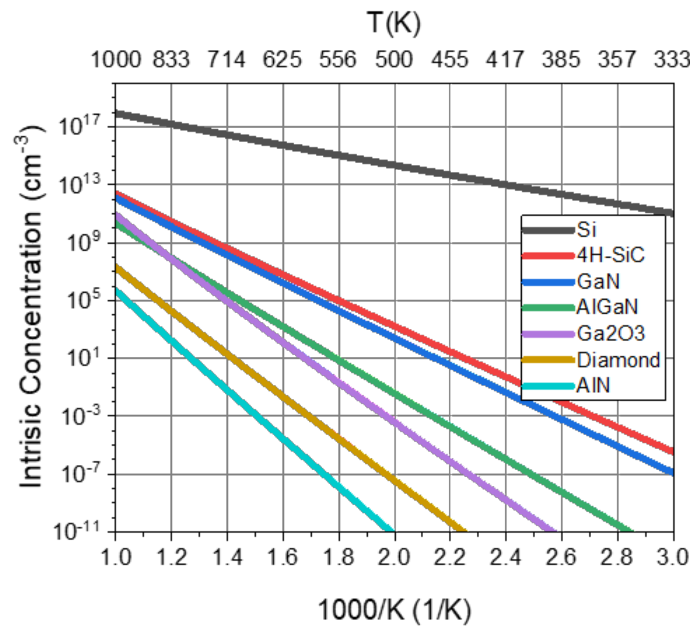

(b)

Figure 1.4: Intrinsic carriers' concentration as a function of the temperature from 50 K to 1000 K (a) and from 333 K to 1000 K (b). In (b) it is seen that at about 833 K, the intrinsic concentration in silicon becomes larger than 1×10^{17} cm^{-3}, suggesting the impracticability of silicon at elevated temperature.

1.3.2 Application Space for Wide- and Ultrawide-Bandgap Semiconductors

Given that wide- and ultrawide- bandgap semiconductors enable the realization of compact yet powerful electronics systems, they are excellent materials for medium- to high-power electronics, namely for fabricating power switches relevant for power conditioning. They are also suitable for the next generation of power devices and for implementing smart grids for power generation. They are also desired for optoelectronics because of the potential for low dark current, high optical gain, and high sensitivity [26]. They are excellent materials for the fabrication of solar blind ultra-violet photodetectors. $\beta-\mathrm{Ga_2O_3}$ has a wide range of applications, including semiconducting lasers, high-temperature gas sensors, switching memories, and field-effect devices [27, 28].

1.4 Assessing the Power Capabilities of Materials

As materials emerge for electronics applications, selecting a material for a specific application requires a ranking process. For power electronics, the Baliga figure-of-merit (BFoM) is the method most commonly used for evaluating the on-resistance versus breakdown voltage limits.

1.4.1 The Baliga Figure-of-Merit: A Metric Commonly Improperly Evaluated

Perhaps, the two most desired properties for power electronics is a low on-resistance and a high breakdown voltage. Devices with internal $p-n$ junctions block high voltages with low-doped materials and are, consequently, highly resistivities. The Baliga figure-of-merit is the metric commonly used to capture the trade-offs between the on-state resistance and the breakdown voltage of semiconductors. The balance between the on-resistance and the breakdown voltage

can be understood by considering Fig. 1.5 which shows the electric field profile at breakdown for a uniformly doped one-sided junction.

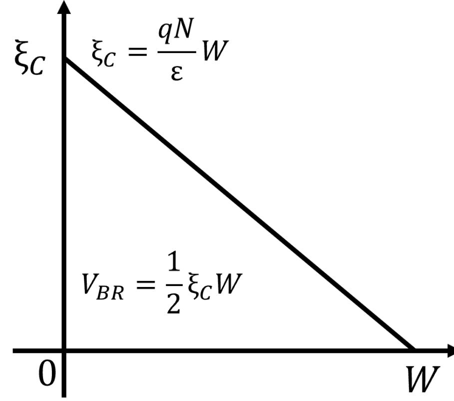

Figure 1.5: Schematic of the triangular electric field profile for the derivation of the Baliga figure-of-merit. The layer is assumed to be uniformly doped; at the breakdown, the width of the depleted region is W, and the maximum electric field is ξ_C.

The area of the triangle represents the voltage at breakdown, which is denoted V_{BR}. ξ_C is the critical field, the maximum electric field at breakdown. W is the depletion width at breakdown and can be expressed as

$$W = \frac{2V_{BR}}{\xi_C} \tag{1.2}$$

For a uniformly doped layer, the electric field profile is triangular, and the critical field is such that

$$\xi_C = \frac{qNW}{\epsilon}, \tag{1.3}$$

where N is the doping concentration. Combining (1.2) and (1.3), the doping concentration can be expressed as

$$N = \frac{\epsilon \xi_C}{qW} = \frac{\epsilon \xi_C}{q} \frac{\xi_C}{2V_{BR}}. \tag{1.4}$$

The electron charge is denoted with q, and ϵ is the permittivity of the medium. Using (1.2)

and (1.4) the on-resistance can be expressed as

$$R_{ON} = \frac{W}{q\mu N} = \frac{4V_{BR}^2}{\epsilon\mu\xi_C^3}. \tag{1.5}$$

The expression $\epsilon\mu\xi_C^3$ is the unipolar Baliga figure-of-merit (BFoM) for power devices; it captures the trade-off between the on-resistance and the breakdown voltage of materials. As seen in (1.5), materials with a larger BFoM exhibit a lower on-resistance for a given breakdown voltage. The Baliga figure-of-merit is used to rank material for power electronics, as seen in Fig. 1.6. Although the relationship between the on-resistance and the breakdown voltage prescribed by Baliga is accurate, the BFoM is commonly misevaluated.

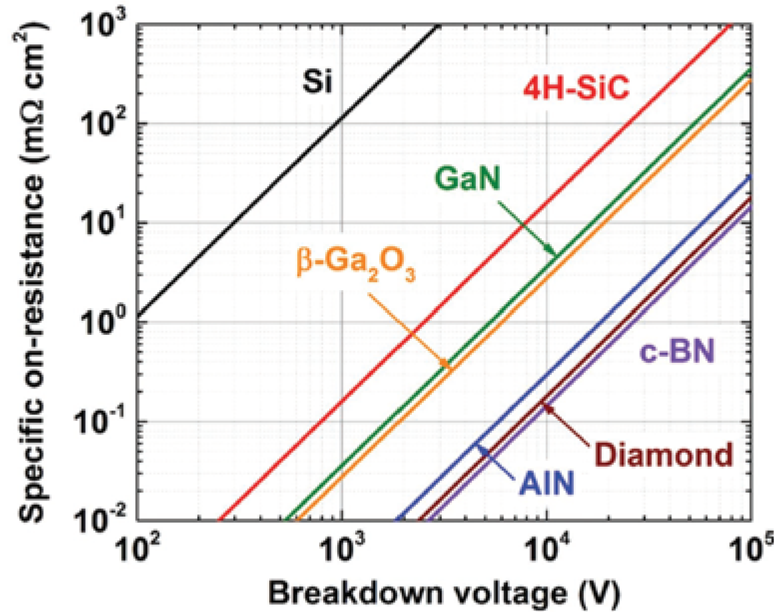

Figure 1.6: Calculated on-resistance versus breakdown voltage limits using the Baliga expression [11]. Failure to account for the effects of underlying physics on material properties results in parallel lines with a slope of 2.

It is common to assume that the critical field is a constant value for a given material; the reality is that it changes with the temperature, the doping of the i-layer, and the geometry of the

device. Similarly, the mobility, which depends on the temperature and the doping concentration, is assumed to be constant. The assumption of a constant critical field and a constant mobility results in Baliga limits that are parallel for all materials. Those limits are inaccurate as they overestimate the on-resistance versus breakdown voltage performance of devices.

1.4.2 Avalanche Breakdown: An Alternative for the Evaluation of the On-resistance Versus Breakdown Voltage Limits of Semiconductors

The Baliga figure-of-merit is a compact expression that captures the trade-offs between the on-resistance and the breakdown voltage of materials; however, it is commonly misevaluated. Also, the critical field is not a parameter readily available for evaluating the trade-offs. Using impact ionization coefficients to capture the breakdown voltage of materials eliminates the need for prior knowledge of the critical field. Impact ionization coefficients are defined as the number of electron-hole pairs generated when a carrier travels 1 cm of the material. When subjected to high electric fields, carriers in semiconductors can acquire enough energy to trigger an avalanche process pictured in Fig. 1.7. The figure illustrates a scenario where the field is oriented from right to left. An electron injected on the left gains sufficient energy to trigger an impact ionization collision, resulting in the creation of an electron-hole pair. After the impact ionization collision, there are three carriers, the hole moves toward the left, and the two electrons move toward the right. Under the force of the field, the three carriers become susceptible sources for new impact ionization events. The process can grow quickly, resulting in large currents and eventually breakdown.

Avalanche breakdown is non-destructive and is the mode of operation of avalanche photo-

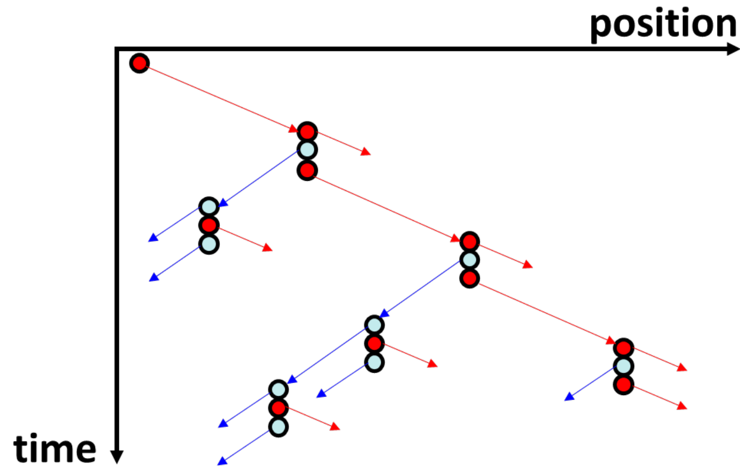

Figure 1.7: Special and time evolution of avalanche breakdown in semiconductors.

diodes. Given that the breakdown mechanism of the materials considered in this study is through the avalanche process (as opposed to Zener breakdown, which happens at high doping, high field, and small depletion widths [29]), using impact ionization coefficients to study carriers multiplication is a more fundamental yet more accurate approach to evaluate the breakdown voltage of a material. The breakdown voltage can be evaluated through the modeling of avalanche multiplication with impact ionization coefficients. Given the doping of a device and its geometry, the on-resistance can be assessed. Knowledge of the breakdown voltage and the on-resistance, evaluated as separate entities, allows the reconstruction of the Baliga figure-of-merit.

1.5 Literature Review and Scope

1.5.1 Literature Review

Concurrently to this work, Zhang et al. have investigated the effect of incomplete ionization on the on-resistance versus breakdown voltage figures-of-merit for power electronic devices [30].

Their work, however, focuses just on the incomplete ionization of the dopants and fails to address the avalanche breakdown process. Their modified Baliga's figure-of-merit treats the critical field as a constant material property. This work expands by providing the temperature dependence of the BFoM; furthermore, the work doesn't rely on existing critical field values, which are byproducts of the breakdown voltage calculation using impact ionization coefficients. Although prior knowledge of the critical field is not needed for calculations, other more basic material parameters are required for the study. Table 1.1 shows the different materials considered in this work with properties that are desired. The checkmarks indicate properties that are well established, while the cross-marks indicate properties that are not well defined. The marks' color also indicates the extent to which the properties are known. For example, a green checkmark indicates that the property has been studied in-depth and is well known. A yellow checkmark indicates that the property has been studied but requires attention, and a red check indicates properties that are available but are questionable. The yellow cross suggests that the properties are not well defined, and the red cross implies that the properties are not available.

The summary of existing material properties shown in Table 1.1 reveals the maturity of the different materials. Silicon is well known as it has been studied for many years. Wide-bandgap materials (4H-SiC and GaN) are gaining maturity. Still, the ultrawide-bandgap materials (the last three columns of the table) are challenging to study because they are relatively new materials with unknown properties. The six properties desired are listed in the table. Knowledge of the crystal type and the band structure is essential for characterizing carriers during transport. The band structure tells the effective mass of the carriers, the densities of states, and the energy dispersion; knowledge of those properties allows a proper understanding of carriers' responses to applied electric fields. Carriers-lattice interactions define the different scattering mechanisms relevant

Table 1.1: Maturity of some materials for electronics. For a given material, the checkmark indicates materials with somewhat established properties, and the cross mark indicates properties that are not so well defined. For entries with two marks, the first is for electrons and the second for holes.

	Si	4H-SiC	GaN	β-Ga_2O_3	Diamond	AlGaN
Crystal and band structure	✓ (green)	✓ (yellow)	✓ (red)	✗ (yellow)	✗ (yellow)	✗ (yellow)
Carriers-lattice Interactions	✓ (green)	✓ (yellow)	✓ (red)	✗ (yellow)	✗ (yellow)	✗ (yellow)
Impact ionization coefficients with temperature dependence	✓ ✓ (yellow, yellow)	✓ ✓ (red, red)	✓ ✗ (red, yellow)	✗ ✗ (yellow, red)	✗ ✗ (yellow, yellow)	✗ ✗ (yellow, yellow)
Mobility models with field, temperature, and doping dependence	✓ ✓ (green, green)	✓ ✓ (green, green)	✓ ✓ (green, green)	✓ ✗ (yellow, red)	✓ ✓ (yellow, yellow)	✓ ✗ (yellow, yellow)
Test structures availability	✓ ✓ (green, green)	✓ ✓ (green, green)	✓ ✗ (yellow, yellow)	✓ ✗ (green, red)	✗ ✓ (red, yellow)	✓ ✗ (yellow, yellow)
Doping feasibility and controllability	✓ ✓ (green, green)	✓ ✓ (green, yellow)	✓ ✓ (yellow, red)	✓ ✗ (green, red)	✗ ✓ (yellow, yellow)	✓ ✗ (yellow, yellow)

for the time evolution of carriers' energy. Impact ionization coefficients allow the modeling of semiconductors beyond Ohm's law; in this work, they are used to model the multiplication and calculate the breakdown voltage. Knowledge of electrons and holes' mobility as a function of the temperature, the electric field, and the doping concentration allows an accurate estimation of the on-resistance. For some materials, it is challenging to make junctions and test structures because of doping challenges.

1.5.2 Scope of the Dissertation

This work aims to develop a framework to properly evaluate electronic devices' on-resistance and breakdown voltage by accounting for incomplete ionization and considering avalanche break-

down. Following this introductory chapter, Chapter 2 discusses the incomplete activation of dopants and the impact of electric fields and temperature on the ionization of dopants. Using the Poisson equation, the extent of incomplete ionization is evaluated in substrates, $p - i - n$ diodes at zero bias, and $p - i - n$ diodes under reverse bias. Solving the Poisson equation yields the potential, the electric field profile, the concentration of ionized carriers, and the concentration of free carriers. In the case of reverse-biased junctions, the obtained electric field profile helps evaluate impact ionization coefficients. The calculated concentration of free carriers helps estimate the resistance of the device. Capacitance-voltage measurements performed at different temperatures on 4H-SiC avalanche photodiodes provide a mechanism to validate the model of incomplete ionization. The goal of Chapter 3 is to requisition data for the experimental portion of the work. Photo multiplication measurements are made on 4H-SiC avalanche photodiodes, on which deep-level transient spectroscopy analysis is performed to assess the nature of the dark current. Chapter 4 discusses the values of impact ionization coefficients needed to evaluate the breakdown voltage. The temperature and electric-field dependence of the coefficients are formulated with a modified Thornber model whose parameters are calibrated with impact ionization coefficients surveyed from the literature, experimentally extracted multiplications, and measured breakdown voltages. The chapter also discusses the ionization integral and the calculation of the breakdown voltage of $p - i - n$ diodes as a function of the doping concentration and the thickness of the i-layer. For each of the materials under investigation, the temperature dependence of the unipolar on-resistance is assessed using the concentration of free carriers calculated in Chapter 5. Additionally, the theoretical breakdown of $p - i - n$ diodes made with each of the materials investigated is calculated as a function of the temperature, leading to an improved assessment of the on-resistance versus breakdown voltage limits of wide-bandgap and ultrawide-

bandgap semiconductors as a function of the temperature. Chapter 6 discusses the effects of impact ionization coefficients, the on-resistance, and the breakdown voltage on the operation of power- and opto-electronics devices. The efficiency of power electronic systems is evaluated using on-resistance and breakdown voltage calculations performed in Chapter 5. Because the diodes are opto-electronic devices, their optical performance is evaluated via measurements of responsivity, quantum efficiency, and single-photon detection efficiency. Chapter 6 serves as the conclusion that discusses a few applications, summarizes the main findings of the work, and highlights venues worth exploring.

Chapter 2: Study of Incomplete Ionization as a Function of Electric Field and Temperature for a More Accurate Assessment of the Resistance

Capturing the power performance of wide- and ultrawide-bandgap semiconductors with the Baliga figure-of-merit is challenging because the process requires knowledge of the mobility and the critical field, two parameters that are not constant for a selected material. Though temperature and doping-dependent mobility models exist for semiconductors, It is not possible to know the critical field beforehand. It is, however, possible to evaluate the power performance of semiconductors by evaluating the breakdown voltage and the on-resistance as two separate entities. While the breakdown voltage can be assessed by modeling the avalanche multiplication process, the on-resistance can be evaluated with the geometry of the devices and the concentration of free electrons and holes. This chapter is devoted to studying the incomplete activation and ionization of dopants in materials to properly evaluate the concentration of free electrons and holes relevant to assessing the on-resistance. Because incomplete ionization is modeled with the Poisson equation, details are also provided on the nature of field profiles needed for evaluating impact ionization coefficients and breakdown voltages in Chapter 5.

The chapter initially discusses the Poisson equation and its use to calculate electric field profiles resulting from a given distribution of charges due to doping. The depletion approximation and the assumption that all carriers are ionized are discussed as a faster approach to calculating

electric field profiles. The devices considered for the study are $p-i-n$ structures because they can reproduce the internal electric field profiles that arise in most electronic devices under various applied bias conditions. Also, $p-i-n$ structures, in practice, can be easily taken to avalanche mode because the absence of a metal-semiconductor interface limits the presence of defects that lead to reliability issues causing devices to fail before avalanche breakdown. Challenges related to the activation and the ionization of dopants are addressed as potential factors that can increase device resistance. Still using the Poisson equation, incomplete ionization is modeled and solved in bulk materials, junctions at zero bias, and junctions that are reversed biased.

Incomplete ionization in the substrate is sufficient to accurately evaluate the on-resistance within Baliga's framework, but the on-resistance should be assessed according to the configuration of the devices. For example, for a $p-n$ junction, the on-state is characterized by the diffusion of excess minority carriers. For avalanche photodiodes, the on-state could correspond to the quenching state where the device is reversed biased. Evaluating incomplete ionization in junctions at zero bias and in reverse-biased junctions is essential for capturing the on-resistance for various types of device configuration. This chapter ends with validating incomplete ionization with capacitance-voltage measurements performed as a function of the temperature on 4H-SiC $p-i-n$ diodes.

The Poisson equation is one of the four Maxwell equations; assuming the devices are not subjected to magnetic fields, the equation is sufficient to model devices in this work. It is expressed as

$$\nabla \cdot \overrightarrow{\xi} = \frac{\rho}{\epsilon}, \tag{2.1}$$

where ρ is the charge density, and ϵ is the permittivity of the selected material. The Poisson equation prescribes that the divergence of the electric field is proportional to the charge density. For semiconductors, the Poisson equation becomes

$$\nabla^2\phi = -\nabla \cdot \overrightarrow{\xi} = -\frac{q}{\epsilon}\left(p - n + N_D^+ - N_A^-\right). \tag{2.2}$$

The variables p and n are the concentration of free electrons and holes, respectively. N_D^+ and N_A^- are the concentration of ionized donors and acceptors, respectively. The following sections evaluate the charge density as a function of underlying assumptions.

2.1 Depletion Approximation and Full Ionization Assumptions

In $p - n$ junctions, the depletion approximation and the assumption that dopants are fully ionized simplify calculations. In semiconductors, the source of the charges relevant to the Poisson equation's formulation arises from free carriers and ionized dopants. In the depletion approximation, it is assumed that there are no free carriers in the depletion region, where the net charge is due to the concentration of ionized dopants. With the two approximations, the net charge within the depletion region is $N_D - N_A$ because p and n are both equal to zero. Outside the depletion region, the net charge is zero because $p = N_A$ and $n = N_D$. The Poisson equation within the depletion region simplifies to

$$\nabla^2\phi = -\nabla \cdot \overrightarrow{\xi} = -\frac{q}{\epsilon}\left(N_D - N_A\right), \tag{2.3}$$

Depending on the selected doping and its thickness, two types of electric field profiles can

generally appear in $p-i-n$ diodes: the triangular field profile and the rectangular field profile.

2.1.1 Triangular Field Profile in $p-i-n$ Diodes

Fig. 2.1 shows the typical schematic of the $p-i-n$ structure with an internal triangular field profile. The diode has three layers and consists of a lowly doped n-type layer (n^-, doped N_{D1}), also called the i-layer or drift layer, sandwiched between a heavily doped p-type (p^+, doped N_A) and heavily doped n-type (n^+, doped N_{D2}) layers. If the two space-charge regions in the i-layer don't merge (this happens at high doping and large thickness), the structure consists of seven regions. When the space charge region is fully depleted of free carriers, the electric field and the potential are calculated by integrating over the fixed charges. It is important to note that the $n^- - n^+$ junction is strictly not depleted but has a space charge region.

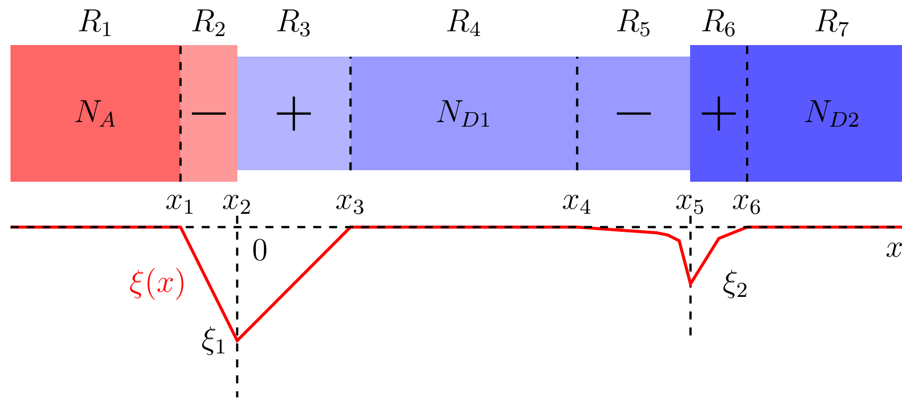

Figure 2.1: Typical triangular field profile (not drawn to scale) within a $p-i-n$ structure. Seven regions are defined to study the electric field and the electric potential.

The equations modeling the electric field profile, $\xi(x)$, and the potential, $V(x)$, within each of the seven regions are summarized in Table 2.1. The seven regions are denoted by R_1 to R_7. The two interfaces formed by the three layers are spatially located at x_2 and x_5. The space charge regions are delimited by x_1, x_3, x_4 and x_6. The slopes of the electric field are given by

$m_1 = (qN_A/\epsilon)$, $m_2 = (qN_{D1}/\epsilon)$, and $m_3 = (qN_{D2}/\epsilon)$. N_A, N_{D1}, and N_{D2} are the doping levels in the p$^+$-layer, n$^-$-layer, and n$^+$-layer, respectively. The dielectric constant of the selected material is denoted by ϵ. V_A is the reverse bias applied to the diode, and ϕ_p is the bulk potential in the quasi-neutral p-region of the $p-i-n$ diode. The total potential is $V_{TOT} = V_{bi1} + V_{bi2} + V_A$. The quality ϕ_p, V_{bi1}, V_{bi2}, are given by

$$\phi_p = V_T \ln\left(\frac{n_i}{N_A}\right) \tag{2.4}$$

$$V_{bi1} = V_T \ln\left(\frac{N_A N_{D1}}{n_i^2}\right) \tag{2.5}$$

$$V_{bi2} = V_T \ln\left(\frac{N_{D2}}{N_{D1}}\right) \tag{2.6}$$

Table 2.1: Mathematical equations to model the electric field (triangular profile) and the potential in $p-i-n$ structures.

	The field, ξ(x)	The potential, $V(x)$
R_1:	0	ϕ_p
R_2:	$m_1(x_1 - x)$	$-0.5m_1(x_1 - x)^2 + \phi_\mathrm{p}$
R_3:	$m_2(x - x_3)$	$-0.5m_2(x - x_3)^2 - V_A + \phi_p$
R_4:	0	$V_{bi1} - V_A + \phi_p$
R_5:	$m_2(x - x_4)$	$-0.5m_2(x - x_4)^2 + V_{bi1} - V_A + \phi_p$
R_6:	$m_3(x_6 - x)$	$-0.5m_3(x_6 - x)^2 + V_{TOT} + \phi_p$
R_7:	0	$V_{bi} + V_{bi2} - V_A + \phi_p$

2.1.2 Trapezoidal Field Profile in $p-i-n$ Diodes

The equations summarized in Table 2.1 cease to be valid when the two space-charge regions originating from the two interfaces start to merge. In this context, the extension of the depletion

region in the p$^+$ and n$^+$ side of the junction cannot be calculated a priori. To compute the electric-field profile, its trapezoidal shape illustrated in Fig. 2.2 is considered, and charge neutrality is applied across the structure. Denoting the extension of the depletion width in the p$^+$ and n$^+$ regions by w_1 and w_2, respectively, charge neutrality requires that

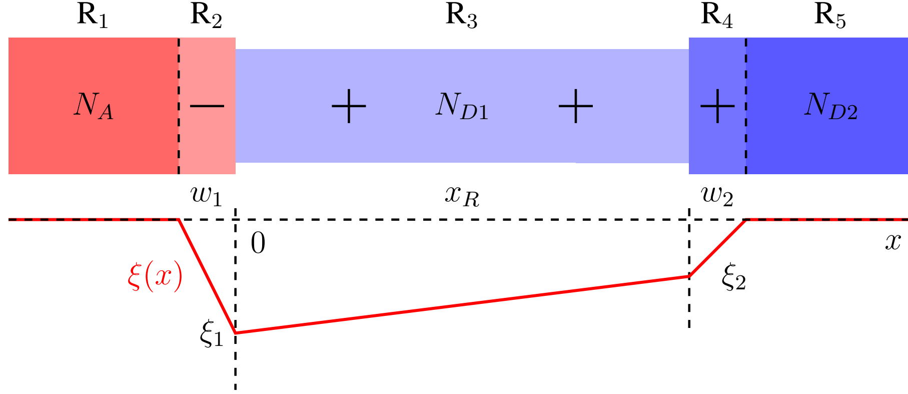

Figure 2.2: Trapezoidal field profile (not drawn to scale) within a $p-i-n$ structure. As the two space charge regions merge, the structure can be described with five regions.

$$w_1 N_A = x_R N_{D1} + w_2 N_{D2}. \tag{2.7}$$

Since the area under the electric field curve gives the potential, the applied bias, V_A, is such that

$$Area = \frac{\xi_1 (w_1 + x_R)}{2} + \frac{\xi_2 (w_2 + x_R)}{2}, \tag{2.8}$$

and

$$Area \approx V_A + V_{bi1} + V_{bi2} \approx V_{TOT}. \tag{2.9}$$

The peak electric fields at the two interfaces are denoted by

$$\xi_1 = \frac{qN_A}{\epsilon} w_1 \tag{2.10}$$

and

$$\xi_2 = \frac{qN_{D2}}{\epsilon} w_2. \tag{2.11}$$

Combining (2.7), (2.8), and (2.9), w_2 can be obtained by solving the following quadratic equation (See Appendix A for derivation of the quadratic)

$$Aw_2^2 + Bw_2 + C = 0. \tag{2.12}$$

With the constants A, B, and C given by

$$A = \frac{qN_{D2}}{\epsilon}\left(\frac{N_A + N_{D2}}{N_A}\right), \tag{2.13}$$

$$B = 2x_R \frac{qN_{D2}}{\epsilon}\left(\frac{N_A + N_{D1}}{N_A}\right), \tag{2.14}$$

$$C = \frac{qN_{D1}}{\epsilon}\left(\frac{N_{D1} + N_A}{N_A}\right) x_R^2 - 2V_{TOT}. \tag{2.15}$$

V_{bi1} and V_{bi2} are the built-in potentials at the p^+-n^- and the n^--n^+ junction, respectively.

Under the depletion approximation, the charges in the different layers appear constant. Performing an integration over the charges gives the electric field profile, and a second integration gives the electric potential. The calculated electric field profile is relevant for evaluating impact ionization coefficients. We will see in the next section that the depletion approximation provides an almost accurate field profile as if incomplete ionization was taken into consideration. The problem with the approximations is that it fails to inform on the concentration of dopants that have

ionized. Before modeling incomplete ionization, it is relevant to discuss the partial activation of the dopants.

2.2 Incomplete Activation of Dopants: A factor that Increases Resistance

2.2.1 Definition and Modeling of Incomplete Activation

The previous section shows that the doping concentration is essential when formulating the Poisson equation for semiconductors. The doping concentration, N_D, for the case of an n-type doped material, is the result of multiple material processing steps. Figure 2.3 illustrates the problem of incomplete activation. When impurities are incorporated into the material, some dopants remain in interstitials and are inactive, while some substitute host atoms in their lattice site and become active. The fraction of inactive dopants in interstitials constitutes the source of incomplete activation. After being activated, only a fraction of dopants in the lattice site will get ionized depending on the position of the Fermi level.

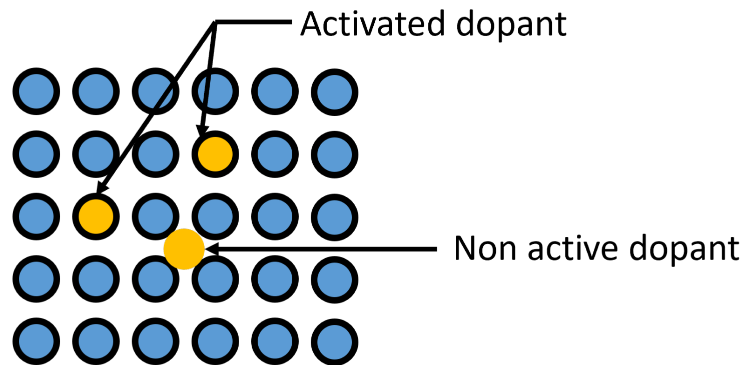

Figure 2.3: Illustration of incomplete activation is semiconductors.

The concentration of active dopants depends on the doping process and should be the concentration to consider when evaluating incomplete ionization in semiconductors. After the ma-

terial has been doped, an annealing process usually helps with the activation of the dopants. To model incomplete activation, we define new terms.

We refer to $N_D^{'}$ and $N_A^{'}$ as the total amount of impurities in the host material for n-type and p-type doping, respectively. The usual N_D and N_A will denote the concentration of active dopants. The concentration of dopants that are not active because they are in interstitials is denoted by N_D^i and N_A^i for electrons and holes, respectively. The concentration of ionized dopants is given by N_D^+ and N_A^- for n-type and p-type doping, respectively. The concentration of active but non-ionized dopants is given by N_D^0 and N_A^0 for p-type and n-type doping, respectively. The total number of added dopants should equal the sum of active and inactive dopants. We have that

$$N_D^{'} = N_D + N_D^i \text{ and } N_A^{'} = N_A + N_A^i. \tag{2.16}$$

The active dopants can either be ionized or not; it results that $N_D = N_D^+ + N_D^0$ and $N_A = N_A^- + N_A^0$. The activation fraction is defined as Υ_D and Υ_A for donors and acceptors, respectively. We can also write that

$$N_D = \Upsilon_D N_D^{'} \text{ and } N_A = \Upsilon_D N_A^{'}. \tag{2.17}$$

Υ_D and Υ_A are between 0 and 1. If the dopants are fully activated, we have that $\Upsilon_{D,A} = 1$. Υ_D and Υ_A are evaluated by comparing the concentration of free carriers modeled theoretically and the concentration of free carriers extracted from Hall measurements. The concentration of free carriers obtained from Hall measurements for an n-type material is given by

$$n_{meas} = \frac{1}{\mu_{Hall} r q \rho_m}, \tag{2.18}$$

where μ_{Hall} is the Hall mobility, r is the Hall factor, and ρ_m is the resistivity of the material. It will be shown in Section 2.4 that the theoretical concentration of free carriers, n_{theo}, can be deduced from the charge neutrality equation and is given by

$$n_{theo} = p + N_D^+ - N_A^-, \tag{2.19}$$

where the concentration of ionized donors, N_D^+, is expressed as

$$N_D^+ = \frac{\Upsilon_D N_D'}{1 + g_D \exp(\Delta E_D/kT)\dfrac{n}{N_C}}, \tag{2.20}$$

where g_D is the factor that accounts for spin and conduction degeneracies; ΔE_D is the energy of the dopants relative to the conduction band; N_C is the density of states in the conduction band, and n is the concentration of free carriers in the conduction band (see section 2.3.2) [31]. Samples with lower activation ratios are expected to be more resistive and display low concentrations of free carriers (n_{meas}) when probed experimentally with Hall measurements. The lower values of the measured free carriers concentration reflect on the theoretical modeling with lower values of Υ_D.

2.2.2 Dopants Incomplete Activation in p-type Doped 4H-SiC

The theory of incomplete activation in 4H-SiC has been experimentally observed thanks to the work of Darmody and Goldsman [31]. The two main methods for doping 4H-SiC include ion implantation and epitaxial growth. For epitaxial growth, the dopants are fully activated (Υ_D and Υ_A become 1). For ion implantation, only a fraction of the dopants gets activated. One way to

improve the activation of the dopants is to follow an annealing procedure following ion implantation. In 4H-SiC, the annealing is done at 1700 °C for 20 minutes; even then, the activation is still partial. Doping with epitaxial growth leads to 100 % activation, but the need to perform selective doping imposes the need for doping via ion implantation.

In the Section 2.2.1, we proposed an approach for evaluation the incomplete activation ratio. Given the availability of test structures, the approach is applicable to 4H-SiC, where Hall mobilities and sample resistivities have been measured and modeled as a function of the doping concentration, allowing the extraction of the concentration of free carriers. The Hall mobility for p-type SiC [31] is shown in Fig. 2.4 and is modeled as

$$\mu_{Hall} = \frac{109.6}{1 + \left(\frac{N_A}{2.92 \times 10^{18}}\right)^{0.6335}} \text{ cm}^2\text{V}^{-1}s^{-1}. \tag{2.21}$$

The measured resistivity in p-type 4H-SiC samples is summarized in Fig 2.5. The samples on which doping was performed using ion implantation appear more resistive and are represented by the outliers of Fig. 2.5. The figure shows that the samples doped with ion implantation are about ten times more resistive, indicating that $\Upsilon_D = 0.1$.

Combining Hall mobility and resistivity measurements, it is possible to estimate the fraction of ionized dopants. The data available in the literature shows that up to 90% of dopants in p-type 4H-SiC can be inactive when doped using the ion implantation method. The incomplete activation of dopants remains a challenge for wide-bandgap and ultrawide-bandgap semiconductors. The samples used for the experimental portion of this work were doped using epitaxial growth; in this case, the challenge is not about dopants' activation but their ionization.

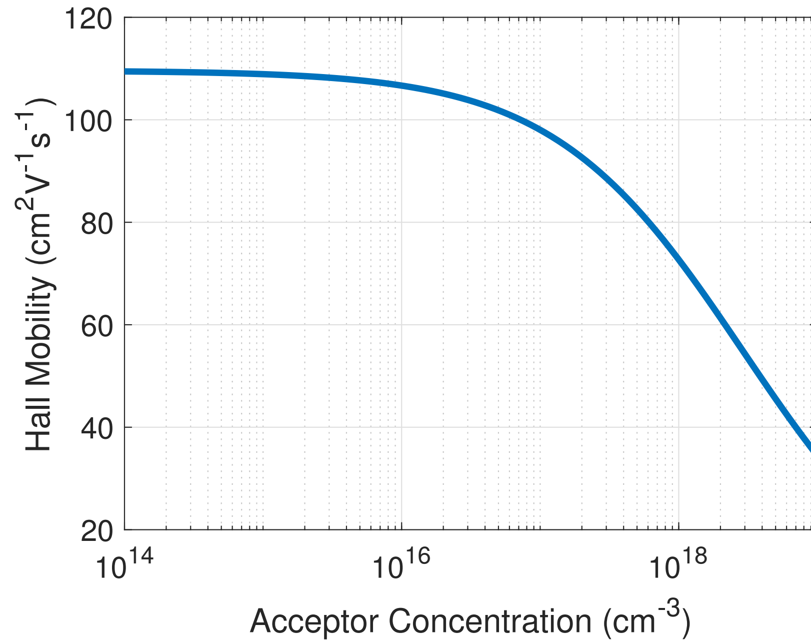

Figure 2.4: Proposed model for the hall mobility in 4H-SiC as a function of the doping concentration. The proposed Hall mobility and the measured resistivity allow the finding of the concentration of free carriers in the sample and the activation ratio.

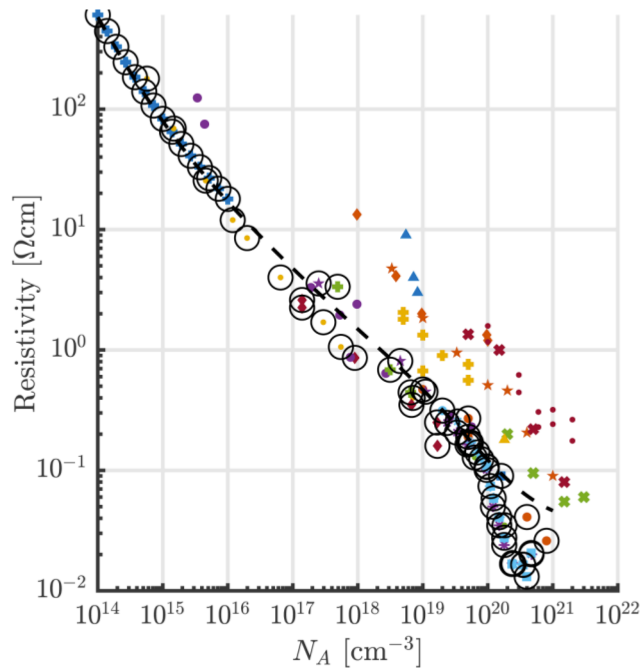

Figure 2.5: Measured resistivity of p-type 4H-SiC samples as a function of the doping concentration. The outliers represent samples doped using ion implantation. A higher resistivity is indicative of a lower activation fraction [31].

2.3 Incomplete Ionization in the Bulk of Wide- and Ultrawide-Bandgap Semiconductors

2.3.1 Ionization Energy of Wide-Bandgap and Ultrawide-Bandgap Semiconductors

The concentration of ionized dopants can be obtained by solving the Poisson equation. An accurate calculation required knowledge of the concentration of active dopants and the ionization energy of the dopants. Only a fraction of dopants is active with ion implantation, and the samples are more resistive. With epitaxial growth, all the dopants get activated. The ionization energy of the dopant is essential when calculating the concentration of ionized dopants as described in (2.29) and (2.29). Surveying the literature, the ionization energies for the materials investigated in this work are summarized in Table 2.2.

Table 2.2: Reported dopants ionization energy for wide- and ultrawide-bandgap semiconductors.

Material	n-dopants	E_D (meV)	p-dopants	E_A (meV)	(g_D, g_A)
Silicon [32]	Phosphorous	45.5	Boron	44.39	(2, 4)
4H-SiC	Nitrogen	55 [33]	Aluminum	210 [33]	(2, 4)
GaN	Silicon [34]	20 [30]	Magnesium	160 [33]	(2, 4)
Diamond [35]	Phosphorous	570	Boron	370	(2, 4)
β-Ga_2O_3	Tin	30 [30]	–	–	(2, –)
AlN [36]	Silicon	280 [30]	Carbon	500 [37]	(2, 4)

From the table, it is seen that the ultrawide-bandgap materials tend to have high activation energies. The exceptionally high ionization energy of diamond suggests ionization difficulties and high resistance. The table has missing entries because p-type doping of Ga_2O_3 is still challenging.

The ionization energy changes with the doping concentration; the Pearson-Barden model

is proposed for the doping dependence of the ionization energy. Table 2.2 gives the ionization energy at moderate doping concentrations; at high doping concentrations, the ionization energy becomes zero (the Mott transition); more details on the ionization of carriers can be found in the work of Darmody and Goldsman [31]. The doping dependence of the ionization energy is given by

$$E_{D,A} = E_0 - aN^{1/3} \text{ eV}, \tag{2.22}$$

where the parameters E_0 and a are provided in Table 2.3 for the materials investigated in this work. The doping concentration is represented by N and is valid for n- and p- type doping.

Table 2.3: Proposed parameters of the Pearson-Barden model for the doping dependence of the ionization energy.

	n-type		p-type	
Material	E_0 (meV)	a (eV · cm)	E_0 (meV)	a (eV · cm)
Si	45.63	5.95×10^{-9}	44.52	5.81×10^{-9}
4H-SiC	55.73	7.27×10^{-9}	212.8	2.78×10^{-8}
GaN	20.26	2.64×10^{-9}	162.1	2.12×10^{-8}
Diamond	579.5	7.56×10^{-8}	376.2	4.91×10^{-8}
β-Ga_2O_3	30.5	3.98×10^{-9}	–	–
AlN	284.7	3.71×10^{-8}	508.4	6.63×10^{-8}

2.3.2 Modeling of Incomplete Ionization with the Poisson Equation

When devices are doped with the epitaxial growth, the dopants are fully activated; however, the ionization of dopants remains a challenge. To model incomplete ionization, we use the Poisson equation without making assumptions. The Poisson equation is given by 2.23, where p is the total concentration of free holes in the valence band, and n is the total concentration of

electrons in the valence band.

$$\nabla^2 \phi = -\nabla \cdot \overrightarrow{\xi} = -\frac{q}{\epsilon}\left(p - n + N_D^+ - N_A^-\right), \tag{2.23}$$

It is no longer assumed that the space charge region is fully depleted of free carriers; instead, the concentration of free carriers is modeled as follows:

$$p = p_i e^{(E_i - E_F)/kT} = N_V e^{(E_V - E_F)/kT}. \tag{2.24}$$

For the concentration of free electrons, we have that

$$n = n_i e^{(E_F - E_i)/kT} = N_C e^{(E_F - E_C)/kT}. \tag{2.25}$$

The concentration of mobile (free) carriers can also be written as $p = p_i e^{(\phi_F - \phi_i)/V_T}$ and $n = n_i e^{(\phi_i - \phi_F)/V_T}$. Defining the band-bending as $\phi = \phi_i - \phi_F$, it results that

$$p = p_i e^{-\phi/V_T} \text{ and } n = n_i e^{\phi/V_T}. \tag{2.26}$$

The concentration of free carriers for electrons and holes is conveniently expressed as a function of the local potential in (2.26). This is useful when formulating the Poisson equation that can be expressed as a function of the local potential, ϕ.

The dopants ionize when the impurities atoms donate electrons to the conduction band (in the case of donors) or receive holes from the valence band (in the case of holes). The concentration of ionized donor, N_D^+, is proportional to the number of empty states in the conduction

band, and the concentration of ionized acceptors is proportional to the number of occupied states in the valence band. The Fermi distribution, $f(E)$, describes the occupation probability. The concentration of ionized dopants is given by

$$N_A^- = N_A f(E_A) \text{ and } N_D^+ = N_D \left(1 - f(E_D)\right), \tag{2.27}$$

where the effective adjusted Fermi functions are such that

$$\begin{cases} f(E) = \dfrac{1}{1 + g_A \exp^{(E-E_F)/kT}} \\ 1 - f(E) = \dfrac{1}{1 + g_D \exp^{(E_F-E)/kT}}. \end{cases} \tag{2.28}$$

Where g_A and g_D are parameters that account for spin and band degeneracies for electrons in the conduction band and holes in the valence band, respectively [31]. Combining (2.27) and (2.28), the concentration of ionized acceptors can be further expressed as

$$\begin{aligned} N_A^- &= \frac{N_A}{1 + g_A e^{(E_A-E_F)/kT}} \\ &= \frac{N_A}{1 + g_A e^{(E_A-E_F+E_V-E_V)/kT}} \\ &= \frac{N_A}{1 + g_A e^{(E_A-E_V)/kT} e^{(E_V-E_F)/kT}} \\ &= \frac{N_A}{1 + g_A e^{\Delta E_A/kT} \dfrac{p}{N_V}} = \frac{N_A}{1 + \dfrac{p_i g_A}{N_V} e^{\Delta E_A/kT} e^{-\phi/V_T}}, \end{aligned} \tag{2.29}$$

Following a similar derivation, the concentration of ionized donors can be expressed as

$$N_D^+ = \frac{N_D}{1 + \dfrac{n_i g_D}{N_C} e^{\Delta E_D/kT} e^{\phi/V_T}} \tag{2.30}$$

For a semiconductor not subjected to an external bias, the Poisson equation becomes

$$\nabla^2\phi = -\frac{q}{\epsilon}\left(p_i e^{-\phi/V_T} - n_i e^{\phi/V_T} + \frac{N_D}{1+K_D e^{\phi/V_T}} - \frac{N_A}{1+K_A e^{-\phi/V_T}}\right), \tag{2.31}$$

where

$$K_A = \frac{p_i g_A}{N_V} e^{\Delta E_A/kT} \text{ and } K_D = \frac{n_i g_D}{N_C} e^{\Delta E_D/kT}. \tag{2.32}$$

The concentration of ionized dopants is a function of the local potential. The Poisson equation, which includes the concentration of free carriers and ionized dopants, becomes a second-order differential equation with the potential as the main variable. Solving (2.31) allows the evaluation of incomplete ionization. The equation is solved for the bulk of selected materials (equilibrium case). After evaluating incomplete ionization in bulk, the study is extended to junctions at zero bias. The equation is also modified to include the effect of reverse biases for the modeling of incomplete ionization in reversed biased junctions.

2.3.3 Accounting for Incomplete Ionization in the Charge Neutrality Equation

A uniformly doped semiconductor is neutral. When unbiased, there is no electric field or electric potential within the material, and the LHS of the Poisson equation can be set to zero. The Poisson equation becomes the charge neutrality equation with the potential as the primary unknown. The equation is

$$\nabla^2\phi = p_i e^{-\phi/V_T} - n_i e^{\phi/V_T} + \frac{N_D}{1+K_D e^{\phi/V_T}} - \frac{N_A}{1+K_A e^{-\phi/V_T}} = 0, \tag{2.33}$$

Here the ϕ is a constant and is related to the position of the Fermi level. It is possible to

solve (2.33) graphically as shown on Fig. 2.6 for a 4H-SiC n-type doped substrate (N_A = 0 and N_A^- = 0).

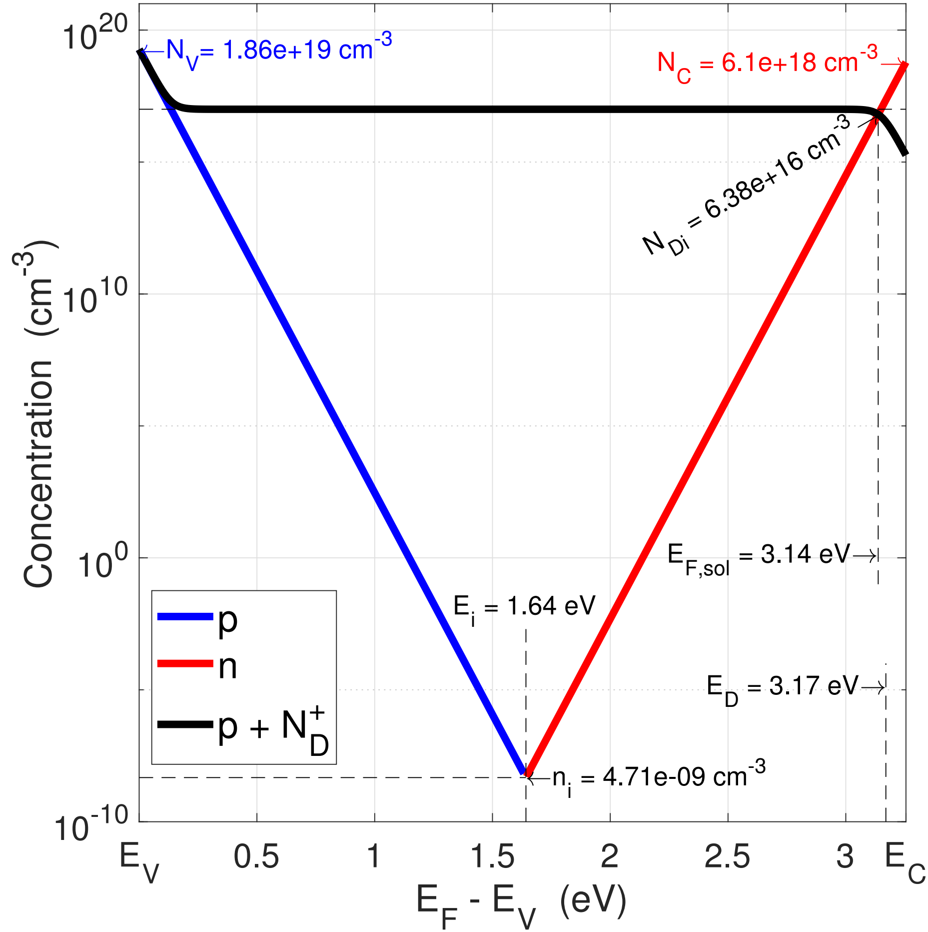

Figure 2.6: Graphical finding of the ionized dopant concentration in an n-type doped 4H-Si substrate at T = 300 K. The concentration of active dopants is 1×10^{17} cm^{-3}; the concentration of ionized dopants is 6.38×10^{16} cm^{-3}.

Solving (2.33) is similar to finding the Fermi level in the material. Note that the potential ϕ represents the potential difference between the Fermi level and the intrinsic level ($\phi = \phi_i - \phi_F = (E_F - E_i)/q$). In Fig. 2.6 the Fermi level, E_F, is swept between the valence band and the conduction band (bandgap). For an n-type substrate, $N_A^- = 0$, and the solution is such that the concentration of free electrons (the red line) equals the concentration of free holes added to the concentration of ionized donors ($n = p + N_D^+$). The intrinsic energy (E_i) and the intrinsic

concentration (n_i) can also be visualized from the figure at the intersection of p and n. The intrinsic energy level is slightly closer to the conduction band (not at the midgap) because holes have a higher effective mass than electrons in 4H-SiC, resulting in a lower density of states in the conduction band (N_C).

The calculated Fermi level for an n-type doped 4H-SiC substrate is shown below on Fig. 2.7. The indicated Fermi level is relative to the position of the intrinsic energy level and decreases with increasing temperature. As the temperature increases, the Fermi level is lowered and brought closer to the intrinsic level; however, the concentration of ionized dopants increases with temperature because the concentration of intrinsic carriers increases significantly.

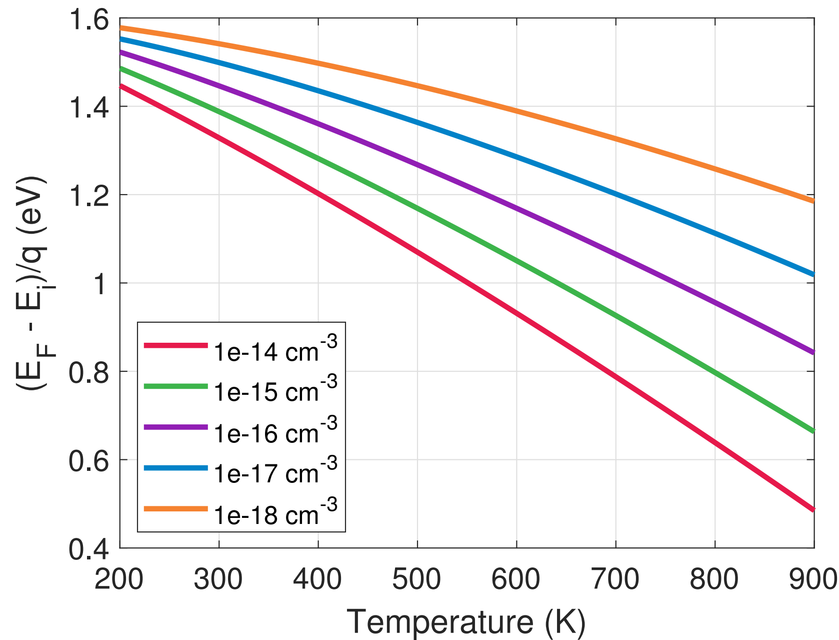

Figure 2.7: Temperature dependence of the Fermi level for n-type doped 4H-SiC substrates. The legend represents the doping concentration of the substrate.

For the case of a p-type substrate, the Fermi energy level is below the intrinsic energy level. When the temperature increases, the Fermi energy level moves up closer to the intrinsic energy level, as seen in Fig. 2.8.

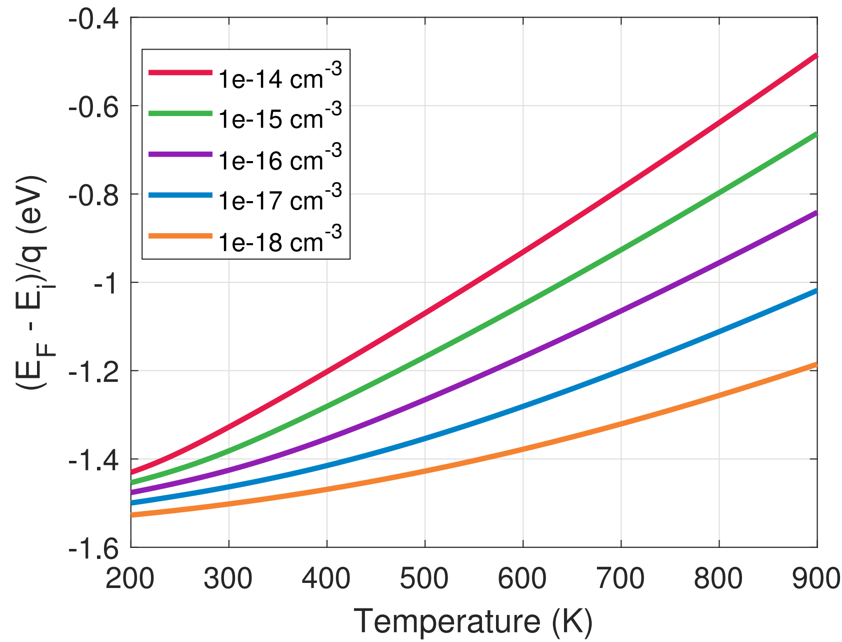

Figure 2.8: Temperature dependence of the ionization ratio in p-type doped 4H-SiC. The legend represents the doping concentration in the substrate.

Using the calculated Fermi level (potential), the ratio of ionized dopants to that of active dopants is calculated as a function of the temperature and presented in Fig. 2.9 for the case of n-type doped 4H-SiC substrates.

The calculated ionization ratio for acceptors in 4H-SiC is shown on Fig. 2.10. Unlike donors, acceptors have a high ionization energy; as a result, the ionization ratio in Fig. 2.10 is much worse than that in Fig. 2.9.

Incomplete ionization in p-type 4H-SiC substrates has been thoroughly investigated by Darmody and Goldsman; their model includes impurity conduction, density-of-states smearing, and energy spreading [31]. The results obtained in this work and those achieved by Darmody and Goldsman are summarized in Fig. 2.11 for p-type 4H-SiC doped with aluminum. The solid lines represent calculations performed in this work. In contrast, the dashed lines represent calculation results achieved by Darmody and Goldsman. The minor difference can be attributed to

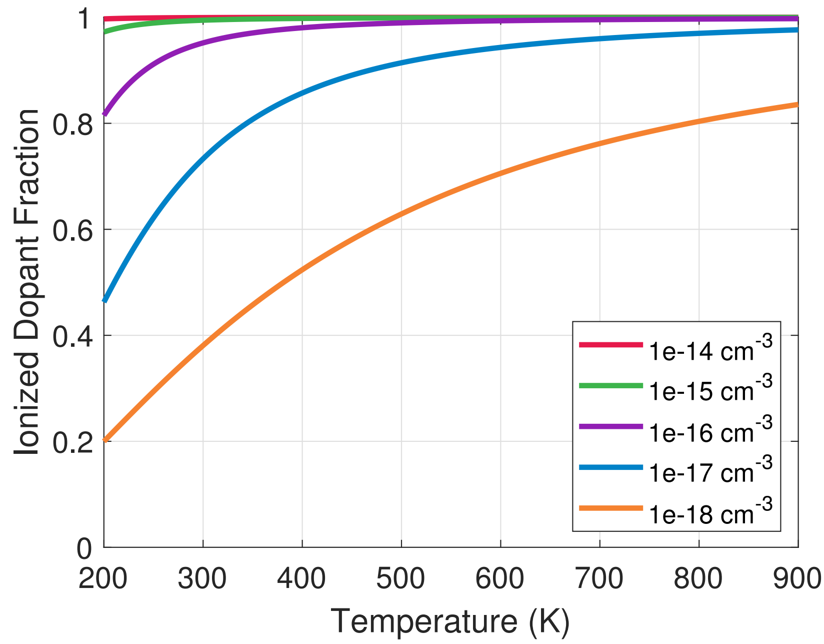

Figure 2.9: Temperature dependence of the ionization ratio in n-type doped 4H-SiC

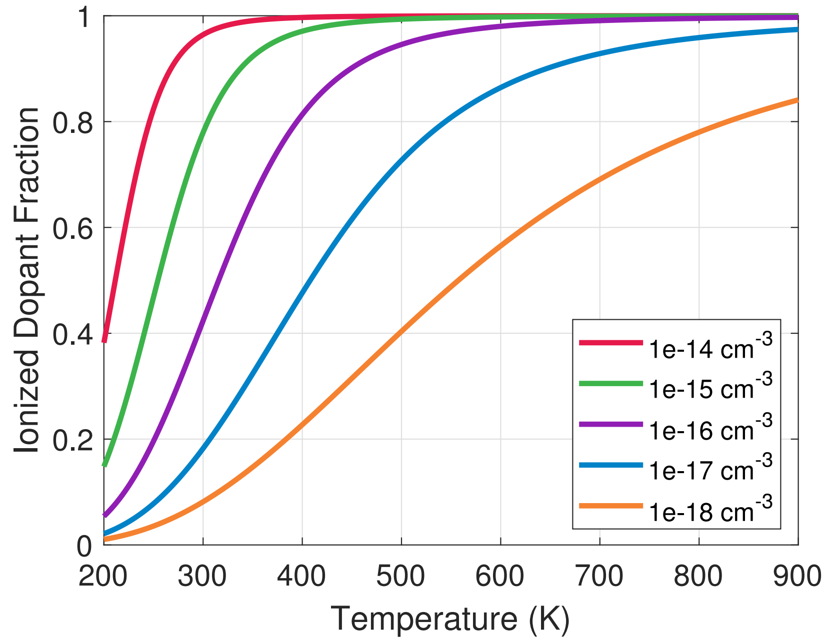

Figure 2.10: Ionized dopants fraction in p-type doped 4H-SiC as a function of the temperature

Darmody's more rigorous approach.

The calculation performed for 4H-SiC can be repeated for the materials investigated in this

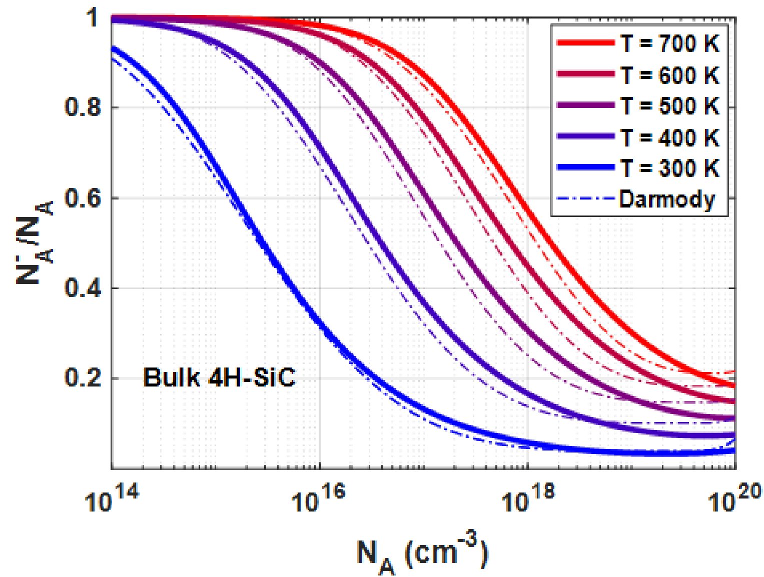

Figure 2.11: Incomplete ionization in p-type 4H-SiC. The solid lines represent the results achieved in this work. The dashed lines depict results obtained by Darmody and Goldsman.

work. Figure 2.12 shows the concentration of ionized dopants versus the concentration of active dopants for n-type doped substrate at 300 K and 500 K. The materials with higher ionization energy are observed to have a low ionization ratio.

For uniformly doped and unbiased substrates, there are no electric fields within the material. The incomplete ionization of dopants can be modeled with Poisson's equation which eventually turns into the charge neutrality equation. Calculations show that dopants don't get ionized when the ionization energy is large. It is seen that wide- and ultrawide-bandgap semiconductors tend to have high ionization energy, indicating that they can be very resistive. This is particularly true for n-type doped diamond whose resistance at room temperature can be 1000 times larger than what it would be if all the dopants had ionized. When the temperature increases, the ionization ratio increases; high-temperature operations can improve the power performance.

Capturing incomplete ionization in the substrate is enough to evaluate the on-resistance considered in the Baliga figure-of-merit. During operations, device resistance in the on-state is

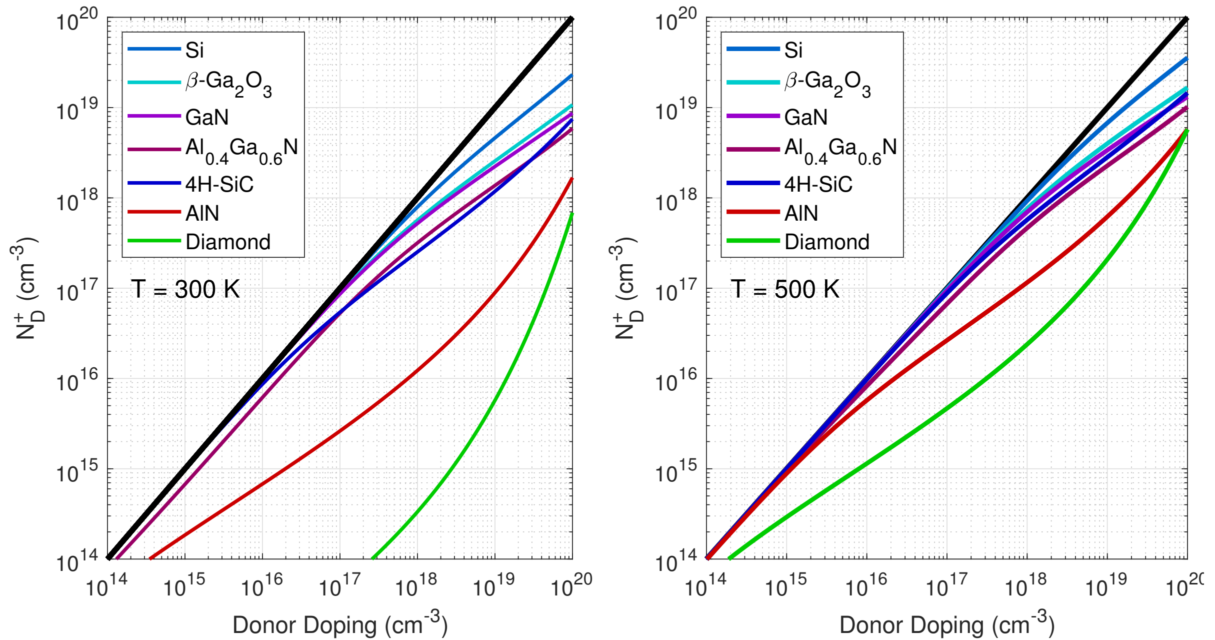

Figure 2.12: Impact of temperature on bulk incomplete ionization in WBG and UWBG semiconductors at 300 K (left) and 500 K (right). The black line represents the line $y = x$, which is the ideal limit for 100% dopant ionization.

not always within unipolar constraints. To accurately calculate the on-resistance for a wide range of devices, it is essential to study incomplete ionization in junctions. Once again, the $p-i-n$ structure is ideal because it provides convenience for studying the effects of electric fields and the temperature on the ionization of dopants.

2.4 Incomplete Ionization in Junctions

2.4.1 The Finite Difference Method for the Calculation of the Potential and the Concentration of Ionized Dopants

When junctions are formed, electric fields arise, and the charge neutrality equation can't longer be used to capture the concentration of ionized dopants. Solving the Poisson equation

allows finding the electric field, the electric potential, the concentration of free carriers, and the concentration of ionized dopants. The challenge here is that the formation of the junction gives rise to electric fields and potentials that are position dependent. The equation to be solved is a second-order non-linear differential equation with the electric potential as the primary variable; solving (2.31) requires a non-linear finite difference iterative computational method. Equation (2.31) is valid for junctions in the absence of an applied bias. It is solved using the non-linear finite difference iterative method. The second derivative of the potential ϕ evaluated at mesh point s neighbored by $s-1$ and $s+1$ in the framework of finite difference can be written as

$$\left.\frac{d^2\phi}{dx^2}\right|_{\phi_s} \approx \frac{\phi_{s-1} - 2\phi_s + \phi_{s+1}}{\Delta x^2} \tag{2.34}$$

A non uniform mesh scheme, illustrated in Fig. 2.13 is essential for speedy calculations. The second derivative for a non-uniform mesh scheme is such that

$$\left.\frac{d^2\phi}{dx^2}\right|_{\phi_s} \approx \frac{2}{h_1\left(h_1+h_2\right)}\phi_{s-1} - \frac{2}{h_1 h_2}\phi_s + \frac{2}{\left(h_2\left(h_1+h_2\right)\right)}\phi_{s+1} \tag{2.35}$$

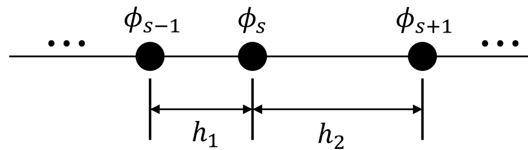

Figure 2.13: Non-uniform mesh for the calculation of the potential using finite difference.

The Poisson's equation, as given by (2.31) can be discretized and evaluated at selected positions within the $p-i-n$ structure to be simulated. By discretizing the Poisson equation, it

is possible to define a function $F = F(\phi_{s-1}, \phi_s, \phi_{s+1})$ such that

$$F = \frac{d^2\phi}{dx^2}\bigg|_{\phi_s} + \frac{q}{\epsilon}\left(p_i e^{-\phi_s/V_T} - n_i e^{\phi_s/V_T} + \frac{N_D}{1 + K_D e^{\phi_s/V_T}} - \frac{N_A}{1 + K_A e^{-\phi_s/V_T}}\right). \tag{2.36}$$

Solving for the potential ϕ is similar to making $F(\phi_{s-1}, \phi_s, \phi_{s+1}) = 0$. This is achieved by using the Newton method. At each mesh point s we have that

$$-F(\phi_{s-1}, \phi_s, \phi_{s+1}) = \sum_{l=-1}^{1} \frac{\partial F(\phi_{s-1}, \phi_s, \phi_{s+1})}{\partial \phi_{s+l}} \Delta\phi_{s+l} \tag{2.37}$$

The potential is solved iteratively using (2.37). The potential profile obtained using the depletion approximation is a good initial value for the electric potential. At each mesh point, there is one equation with three unknowns; all the equations arising at the mesh points of the system can be tabulated in a matrix equation of the form $Ax = -F_s$ as shown in (2.41). A is the large matrix on the left-hand side of (2.41) and represents the Jacobian matrix. The unknown vector to be solved is x; it represents the incremental error in the electric potential at each mesh points. The elements of the vector x become very small when Poisson's equation is satisfied at each mesh point. The iteration is stopped when all the elements of x are below a certain threshold (1×10^{-8} V). The vector F_s on the right-hand side is evaluated with (2.36); the vector F also captures the boundary conditions.

For a potential profile, the function $F(\phi_{s-1}, \phi_s, \phi_{s+1})$, which is a function of three variables is evaluated at each mesh point to form the vector F_s. The mesh points are numbered s, ranging from 1 to N. The error in the electric potential is obtained by solving the matrix equation given by (2.41). As boundary conditions (for the case of a $p - i - n$ structure), in the absence

of an external bias, the electric potential on the first mesh point on the heavily doped p-side is the bulk potential (calculated assuming incomplete ionization in the bulk as previously discussed in Section 2.3.3). The electric potential on the heavily doped n-side is also calculated with incomplete ionization in the substrate. The Jacobian matrix is obtained by evaluating three partial derivatives at each mesh point.

Except for the two outmost mesh points, each mesh point s has an environment similar to the illustration of Fig 2.13 but with different values of h_1 and h_2. The three partials that set the coefficients $a_s,\ b_s,$ and c_s are given by (2.38), (2.39), and (2.40), respectively. Solving (2.41) gives the potential profile $\phi(x)$. From the electric potential profile, the concentration of ionized dopants is calculated as a function of position. Additionally, the potential allows the calculation of the concentration of free carriers as a function of position. The derivative of the potential gives the electric field profile (multiplied by minus one), which is denoted $\xi(x)$. The equations capture the temperature dependence of the potential and the other byproducts of the calculations through the intrinsic carrier concentration, n_i, and the thermal voltage V_T.

$$a_s = \frac{\partial F}{\partial \phi_{s-1}}\Big|_s = \frac{2}{h_1(h_1+h_2)}\Big|_s, \tag{2.38}$$

$$\begin{aligned} b_s = \frac{\partial F}{\partial \phi_s}\Big|_s = \frac{-2}{h_1 h_2} - \frac{1}{V_T}\left(\frac{qp_i \exp^{-\phi_s/V_T}}{\epsilon} + \frac{qn_i \exp^{\phi_s/V_T}}{\epsilon}\right)\Big|_s \\ + \left(\frac{N_D K_D e^{\phi_s/V_T}}{(1+K_D e^{\phi_s/V_T})^2} + \frac{N_A K_A e^{-\phi_s/V_T}}{(1+K_A e^{-\phi_s/V_T})^2}\right)\Big|_s \end{aligned} \tag{2.39}$$

$$c_s = \frac{\partial F}{\partial \phi_{s+1}}\Big|_s = \frac{2}{h_2(h_1+h_2)}\Big|_s \tag{2.40}$$

$$\begin{bmatrix} 1 & 0 & 0 & 0 & \cdot & \cdot & \cdot & 0 & 0 & 0 \\ a_2 & b_2 & c_2 & 0 & & & & 0 & 0 & 0 \\ 0 & a_3 & b_3 & c_3 & & & & 0 & 0 & 0 \\ 0 & 0 & a_4 & b_4 & c_4 & & & 0 & 0 & 0 \\ \cdot & & & \cdot & \cdot & \cdot & & & & \cdot \\ \cdot & & & & \cdot & \cdot & \cdot & & & \cdot \\ \cdot & & & & & a_{N-3} & b_{N-3} & c_{N-3} & 0 & 0 \\ 0 & & & & & & a_{N-2} & b_{N-2} & c_{N-2} & 0 \\ 0 & & & & & & 0 & a_{N-1} & b_{N-1} & c_{N-1} \\ 0 & \cdot & \cdot & \cdot & \cdot & \cdot & 0 & 0 & 0 & 1 \end{bmatrix} \begin{bmatrix} \Delta\phi_1 \\ \Delta\phi_2 \\ \Delta\phi_3 \\ \Delta\phi_4 \\ \cdot \\ \cdot \\ \Delta\phi_{N-3} \\ \Delta\phi_{N-2} \\ \Delta\phi_{N-1} \\ \Delta\phi_N \end{bmatrix} = - \begin{bmatrix} 0 \\ F_2 \\ F_3 \\ F_4 \\ \cdot \\ \cdot \\ F_{N-3} \\ F_{N-2} \\ F_{N-1} \\ 0 \end{bmatrix} \tag{2.41}$$

Equation 2.41 can be arranged for multiple layers junctions in forward and reverse bias.

2.4.2 Effects of Temperature on the Incomplete Ionization of Dopants in $p - i - n$ Diodes at Zero Bias

The finite difference method provides a way to solve the discretized Poisson's equation when there is no equilibrium. Fig. 2.14 shows the calculation results for a 4H-SiC $p-i-n$ structure at room temperature. The simulated structure is such that the heavily p-type doped region is 0.1 μm and doped at N_A = 1×10^{18}cm^{-3}. The i-layer is doped n-type at N_D =2×10^{17} cm^{-3} and is 2 μm thick. The second cladding layer is heavily n-type doped at N_{D2} = 1×10^{18} cm^{-3} and is 0.1 μm thick. The vertical dashed lines represent the two junctions of the device. The calculations

yield the potential profile, the concentration of free electrons and free holes, the concentration of ionized dopants, and the electric field profile, which is the derivative of the electric potential. The concentration of free carriers is seen to invalidate the depletion approximation; the concentration of free electrons n becomes very small when observing the depletion region from left to right but is not zero. In the p^+ region, the concentration of ionized acceptors is seen to be about just 2×10^{16} cm^{-3} for an active doping concentration of 1×10^{18} cm^{-3}.

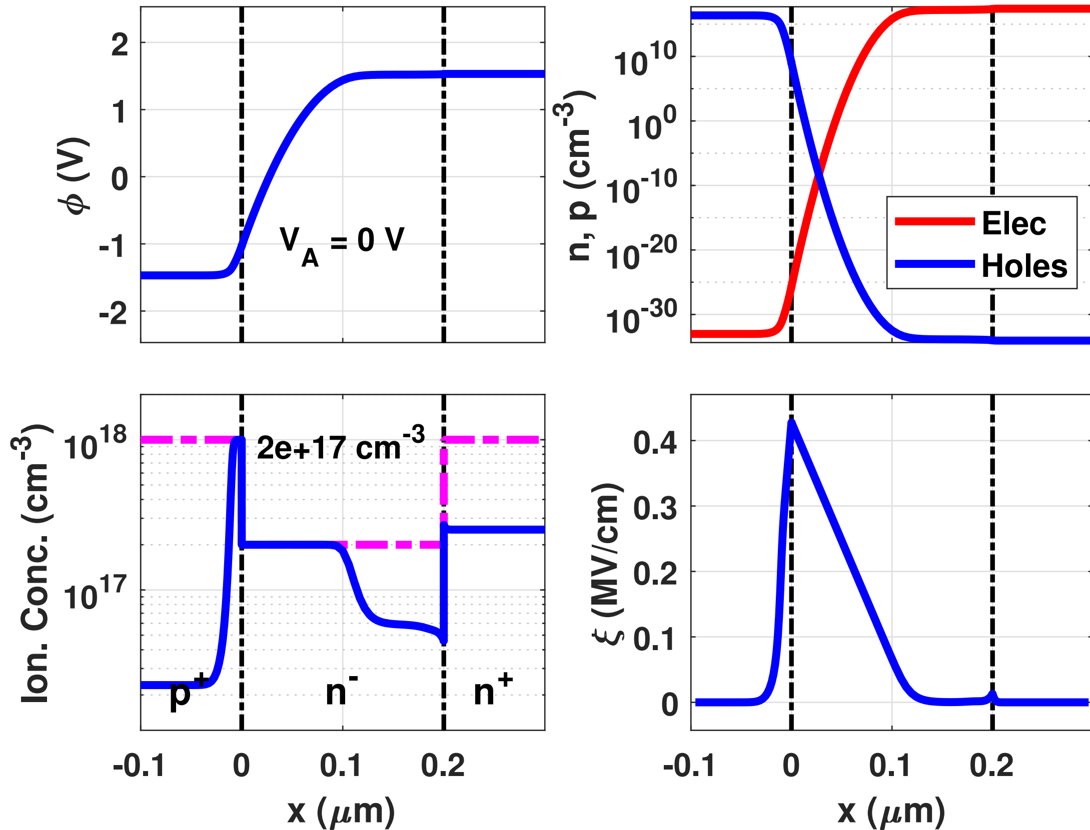

Figure 2.14: Simulated potential (ϕ), free carriers concentration (n, p), ionized dopants concentration (N_D^+, N_A^-), and electric field (ξ) in a 4H-SiC $p-i-n$ diode at 300 K.

It is seen that the electric field extends into part of the p^+ region, causing the complete ionization of active acceptors. In the n^- regions, the part of the i-layer that is not depleted is seen to suffer from incomplete ionization; The phenomenon, which could be termed ionization erosion, is an essential factor to consider when modeling device capacitance.

The calculated potential profile within the $p-i-n$ structure is shown in Fig. 2.15. The simulation of the potential is performed as a function of the temperature with 4H-SiC as the based material. Since there is no external bias applied, this potential profile gives the built-in potential of the $p-i-n$ structure. It is seen that the built-in potential decreases with the temperature. When the temperature increases, the thermal voltage and the intrinsic carrier concentration have competing effects on the built-in potential, but the effects of the intrinsic carrier concentration are more pronounced, resulting in the decrease of the built-in potential with increasing temperature.

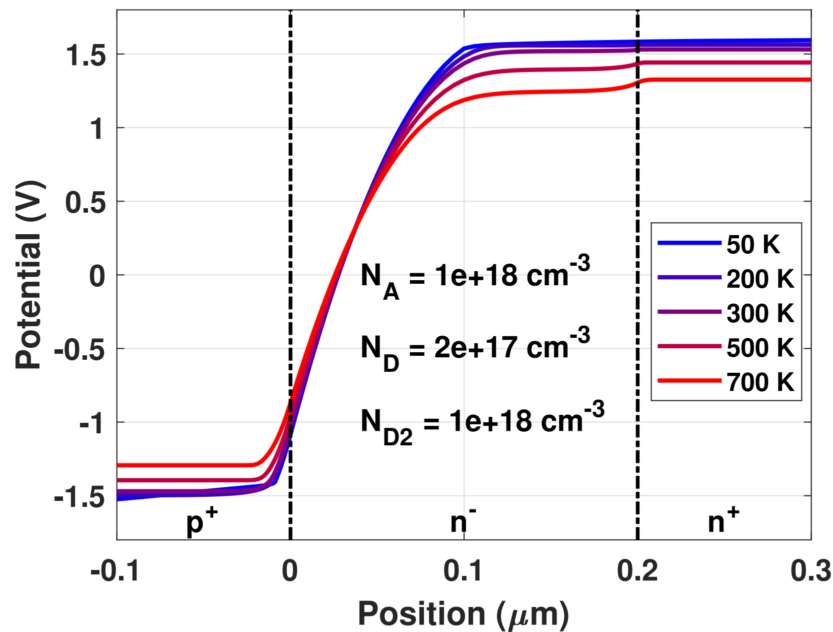

Figure 2.15: Simulated potential profile of a $p-i-n$ diode as a function of temperature. The results are shown for 4H-SiC at zero bias.

The electric field profile obtained by evaluating the derivative of the potential is shown in Fig. 2.16. One would expect higher electric fields at elevated temperatures because of the higher ionization of dopants. It is seen that the peak electric field decreases with increasing temperatures. The increase in temperature enhances the intrinsic carrier concentration, thus lowering the built-in potential that shapes the field profile.

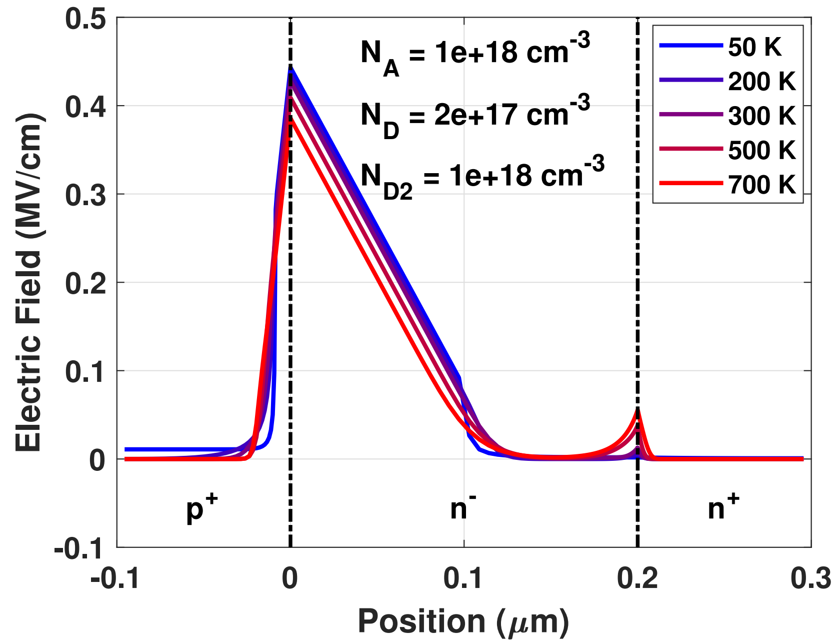

Figure 2.16: Simulated temperature dependence of the electric field within a $p-i-n$ diode at zero bias. The calculated electric field profile considers the incomplete ionization of the dopants.

The concentration of ionized dopants is shown in Fig. 2.17 for a $p-i-n$ structure with 4H-SiC as the base material. The i-layer is doped n-type at 2×10^{17} cm^{-3}. It is seen that the field promotes the ionization of dopants. In the depletion region, the concentration of ionized dopants is equal to the concentration of active dopants. It is also seen that the effect of the temperature on the field within the depletion region is insignificant; carriers don't freeze out in the depletion region.

As the electric field fades out, going away from the active junction, the impact of temperature on the incomplete ionization of dopants becomes noticeable, and the concentration of ionized dopants settles to what it should be in the substrate. The calculation shows that the dopants in the space-charge region tend to be fully ionized while dopants in the quasi-neutral region of the device are partially ionized. Since the electric field strongly promotes the ionization of dopants, assuming that dopants are fully ionized when calculating the electric field results in minor errors.

If finding the electric field is the only thing that matters, it may not be necessary to model incomplete ionization to obtain an accurate field profile. However, the series resistance is affected by incomplete ionization; this is discussed later in the thesis in Section 3.1.2. Despite dopants ionization challenges, the formation of junctions is still possible because built-in electric fields are enough to promote complete ionization in the space close to the junction.

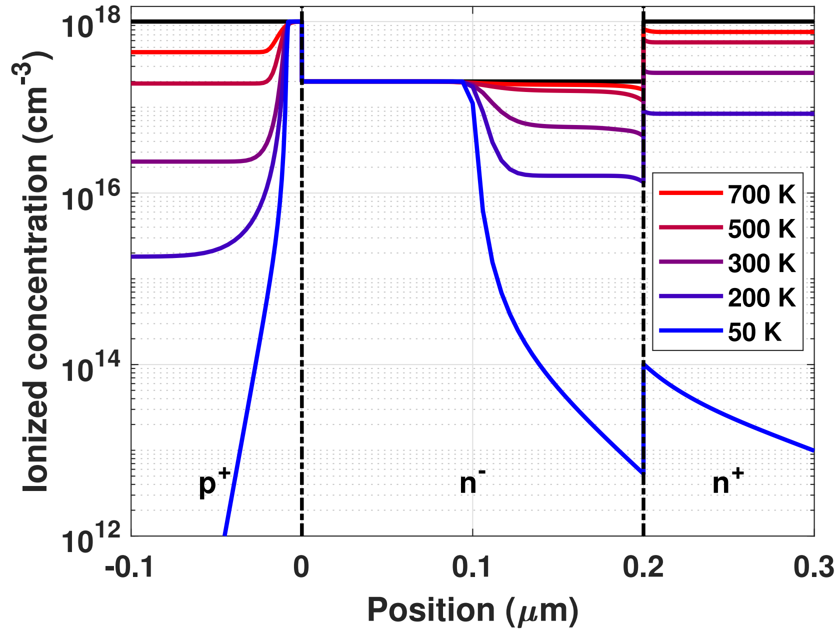

Figure 2.17: Simulated profile of the concentration of ionized dopants as a function of the temperature.

2.4.3 Electric Potential, Electric Field, and Incomplete Ionization in Reverse Biased $p-i-n$ Diodes

In the previous sections, incomplete ionization is studied on substrates materials and junctions in equilibrium. The study of incomplete ionization on substrates is enough to capture the unipolar on-resistance through Baliga's framework. The study of incomplete ionization in junc-

tions at zero bias gives insight into the internal field and the distribution of charges within the structure. It is essential to gain a similar understanding on devices subjected to reverse bias measurements. The study of incomplete ionization in reverse bias conditions is important because the on-state of some devices could be when they are reverse biased. For avalanche photodiodes, the on-state could correspond to Geiger mode operation, where the diode is biased to avalanche breakdown. Knowledge of the field and the distribution of charges within the devices allow accurate modeling and prediction of device performance. For avalanche photodiodes, the knowledge of the effective resistance and the effective capacitance in avalanche mode leads to the accurate modeling of the RC constant, which predicts how fast a device can quench.

When a bias is applied across the junction, the Fermi splits as shown in Fig. 2.18. The figure shows the effects of a reverse bias V_A on the band diagram of a $p-n$ junction. The shaded region represents the difference between the midgap and the Fermi level, represented by ϕ in this work; the difference can be expressed in terms of energy and potential.

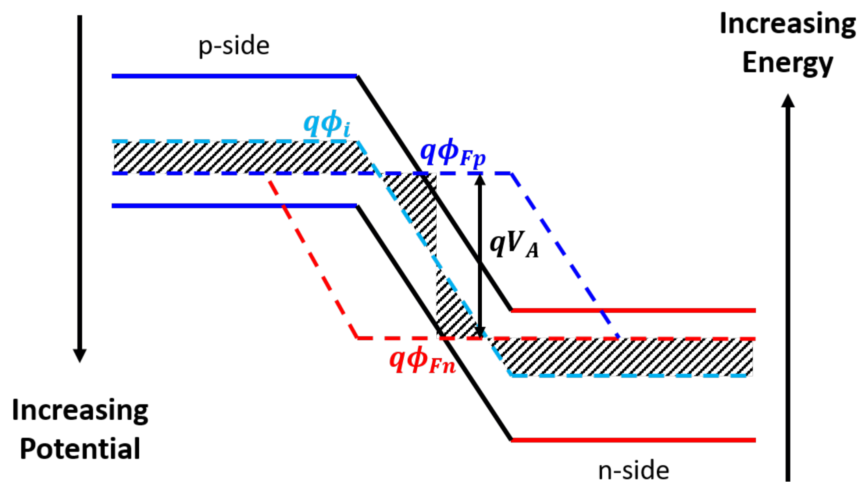

Figure 2.18: Location of the quasi-Fermi level for a $p-n$ junction under a reverse bias condition.

Under reverse bias, the Fermi level is shifted by qV_A; this is true not just for the p-n junction

but also for the $p-i-n$ structures. In this work, the p-region is used as the reference, and the Fermi level in the n-region is offset to capture the applied bias; that is $\phi_{Fp} = \phi$ and $\phi_{Fn} = \phi - V_A$. By accounting for the reverse bias, the Poisson equation can be written as

$$\nabla^2\phi = -\frac{q}{\epsilon}\left(p_i e^{-\phi/V_T} - n_i e^{(\phi-V_A)/V_T} + \frac{N_D}{1+K_D e^{(\phi-V_A)/V_T}} - \frac{N_A}{1+K_A e^{-\phi/V_T}}\right). \tag{2.42}$$

The non-linear finite difference method discussed earlier can be used to solve (2.42). The profile of the electric potential for a $p-i-n$ structure that used 4H-SiC as the base material is shown in Fig. 2.19 at a reverse voltage of 170 V. The inset figure shows that the temperature lowers the potential, but the effects of the temperature on the electric potential are insignificant because the reverse bias voltage is much larger than the built-in potential. For the reverse bias study, the thickness of the cladding layers is 0.1 μm, and the thickness of the drift region is 1.2 μm. The p^+ region is doped at 5×10^{18} cm^{-3}, the i-layer at 2×10^{17} cm^{-3}, and the n^+ region at 1×10^{18} cm^{-3}.

The electric field profile obtained by taking the derivative of the potential is shown in Fig. 2.20. It is seen that the temperature has a weak effect on the electric field profile because the built-in potential, which changes with temperature, is insignificant compared to the applied bias.

The concentration of ionized dopants in the $p-i-n$ structure is shown on Fig. 2.21. It is seen that the active dopants are getting fully ionized in the depletion region, and the temperature does not affect the concentration of ionized dopants. Because p-type dopants in 4H-SiC have a higher activation energy than n-type dopants, incomplete ionization is more pronounced in the quasi-neutral region of the p^+ side of the structure. It is also seen that the temperature promotes the ionization of dopants in the quasi-neutral region of the $p-i-n$ structure. Fig. 2.21 tells the

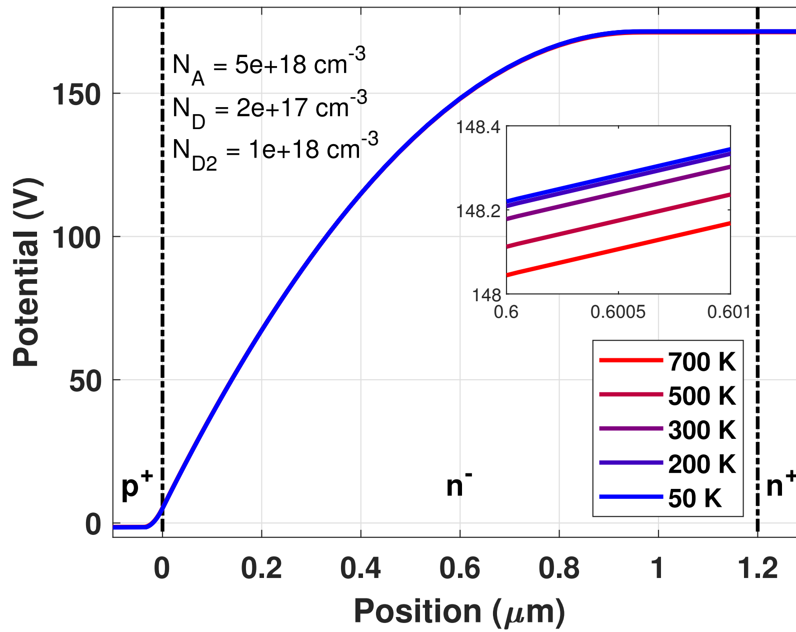

Figure 2.19: Electric potential's profile of a $p-i-n$ diode as a function of the temperature. The base material is 4H-SiC, and the applied reverse bias is 170 V.

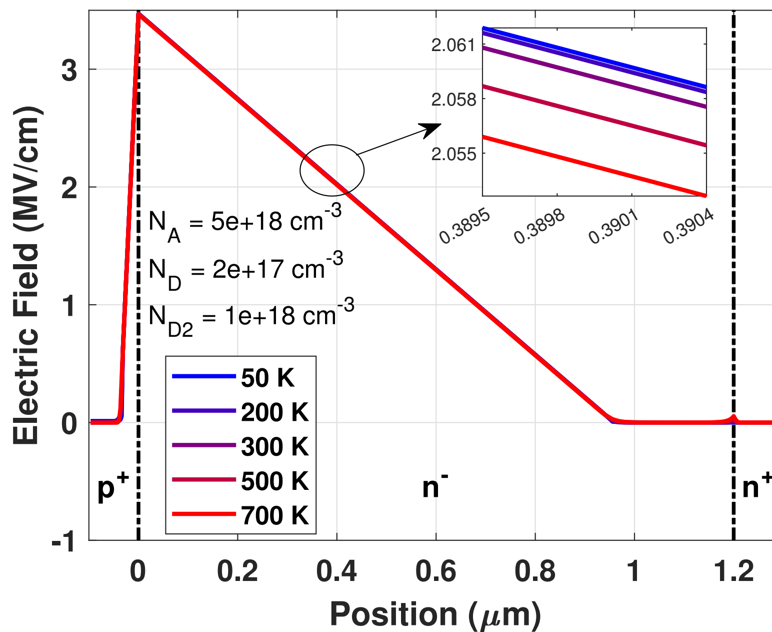

Figure 2.20: Electric field profile in a $p-i-n$ diode as a function of the temperature. The base material is 4H-SiC, and the applied reverse bias is 170 V.

resistance of the $p-i-n$ diode under reverse bias operation.

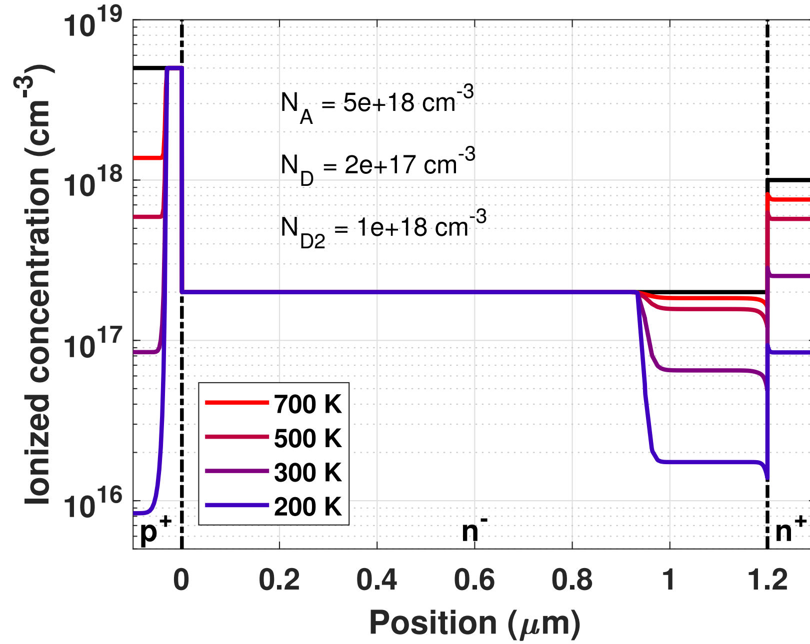

Figure 2.21: Calculated concentration of ionized dopants in a $p-i-n$ diode as a function of the temperature. The base material is 4H-SiC, and the applied reverse bias is 170 V.

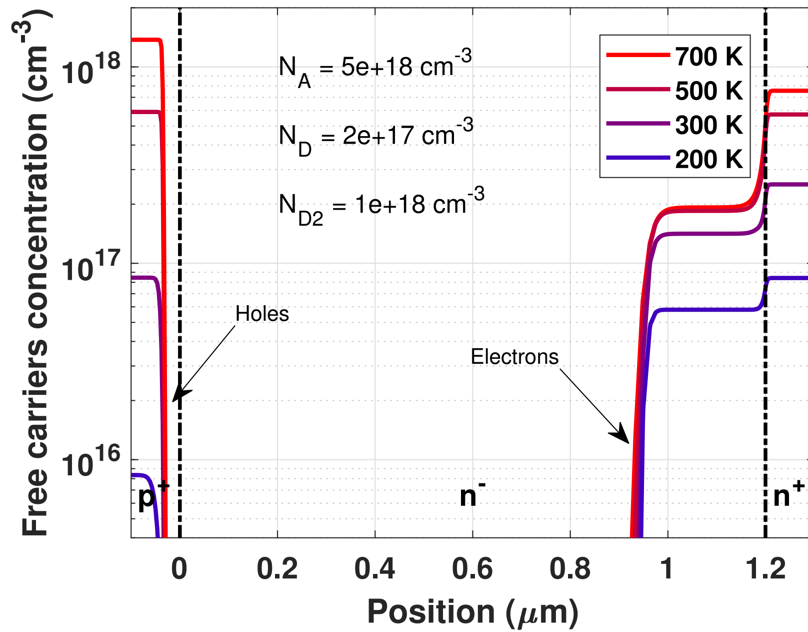

Figure 2.22: Calculated profile for the concentration of free carriers as a function of the temperature. The calculation is performed on 4H-SiC

One important physics worth describing on Fig. 2.21 is the deionization of dopants on the n$^-$ side of the $n^- - n^+$ junctions. The diffusion of electrons from the n$^+$ side of the junction to the n^- side results in the neutralization of ionized donors. The effect is the slight reduction of the ionized donor concentration on the n$^-$ side of the $n^- - n^+$ interface as seen in Fig. 2.21.

The calculated concentration of free carriers is shown on Fig. 2.22. because the reverse bias is large, the $n \times p$ product becomes insignificant. Part of the space charge region away from the edges can be assumed to be fully depleted because the concentration of free carriers present is too small that it is computationally zero.

2.4.4 Background Currents in Devices Fabricated with Wide- and Ultrawide-Bandgap Semiconductors

Given that at large reverse biases, the $p-i-n$ structure appears to be fully depleted in part of the i-layers, the origin of the leakage currents remains a challenge for photodiodes fabricated with wide- and ultrawide-bandgap materials. Fig. 2.23 shows pulses resulting from dark counts in a 4H-SiC avalanche photodiode. In an ideal situation, one wants the pulse to be triggered by an incident photon, but the pulses are occasionally encountered in the dark due to background emissions. Several factors contribute to the background current in semiconductors; for avalanche photodiodes operating in the dark, some components of the background current are the diffusion current (I_{diff}), the generation current (I_{gen}), and the sidewall leakage current (I_{SW}) [38,39]. The off-state current, modeled as the sum of the components, can be expressed with (2.43).

The reverse saturation current of $p - n$ junctions is given by (2.44). A denotes the area of the devices. D_n and D_p are the diffusion coefficients for electrons and holes. L_n and L_P are

the diffusion length of electrons and holes. the lifetime for electrons and holes is given by τ_n and τ_p. The reverse saturation current is written in terms of the mobility and the lifetimes of the minority carriers. The equation indicates that the diffusion current gets smaller for devices with high doping concentrations and long minority carriers' lifetime.

$$I_{dark} = I_{diff} + I_{gen} + I_{SW}. \tag{2.43}$$

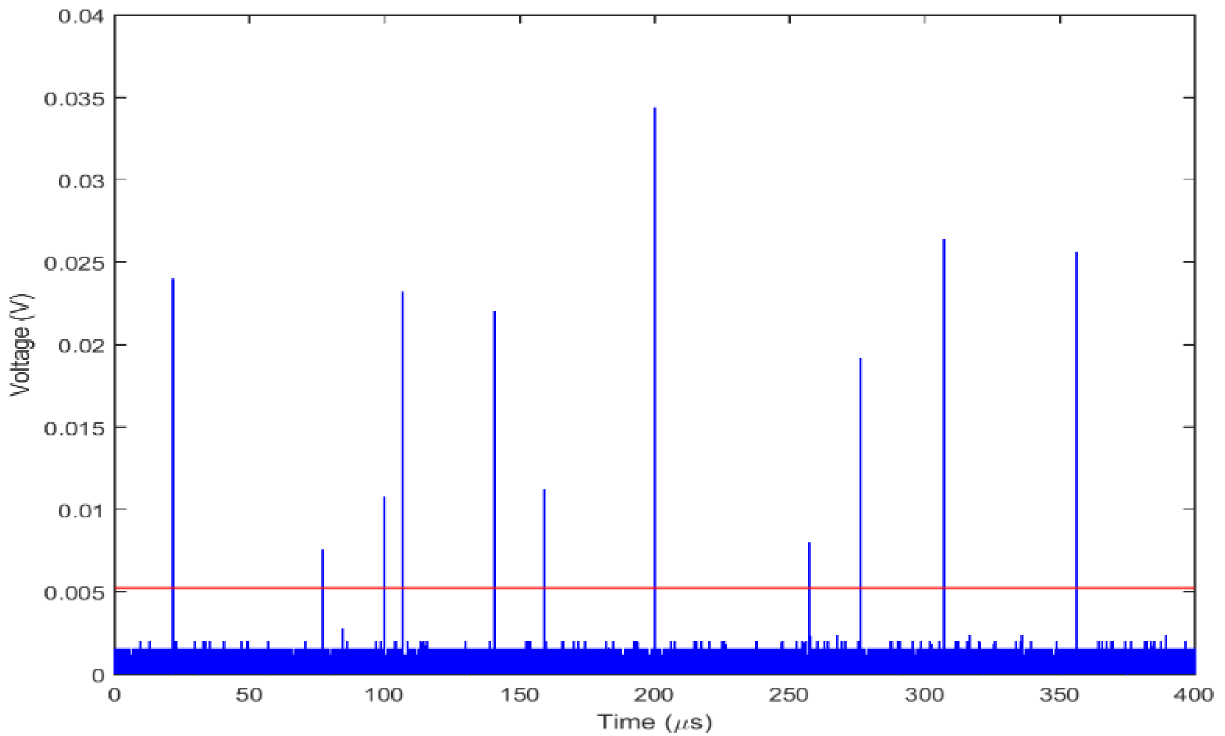

Figure 2.23: Measured dark count rate in a 4H-SiC avalanche photodiode.

A plot of the reverse saturation current in 4H-SiC is shown in Fig. 2.24 for 4H-SiC $p-n$ junction with the p-layer doped at 1×10^{18} cm^{-3} and the n-layer doped at 2×10^{17} cm^{-3}. The area of the diode is 2.25$\times$ 10^{-4} cm^2. and the lifetime for electrons and holes are 1×10^{-9} s and 6×10^{-7} s [40], respectively. Because the intrinsic carrier concentration is very small, the theoretical saturation current is small for wide- and ultrawide-bandgap semiconductors. As seen Fig. 2.24

the diffusion current at room temperature is 4.4×10^{-51} A for 4H-SiC, considerably insignificant compared to 6.7×10^{-16} A as calculated silicon.

$$
\begin{aligned}
I_{diff} &= A\left[\frac{qD_n n_{p0}}{L_n} + \frac{qD_p p_{n0}}{L_p}\right] \\
&= Aqn_i^2\left(\frac{D_n}{L_n N_A} + \frac{D_p}{L_p N_D}\right) \\
&= An_i^2\sqrt{qkT}\left(\frac{1}{N_A}\sqrt{\frac{\mu_n}{\tau_n}} + \frac{1}{N_D}\sqrt{\frac{\mu_p}{\tau_p}}\right)
\end{aligned}
\tag{2.44}
$$

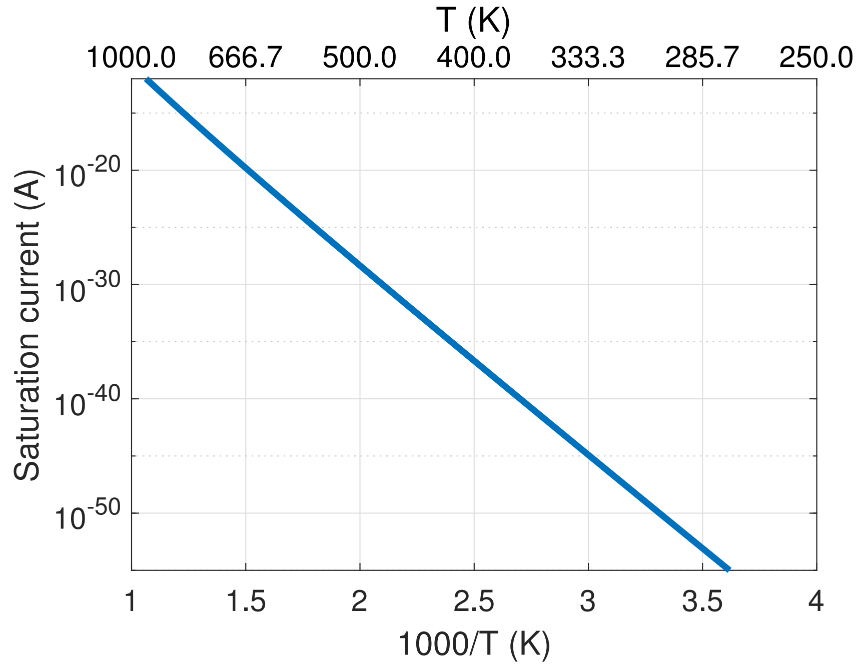

Figure 2.24: Reverse saturation current in 4H-SiC as a function of the temperature. The theoretical saturation current is so small that it is below the resolution limits of modern-day measuring instruments; an increase in temperature results in an increase in leakage current.

In addition to the diffusion current, the generation current is another component of the background current. The generation current [38] in the space charge region is given by (2.45), where τ_e is the lifetime associated with the emission of carriers, A is the area of the devices; q is the electron charge, and W_i is the width of the depletion region in reverse bias where the free carriers concentrations are smaller than the intrinsic carrier concentration n_i.

$$I_{gen} = \frac{Aqn_iW_i}{2\tau_e}. \tag{2.45}$$

At large reverse biases, the depletion is enhanced, and W_i can be assumed to be the total depletion width. The generation current depends on the lifetime of carriers; the topic is revisited after deep-level transient spectroscopy analysis in Section 3.2, where more details are provided on the lifetime.

The sidewall leakage current is external to the material and does not get multiplied. It has an ohmic behavior observable via the fabrication of diodes with different areas. The base current measured in Fig. 2.23, by its nature of being constant for a bias, is likely attributable to the parallel leakage. The parallel leakage is experimentally investigated in Section 3.4.2, where dark- and photo-current analyses are performed.

The simulated profile of free carriers shown in Fig. 2.22 reveals that free holes tail in the depletion region. The electric field is such that those holes are pulled back to the p^+ region. There is a short distance that holes travel before reaching the cladding layer. Fig. 2.25 shows the potential energy holes tailing in the depletion region can get when reaching the cladding layer. In future Chapters, deep-level transient spectroscopy analysis is considered to study the nature of generation-recombination centers that may influence the leakage current of devices. Such low currents are a challenge because the origin of carriers that initiate avalanche breakdown remains unknown.

The figure shows that the potential energy can be more than 10 eV, but the concentration of holes that can have such energy is minimal (nonexistent). A few carriers (concentration $\approx 10^6$ cm^{-3}) in the depletion region on the p^+ side can get 1 eV of energy; This energy is not enough to

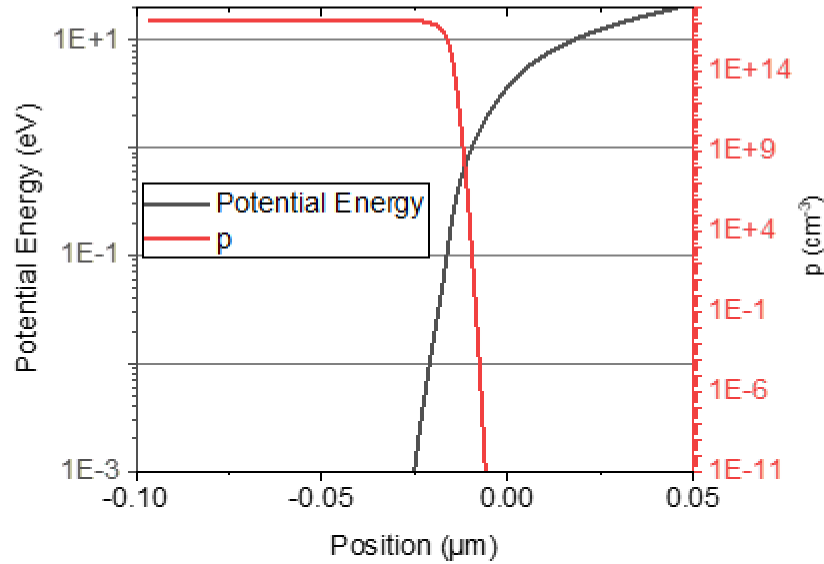

Figure 2.25: Potential energy of free carriers tailing in the space charge region as they drift back to the cladding layer. The material considered is 4H-SiC, and the calculations are performed on a $p-i-n$ structure biased at 170 V.

trigger a breakdown. The leakage in wide- and ultrawide-bandgap semiconductors will be further addressed in the coming chapters with deep-level transient spectroscopy analysis.

2.5 Validation of Incomplete Ionization with Capacitance-Voltage-Temperature Measurements

The incomplete ionization of dopants is reflected in capacitance measurements. Measuring 4H-SiC avalanche photodiodes at different temperatures is a good way to validate the model of incomplete ionization. Fig. 2.26 shows the schematic of the avalanche photodiodes used for capacitance measurements as a function of the temperature. The diode is positively beveled; the i-layer is 2 μm thick and doped at 2×10^{17} cm^{-3}.

The top view of the diode is shown in Fig. 2.27. As seen in the figure, the measured diameter of the top contact is about 115 μm. The outermost red circle indicates the foot of the

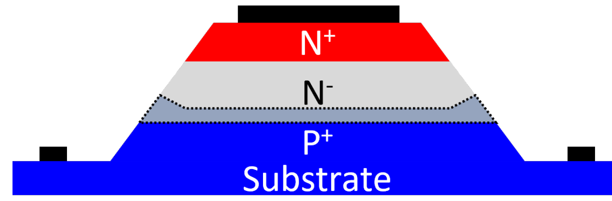

Figure 2.26: Schematic of the diode used for capacitance measurements.

bevel; its measured diameter is 185 μm. The structure is n-illuminates because the n$^+$ layer is on the top.

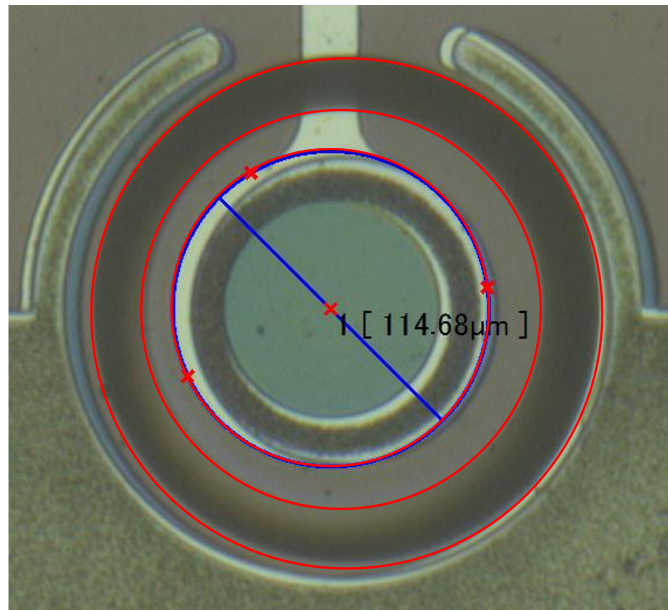

Figure 2.27: Top view of the $p-i-n$ diode used for capacitance measurements.

Avalanche photodiodes are ideal for studying the breakdown voltage because they offer the opportunity to capture the full voltage that a material can support. Compared to Schottky diodes with metal/semiconductor interfaces, avalanche photodiodes are less affected by defects. Because avalanche photodiodes are used for non-line of sight communication, we will also study the diodes for their single-photon detection efficiency.

Capacitance-voltage measurements were performed on the 4H-SiC photodiodes as a function of the temperature. As seen in Fig. 2.28, the capacitance increases with the temperature,

likely because there are more charges in the depletion region when the temperature increases. To extract of the effective concentration of ionized dopants in the depletion region, we consider the expression for the depletion capacitance and the temperature dependence of each of its parameters. The depletion capacitance is given by (2.46), where C_0 is the parallel offset capacitance resulting from the measurement setup. The built-in potential can be fully expressed as a function of the temperature as given by (2.47); it uses the concentration of intrinsic carriers, which also depends on the temperature.

$$C(T) = A\sqrt{\frac{qN_A^- N_D^+(T)\epsilon}{2\left(V_{bi}(T) + |V_A|\right)\left(N_A^- + N_D(T)^+\right)}} + C_0 \tag{2.46}$$

$$V_{bi}(T) = \frac{kT}{q}\ln\left(\frac{N_A^- N_D^+(T)}{n_i^2(T)}\right) \tag{2.47}$$

The temperature dependence of the intrinsic carrier concentration is given by

$$n_i(T) = \sqrt{N_C(T)N_V(T)}e^{-E_G(T)/(2kT)}, \tag{2.48}$$

where N_C and N_V are the density of states in the conduction and valence band, respectively, their temperature dependence is such that

$$N_{C,V} = \left(\frac{2\pi m_{n,p}kT}{\hbar}\right)^{3/2}. \tag{2.49}$$

For 4H-SiC, the temperature dependence of the bandgap is given by

$$E_g(T) = 3.285 - \frac{3.3 \times 10^{-2}T^2}{T + 10^5}\ \text{eV} \tag{2.50}$$

Figure. 2.28 shows the measured capacitance along with the calculated capacitance using an effective ionized donors' concentration. A fitting scheme using (2.46) is used to model the measured capacitance. The unknown parameters found with the fitting process are the offset capacitance, the area of the diodes, and the concentration of ionized donors. The offset capacitance and the area of the diode are assumed constant. An effective ionized concentration is extracted for each temperature measurement.

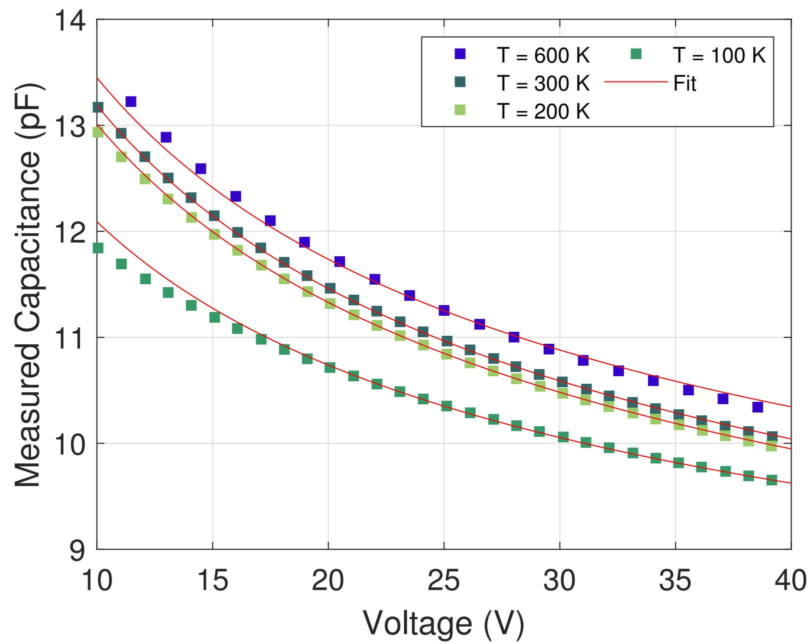

Figure 2.28: Calculated and measured capacitance in $p-i-n$ diodes as a function of the voltage and the temperature.

The effective ionized donor doping concentration is considered the measured ionized concentration. Table 2.4 shows the measured ionized donor doping concentration (Measure Doping) for temperatures in the range of 200 K to 600 K. For comparison, the concentration of ionized dopants calculated with the model of incomplete ionization is also shown in the table (Measured Doping).

The calculated and measured ionized doping concentrations agree, **suggesting a successful**

Table 2.4: Measured and calculated effective doping concentration.

T (K)	200	250	300	350	400	500	600
Measured Doping $\times 10^{17}$cm^{-3}	1.71	1.79	1.80	1.84	1.87	1.93	1.99
Calculated Doping $\times 10^{17}$cm^{-3}	1.71	1.77	1.82	1.85	1.88	1.92	1.94

modeling of incomplete ionization.

Conclusion

Wide- and ultrawide- bandgap semiconductors are promising materials for power electronics because they enable the fabrication of devices that are simultaneously small, efficient, and capable of high voltage operation. The Baliga figure-of-merit provides a means to evaluate the performance of those materials for power electronics; however, the Baliga metric is challenging to assess because it highly depends on underlying physics that are not explicitly expressed. A more reasonable approach to evaluating the on-resistance versus breakdown voltage of emerging materials is to study the factors that may influence the on-resistance and the breakdown voltage. This section has investigated incomplete ionization in wide- and ultrawide- bandgap semiconductors as a function of the temperature and the electric field. Before ionization, the incomplete activation of dopants is a factor that also increases the device resistivity. By comparing theoretical and measured resistivity in p-type 4H-SiC doped with aluminum, it is found that up to 90% of dopants can be inactive; thankfully, doping by epitaxial growth results in 100% activation of the dopants. The ionization energy of dopants for the different wide- and ultrawide-bandgap materials studied was surveyed from the literature, and their doping dependence was proposed using the Pearson-Barden model. By assuming that all the dopants are ionized and that the space charge region is fully depleted of free carriers, the electric field profile and the electric potential

profile are obtained by integrating over the fixed charges in the depletion region, but the process hides insight into device's operation. Incomplete ionization is modeled with Poisson's equation. For the case of substrates, the Poisson equation becomes the charge neutrality equation. The ionization ratio computed in this work agrees with the calculations of Darmody and Goldsman. for p-type doped 4H-SiC. An implemented finite difference scheme is proposed for solving the Poisson equation in $p-i-n$ structures. Simulations show that the electric field strongly affects the ionization of carriers, and it is challenging to freeze carriers in the depletion region. Field-assisted dopants' ionization helps junction formation and reduces errors associated with complete ionization assumptions. For material with high ionization energy dopants, incomplete ionization is more pronounced in the quasi-neutral regions, where the temperature has the most effects. It is seen that the Baliga unipolar on-resistance is underestimated; some materials, such as diamond, can be up to 1000 times more resistive depending on the activation energy of the dopants and the operating temperature. Operating at high temperatures can make devices less resistive, provided reductions in mobility are overcompensated by the improved ionization of the dopants. Calculations in this section show that the reverse bias diffusion current is insignificant, and the dark current is most likely due to leakage through the side wall. This effect will continue to be evaluated in the thesis.

Chapter 3: Characterization of 4H-SiC $p-i-n$ diodes for the Validation of Incomplete Ionization and the Calculation of Impact Ionization Coefficients

The on-resistance and the breakdown voltage are two quantities that are very important when assessing the performance of a device for power electronics. A device with a low on-resistance is more efficient as less energy is wasted to joule heating. A low resistance also implies a low RC constant and high operational frequencies. Being an important parameter that controls the charge and discharge time of the quenching cycle, the resistance can also impact the photo counts of avalanche photodetectors. A low resistance allows fast charge and discharge times, resulting in high photo counts. A higher breakdown voltage is important because it allows a safe expansion of electronics devices on more energized platforms such as electric vehicles.

In Chapter 2, incomplete ionization was studied for a more accurate calculation of the on-resistance. It was demonstrated that the partial activation and the incomplete ionization of dopants could significantly increase the resistance of devices fabricated with wide- and ultrawide-bandgap materials that have a high ionization energy. In this chapter, measurements are performed on 4H-SiC $p-i-n$ diodes for an experimental assessment of the on-resistance and the breakdown voltage. The total resistance and the series resistance of the diode are measured as a function of the temperature. As demonstrated by modeling efforts in Chapter 2, the enhanced ionization

of dopants with increasing temperature helps lower the resistance. Unlike silicon which has a low ionization energy, incomplete ionization is severe in wide-bandgap (WBG) and ultrawide-bandgap (UWBG) materials; however, the severity of incomplete ionization is reduced when the temperature is increased.

Following the measurement of the resistance, the diodes are characterized for a more accurate assessment of the multiplication from which impact ionization coefficients can be extracted for the calculation of the breakdown voltage. Deep Level Transient Spectroscopy (DLTS) is performed to extract the concentration of generation-recombination centers for understanding the generation current in material with a large bandgap. The effects of deep traps on the electrical characteristics of devices and the extraction of those deep traps via DLTS analysis are discussed. The diodes are then characterized in linear mode for their gain (multiplication). The voltage dependence of the multiplication is calculated from dark and photocurrent measurements; the use of the measured multiplication for establishing the value of impact ionization coefficients is discussed in the next chapter.

3.1 Effects of Incomplete Ionization on Measured Resistance

When assessing the on-resistance versus breakdown voltage of emerging semiconductors in the literature, the on-resistance is usually evaluated by considering a uniformly doped semiconductor bar. Such a bar is shown in Fig. 3.1. The resistance of the bar is given by

$$R = \frac{1}{q\mu n}\frac{W}{A}\,(\Omega) \tag{3.1}$$

Where A is the cross-sectional area of the bar, and W its thickness as shown in Fig. 3.1.

The resistance depends on the electron charge, q, the mobility μ, and the concentration of free carriers, n. The product $q\mu n$ is the conductivity of the bar, and $1/(q\mu n)$ is its resistivity.

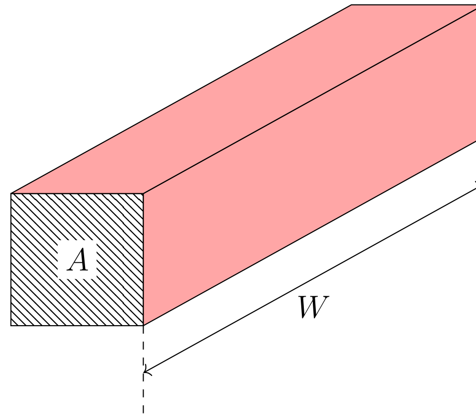

Figure 3.1: A uniformly doped semiconductor bar for the evaluation of the resistance. The cross-sectional area of the bar is A, and its thickness is W.

As seen in the literature, the use of on-resistance is more convenient; it is expressed as

$$R_{ON} = \frac{W}{q\mu n}\,(\Omega \cdot cm^2) \tag{3.2}$$

The on-resistance given by (3.2) is what is generally considered when evaluating the on-resistance versus breakdown voltage of semiconductors [10]. Note that this equation applies only to a limited number of electronic devices. In the case of diodes, for example, the on-state is dominated by the diffusion of minority carriers; the drift resistance given by (3.2) cannot be used to assess the on-resistance of diodes.

The on-resistance given by (3.2) is useful for power electronics because it applies to vertical power devices. The schematic of a vertical device, the double diffuse MOSFET (DMOS), is shown in Fig. 3.2. In the on-state, a positive bias is applied to the gate terminal of the device, and the p-region of the device under the gate insulator gets inverted, creating a path for electrons

between the n$^+$ source regions and the n-drift region. In the on-state, the resistance of the device is the resistance of the n$^-$-drift layer. The on-resistance given by (3.2) is applicable on the vertical MOSFET shown in Fig. 3.2.

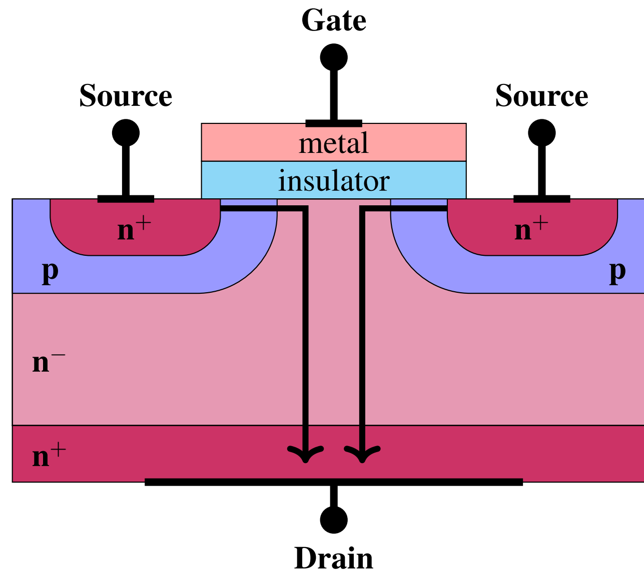

Figure 3.2: Schematic of the double-diffuse MOSFET (DMOS).

When discussing the on-resistance versus breakdown voltage limits, the literature considers the resistance of a uniformly doped semiconductor bar. The current in such a uniformly doped bar is due to the drift of majority carriers, and the resistance is referred to as the unipolar on-resistance because conduction is achieved with one type of carrier. Although the $p-n$ junctions or $p-i-n$ diodes are not unipolar devices, it is important to assess their on-state resistance for an improved modeling of the multiplication.

3.1.1 Effect of the Temperature on the Total Resistance of the $p-i-n$ Diodes

For power electronics, achieving low on-resistances is useful for the energy efficiency of systems. The on-resistance needs to be evaluated depending on device architecture because the

conduction mechanism depends on device's operation. The on-resistance of a diode is different from that considered in the Baliga figure-of-merit (BFoM) [10]; nonetheless, it is worth measuring the diode resistance because it allows better modeling of the multiplication by accounting for the effective voltage across the diode. Also, measuring the resistance of the diode as a function of the temperature tells the combined effect of mobility reduction and dopants ionization enhancement. The measured forward I-V characteristics of a 4H-SiC $p-i-n$ diode is shown on Fig.3.3. The measurements were performed from 100 K to 600 K. For each temperature, the total resistance is estimated as the slope of the I-V in the linear region.

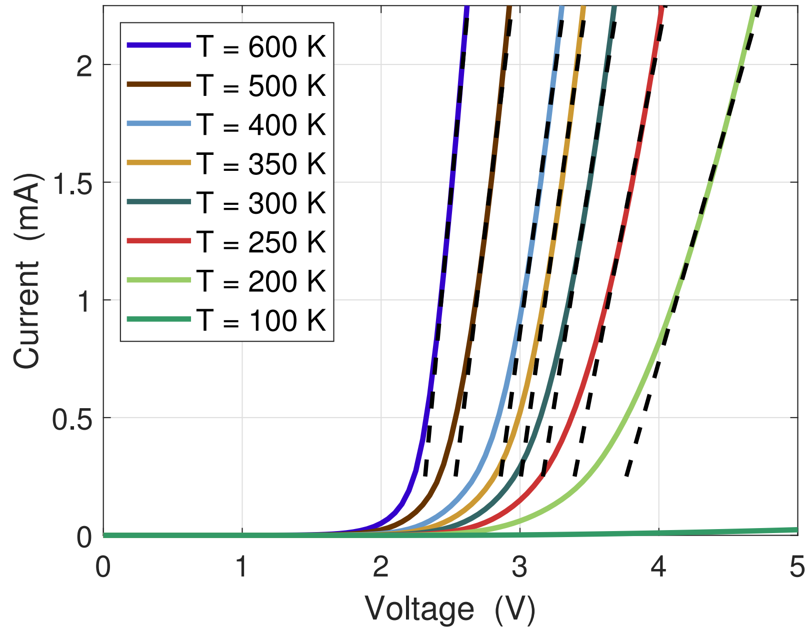

Figure 3.3: Forward I-Vs measured on 4H-SiC $p-i-n$ diodes in the temperature range of 100 K to 600 K. The drawn slopes in strong forward bias indicate the total small-signal resistance of the diode.

In $p-i-n$ diodes, the physics at the $p^+ - n^-$ junction is similar to that of $p-n$ junctions. For a given forward bias, the charge injection's mechanism is similar for $p-n$ and $p-i-n$ diodes. When accounting for the non-ideality factor, the current equation is given by 3.3, where

I_{diff} is the reverse saturation current; V_D is the voltage across the diode. The non-ideality factor is given by n. The temperature is denoted with T.

$$I_D = I_{diff}\left(\exp\left(\frac{qV_D}{nkT}\right) - 1\right), \tag{3.3}$$

The diode non-ideality results from the fact that the excess minority carriers at the edge of the depletion region in a p-substrate for a forward bias, V_D is $n_{p0}(\exp(V_D/(nV_T)) - 1)$ instead of $n_{p0}(\exp(V_D/(V_T)) - 1)$. In other words, the injection of carriers is suppressed by a factor n. For ideal diode, n = 1. Neglecting the one in the diode equation and taking the natural logarithmic results to

$$\ln(I_D) = \ln(I_{diff}) + \frac{V_D}{nV_T}. \tag{3.4}$$

The plot of $\ln(I_D)$ versus the applied forward bias, V_D, is such that its slope is $1/(nV_T)$. The current is plotted in Fig. 3.4 on the logarithmic scale. The curves show that the turn-on voltage is less than a volt. The current appears linear at around two volts. At around three volts, the slopes decrease, likely due to the series resistance, which reduces the injection voltage. When the current is small, the voltage drop across the series resistance becomes negligible, and the non-ideality factor can be more easily extracted. The natural logarithmic of the current is plotted as a function of the applied bias in Fig. 3.5 at around 1.8 V. The non-ideality factors are extracted from the slope of the fitting lines ($n = 1/(V_T \times slope)$). They are summarized in Table 3.1.

From Fig 3.3 and Fig. 3.4 it is seen that the current increases with the temperature. The extracted total resistance of the diode, which includes the series resistance, and the space charge resistance, is summarized in Table 3.1 as a function of the temperature. The table also summarizes the measured non-ideality factor extracted at 1.8 V. The diodes approach ideality at elevated

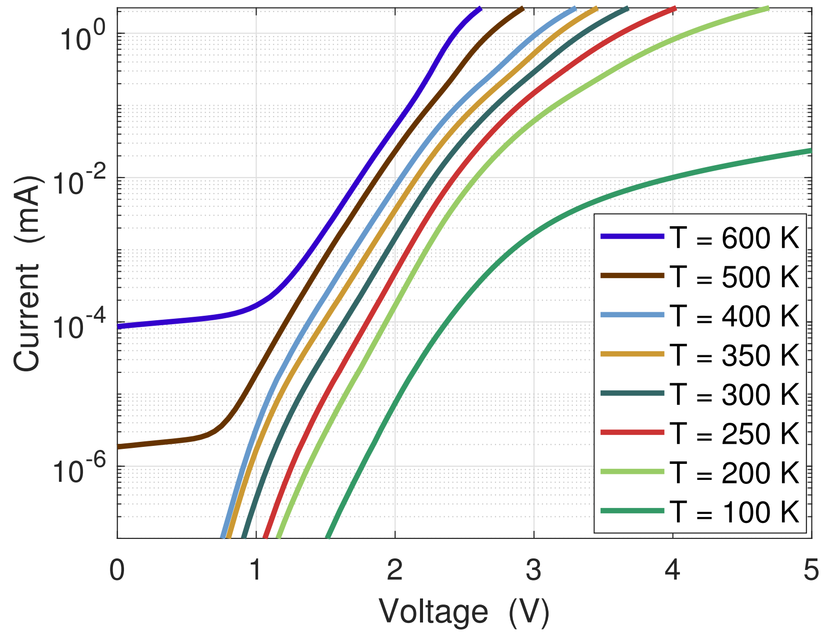

Figure 3.4: Measured forward I-Vs characteristics of $p-i-n$ diodes plotted on the logarithmic scale as a function of the temperature.

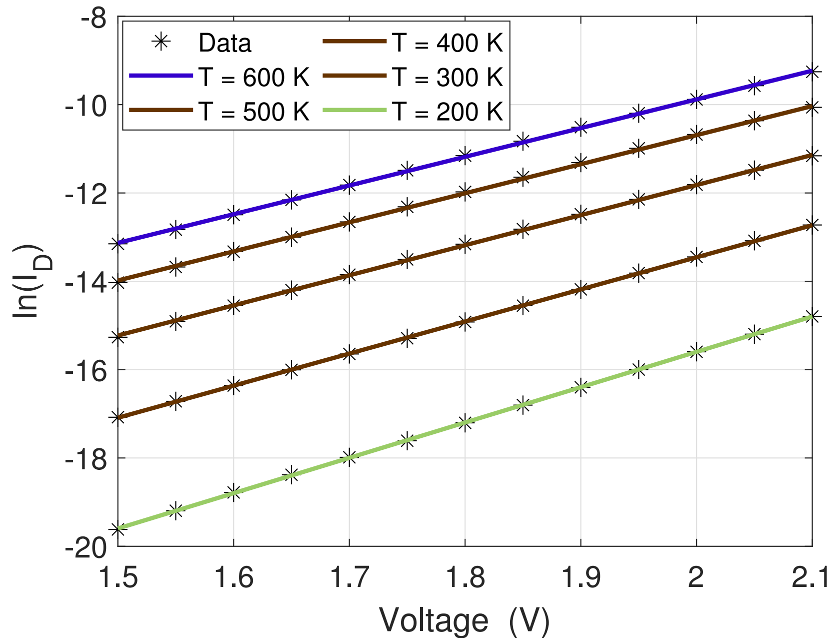

Figure 3.5: Natural logarithmic of the diode current for the extraction of the non-ideality factor.

temperature, likely due to the lowering of the series resistance narrowing the gap between the applied bias and the injection voltage. The investigated diodes' series resistance is discussed and

extracted in the next section as a function of the temperature.

3.1.2 Extraction of the Series Resistance

The effective voltage across the diode is corrected by considering the voltage drop across the series resistance. The schematic of a diode ($p - n$ junction) in forward bias is shown in Fig. 3.6. The device is described by referencing three regions denoted by R_1, R_2, and R_3. The space charge region is R_2, and the regions outside the space charge region are R_1 and R_3. The series resistance is the sum of the contact and quasi-neutral regions' resistance.

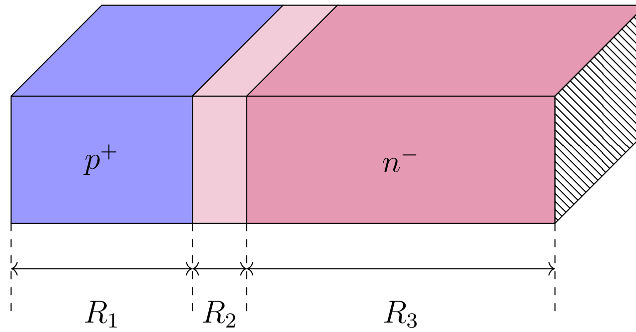

Figure 3.6: Regions of a forward-biased $p - n$ junction. The region R_2 is thin, and the regions R_1 and R_3 are not neutral because of the injection of minority carriers.

In forward bias, charge injection occurs, resulting in a profile of minority carriers in the regions R_1 and R_2, which become non-neutral. The concentration of minority carriers peaks at the edges of the depletion region and exponentially decays to n_i^2/N_A in R_1 and to n_i^2/N_D in R_3. Because the regions R_1 and R_3 are not neural in forward bias, there is a weak electric field that causes the drift of majority carriers. The series resistance is denoted r_s and can be used to correct the voltage across the diode. The effective voltage across the diode is

$$V_D = V - I_D r_s, \tag{3.5}$$

where I_D is the current in the diode. The corrected current-voltage relationship for the diode with an account of the non-ideality factor and the series resistance is given by

$$I_D = I_{diff} \left(\exp\left(\frac{q(V - I_D r_s)}{nkT} \right) - 1 \right). \tag{3.6}$$

In forward bias, the one can be neglected, and the current equation becomes

$$I_D = I_{diff} \exp\left(\frac{q(V - I_D r_s)}{nkT} \right). \tag{3.7}$$

Using the chain rule, the derivative of the current with respect to the voltage can be expressed as

$$\frac{dI_D}{dV} = I_{diff} \exp\left(\frac{q(V - I_D r_s)}{nkT} \right) \frac{d}{dV} \left(\frac{V - I_D r_S}{nV_T} \right). \tag{3.8}$$

Since $\frac{dI_D}{dV} = g_D$, the equation above leads to

$$g_D = I_D \left(\frac{q}{nkT} - \frac{r_s g_d}{nkT} \right). \tag{3.9}$$

Rearranging equation 3.9 leads to.

$$\frac{I_D}{g_D} = \frac{nkT}{q} + I_D r_s. \tag{3.10}$$

Equation 3.10 shows that it is possible to extract the series resistance by plotting I_D/g_D against I_D as shown in figure 3.7 [41]. In such a plot, the series resistance is just the slope of the linear fit. The y-intercept can yield the diode's non-ideality factor, n; however, this is unpractical

because the current is high, and the injection voltage is no longer the bias applied on the diode. The series resistance associated with the $p-i-n$ diode, useful for the experimental extraction of the multiplication and the validation of the incomplete ionization model, is shown in Table 3.1. The total resistance is the slope of the measure I-V characteristics in the linear regime; those slopes are drawn in Fig. 3.3.

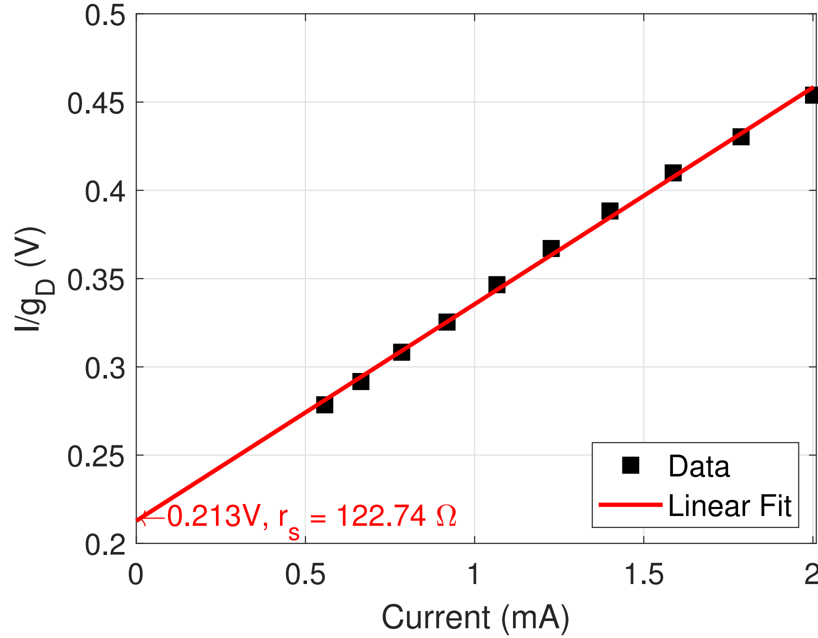

Figure 3.7: Extraction of the series resistance in a 4H-SiC $p-i-n$ diode at 300 K.

Table 3.1: Extracted resistances of the 4H-SiC $p-i-n$ diodes described in Section 2.5.

Temperature (K)	200	300	500	600
Total Resistance (Ω)	580.57	267.20	203.16	154.26
Series Resistance, r_s (Ω)	257.28	122.74	99.97	99.49
Non-ideality Factor	7.26	5.33	3.53	2.98

Experiments show that the series resistance, which is the sum of the contact resistance and the resistance ((3.11)) of the quasi-neutral regions, R_{qnr}, (R_1 and R_3 in Fig. 3.6), decrease with the temperature. The contact resistance is the the sum of the n-contact, R_{Cn} and p-contact resistance, R_{Cp}. At elevated temperature, the quasi-neutral region's resistance is affected by the

enhancement of dopants' ionization and mobility reduction; this is discussed in Section 5.1.2 and 5.3.2.

$$r_s = R_{qnr} + R_{Cn} + R_{Cp} \tag{3.11}$$

The contact resistance can be evaluated from the specific contact resistivity, whose typical value is ρ_c = 4 $\times$ 10^{-4} Ω cm^2 for contact on n-type 4H-SiC [42, 43] substrate. For the $p - i - n$ diodes investigated in this work (see Fig. 2.27), the top area is about 5.6 $\times$ 10^{-5} cm^2, and the specific contact resistance are reported to be about 1×10^{-3} $\Omega \cdot$ cm^2 [44]. Assuming that the specific contact resistance is ten times higher for contact on p-type 4H-SiC substrates and that the area for the p-type contact is twice that of the n-type contact, the calculated series resistance is 107.14 Ω, close to the value reported in Table 3.1. The difference in resistance is about 15 Ω and could be attributed to the resistance of the quasi-neutral region and errors made when estimating the device's dimensions. Calculation shows that the contact resistance is the major source of the series resistance, which decreases with the temperature. The series resistance decreasing with temperature can be attributed to contact resistance reduction.

Experimental studies show that the series resistance of the diode is less than 260 Ω at temperatures higher than 200 K. If the breakdown voltage current is one mA, the voltage drop across the series resistance is less than 0.26V, depending on the operating temperature. The breakdown voltage of the device investigated in this work is around 180 V, so the effect of the series resistance can be neglected for breakdown voltage measurements of power electronic devices. In the multiplication regime, however, the change in current becomes highly sensitive to the voltage. Accurate modeling of the multiplication requires consideration of the series resistance. Measuring the current in forward bias allows understanding of devices' resistivity. For diodes, the tem-

perature affects the ionization of the dopants, but this effect is not directly observable in the series resistance, which is dominated by the contact resistance. The ohmic-specific contact resistivity depends on the metal-semiconductor work function, the doping concentration of the semiconductor, and the effective mass of the carrier. Ohmic contact improvement could significantly lower the RC constant of diodes and boost their efficiency.

While forward I-V characteristics helped understand the source of resistance in the investigated diodes, the reverse I-V characteristics are essential for quantifying charge multiplication. In Section 2.4.4, it was found that the reverse saturation current for material with a large bandgap is insignificant compared to that of silicon. Dark measurements of the investigated 4H-SiC $p-i-n$ show avalanche count, indicating that there are other sources of current than the saturation current. It is important to analyze diodes for the nature of the generation current from deep traps.

3.2 Deep-Level Transient Spectroscopy Analysis for the Study of the Dark Current, the Multiplication, and Impact Ionization Coefficients

It is possible to extract impact ionization coefficients from multiplication data (gain) calculated from the measured reverse I-V characteristics of $p - i - n$ diodes. However, before processing measured I-V characteristics for the multiplication, it is essential to understand the nature of the measured current, especially at low reverse voltage. The previous chapter shows that the reverse saturation current is so insignificant that it is below the measurement limits of modern instruments. The question remains: What is the nature of the current measured when a device like a 4H-SiC $p - i - n$ diode is reverse biased? It turns out that the saturation current is only a component of the dark current. In this section, we will use deep-level transient

spectroscopy to study generation-recombination centers, also called deep traps, that can promote the dark current through successive emissions and captures of carriers. The deep-level transient spectroscopy (DLTS) approach is a powerful technique for characterizing materials. More on DLTS analysis can be found in the work of Barbot et al. [45] for silicon and in The work of Gotz and Johnson [46] for III-V related materials.

3.2.1 Generation-Recombination Centers and their Impact on Devices Performance

Depending on their distance from the band edges, impurities in semiconductors can be shallow or deep. Shallow impurities are close to the band edges, while deep impurities are closer to the mid-gap [47]. A good example of shallow impurities are dopants that can be intentionally incorporated into the material to modulate its conductivity. The concentration of deep traps can also be controlled, but they often appear unintentionally in materials. When impurities are closer to the band edges (shallow), they act like traps; closer to the mid-gap, they act like generation-recombination (G-R) centers. More details on traps and G-R centers are be found in [47]. This work focuses on G-R centers to understand the dark current measured on devices fabricated with wide- and ultrawide-bandgap materials.

This section aims to establish a framework for extracting the concentration of G-R centers when available; it is done by first studying their characteristics and potential impact on devices' electrical performance. As illustrated in Fig. 3.8, G-R centers can be occupied by an electron (filled circle) or by a hole (empty circle). A G-R can become charged depending on its nature.

When an electron occupies the G-R center, it is in the n_T state. When a hole occupies it,

it is in the p_T state. The G-R centers can also be donors or acceptors in nature. Being a donor center, the G-R center is neutral under electron occupation and positively charged under hole occupation. An acceptor center is neutral when occupied by a hole and negatively charged when occupied by an electron. The four possibilities related to nature and occupancy are summarized in Table 3.2.

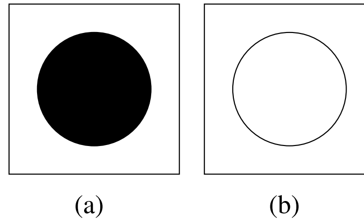

Figure 3.8: The two possible states of a generation-recombination center. in the n_T-state ((a)) the center is occupy by an electrons. In the p_T-State ((b)) the center is occupied by a hole.

Table 3.2: Possible states of generation recombination centers.

	Donors	Acceptors
n_T State	neutral	negative
p_T State	positive	neutral

Because they can be charged, G-R centers are electrically active defects and can alter the electrical performance of semiconductors devices. In 4H-SiC, the main know deep defects are the Z_1/Z_2 [48–51] and the EH_6/EH_7 [52–54], which are known to significantly deteriorate the lifetime of carriers. The traps mentioned above are thermally stable; it is known the $Z_{1/2}$ are double acceptors while the $EH_{6/7}$ are donors. The band diagram of 4H-SiC is shown in Fig. 3.9, with the relevant traps centers [54]. The existence of generation-recombination centers in 4H-SiC is due to carbon vacancies. The concentration of G-R centers can be suppressed by considering a carbon-rich growth of the substrate; it is also possible to lower the concentration of G-R centers by performing enhanced lifetime oxidation annealing [50].

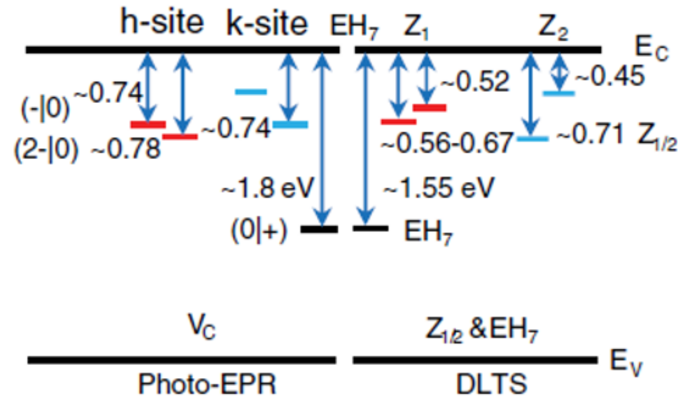

Figure 3.9: Reported deep centers in 4H-SiC [54].

3.2.2 Modeling the Transient of Generation-Recombination Centers Occupied by Electrons

Generation-recombination centers are electrically active defects, and their presence in materials can alter the electrical performance of a material. G-R centers can distort the measured capacitance and current of electronics devices. Measuring electrical signals over time makes it possible to extract the concentration of deep centers that might have distorted it because the effects of deep traps can be modeled mathematically [41, 51]. The occupation of deep traps can be modulated with an external signal, as shown in Fig. 3.10 for the case of a one-sided $p^+ - n$ junctions.

When the junction is forward biased, the Fermi level is raised above the trap energy level, as seen in Fig. 3.10(a). Being below the Fermi level, all the G-R centers get occupied by an electron and go into the n$_T$-state. When the diode is reverse biased, as shown in Fig. 3.10(b), the barrier high is increased, and some of the trap states get above the Fermi level and start to emit. Modeling the number of traps that remain under electron occupancy during the emission process

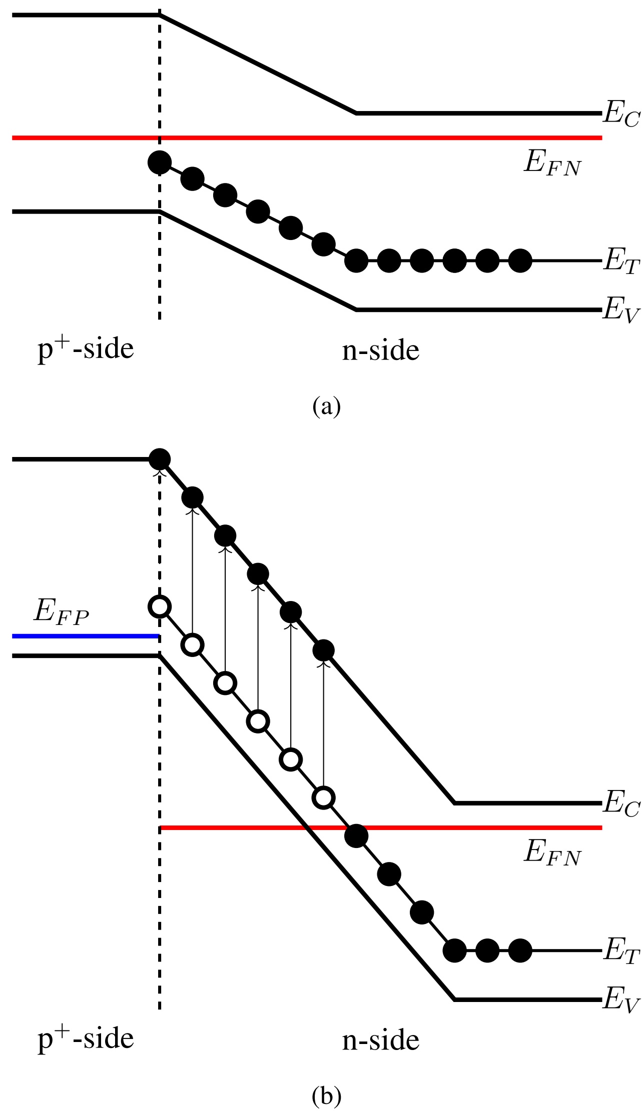

Figure 3.10: Change of the band diagram during DLTS measurements. The filling regime is shown in (a). Applying a slight forward bias on the diode reduces the barrier height and drops the trap energy level below the Fermi level, resulting in the occupation of generation-recombination centers. When a reverse bias is applied (b), the energy barrier is increased, and the centers located above the Fermi level start to emit.

is essential for deep-level transient spectroscopy (DLTS) analysis.

Generation-recombination centers interact with the band of the materials. Electron capture decreases the concentration of free electrons in the conduction band, n; similarly, hole capture decreases the concentration of holes in the valence band. Emission increases the concentration

of free electrons while capture decreases it. The net change in electron concentration due to the change in occupancy of the generation-recombination centers is given by

$$\frac{dn}{dt} = e_n n_T - c_n n p_T, \tag{3.12}$$

where e_n, and c_n are, respectively, the emission and capture coefficients t [47]. The emission is controlled only by the number of states under electron occupancy; however, for an electron capture event to happen, there must be electrons present in the conduction band and available p$_T$-states to host it. Similarly to the case of electrons, the concentration of holes in the valence band can be altered due to G-R centers and can be modeled as

$$\frac{dp}{dt} = e_p p_T - c_p p n_T. \tag{3.13}$$

During emission or capture, the number of G-R traps occupied by electrons is such that

$$\left.\frac{dn_T}{dt}\right|_{G-R} = \frac{dp}{dt} - \frac{dn}{dt} = (c_n n + e_p)(N_T - n_T) - (c_p p + e_n)\, n_T, \tag{3.14}$$

where n_T in the total concentration of generation-recombination centers. The solution [47] to the first-order differential equation is given by

$$n_T(t) = n_T(0)\exp\left(-\frac{t}{\tau}\right) + \frac{N_T(e_p + c_n n)}{e_n + c_n n + e_p + c_p p}\left(1 - \exp\left(-\frac{t}{\tau}\right)\right). \tag{3.15}$$

For traps in the upper half of the bandgap, $e_n \gg e_p$. During emission, the concentration of traps occupied by electron is given by

$$n_T(t) = n_T(0) \exp\left(-\frac{t}{\tau_e}\right), \tag{3.16}$$

where $\tau_e = 1/e_n$ is the emission time constant of the trap, which is expressed as [47, 55]

$$\tau_e = \frac{\exp\left[(E_C - E_T)/(kT)\right]}{\gamma_n \sigma_n T^2}. \tag{3.17}$$

3.2.3 Experimental Setup for Deep-Level Transient Spectroscopy Measurements

3.2.3.1 Modeling the Capacitance for DLTS Analysis

In the previous sessions, the concentration of generation-recombination (G-R) centers under electrons occupancy during emission was modeled as a function of time using (3.16). The change in occupancy over time affects the total charge in the depletion region. Table 3.3 shows the changes in charges concentration due to changes in G-R center occupancy [47]. In an n-type substrate, if the G-R centers are acceptors in nature, under electron occupancy, the total concentration of charges is $N_D^+ - n_T^-$. If all the G-R centers go under hole occupancy, the concentration of charges decreases to N_D^+ [47]. For donor G-R centers, the concentration of charges increases from N_D^+ under electrons occupancy to $N_D^+ + p_T^+$ under holes occupancy [47].

Table 3.3: Change in charges due to change in G-R center occupancy in an n-type substrate.

n-type substrate		
	Electron Occupancy	Hole Occupancy
Acceptor G-R centers	$N_D^+ - n_T^-$	N_D^+
Donor G-R centers	N_D^+	$N_D^+ + p_T^+$

The same study can be done on a p-type substrate with acceptors G-R centers, where the concentration of charges in the depletion region decreases from $N_A^- + n_T^-$ under electrons occupancy to N_A^- under holes occupancy. In a p-type substrate, if the G-R centers are donors in nature, the concentration of charges decreases from N_A^- under electron occupancy to $N_A^- - p_T^+$ under hole occupancy.

Table 3.4: Change in charges due to change in G-R center occupancy in a p-type substrate.

p-type substrate		
	Electron Occupancy	Hole Occupancy
Acceptor G-R centers	$N_A^- + n_T^-$	N_A^-
Donor G-R centers	N_A^-	$N_A^- - p_T^+$

The speed of the emission process depends on the emission time constant τ_e. During emission, the charges gradually change, and the change in charges can be reflected in capacitance measurements. For example, in an n-type substrate with G-R centers under electron occupancy, the capacitance can be written as

$$\begin{aligned} C &= \sqrt{\frac{q\epsilon\left(N_D^+ - n_T^-\right)}{2\left(V_{bi} + |V_R|\right)}} \\ &= \sqrt{\frac{q\epsilon N_D^+}{2\left(V_{bi} + |V_R|\right)}}\sqrt{1 - \frac{n_T^-}{N_D^+}} = C_0\sqrt{1 - \frac{n_T^-}{N_D^+}}. \end{aligned} \tag{3.18}$$

Using a first-order Taylor's series expansion, the capacitance can be approximated with (3.19). The capacitance given by (3.19) is a function of the time and temperature. It shows that the capacitance is expected to increase with time during the emission of majority carriers in an n-type substrate with acceptors G-R centers. Other scenarios for the change in capacitance are sum-

marized in Table 3.5 for an n-type substrate. In all four scenarios, the traps are acceptors in nature.

$$C(t,T) = C_0\sqrt{1-\frac{n_T(t)}{N_D}} \approx C_0\left(1-\frac{n_T(t)}{2N_D}\right) \\ \approx C_0\left(1-\frac{n_T(0)\exp\left(-\frac{t}{\tau_e(T)}\right)}{2N_D}\right) \tag{3.19}$$

The emission of majority carriers happens on Schottky diodes and results in an increase in capacitance. The second scenario depicts the emission of minority carriers, which is likely realized on a one-sided $p^+ - n$ junction. In forward bias, holes are injected in the n-regions, switching the states to p_T. Following a reverse bias, the states emit holes resulting in a decrease of charges from N_D^+ to $N_D^+ - n_T(t)$ and a decrease in capacitance. The third scenario is the capture of majority carriers in Schottky diodes. First, the Schottky diode is reverse biased, forcing the emission of electrons. When a forward bias is applied, electrons rush into the space charge region where they are captured. During the capture, the charges decrease from N_D^+ to $N_D^+ - n_T(t)$, resulting in a decrease in the capacitance [47]. The last and fourth scenario illustrates the capture of minority carriers on $p - n$ or Schottky diodes. The devices in reverse biased, and the G-R centers are in the n_T state. Upon an optical illumination, minority holes are generated and captured, increasing the total charge and the capacitance.

Regardless of which scenario takes place for the transient of G-R centers occupancy, the form of the capacitance is given by (3.19). The difference in capacitance between time t_2 and t_1 gives a signal which is a function of the emission time constant and has a peak. More precisely

Table 3.5: Predicted changes in capacitance due to changes in generation-recombination centers occupancy.

	Majority Carriers	**Minority Carriers**
Emission	Acceptor traps Schottky diodes $e_n > e_p$ **C increases overtime**	Acceptor traps $p^+ - n$ diodes $c_p > c_n$ **C decreases over time**
Capture	Acceptor traps Schottky diodes F.B. after R.B. **C decreases over time**	Acceptor traps $p - n$ or Schottky diodes Carriers generated optically **C increases over time (R.B.)**

the difference of capacitance between time t_1 and time t_2 is $C(t_2, T) - C(t_1, T) \propto f(\tau_e) = \mathrm{e}^{(-t_1/\tau_e)} - \mathrm{e}^{(-t_2/\tau_e)}$. The signal $f(\tau_e)$ has a peak as illustrated in Fig. 3.11; the peak occurs at

$$\tau_{e,max} = \frac{t_2 - t_1}{\ln(t_2/t_1)} \tag{3.20}$$

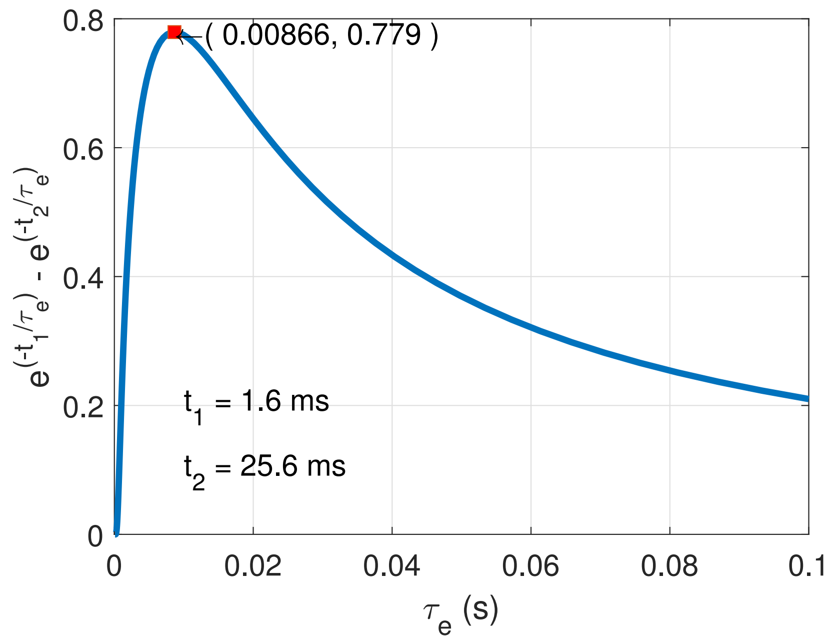

Figure 3.11: Predicted peak in the function f(τ_e) = e^{-t_1/τ_e} - e^{-t_2/τ_e}. Illustration for the case when t_1 = 1.6 ms and t_2 = 25.6 ms.

The emission time constant is a function of the temperature. By measuring the capacitance over time as a function of the temperature, it is possible to experimentally extract the temperature corresponding to the maximum DLTS signal and correlate it to the emission time constant.

3.2.3.2 Setup for DLTS Measurements

It is possible to obtain the characteristics of G-R centers in semiconductors by measuring the capacitance as a function of time and temperature. DLTS measurements and analysis were performed on 4H-SiC avalanche photodiodes in this work. The setup for measuring the DLTS data is shown in Fig. 3.12. The setup consists of a cryogenic chamber hooked to a vacuum pump.

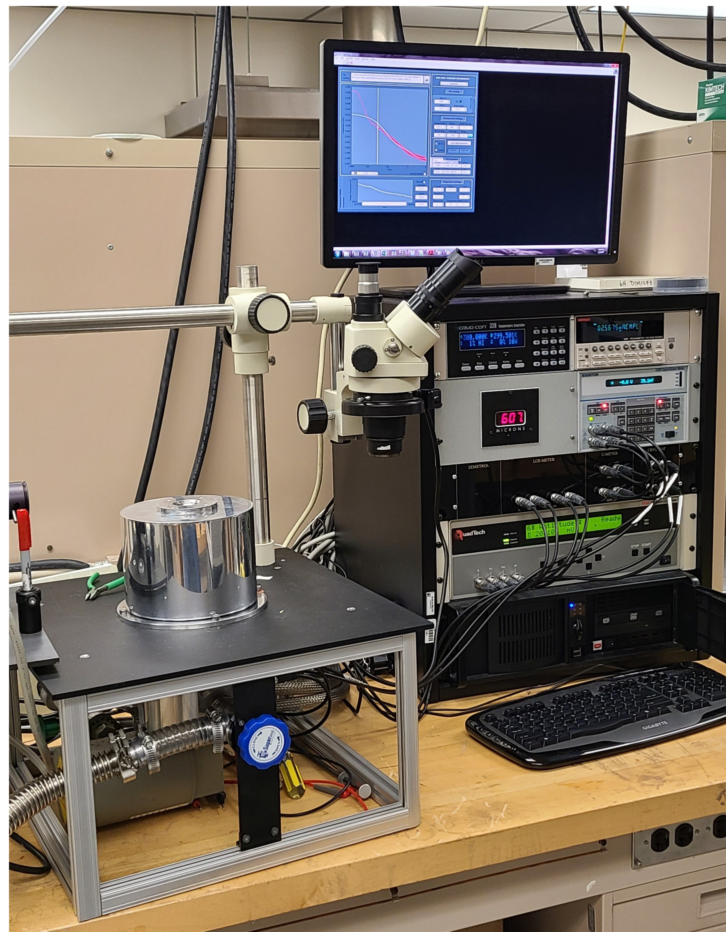

Figure 3.12: Setup for the deep-level transient spectroscopy measurements.

The device under test is mounted on a stage inside the cryogenic chamber; the mounting stage can be heated up to 800 K, and the chamber can be cooled down to 100 K with nitrogen. A temperature controller is used to set and monitor the temperature of the stage. A program developed by SEMETROL [56] is used to acquire the DLTS data. The schematic presented in Fig. 3.13 shows how the controller drives the temperature of the stage and capacitance measurements. The measurement starts by setting temperature points. After the temperature is established in the chamber, a small positive bias, the filling pulse, is applied to the devices to fill the G-R centers. The device is then reverse biased with a small negative voltage, and the capacitance is monitored over time.

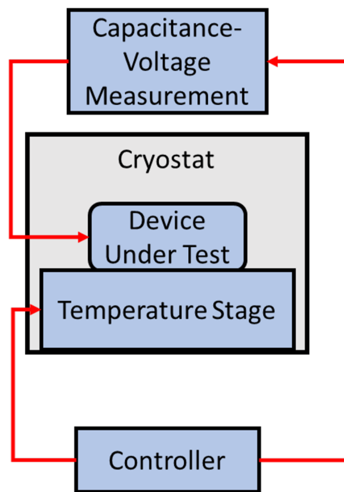

Figure 3.13: Illustrative diagram for DLTS measurements.

3.3 Baseline for the Dark Current in Wide-Bandgap Semiconductors from DLTS Characterization of 4H-SiC $p-i-n$ Diodes

The theoretically calculated saturation current for diode fabricated with wide- and ultrawide-bandgap semiconductors appear to be so small that it is necessary to investigate the source of

the dark current at low applied biases (unity gain). The previous section discussed generation-recombination centers (deep traps) and their effect on electrical characterization. This section presents capacitance measurements and the main results of DLTS analysis on 4H-SiC $p-i-n$ diodes. The DLTS analysis improved the understanding of 4H-SiC; the main conclusion drawn on 4H-SiC can be extended to other wide bandgap semiconductors. Because ultrawide-bandgap semiconductors represent a new class of material, it is necessary to fabricate a test structure with diamond, gallium oxide, or aluminum nitride to perform experiments that could help reinforce the understanding of ultrawide-bandgap materials.

3.3.1 Measured Capacitance as a Function of the Temperature for Extracting the Characteristics of Deep-Level Centers in 4H-SiC

Following the method described in Section 3.2.3.2, capacitances were measured in 4H-SiC $p-i-n$ diodes over time for several temperatures. The device measured is shown in Fig.2.27. The capacitances were measured from 100 K to 700 K. For each temperature setpoint, the capacitance was monitored for 10 seconds. The results of the measurement are shown in Fig. 3.14 For more details, the measured capacitance is shown in Fig. 3.15 as a function of the temperature; the data shown represent two horizontal cut-line of Fig. 3.14. The capacitance traces shown are measured 1.6 milliseconds and 8 seconds after the filling pulse.

It is observed that the capacitance increases with temperature but appears to be invariant to the time after the filling pulse, except in the range of 110 K to 220 K. For DLTS analysis, it is best to visualize the capacitance as a function of the time after the filling pulse as shown in Fig. 3.16; the plots on the figure represent vertical cut-lines in Fig. 3.14.

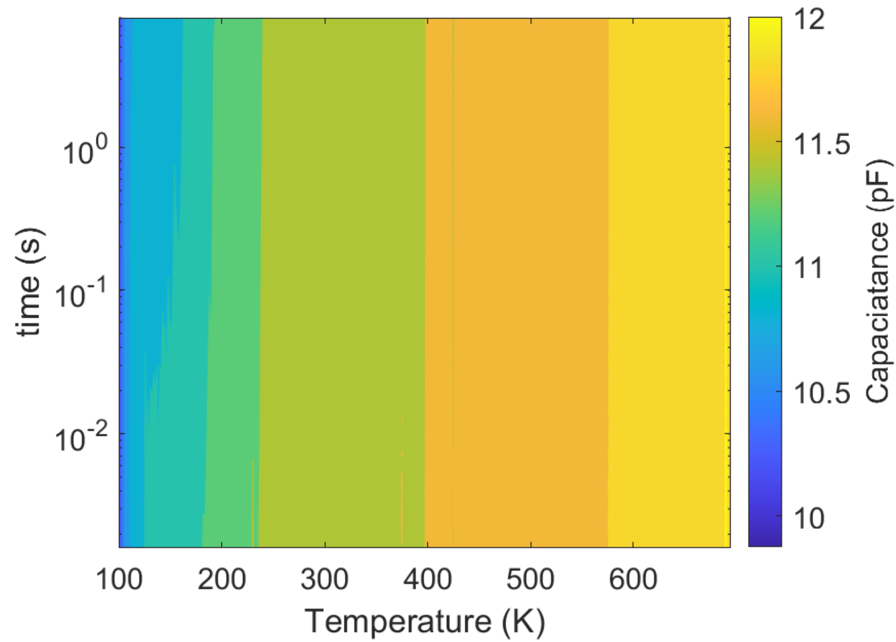

Figure 3.14: Measured capacitance transient as a function of the temperature in 4H-SiC $p-i-n$ diodes for DLTS analysis.

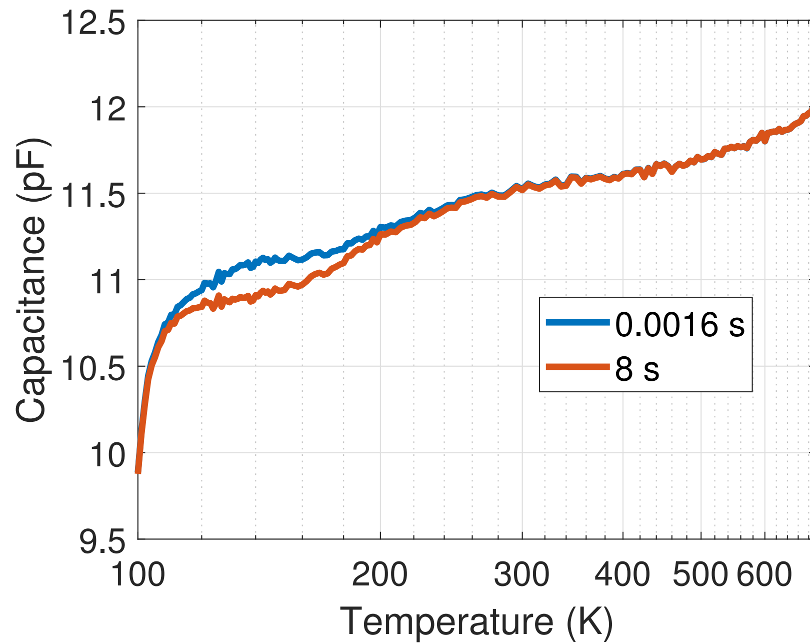

Figure 3.15: Capacitance versus temperature measured after 1.6 milliseconds and 8 seconds after the filling pulse.

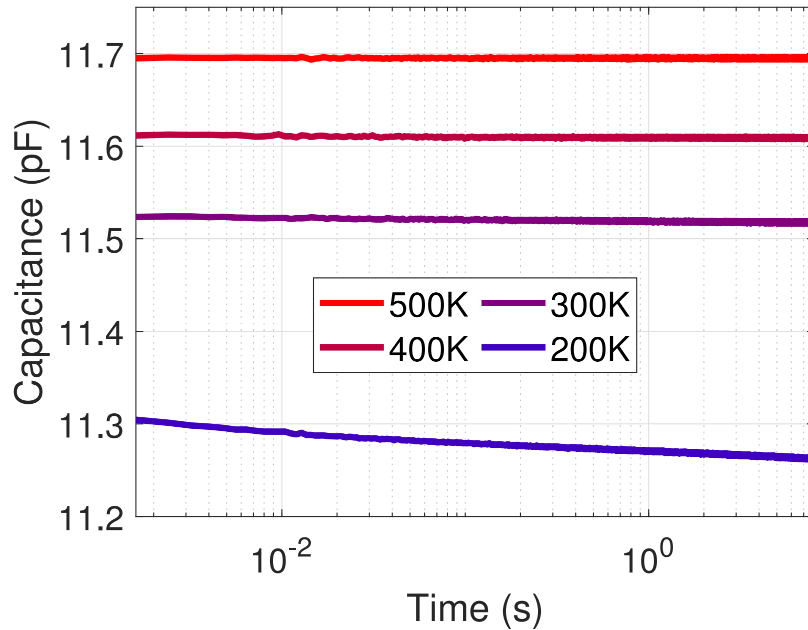

Figure 3.16: Capacitance measured as a function of the time after the filling pulse. At 200 K, the capacitance decreases, indicating that the generation-recombination centers are acceptors in nature.

The DLTS data shows that the capacitance is constant at high temperatures (> 300 K). Between 100 K and 220 K, the capacitance decreases over time. The observed trend in capacitance corresponds to the second scenario described in Section 3.2.3.1; the observed distortion in capacitance appears to be related to the emission of minority holes during the measurement pulse (in reverse bias). Processing the measured capacitance transient allows the characterization of the deep traps.

3.3.2 Extracted Density of Deep Traps, Temperature Dependence of the Emission Time Constant, and Implication on the Dark Current

The DLTS signal is the difference in measured capacitance between time t_1 and t_2 and is expressed as [47]

$$\delta C = C(t_1) - C(t_2) = \frac{C_0 n_T(0)}{2N_D}\left(\exp\left(-\frac{t_2}{\tau_e}\right) - \exp\left(-\frac{t_1}{\tau_e}\right)\right). \tag{3.21}$$

For a given measurement window given by t_1 and t_2, the DLTS signal is a function of the emission time constant τ_e, which is a function of the temperature T [47]. The relationship between the τ_e and T is given by (3.17), but the lack of knowledge about the energy of the traps and its cross-section makes the expression difficult to use. DLTS analysis combines theoretical and experimental findings to establish the dependence of the emission time constant on the temperature, leading to the extraction of traps' energy. From (3.21), it is possible to calculate the emission time constant that would result in the maximum DLTS signal [47]. This is accomplished by taking the derivative of the DLTS signal with respect to the emission time constant.

$$\frac{\partial \delta C}{\partial \tau_e} = \frac{C_0 n_T(0)}{2N_D}\left(\frac{t_2}{\tau_e^2}\exp\left(-\frac{t_2}{\tau_e}\right) - \frac{t_1}{\tau_e^2}\exp\left(-\frac{t_1}{\tau_e}\right)\right) \tag{3.22}$$

Setting the partial to zero results to

$$\frac{t_2}{\tau_e^2}\exp\left(-\frac{t_2}{\tau_e}\right) = \frac{t_1}{\tau_e^2}\exp\left(-\frac{t_1}{\tau_e}\right) \tag{3.23}$$

Therefore, the DLTS signal is maximum when

$$\frac{t_2}{t_1} = \exp\left(\frac{t_2 - t_1}{\tau_e}\right). \tag{3.24}$$

$$\tau_{e,max(\delta C)} = \frac{\ln(t_2/t_1)}{t_2 - t_1}. \tag{3.25}$$

The emission time constant corresponding to the maximum DLTS signal is given by (3.25). It is possible for a given gate window to theoretically predict the emission time constant that will result in the maximum change in capacitance. The measurement of the capacitance is done as a function of the temperature. From the measured data and for a gate window, it is possible to recover the temperature at which the difference in capacitance is maximum. The difference in capacitance ($C(t_1) - C(t2)$) is called the DLTS signal [47]. Evaluating the DLTS signal as a function of the temperature gives the DLTS spectra. The normalized DLTS spectra ($(C(t_1) - C(t_2))/C_0$) for the 4H-SiC $p - i - n$ diodes investigated is shown in Fig. 3.17 for five different gate windows.

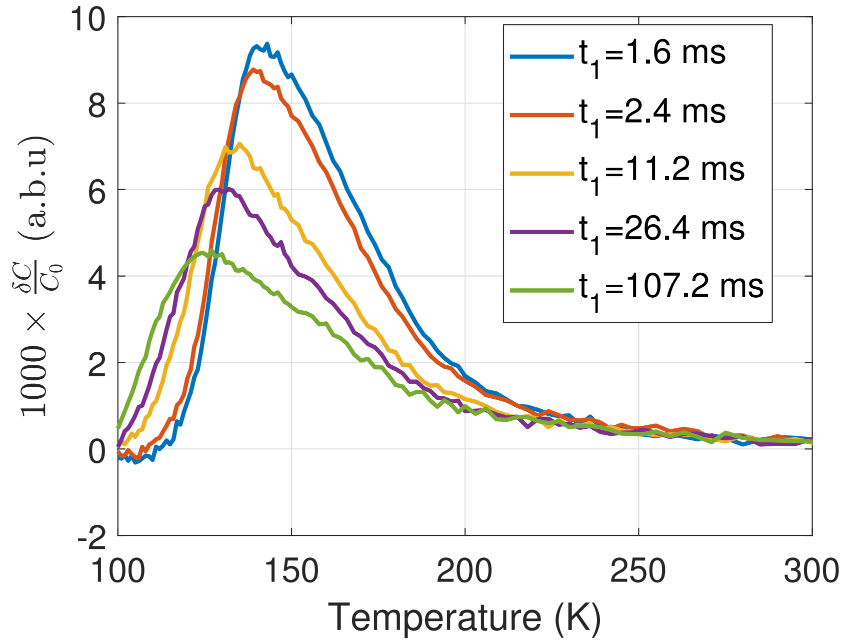

Figure 3.17: Normalized DLTS spectra for five selected gate windows. The windows are such that $t_2 = 16 \times t_1$. The temperature at which the maximum of the DLTS spectra occurs depends on the selected gate window.

The gate windows used to calculate the DLTS spectra are such that $t_2 = 16t_1$. Setting the ratio between t_2 and t_1 to 16 is somewhat arbitrary; however, the ratio should be sufficiently long

to measure an appreciable change in capacitance. It should be noted that the time t_2 is limited by the measurement duration. The DLTS spectra can be calculated for several windows; Fig. 3.18 shows the DLTS spectra for several gate windows with $r = t_2/t_1 = 16$. The color map highlights the region where the DLTS signal tends to be maximum.

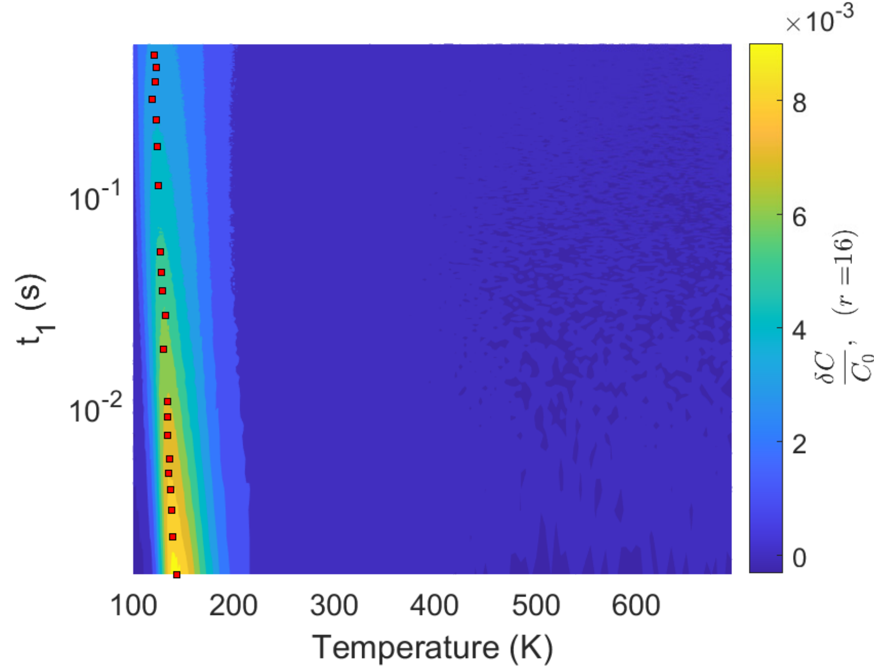

Figure 3.18: Calculated DLTS spectra for several gate windows. The gate windows are such that $t_2 = 16t_1$. A few DLTS spectra's peaks are appended to the figure.

The peaks of the DLTS spectra were calculated and appended to Fig. 3.18. For a gate window, the theoretical emission time constant and the experimental temperature, which tell the DLTS spectra' peak, are matched. Based on the relationship between the emission time constant and the temperature (3.17), the following equation can be obtained

The density of generation-recombination center can be calculated using (3.26) [47].

$$N_T = \frac{2N_D r^{r/(r-1)} \delta C_{max}}{C_0(1-r)}, \tag{3.26}$$

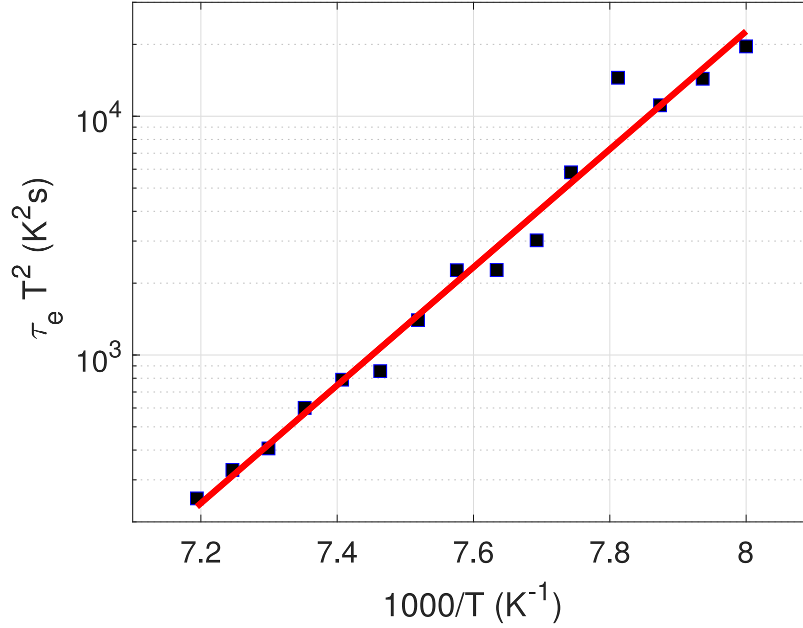

Figure 3.19: Extracted density of generation-recombination centers for different gate windows ($t_2 = 16 \times t_1$).

where $r = t_2/t_1$ [41]. For acceptors traps the lifetime of the is related to the traps energy by [51]

$$\tau_e = \frac{\exp(E_T - E_V)}{\sigma_p v_{th} N_V}, \tag{3.27}$$

with $E_T - E_V$ being the location of the center w.r.t. the valence band. The holes' velocity, v_{th}, is given by

$$v_{th} = \sqrt{3kT/m_p^*}, \tag{3.28}$$

where m_p^* is the effective mass for holes. The density of states in the valence band, N_V is

$$N_V = 2\left(\frac{2\pi m_h^* kT}{h^2}\right)^{3/2}. \tag{3.29}$$

The emission lifetime for holes and the cross-section obtained by considering the equations above

are given by

$$\tau_e = \frac{h^3 \exp\left(\dfrac{E_T - E_V}{kT}\right)}{2\sigma_p T^2 k^2 m_p^* \sqrt{3}(2\pi)^{3/2}}. \tag{3.30}$$

Multiplying (3.30) by T^2 and taking the natural logarithmic lead to

$$\ln\left(\tau_e T^2\right) = \ln\left(\frac{h^3}{2\sigma_p k^2 m_p^* \sqrt{3}(2\pi)^{3/2}}\right) + \frac{1}{T}\frac{(E_T - E_V)}{k} \tag{3.31}$$

The plot of $\ln\left(\tau_e T^2\right)$ versus $1/T$ is shown in Fig. 3.19. The depth of the traps extracted from the slope of the fit is 0.49 eV. Based on the extracted data, the emission time constant is plotted as a function of the temperature in Fig. 3.20. The cross-section can be calculated using

$$\sigma_p = \frac{h^3}{2\exp(y_{int}) k^2 m_p^* \sqrt{3}(2\pi)^{3/2}} \tag{3.32}$$

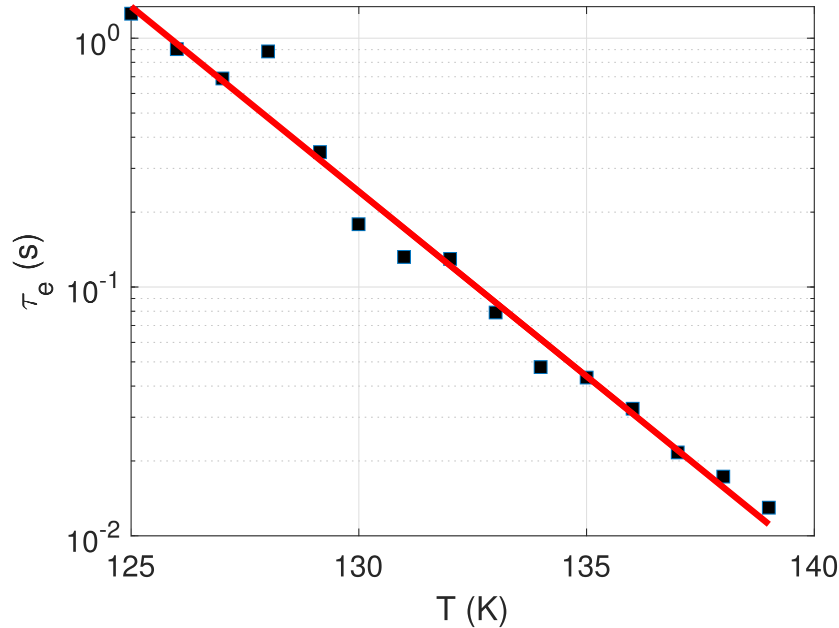

Figure 3.20: Measured emission constant as a function of the temperature.

Deep level transient spectroscopy (DLTS) analysis revealed the presence of deep levels ($\approx 1 \times 10^{15}$ cm^{-3}, calculated with (3.26)) in the characterized 4H-SiC avalanche photodiodes ($p-i-n$ diodes). The extracted cross-section, however, is too large and works as a fitting parameter. The analysis shows that the emission time constant of the traps decreases with temperature; this indicates that at elevated temperature, the emission could be so fast that instruments may be too slow to capture changes in signal due to trap emission. Understanding the measured I-V characteristics is important for calculating the multiplication (gain) and extracting impact ionization coefficients for breakdown voltage predictions.

3.4 Extraction of the Multiplication from Reverse I-V Measurements

In the previous sessions, deep-level transient spectroscopy analyses were performed to understand the source of the dark current in devices fabricated with wide- and ultrawide-bandgap semiconductors. It was seen that, for the case of 4H-SiC, the emission time constant decreases with the temperature, suggesting emission of carriers at a faster rate at elevated temperature. This section presents reverse current-Voltage measurements performed on 4H-SiC $p-i-n$ diodes. The measured current-voltage characteristics are used in future sessions to assess impact ionization coefficients relevant to breakdown voltage predictions.

3.4.1 Modeling The Photo Current of $p-i-n$ Diodes

Several factors can influence the resulting current and multiplication when a reverse bias is applied to diodes. Under illumination, the total current across a $p-i-n$ diode can be written as

$$I_D = I_{opt} + I_{dark} + I_{SW}, \tag{3.33}$$

where I_{opt} is the optical current (under illumination), which is bias-dependent. Note that when the $p-i-n$ diode is illuminated, it operates as a photodetector, and the current at unity gain ($I(V_A = 0V)$) is large enough to be well measured. I_{dark} is the dark current made up of the saturation current and the current emanating from the deep traps. I_{SW} is the parallel leakage, generally, through the sidewalls of the devices. The sidewall leakage is external to the diode and does not get multiplied; it can be extracted as the slope of the fit through the current at low voltage (before the avalanche process). For some of the 4H-SiC devices measured in this work, the current in the dark was still below the noise level. With the current being less than 1×10^{-14} A at a 100 V (see Fig 6.6) in the dark, the sidewall resistance can be estimated to be at large as 1×10^{16} Ω.

Besides the reverse saturation current, the generation current is another component of the dark current. The generation current in the depletion is given by (2.45). The current depends on the emission lifetime of the carriers. In the previous section, the emission lifetime is extracted at low temperatures. The lifetime is modeled using (3.27); it decreases with the temperature; however, in the case of holes, there must be a minimum lifetime given by (3.34) [38]. N_T is the concentration of deep centers, v_{th} is the carrier velocity, σ_p is the carrier cross-section, and m_h^* is the effective mass for hole. The plot of the lifetime and its lower limit is shown in Fig. 3.21.

$$\tau_e = \frac{1}{N_T v_{th} \sigma_p} = \frac{\sqrt{m_h^*}}{N_T \sqrt{3kT} \sigma_p} \tag{3.34}$$

The calculations are performed with $N_T = 2\times10^{15}$ cm^{-3} = 2×10^{21} m^{-3}; the effective mass

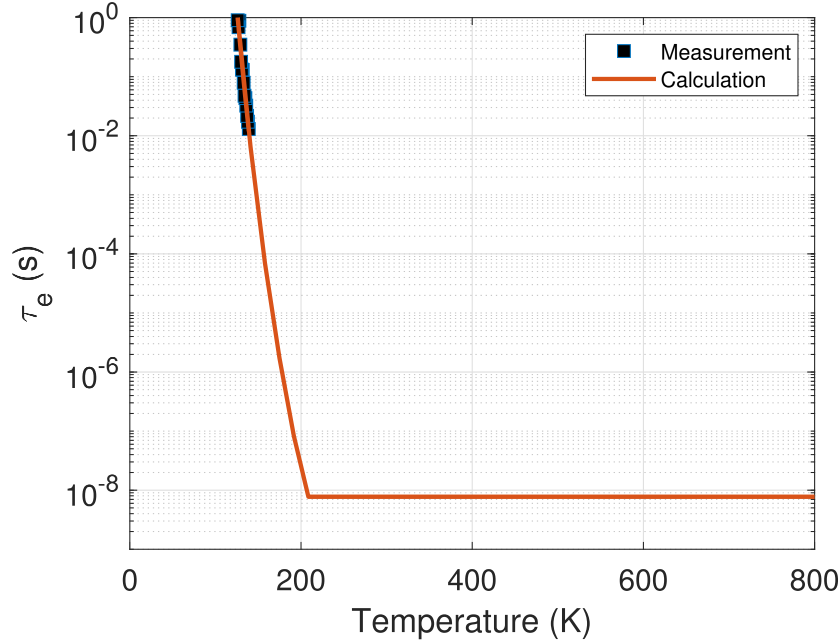

Figure 3.21: Calculated lifetime in 4H-SiC $p-i-n$ diodes.

for hole is m_h^* = 0.82m_e [57, 58], leading to the velocity, v_{th} = 1.29×10^7 cm/s. With the reported cross section for 4H-SiC being 5×10^{-16}, the calculated emission lifetime for hole is τ_e = 7.75×10^{-9}s. The measured diodes are doped at 2×10^{17} cm^{-3}, and the depletion width at breakdown is about $1\mu m$. The generation current [38] is

$$I_{gen} = \frac{Aqn_iW_i}{2\tau_e} \approx 1.1 \times 10^{-27}\text{A}. \tag{3.35}$$

In silicon, the intrinsic carrier concentration is n_i = 8.71 × 10^9 cm^{-3} at room temperature, the corresponding generation current is 2.02 × 10^{-9} A. The intrinsic carrier concentration has a strong influence on the generation current. In 4H-SiC and materials with a large bandgap, the intrinsic carrier concentration is very small, resulting in insignificant generation currents.

The generation current can be experimentally determined from the dark count using the continuity equation [59]. The expression for the generation current is

$$I_{gen} = Aq \int_0^W \frac{\partial n}{\partial t}\bigg|_{gen} dx, \tag{3.36}$$

where the generation rate is the count rate (CPS) divided by the volume of the depletion region. If the generation rate is uniform over the length of the depletion, the generation current becomes the count rate per second multiplied by the electron charge. The diode investigated shows 11 counts in 400 μs in Fig. 2.23, resulting in 27.5 k counts per second and a generation current of 4.41 $\times 10^{-15}$ A. The large difference between the generation current extracted with DLTS measurement and Geiger mode measurement can be attributed to the low speed of the DLTS setup. In DLTS measurements, the capacitance is sampled every 1.6 ms, while the resolution is far improved in Geiger mode. Deep traps in the characterized diodes seem to have a fast transient, making them undetectable with the DLTS setup.

The equivalent circuit of the diode is shown in Fig. 3.22. In the multiplication regime, the gain is highly sensitive to the change in applied bias; an increment of the bias by 0.1 V could take the gain from the thousands to the millions. For the multiplication modeling, it is essential to adjust the effective voltage across the diode by considering the effect of the series resistance. The effective voltage across the diode is $V_D = V_{DD} - R_S I_D$.

For devices with good edge termination, the leakage through the sidewall can be significantly reduced so that R_P is very large (10^{16} Ω) for 4H-SiC. When R_P is small, a considerable amount of current flows through the sidewall, causing early failure and preventing the avalanche process. Fabricating devices with good passivation and edge termination is crucial for the possibility of measuring avalanche current for breakdown studies.

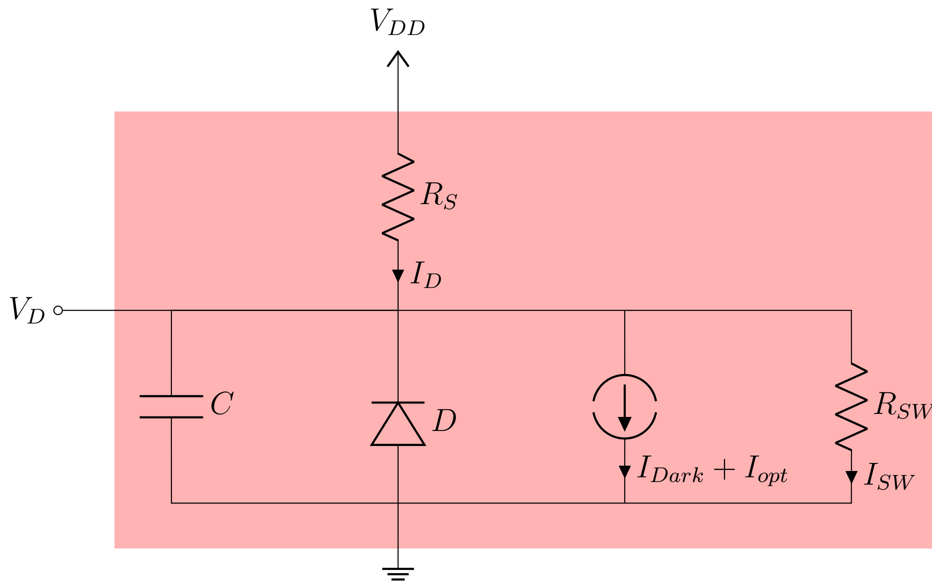

Figure 3.22: Equivalent model of the diode. This model allows the extraction of the effective voltage across the multiplication layer. The series resistance R_S is obtained from the Forward I-V measurement, The parallel resistance capture the device leakage.

3.4.2 Dark and Photo Measurements for the Experimental Evaluation of the Multiplication and the Establishment of the $p-i-n$ Diode Equivalent Circuit Model

The measured reverse current-voltage characteristics of the 4H-SiC $p-i-n$ diode described in Section 2.5 is shown on Fig. 3.23. The current reading is done with a Keithley 6514 mounted in series with the diode under test. The voltage was supplied by a Keithley 2400. In the figure, the photocurrent is large enough to be measured on the entire voltage range. The dark current at unity gain (low biases) is below the resolution limit of the instrument (early data is missing for the dark current).

Since the current in the reverse bias regime is very small, measurements were performed with additional care. A waiting time of 30 seconds was used for all bias points. The long wait

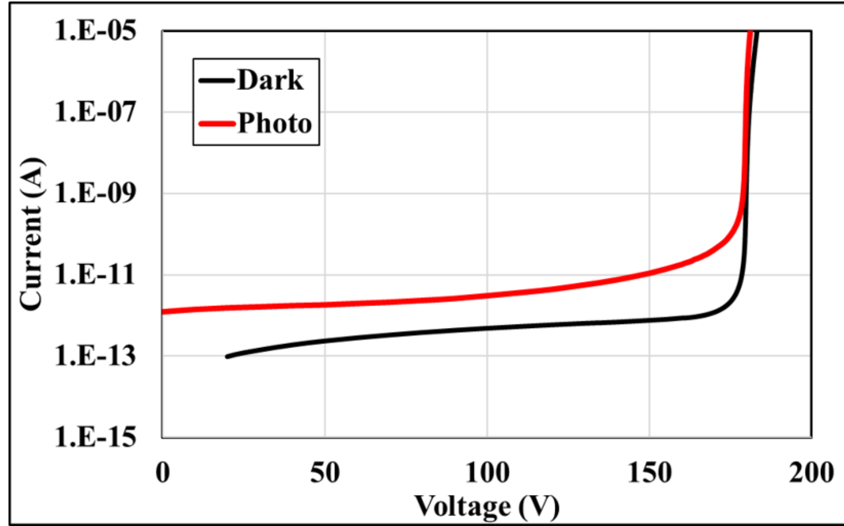

Figure 3.23: Measured dark- and photo-current in 4H-SiC $p-i-n$ diodes for the extraction of impact ionization coefficients. The measurements are performed at room temperature.

time allows ripples due to changes in voltage to disappear before the measurement is done. Also, the wait time accommodates the diode response time (driven by the RC constant). Because of the long wait time, a non-uniform voltage mesh is necessary to shorten the total duration of the measurement. The voltage mesh is finer at low voltages and denser in the avalanche region. The photo multiplication (the gain) is calculated by correcting the measured current. The photo current is recovered by subtracting the dark current from the total current (photo + dark). The gain associated with the current measurement is calculated using

$$M_{ph}(V_A) = \frac{I(V_A) - I_{MD}(V_A)}{I_P(V_A = 0\ V) - I_D(V_A = 0\ V)}, \tag{3.37}$$

where $I(V_A)$ is the total multiplied current (photo + dark); $I_{MD}(V_A)$ is the multiplied dark current; $I_P(V_A = 0\ V)$ is the total primary current (photo + dark) measured at $V_A = 0\ V$, also referred as the unity gain total current, and $I_D(V_A = 0\ V)$ is the primary dark current measured at $V_A = 0\ V$. V_A is the applied reverse bias. In practice, for 4H-SiC devices, the primary dark

current is considered a system-induced error that is subtracted from the photocurrent, usually much larger in magnitude. The gain associated with the measured current plotted in Fig. 3.23 is shown in Fig 3.24. Given the nature of the calculation, the gain is unity at 0 V and increases with the applied bias. In the avalanche region ($V_A > 170\ V$), the gain increases significantly.

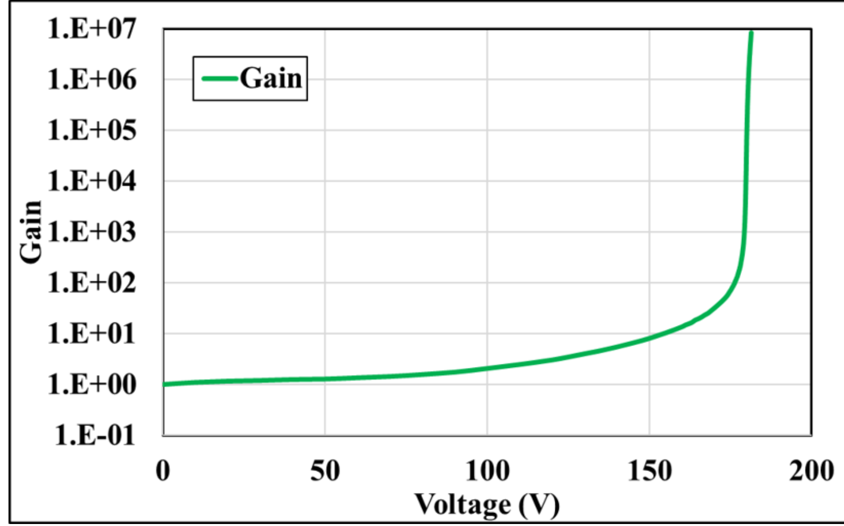

Figure 3.24: Bias dependent measured photo-multiplication in 4H-SiC $p-i-n$ diodes.

3.4.3 Extraction of the Unity-Gain Dark Current

From the experimentally calculated gain, it is possible to recover the dark current of the device at zero volts. Assuming that all carriers are multiplied in the same fashion and that the dark current is well measurable at high biases, the unity-gain dark current can be recovered by applying the known multiplication to the measured dark current. If the carriers are multiplied in the same fashion, the multiplication of the dark current is such that

$$I_{MD} = M_{ph} \times I_D, \tag{3.38}$$

where I_{MD} is the multiplied dark current and I_D is the dark current at unity gain. Taking

the logarithmic of (3.38) results to

$$\log\left(I_{MD}\right) = \log\left(M_{ph}\right) + \log\left(I_{D}\right) \tag{3.39}$$

Plotting $\log\left(I_{MD}\right)$ against $\log\left(M_{ph}\right)$ should ideally yield a line with a slope of 1 and a y-intercept equal to the logarithmic of the dark current. The plot of $\log\left(I_{MD}\right)$ versus $\log\left(M_{ph}\right)$ is shown on Fig. 3.25, for gain that are large enough for the dark current to be measurable. The data shows a linear trend, and the slope is close to 1, supporting the idea that the dark current is multiplied in the same fashion as the photo-current. The dark current can be extracted from the plot; the extracted dark current is

$$I_{dark} = 10^{-13.596} = 2.54 \times 10^{-14}\text{A}. \tag{3.40}$$

The measured dark current is much greater than the theoretical saturation current calculated in Section 2.4.4, suggesting that the unity-gain dark current may have multiple origins, one of them being the emission of deep centers.

From the deep level transient analysis, it is arguable that the saturation current in wide- and ultrawide-bandgap semiconductors is negligible compared to the background current generated by generation-recombination centers. In the dark, the main component of the current comes from the deep traps and the leakage at the sidewall. From the investigation of the dark current, it is essential to establish an equivalent model for the $p-i-n$ diodes. Such a model allows proper evaluation of the gain as a function of the effective voltage across the diode.

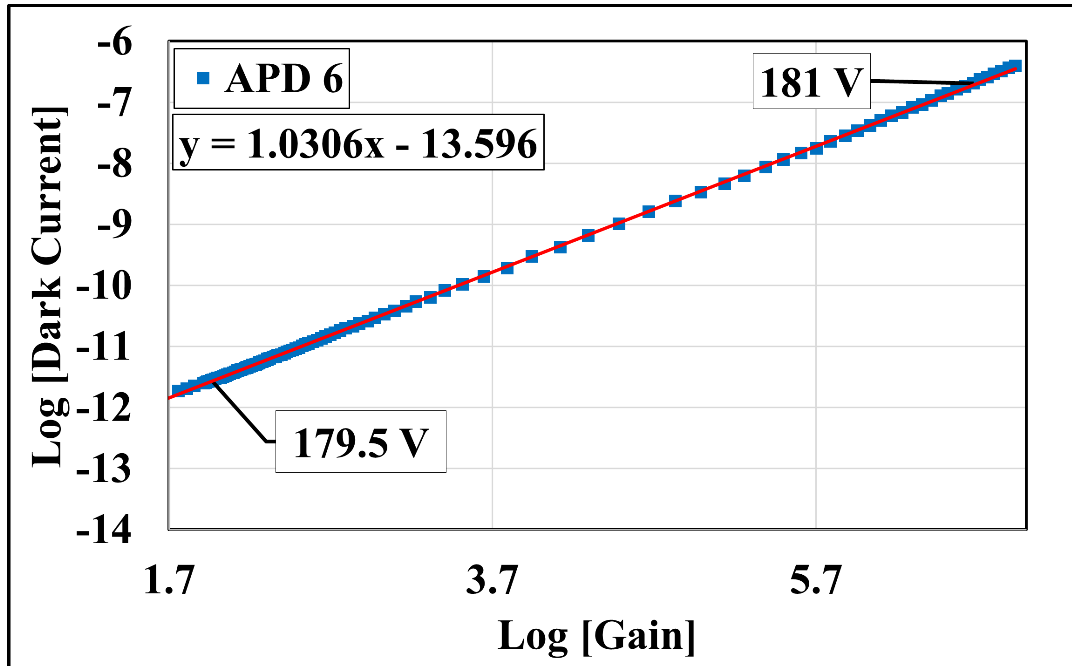

Figure 3.25: Extraction of the unity-gain dark current at room-temperature in 4H-SIC avalanche photodiodes using the $\log(I_{dark})$ versus $\log(M)$ method.

Conclusion

As materials emerge to fabricate power electronics devices, one of the main objectives is to achieve low resistance for increased efficiency and high breakdown voltages to improve functionality. The breakdown voltage and the on-resistance tend to oppose each other as high doping and low thicknesses result in low on-resistance and, undesirably, low breakdown voltage. To better evaluate the on-resistance versus the breakdown voltage limits of semiconductors, the effects of dopants' partial activation and incomplete ionization on the on-resistance of materials are investigated in Chapter 2. In this chapter, measurements performed on 4H-SiC $p-i-n$ diodes revealed that, though not often accounted for, the contact resistance in wide- and ultrawide-bandgap semiconductors is the dominant resistance.

Calculations in Chapter 2 showed that the concentration of free carriers in the depletion

regions of reverse biased $p-i-n$ diodes is very small, especially for the WBG and UWBG materials, and their potential energy is not enough to trigger an avalanche process. In this chapter, deep-level transient spectroscopy measurements were performed to reinforce the understanding of measured reverse current-voltage characteristics. The emission time constant of deep traps in 4H-SiC $p-i-n$ was characterized as a function of the temperature. The cross-section of the traps present in the 4H-SiC samples was too large and is considered a fitting parameter. The generation current in 4H-SiC, calculated from the carrier lifetime and the intrinsic carrier concentration, is insignificant for WBG and UWBG materials. Modern instruments cannot resolve the dark current of 4H-SiC at low applied biases (V_A < 100 V); if any, the dark current at those low applied biases seems to be dominated by the sidewalls.

For an improved accuracy in breakdown voltage calculation, reverse the measured current-voltage characteristics of $p-i-n$ diodes are used to extract impact ionization coefficients in the next chapter. The gain calculated from photo measurements is essential for establishing those coefficients.

Chapter 4: Survey of the Literature and Use of Experimental Data for the Calibration of Impact Ionization Coefficients Needed for Breakdown Voltage Calculations

Wide- and ultrawide-bandgap semiconductors are excellent candidates for expanding the capabilities of electronics devices beyond the limits of silicon. For power electronics, WBG and UWBG materials are desired because predictions show that they can block high voltages while maintaining a low on-resistance. The metric generally used to assess the trade-offs between the breakdown voltage and the unipolar on-resistance is the Baliga figure-of-merit (BFoM); however, the metric is commonly misevaluated, resulting in over-performance prediction. Instead of evaluating a set expression ($R_{ON} = 4V_{BR}^2/(\mu_n \epsilon \xi_C^3)$) for the power limits of a material, a more accurate approach is to assess the breakdown voltage and the on-resistance as separate entities. In the previous chapters, the partial activation and the incomplete ionization of dopants were studied for a more accurate assessment of the on-resistance. This chapter aims to set a framework for calculating the on-resistance and the breakdown voltage of $p-i-n$ structures and establish improved on-resistance versus breakdown voltage limits for wide- and ultrawide-bandgap semiconductors as a function of the temperature.

The chapter starts with the modeling of the avalanche process in semiconductors. The expressions for the multiplication process are derived as a function of impact ionization coefficients,

and the condition that indicates breakdown is discussed. Impact ionization coefficients drive the multiplication process and are essential for evaluating the breakdown voltage of devices based on their geometry and doping concentration of the constituent layers. A temperature-dependent model for impact ionization coefficients is proposed for more accurate multiplication and breakdown voltage modeling. The model is calibrated with measured multiplication, measured breakdown voltages, and reports from the literature. Impact ionization coefficients proposed for wide- and ultrawide-bandgap materials allow a more accurate calculation of the breakdown voltage.

The breakdown voltages of $p-i-n$ structures are calculated using established impact ionization coefficients. The optimum structures, which set on-resistance versus breakdown voltage limits, are discussed. The on-resistance and the breakdown voltage are evaluated as a function of the temperature, and improved power limits (on-resistance versus breakdown voltage) are proposed as a function of the temperature. Results indicate a significant improvement in the performance of ultrawide-bandgap materials (with high ionization energy) when the temperature is increased. It is observed that the background doping of semiconductors significantly deteriorates their ability to block high voltages. The failure to consider the incomplete ionization of dopants (as commonly done in the literature) results in performance overestimation.

4.1 Modeling the Avalanche Process with Impact Ionization Coefficients

The depletion region of semiconductor devices can hold applied reverse biases. Applied biases give rise to an electric field contained within the depletion region. A carrier injected in the depletion region can, under the effect of the electric field, drift and gain enough energy to trigger impact ionization events, resulting in charge multiplication. Depending on the direction of the

electric field, carriers must be injected appropriately to travel the depletion region. If the electric field in the depletion region is oriented from left to right, holes must be injected from the left edge, and electrons must be injected from the right edge. Carriers can also originate within the depletion region (under illumination) at a considerable distance away from the edges and gain enough energy from the electric field to initiate impact ionization events. Impact ionization collisions from carriers that have obtained high energy by drifting under the influence of the electric field result in the creation of new electron-hole pairs. The newly created carriers, in turn, can also drift under the electric field to generate new electron-hole pairs. Under high-electric fields, the creation of electron-hole pairs occurs in cascade successions of impact ionization collisions, resulting in charge multiplication. When out of control, the multiplication of carriers within the depletion region results in large currents and in the avalanche breakdown of the material. Modeling the avalanche multiplication allows the formulation of the breakdown voltage condition.

4.1.1 The Multiplication Process in The Depletion Region of Semiconductors

To model the multiplication process, a drift region of width W is considered, as shown in Fig. 4.1. An initial electron current, I_{n0}, is injected from the left side of the depletion, and the electric field, $\overrightarrow{\xi(x)}$, is oriented from right to left. For simplicity, only the depletion region, where the multiplication takes place, is presented. The depletion region is assumed to be delimited by 0 and W. For a $p-i-n$ diode, W could be the thickness of the i-layer; however, because the field extends slightly into the cladding layers, W is somewhat greater than the thickness of the i-layer. The depletion width, W, can also be smaller than the thickness of the i-layer if the i-layer is too thick or highly doped so that it is not fully depleted. Because of the multiplication due

to the electric field, the electron current increases when traversing the depletion region from left to right. A quantitative description of the charge multiplication process involves the continuity equations.

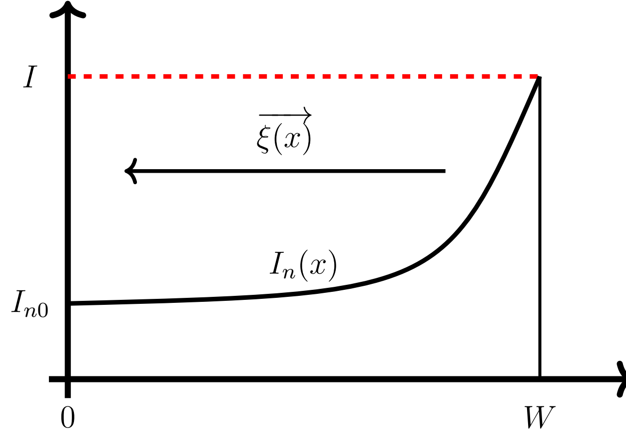

Figure 4.1: Illustration of current injection and charge multiplication in the depletion region. The current injected from the left side of the depletion region is multiplied under the influence of the electric field. At steady state, the total current ($I = I_n(x) + I_p(x)$) is constant with position.

Under high electric fields, the generation rate due to impact ionization collisions is much greater than the recombination rate. When the recombination rate is neglected, the electron continuity equation can be expressed as

$$\frac{\partial n}{\partial t} = \frac{1}{q}\frac{\partial J_n}{\partial x} + G_n, \tag{4.1}$$

where q is the electron charge; t is the time; J_n is the electron current density; G_n is the generation rate, and x is the position. Similarly, using the subscript p to denote holes, the hole continuity equation is

$$\frac{\partial p}{\partial t} = -\frac{1}{q}\frac{\partial J_p(x)}{\partial x} + G_p \tag{4.2}$$

At steady state, $\frac{\partial n}{\partial t} = 0$ and $\frac{\partial p}{\partial t} = 0$. Combining (4.1) and (4.2) results to

$$\frac{1}{q}\frac{d}{dx}\left(J_n(x) + J_p(x)\right) + G_n - Gp = 0. \tag{4.3}$$

Impact ionization collisions result in the creation of electron-hole pairs, and it can be assumed that the generation rate of electrons is equal to that of holes. Combining both the electrons and the holes continuity equation under impact ionization regime leads to

$$\frac{d}{dx}\left(J_n(x) + Jp(x)\right) = 0. \tag{4.4}$$

As implied by (4.4), at steady state, the derivative of the total current with respect to position is zero; therefore, the current is constant with the position at steady state, and the constant total current is

$$I = I_n(x) + I_p(x). \tag{4.5}$$

In the case where electrons are injected from the left as shown in Fig. 4.1, the electron current grows from left to right, but the total current, I, is constant. The hole current, $I_p(x)$, is not shown in Fig. 4.1; it can be evaluated as $I_p(x) = I - I_n(x)$. The hole current at steady state is such that $I_p(W) = 0$, and $I_p(0) = I - I_{n0}$.

By the nature of the impact ionization process, the increase in hole current at a position x is opposite to the incremental increase in the electron current. Because the gradual increase in current is related to the number of electron-hole pairs generated by impact ionization, the change in current is such that

$$\frac{dI_n(x)}{q} = -\frac{dI_p}{q} = \frac{\alpha(x)I_n dx + \beta(x)I_p dx}{q}, \tag{4.6}$$

where α represents impact ionization coefficients for electrons, and β represents impact ionization coefficients for holes. Impact ionization coefficients represent the number of electron-hole pairs generated by impact ionization collisions when a carrier travels one centimeter of the material. In this work, Impact ionization coefficients are indirectly a function of position; that is, impact ionization coefficients are evaluated as a function of the electric field, which is space-dependent. The multiplication process in the depletion region can be modeled with (4.7) [41,60].

$$\begin{cases} dI_n(x) = \alpha I_n(x)dx + \beta I_p(x)dx \\ -dI_p(x) = \alpha I_n(x)dx + \beta I_p(x)dx \\ I = I_n(x) + I_p(x) \end{cases} \tag{4.7}$$

The equations given by (4.7) lead to two differential equations that can be solved for the modeling of the multiplication and for establishing the breakdown voltage condition.

4.1.2 The Ionization Integral for the Breakdown Voltage Condition

By combining the first and the third equation of (4.7), a differential equation is obtained for the electron current in the depletion region described in Fig. 4.1 [41]. The equation is given by

$$\frac{\mathrm{d}I_n(x)}{\mathrm{d}x} - I_n(\alpha(x) - \beta(x)) = \beta I. \tag{4.8}$$

The equation is a first-order differential equation; for simplicity and conciseness, the space-dependence of impact ionization coefficients is not always stated; $\alpha(x)$ and $\beta(x)$ are occasionally

expressed as α and β. Multiplying all terms of (4.8) by the integration factor yields

$$\frac{dI_n(x)}{dx}e^{\int_0^x -(\alpha-\beta)du} - I_n(x)(\alpha-\beta)e^{\int_0^x -(\alpha-\beta)du} = \beta I e^{\int_0^x -(\alpha-\beta)du} \tag{4.9}$$

Using the chain rule, the equation can be arranged to give

$$\frac{d}{dx}\left[I_n(x)e^{\int_0^x -(\alpha-\beta)du}\right] = \beta I e^{\int_0^x -(\alpha-\beta)du}. \tag{4.10}$$

Integrating both sides of the equation over the depletion regions results to

$$\int_0^W \frac{d}{dx}\left[I_n(x)e^{\int_0^x -(\alpha-\beta)du}\right]dx = \int_0^W \beta I e^{\int_0^x -(\alpha-\beta)du}dx. \tag{4.11}$$

Applying the fundamental theorem of calculus and realizing that $I_n(0) = I_{n0}$ and that $I_n(W) = I$, the previous equation yields

$$I e^{\int_0^W -(\alpha-\beta)du} - I_{n0} = I\int_0^W \beta e^{\int_0^x -(\alpha-\beta)du}dx. \tag{4.12}$$

The right-hand side of the previous equation can be broken into two integrals; this is accomplished by using the fact that $\beta = -(\alpha-\beta)+\alpha$. It follows that

$$I e^{\int_0^W -(\alpha-\beta)du} - I_{n0} = I\int_0^W \alpha e^{\int_0^x -(\alpha-\beta)du}dx - I\int_0^W (\alpha-\beta)\, e^{\int_0^x -(\alpha-\beta)}dx. \tag{4.13}$$

Further rearrangement results to

$$e^{\int_0^W -(\alpha-\beta)du} - \frac{I_{n0}}{I} = \int_0^W \alpha e^{\int_0^x -(\alpha-\beta)du} dx - \int_0^W (\alpha-\beta) e^{\int_0^x -(\alpha-\beta)du} dx. \tag{4.14}$$

Realizing that $I_{n0}/I = 1/M$ leads to

$$e^{\int_0^W -(\alpha-\beta)du} - \frac{1}{M_n} = \int_0^W \alpha e^{\int_0^x -(\alpha-\beta)du} dx - \int_0^W (\alpha-\beta) e^{\int_0^x -(\alpha-\beta)du} dx. \tag{4.15}$$

The following is an identity needed to further simplify the expression for the modeling of the multiplication

$$\int_0^W f(x) e^{-\int_0^x f(u)du} dx = 1 - e^{-\int_0^W f(u)du}. \tag{4.16}$$

The identity stated above can be used to rewrite the second term of (4.15), which becomes

$$e^{\int_0^W -(\alpha-\beta)du} - \frac{1}{M_n} = \int_0^W \alpha e^{\int_0^x -(\alpha-\beta)du} dx - 1 + e^{\int_0^W -(\alpha-\beta)du} \tag{4.17}$$

The first term of the LHS and the last term of the RHS can be dropped since they are equal. The result is the following equation, which gives a relationship between the total multiplication and impact ionization coefficients under electron injection.

$$1 - \frac{1}{M_n} = \int_0^W \alpha e^{\int_0^x -(\alpha-\beta)du} dx \tag{4.18}$$

The right-hand side of (4.18) is the ionization integral. At the breakdown, the electron

initiated multiplication, M_n, is very large (infinity), and the ionization integral equals 1.

4.2 Key Differences Between $p-i-n$ and $n-i-p$ Structures

The avalanche multiplication of carriers given by (4.18) is specific for the case when electrons are injected from the left edge of the depletion regions, and the electric field is oriented from right to left. It is also possible for the electric field to be oriented from left to right. In the case of diodes with an i-layer, the electric field's direction depends on the type of the structure, which can be $p-i-n$ or $n-i-p$.

4.2.1 The Ionization Integral for $p-i-n$ Structures

There can be two versions of the $p-i-n$ diodes as shown in Fig. 4.2(a) and Fig. 4.2(b). Normally, the layers are stacked vertically; in the case of the $p-i-n$ diode, the p^+ layer faces upward, and the structure is also called a p-illuminated device. in both structures shown in Fig. 4.2, the electric field is oriented from right to left. Illuminating the device from the top results in electron injection, and illumination from the bottom results in holes injections.

There is a significant difference in how multiplication is achieved in the two $p-i-n$ structures presented above. In the case of electron injection, in the case illustrated in Fig. 4.2(a) the injected electrons are first subjected to a high electric field, which gradually decreases, whereas in the case presented in Fig. 4.2(b) the electrons experience a low electric field, which gradually increases. In both cases, because the electric field has the same direction, the equations for modeling the multiplication are similar; one should be careful to properly align the electric field with the position of the devices when evaluating impact ionization coefficients. The system of

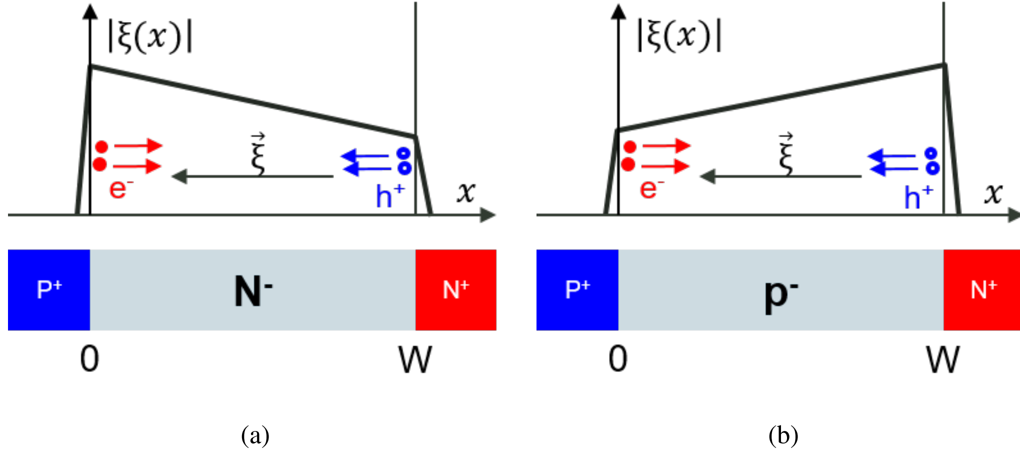

Figure 4.2: Two possible $p-i-n$ structures and their resulting field profile. In both structures, the electric field is oriented from right to left (bottom to top for vertical stacking). In the case of (a) the i-laver is n-type doped, and the peak electric field is toward the surface. In the case of (b), the i-layer is p-type doped, and the peak electric field is toward the bottom of the structure.

equations below models the multiplication for pure electron injection (first equation) and pure holes injection (second equation). The case of electron injection was treated in Section 4.1.2; a analogous derivation gives the following for hole multiplication.

$$\begin{cases} 1-\dfrac{1}{M_n} = \displaystyle\int_0^W \alpha e^{\int_0^x -(\alpha-\beta)du} dx \\ 1-\dfrac{1}{M_p} = \displaystyle\int_0^W \beta e^{\int_x^W (\alpha-\beta)du} dx \end{cases} \tag{4.19}$$

4.2.2 The Ionization Integral for $n-i-p$ Structures

Two possible $n-i-p$ structures are shown in Fig. 4.3. When stacked vertically, the n^+ layer faces upward, and the device is called n-illuminated. Illuminating the device from the top results in holes injection, and illumination from the bottom results in electrons injection. In the case of $n-i-p$ structures, the electric field is oriented from left to right (top to bottom if stacked vertically). The multiplication for $n-i-p$ diodes can be derived following the steps of

Section 4.1.2; however, there is a symmetry that simplifies the problem. Electrons in Fig. 4.2(a) behave like holes in Fig. 4.3(a). The expression for the $n-i-p$ structure is deduced from those of $p-i-n$ structures by just substituting α for β, β for α, and M_n for M_p.

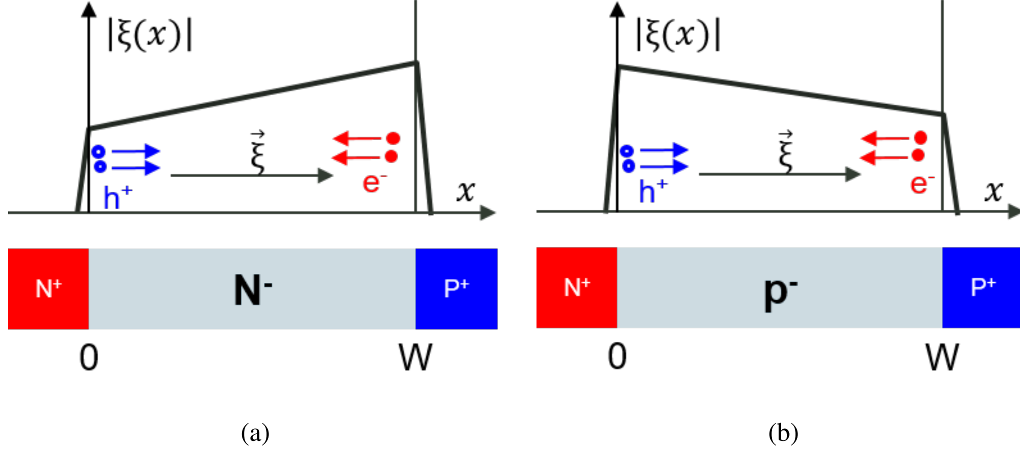

(a) (b)

Figure 4.3: Possible field profiles in *n-i-p* structures. In (a), holes travels in an increasing field, and in (b), holes travel a decreasing field.

For the cases illustrated in Fig. 4.3(a) and Fig. 4.3(b) the multiplications for pure electrons injection and pure holes injection are given, respectively, by the first and second equation of the following system of equations.

$$\begin{cases} 1-\dfrac{1}{M_n} = \displaystyle\int_0^W \alpha e^{\int_x^W -(\alpha-\beta)du} dx \\ 1-\dfrac{1}{M_p} = \displaystyle\int_0^W \beta e^{\int_0^x (\alpha-\beta)du} dx \end{cases} \tag{4.20}$$

4.2.3 Impact of the Injection Method on the Multiplication

In the previous section, four equations were derived for modeling the multiplication in $p-i-n$ and $n-i-p$ structures. The four equations exist in the literature, but it is essential to know which equation to use depending on the case presented. The equations derived for $p-i-n$

structures are found in the work of [61, 62], and the equation proposed for $n - i - p$ structures can be found in the work of [63].

Pure electron injection and pure hole injection result in different multiplication processes but lead to the same breakdown voltage as shown in Fig. 4.4. The multiplication shown in Fig. 4.4 is calculated using (4.19) and assuming that the i-layer of the $p - i - n$ diode is n-type doped. The figure shows the multiplication for pure electron injection from the left side and pure hole injection from the right side of the device. The geometry of the device is given in Table 5.1. The material simulated is 4H-SiC, and the impact ionization coefficients used for the simulation are summarized in Table 4.2. Note that the breakdown voltage is defined as the voltage at which the multiplication becomes very large, and the current in the devices grows significantly in reverse bias. In other word, breakdown occurs when the multiplication is infinity, and the right-hand side of equations given by (4.19) and (4.20) equals to one.

As illustrated in Fig. 4.2 there are two version of the $p - i - n$ structure. In Fig. 4.2(a), holes are injected from the low field side to the high field side; in Fig. 4.2(b) holes are injected from the high field side to the low field side. Fig. 4.5 illustrate how the multiplication changes depending on how holes traverse the electric field. When the i-layer of the $p - i - n$ structure is n-doped, holes travel the depletion region from the low field side to the high field side (increasing field), and calculation shows that the breakdown voltage in this scenario is larger. For $p - i - n$ devices with a p-type i-layer (decreasing field), the breakdown voltage appears smaller with hole injection. A $p - i - n$ structure with an n-type doped i-layer could result in higher breakdown voltages for diodes with non-uniform internal fields.

Another physics worth considering for modeling the avalanche multiplication is the dark-space, which accounts for the distance the carriers must travel to gain the threshold energy needed

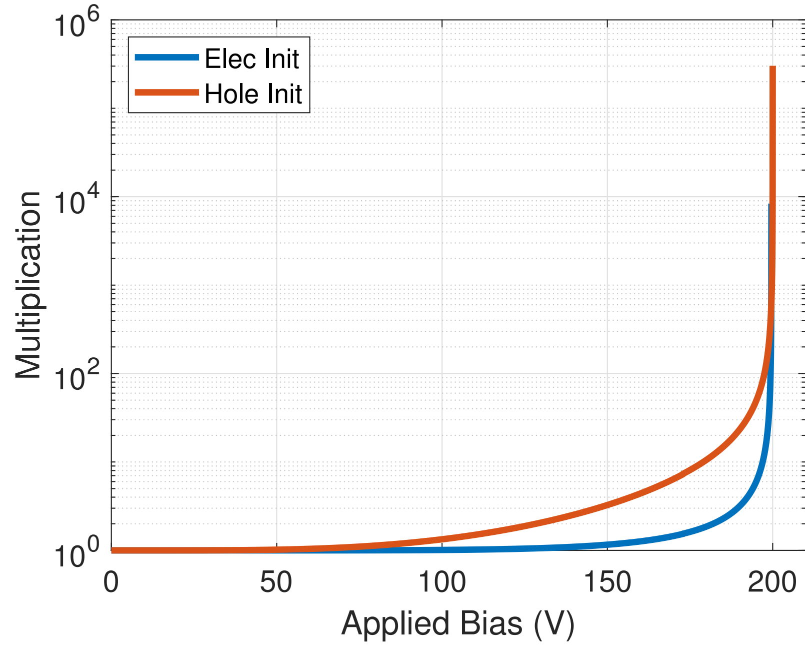

Figure 4.4: Comparison of the multiplication initiated by electrons and holes injection in a 4H-SiC $p-i-n$ diode. Though the multiplication is different with the reverse bias, both electrons and holes lead to the same breakdown voltage.

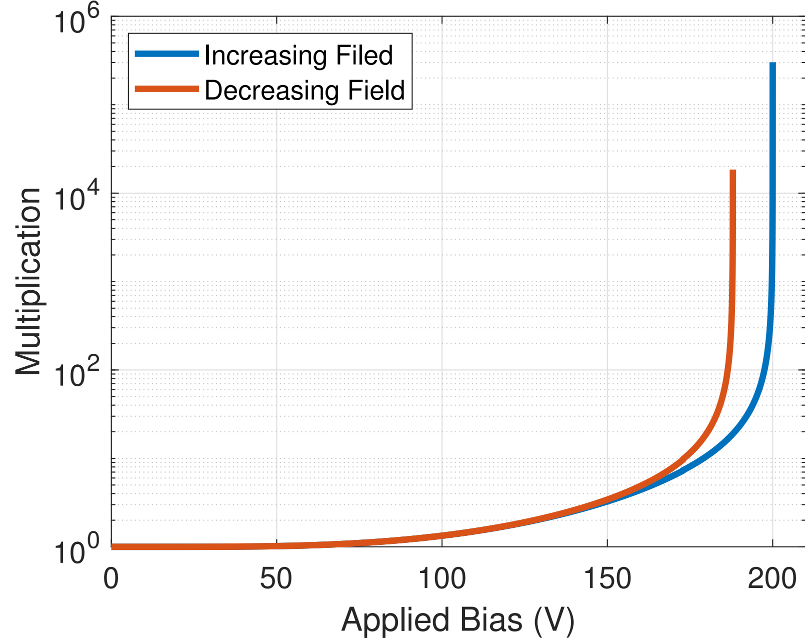

Figure 4.5: Comparison of multiplication with holes injection in a 4H-SiC $p-i-n$ diodes for an n-doped i-layer and a p-doped i-layer. It is seen that the injection of carriers with dominant impact ionization coefficients in an increasing field leads to higher breakdown voltages.

for an impact ionization collision. The main effect of dark-space is the reduction of the available distance for impact ionization collisions, so accounting for the dark-space results in less multiplication and slightly higher breakdown voltage. The effects of the dark-space are discussed in the work of Okuto [64]; it is reported that the impact of the dark-space is severe for devices with small geometry. In this work, the effects of the dark-space are neglected because the focus is on the studies of power devices that somewhat require large geometries to block high voltages.

In most cases, the diodes experience both electron and hole injection. In this scenario, the resulting multiplication combines the results of both pure electrons and hole injection. The resulting multiplication [65] is given by (4.21). The injection mixture is indicated with k; k equals 0 for pure electron injection and 1 for pure hole injection.

$$1 - \frac{1}{M} = \frac{(1-k)\int_0^W \alpha e^{-\int_0^x (\alpha-\beta)du} dx + k e^{-\int_0^W (\alpha-\beta)dx} \int_0^W \beta e^{\int_x^W (\alpha-\beta)du} dx}{1 - k + k e^{-\int_0^W (\alpha-\beta)dx}}. \tag{4.21}$$

There are more reports in the literature on the modeling of the multiplication with impact ionization coefficients. The time dependence of impact ionization coefficients is discussed by Lee et al. [66], and Woods e al. [61] have addressed the effect of local generation on the multiplication.

4.3 History of Impact Ionization Coefficients and Proposed Model

The modeling of the multiplication and the breakdown voltage requires knowledge of impact ionization coefficients. For the more mature materials such as silicon, 4H-SiC and gallium nitride, several studies have been taken to establish the electric field dependence of impact ionization coefficients, but for the most recent materials such as ultrawide-bandgap semiconductors,

more studies are needed for those coefficients. In this work, the breakdown voltage is evaluated from the ionization integral, and the need for accurate values of impact ionization coefficients and their temperature dependence is paramount.

Several authors have reported values for impact ionization coefficients for silicon and 4H-SiC. For 4H-SiC, the temperature dependence of impact ionization coefficients has been proposed by Nida and Grossner [67], Hatakeyama [68], and Niwa et al. [69]. Using existing temperature-dependent impact ionization coefficients models to evaluate the temperature dependence of the breakdown voltage of a 4H-SiC $p-i-n$ diode yields results shown in Fig. 4.6.

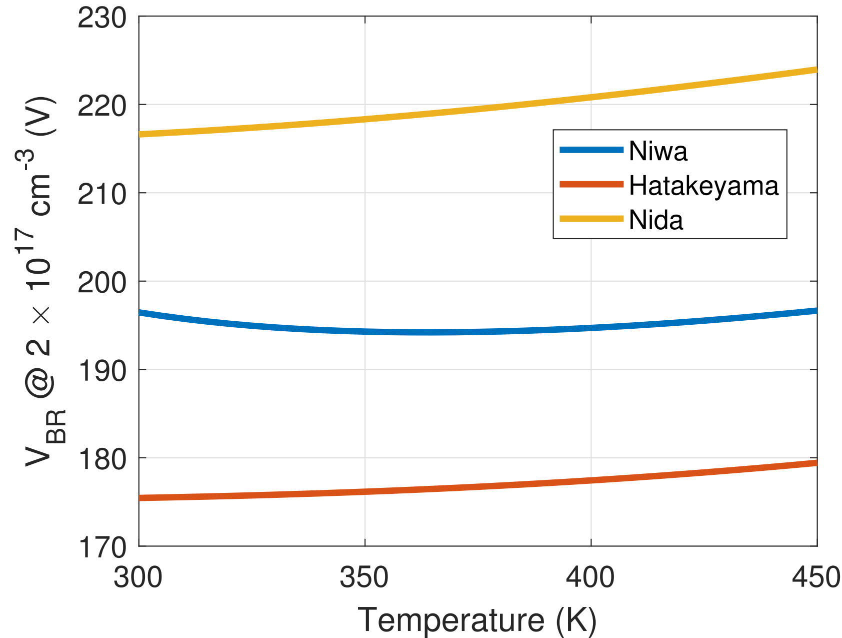

Figure 4.6: Predicted temperature dependence of the breakdown voltage based on impact ionization coefficients surveyed from the literature. The discrepancy in breakdown voltage calculated with different models shows the need for more reliable values of impact ionization coefficients.

The i-layer of the simulated diode is 2 μm thick, and its doping concentration is 2×10^{17} cm^{-3}. Measurement of a $p-i-n$ diodes with similar characteristics indicates a breakdown voltage around 184 $\pm$ 5 V. The predicted breakdown voltages shown in Fig. 4.6 are different de-

pending on the impact ionization coefficient model used. To effectively compute more accurate breakdown voltage values, this work undertakes efforts to establish more reliable values of impact ionization coefficients. After a brief review of the history of impact ionization coefficients, a modified Thornber model is proposed for those coefficients. The modified Thornber model is calibrated with experimentally measured multiplication, measured breakdown voltage, and reports from the literature.

4.3.1 History of Impact Ionization Coefficients

Impact ionization coefficients are essential parameters for evaluating the performance of semiconductors. There are numerous models for impact ionization coefficients across the literature; the earliest models come from plasma theory [70]. In the early studies of avalanche breakdown in semiconductors, the two predominant models for impact ionization were the Wolf and the Shockley models, also known as the high- and low-field models. In the Wolf model, the carrier's energy (from the field) is high compared to the energy loss due to collision. As such, the electrons that undergo collision have a quasi-Maxwellian distribution in which the electron temperature (T) is related to the mean-free-path (λ), the electric field (ξ), and the optical phonon energy (E_R) by $T = q\xi\lambda/(3E_R)$ [71], leading to the $1/\xi^2$ model for impact ionization coefficients. In Shockley's model, the energy of the carriers is low, and only carriers that do not undergo a collision (lucky carriers) create impact ionization. The distribution of those electrons that are able to reach the ionization energy, E_i, without undergoing a collision is proportional to $\exp\left(-E_i/(q\xi\lambda)\right)$, leading to the $1/\xi$ model for impact ionization coefficients. Several authors have proposed models that consolidate both the high- and low-field models for impact ionization coefficients. Baraff's model

is based on a maximum anisotropy electron distribution function [71]. Okuto and Crowell have proposed two models [72, 73]; they rely on nonphysical parameters. In Silicon, Goldsman extracted impact ionization coefficients by solving the Boltzmann Transport Equation (BTE), from which he obtained the non-equilibrium distribution function [74].

Although there are several models for impact ionization coefficients, their actual values are more important than the formulas used to obtain them. The correct values of impact ionization coefficients are the ones that can predict experimentally observed multiplications. For optical application, it is desired to have a large ratio between the impact ionization coefficients of electrons and that of holes for low noise [26].

The literature also reports on the anisotropy of impact ionization coefficients; the breakdown voltage of $p^+ - n$ diodes on a $(11\overline{2}0)$ 4H-SiC wafer was found to be only 60 % that on a (0001) 4H-SiC wafer [68]. The anisotropy of the impact ionization is related to the anisotropy of the drift velocity, scattering mechanisms, and the electronic band structure [68]. It is also reported that wide bandgap semiconductors have smaller impact ionization coefficients compared to silicon and that the junction type has little effect on the breakdown voltage [75]. It is worth noting that the avalanche process is primarily dominated by the carrier having the dominant impact ionization coefficient [76]. The time dependence of the avalanche process is discussed by Lee et al. [66].

For AlGaN alloys, the dependence of impact ionization on the alloy composition has been discussed by Bulutay [77]. Although there is no empirical expression for evaluating impact ionization coefficients as a function of the alloy composition, it is stated that the alloy composition significantly affects the alloy scattering. The overall effect of alloy composition is the reduction of impact ionization coefficients due to the decrease in the mean-free path of carriers.

4.3.2 Proposed Model for the Temperature Dependence of Impact Ionization Coefficients

Impact ionization coefficients are modeled as a function of the electric field and the temperature. The coefficients for electrons are denoted α, and that of holes are denoted β. The proposed modified Thornber model for impact ionization coefficients are given by (4.22) and (4.23), where E_G represents the bandgap of the material. The parameters of the proposed model have expected effects on impact ionization coefficients; however, when used in the expression, they do not necessarily retain their physical values. The ionization threshold energy, one of those physical parameters, is theoretically 3/2 E_G [78] for parabolic energy band; however, findings shows that this value may vary [79]. The parameters for electrons are denoted with the subscript e, and the parameters for holes are denoted with the subscript h. The high field effective ionization energies are expressed with the parameters E_{ie} and E_{ih} for electrons and holes, respectively.

$$\alpha\left(\xi,T\right)=\frac{q\xi}{E_{ie}(T)}\exp\left(\frac{\frac{3}{2}E_G(T)}{q\xi\lambda_e(T)+\frac{q^2\xi^2\lambda_e(T)^2}{E_{re}}+E_{kTe}(T)}\right) \tag{4.22}$$

$$\beta\left(\xi,T\right)=\frac{q\xi}{E_{ih}(T)}\exp\left(\frac{\frac{3}{2}E_G(T)}{q\xi\lambda_h(T)+\frac{q^2\xi^2\lambda_h(T)^2}{E_{rh}}+E_{kTh}(T)}\right) \tag{4.23}$$

The parameters λ_e and λ_h capture the effects of the mean free path. The effects of the Raman phonon energy are considered with the parameters E_{re} and E_{rh}. The effects of thermal deacceleration [80] are accounted for with E_{kTe} and E_{kTh}. To account for the temperature dependence of impact ionization coefficients, the parameters are modeled as a function of the

temperature. The temperature-dependence of the bandgap can be found in the literature for silicon [81], SiC [81], GaN [81], β-Ga_2O_3 [25, 82], diamond [83], and $Al_xGa_{1-x}N$ [84]. For the other parameters, the temperature dependence is given by [41, 67, 80]

$$E_{kTe,h}(T) = E_{kTe,h}(300K) = \frac{300K}{T} \tag{4.24}$$

$$E_{i,e}(T) = E_{i,e}(300K)\frac{E_G(T)}{E_G(300K)} \tag{4.25}$$

$$\lambda_{e,h}(T) = \lambda_{e,h}(300K)\frac{\sqrt{\tanh\left(\frac{E_{re,h}}{2kT}\right)}}{\sqrt{\tanh\left(\frac{E_{re,h}}{2k300K}\right)}} \tag{4.26}$$

The proposed model shows that impact ionization coefficients increase with the parameters E_i and E_r and decrease with the parameters λ and E_{k_T}. The model has eight parameters in total (four for electrons and four for holes). The advantage of using four parameters for each carrier (as opposed to just two, as in the case of the Chynoweth model) is that impact ionization coefficients can be more accurately modeled at both low and high electric fields simultaneously. It is possible for the parameters to compensate each other; If for, example, $E_r^2 + 2q\xi\lambda E_r - q\xi\lambda^2 = 0$ then λ and E_r will compensate their effect on the values of impact ionization coefficients. There are possible scenarios where E_i compensates the effect of λ; where E_i compensates the effect of E_{k_T}, and where E_r can compensate the effect of E_{k_T}. One way to prevent the compensation is to avoid constant (uniform) field profiles when establishing the value of impact ionization coefficients. Other than the fact that the Chynoweth model fails when the electric field is zero (division by zero), another advantage of the proposed model is that it meets required asymptotic

requirements. At high electric fields, the term in the exponential approaches zero, and $\alpha E_i \approx q\xi$, suggesting that the energy lost to phonon scattering is negligible, and work done by the electric field is approximately equal to the energy lost to impact ionization collisions. Having $E_r = 0$ implies that there is no energy lost to phonon scattering, resulting once again to $\alpha E_i \approx q\xi$. The model works like the Shockley model at low electric fields, and, at high electric fields, the model is similar to Wolff's model.

4.4 Establishing the Value of Impact Ionization Coefficients by Accounting for both Measured Multiplication and Impact Ionization Coefficients Reported in the Literature

Establishing an adequate equation for the modeling of impact ionization coefficients is a challenge, but more challenging is acquiring the values of those coefficients. Predicting accurate breakdown voltages (for power-electronics) and gain (for opto-electronics) requires reliable values of impact ionization coefficients. The parameters of the proposed Thornber model can be found from the known values of impact ionization coefficients. Because the model has four parameters, it fits impact ionization values well at the detriments of the parameters losing their realistic physical values. The main challenge is obtaining values of the coefficients to be modeled. Multiple approaches exist to extract values of impact ionization coefficients. Theoretically, impact ionization coefficients can be obtained by solving the Boltzmann equation as done in the work of Goldsman et al. [74, 85]; they can be obtained from Monte Carlo simulations as done in the work of [86, 87]. Impact ionization coefficients can also be extracted experimentally [88, 89]. Regardless of how they are determined, impact ionization coefficients, when accurate, should

correctly predict breakdown voltages and multiplication. This work undertakes efforts to establish more accurate values of impact ionization coefficients by considering several factors. As presented in Fig. 4.7, values of the coefficients are crafted by simultaneously accounting for measured breakdown voltage, measured multiplication, and values reported in the literature. The accuracy of the coefficients relies on the fact that they are generated from multiple sources and hence are more trustworthy and representative.

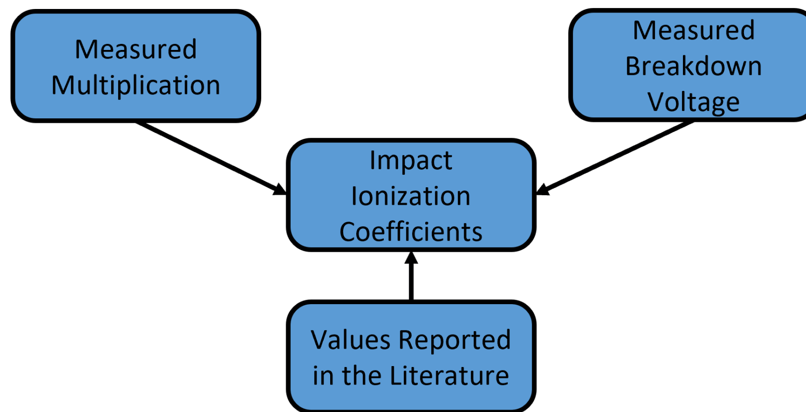

Figure 4.7: Establishing values for impact ionization coefficients by accounting for measured multiplication, measured breakdown voltages, and reports from the literature.

The proposed model for impact ionization coefficients has eight parameters; for each material, a unique set of parameters is needed to evaluate the values of impact ionization coefficients as a function of the local field and the temperature. The desired eight-parameters set for the modified Thornber model lives in a solution space, as shown in Fig. 4.8. For a given material, the best set of parameters accurately predicts the breakdown voltage and the multiplication; it also generates values of impact ionization coefficients that somewhat match values reported in the literature. Finding the best set of parameters in the solution space is done using an iteration process described in Section 4.4.3. Measured multiplication data needed for the calibration of impact ionization coefficients were discussed in the previous chapter. Measured breakdown voltages and

values of impact ionization coefficients reported in the literature are reviewed for the calibration process.

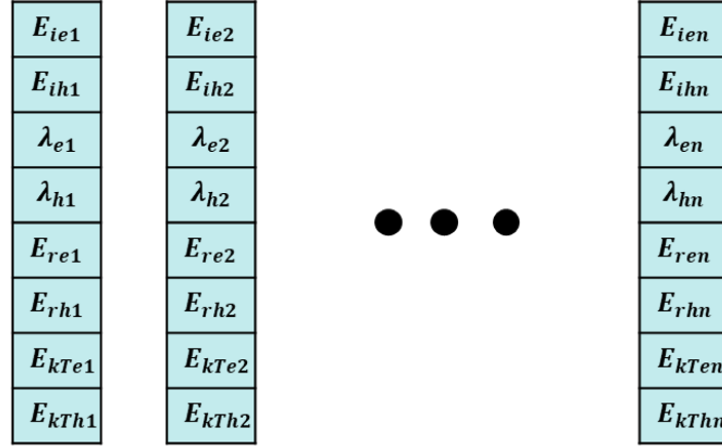

Figure 4.8: Illustration of the solution space for the eight-parameters proposed model of impact ionization coefficients.

4.4.1 Measured Breakdown Voltage for the Calibration of Impact ionization Coefficients

Breakdown voltages are measured on 4H-SiC $p-i-n$ as a function of the temperature for the calibration of impact ionization coefficients. The drift layer of the measured diode is 2 μm thick, and its doping concentration is 2×10^{17} cm^{-3}. The reverse characteristics of the measured diode are shown in Fig. 4.9. The reverse current-voltage characteristics are measured in the temperature range of 100 K to 600 K, and the measurements indicate a significant increase of the background current with the temperature. For measurements done at 350 K and below, the background current appears limited by the instrument's resolution. For measurements above 400 K, the background current increases significantly with the temperature. The increase of the background current with the temperature is expected because the saturation current rises

considerably with the temperature; thermionic emission and a faster emission from the deep centers contribute to the increase of the background current.

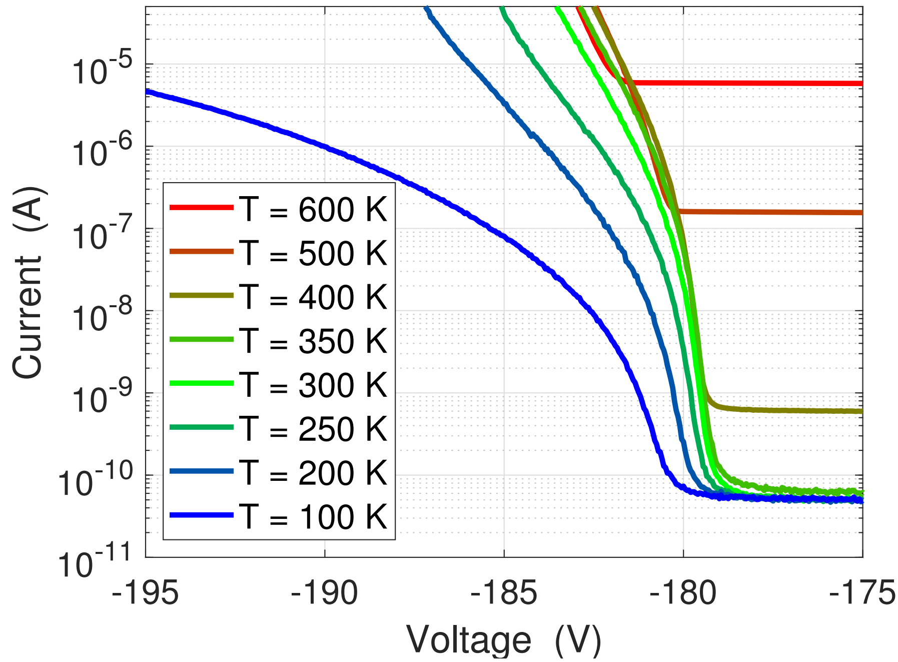

Figure 4.9: Measured reverse I-V characteristics of 4H-SiC $p-i-n$ diodes as a function of the temperature. The background current increases significantly with temperature for measurements above 400 K.

For the experimental extraction of the breakdown voltage, the reverse I-V characteristic of the $p-i-n$ diode is close-in in the avalanche region, as shown in Fig. 4.10. The breakdown voltage is obtained as the reverse voltage at which the current is double the saturation current and is plotted in Fig. 4.11 as a function of the temperature. It is seen that the breakdown voltage initially decreases with the temperature, and at 350 K, there is a turnaround, and the breakdown voltage starts to increase with the temperature.

The decrease in breakdown voltage at low temperature (below 350 K) appears to be related to the incomplete ionization of dopants. A lower temperature implies more severe incomplete ionization, a lower effective doping concentration, a lower internal field, and thus a higher break-

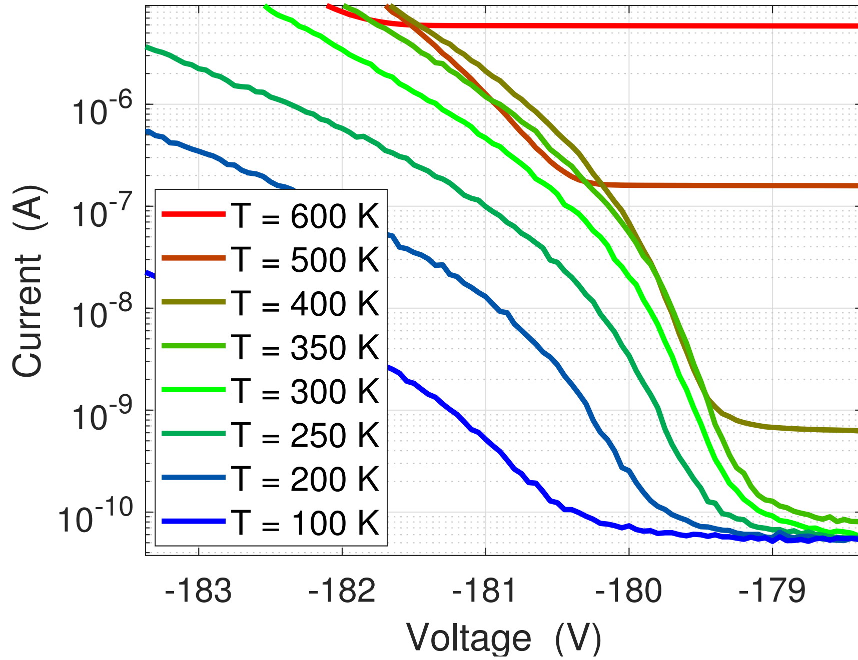

Figure 4.10: Current-voltage characteristics of a 4H-SiC $p-i-n$ diode in the avalanche regime.

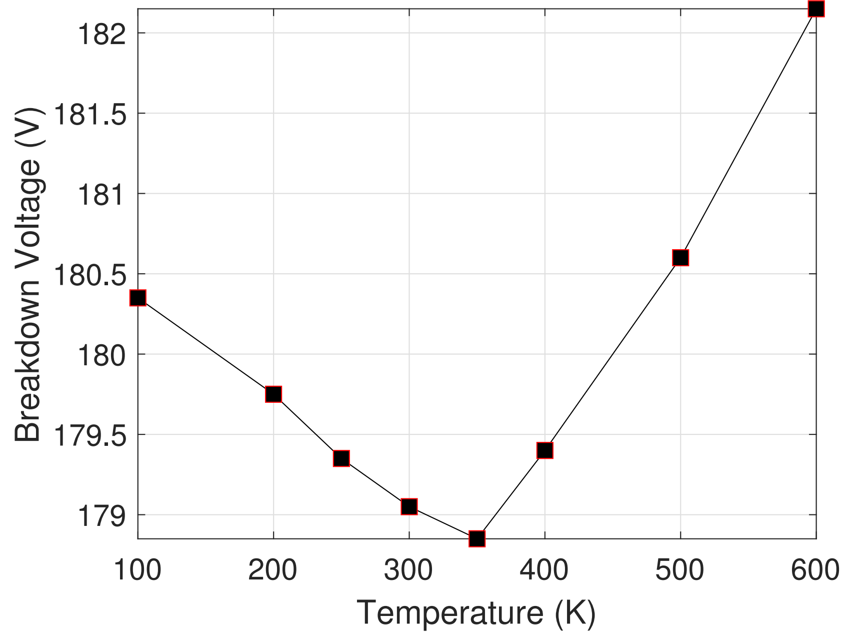

Figure 4.11: Temperature dependence of the breakdown voltage in a 4H-SiC $p-i-n$ diode. For measurements below 350 K, the breakdown voltage decreases with the temperature. Above 350 K, the breakdown voltage increases with the temperature, and the increase in breakdown voltage appears more substantial with temperature rise.

down voltage. At elevated temperatures (above 350 K), the increase of the breakdown voltage with the temperature conforms with the rise of the phonon population at high temperatures. Note that the phonons population is given by

$$< n >= \frac{1}{e^{\hbar\omega/(KT)} - 1}. \tag{4.27}$$

The number of phonons increases non-linearly with the temperature; the population rises even faster at elevated temperatures, resulting in more scattering. The enhanced scattering of carriers with phonons leads to a reduction of carriers' energy and an increase of the breakdown voltage.

Additional breakdown voltage measurements were surveyed in the literature to calibrate impact ionization coefficients. The data considered are discussed by Niwa et al. [69]. The summary of devices used for the calibration of impact ionization coefficients is shown in Table. 4.1. The $p - i - n$ diodes have different thicknesses and doping concentrations, and the breakdown voltages are measured for several temperatures.

The fitting process with measured breakdown voltages is global. Instead of finding room-temperature models and expanding them to temperature, all data at various temperatures are fitted concurrently. Accounting for all data at various temperatures at once also ensures the calibration of the temperature model proposed in Section 4.3.2. The challenge with the proposed model is that at room temperature, the values of the parameters should be within a given range; otherwise, the parameters become invariant with temperature in some cases or change drastically with temperature in others. The need to calibrate all temperature measurements at once is particularly needed for the parameter representing the Raman phonon energy, E_r, which strongly affects the

Table 4.1: Device characteristics and measured breakdown voltage as a function of the temperature for the calibration of impact ionization coefficients in 4H-SiC. The data in the table are gathered from measuring APDs from CoolCAD electronics and the work of Niwa et al. [69].

Devices	Temperature (K)	Measured V_{BR} (V)
CoolCAD Avalanche Photodiodes (This work) $N_D = 2\times10^{17}$ cm^{-3} W = 2 μm	100	180.35
	300	179.05
	400	179.4
	600	182.15
Avalanche Photodiodes from (Kimoto) NPT1 $N_D = 4\times10^{16}$ cm^{-3} W = 13 μm	298.15	605.21
	323.08	607.81
	373.13	613.02
	423.09	618.75
Avalanche Photodiodes from (Kimoto) NPT2 $N_D = 2\times10^{16}$ cm^{-3} W = 13 μm	298.16	1032.81
	323.09	1038.02
	373.14	1047.92
	423.10	1061.98
Avalanche Photodiodes from (Kimoto) PT1 $N_D = 5\times10^{14}$ cm^{-3} W = 4.75 μm	298.05	971.35
	323.08	975.00
	373.04	984.90
	423.08	993.75

variation of λ with temperature.

4.4.2 Survey of the Literature for the Values of Impact Ionization Coefficients

The literature is surveyed for the values of impact ionization coefficients needed to calibrate the proposed modified Thornber model given by (4.22) and (4.23). The literature provides the impact ionization coefficients for Si [72, 73, 79, 80, 90–94]; SiC [67–69, 95–101]; GaN [77, 89, 102]; β-Ga_2O_3 [25, 76, 103], diamond [104], and $Al_xGa_{1-x}N$ [26, 77, 86, 105, 106]. The plots of impact ionization coefficients surveyed are shown in Fig 4.12 for silicon and Fig. 4.13 for 4H-SiC. The plots also show the fit obtained by using the reported values to find the parameters of

the modified Thornber model.

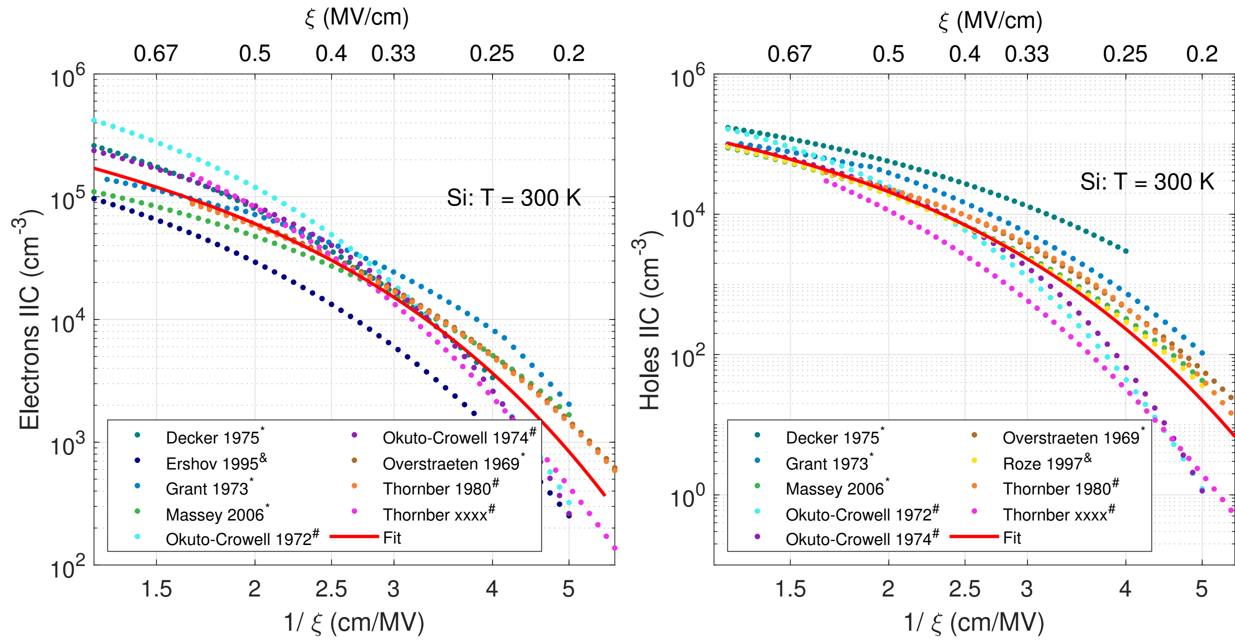

Figure 4.12: Impact ionization coefficients reported in the literature for silicon at room temperature. The reported coefficients are used to find the parameters of the modified Thornber model for silicon.

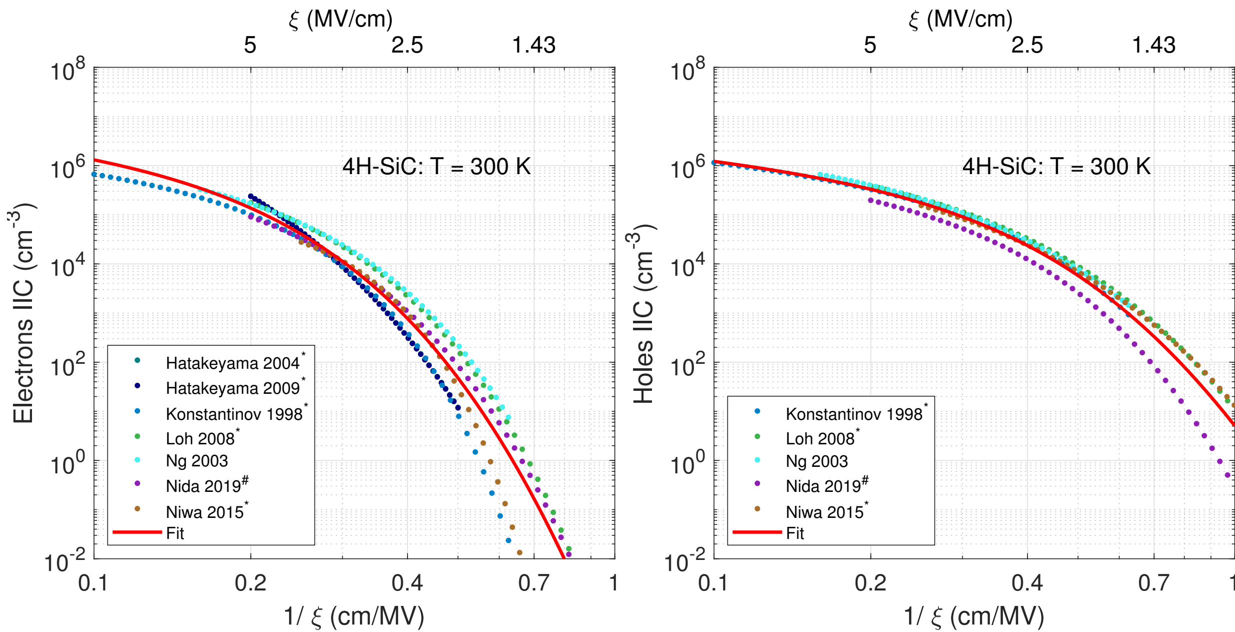

Figure 4.13: Impact ionization coefficients reported in the literature for 4H-SiC at room temperature. The values reported in the literature are used to calibrate the model for impact ionization coefficients.

The method used to determine the values of impact ionization coefficients is indicated in the legend of the plots. Coefficients obtained from measurements have the asterisk ($*$) symbol in front of the author's name. Similarly, the and ($\&$) symbol indicates coefficients obtained from Monte Carlo simulations; the pound key symbol ($\#$) indicates values from a fitting process. The difficulty with impact ionization coefficients is that there are multiple reports on mature materials, such as silicon and 4H-SiC, and fewer and less reliable reports of mature materials such as ultrawide-bandgap materials. For the more mature materials, the reported coefficients do not fully agree with each other, resulting in different performance predictions depending on the model used. Establishing the values of impact ionization coefficients for $Al_xGa_{1-x}N$ poses additional challenges because one has to consider the effects of aluminum mole fraction. It is reported that at low aluminum content, holes' coefficients are larger than those of electrons; however, as the aluminum mole fraction increases, holes' impact ionization coefficients drastically drop so that toward AlN, impact ionization coefficients for electrons are larger than those of holes [105]. As the mole fraction increases, the material's bandgap rises, and the width of the valence band decreases. The drastic reduction of holes' impact ionization coefficients is due to the lowering of the valence band energy available to accommodate holes' ionization collisions. It is reported [105] that the energy range of the valence band is 4.5 eV in GaN and is only about 1.0 eV in AlN.

4.4.3 Established Models for the Impact Ionization Coefficients of Wide- and Ultrawide-Bandgap Semiconductors

The extraction of impact ionization coefficients can be achieved experimentally [60] from measured multiplication; the approach used typically depends on the type of electric field en-

countered. This work expresses the coefficients with a modified Thornber model and calibrates them with measured multiplication, breakdown voltages, and values reported in the literature. The method used to calibrate the modified Thornber model and evaluate the value of impact ionization coefficients is shown in Fig. 4.14. The calibration process starts with the definition of a device and a couple of bias points informed by the measurements of the multiplication and the breakdown voltage (Step A). In Step B, the electric field profile is calculated as a function of applied biases. Step C calculates the position-dependence of impact ionization coefficients from electric profiles. Because the calculated electric field is position-dependent, impact ionization coefficients are also a function of the position, as seen in Fig. 5.3. The impact ionization coefficients are evaluated based on an initial guess of the parameters of the Thornber model from the solution space shown in Fig. 4.8. The theoretical gain is calculated, and breakdown requirements are checked in Step D. The theoretical multiplication is compared to measurements, and error one is defined to evaluate the effectiveness of the selected parameter set in modeling the multiplication. A second error (error 2) is used to determine how far off the breakdown voltages predicted by the coefficients are from measurements. A third error (error 3) is used to assess how well the selected set of parameters matches the coefficients reported in the literature. As indicated in step E, the best parameter minimizes the sum of all three errors and is searched using an iterative feedback loop.

The search for the best parameter is done using a multi-mode iteration approach. The iteration runs on four modes (mode 4, mode 3, mode 2, and mode 1). Each potential solution has nine parameters: the eight parameters used to model impact ionization coefficients and one for the carrier injection ratio. Since it is difficult to realize pure carrier injection during measurement, mixed injection is assumed. In mode 4, four of the nine parameters are selected and are each

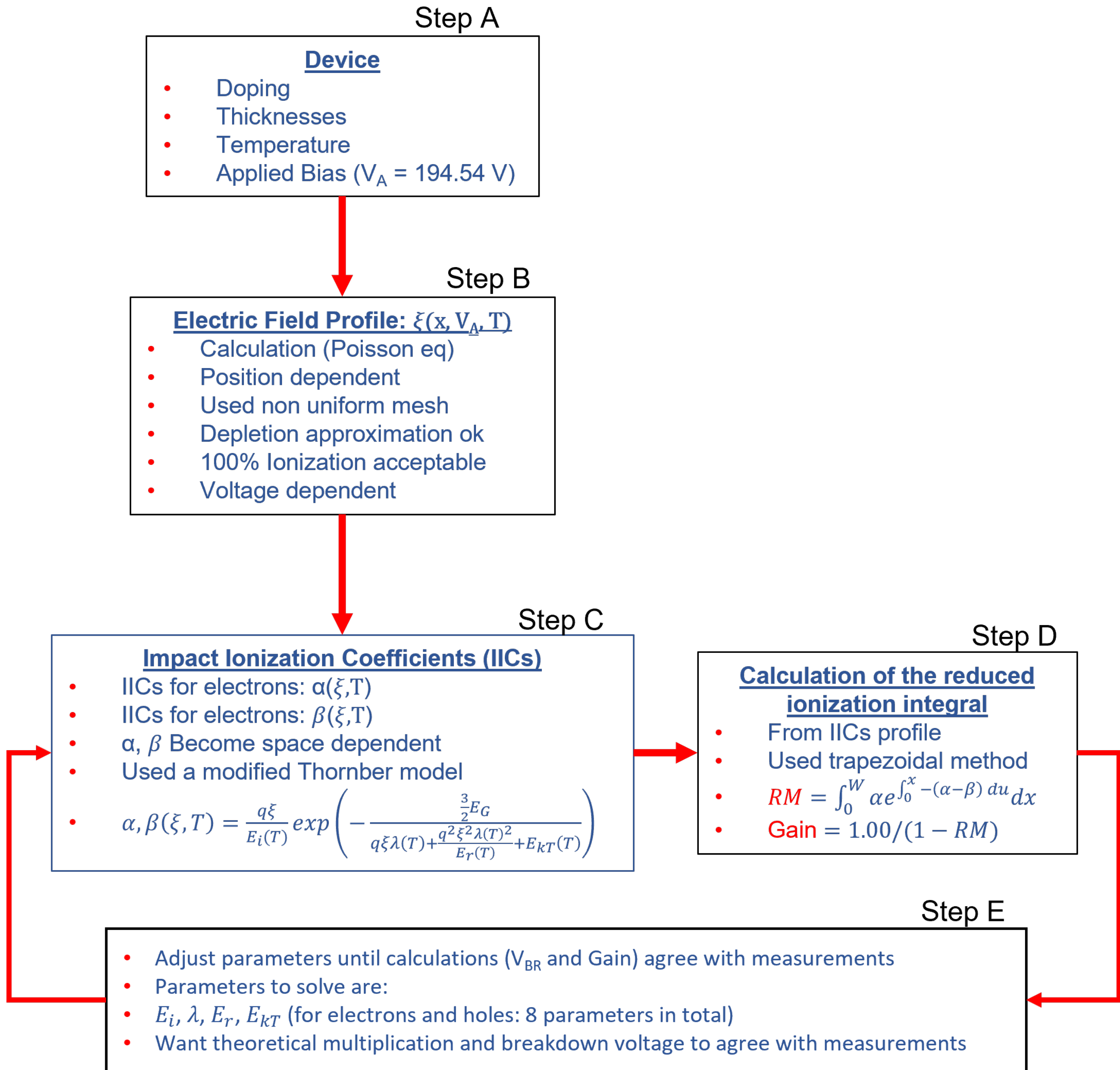

Figure 4.14: Block diagram explaining the calibration process of impact ionization coefficients.

attributed six different values, resulting in a solution space with 6^4 = 1296 possible candidates. All the candidates are evaluated in one generation, and the candidate that minimizes the fitting error is retained. A generation is associated with selecting the four parameters to be multi-valued. Because there are 9 parameters, in mode 4 there are $\binom{9}{4}$ = 126 generations. In mode 3, three parameters are selected at once and are each assigned twelve different values. The solution space

has $12^3 = 1728$ candidates, and there are 84 generations. In mode 2, the two parameters selected are each assigned forty-nine different values, and there are thirty-six generations. In mode 1, only one parameter is selected and is first attributed one thousand possible values; then 1500 more values are added between the two mesh points, which bracket the solution for more accuracy. The number of different values attributed (six, twelve, and nine) is chosen to have a decent mesh and a decent computational speed; they can be adjusted depending on one computing resource.

For 4H-SiC, the experimental data used for the modeling of the gain was discussed in the previous chapter. The modeled multiplication is limited to 2000 to avoid the effect of the series resistance. The experimentally measured multiplication and its modeling with calibrated impact ionization coefficients are shown in Fig. 4.15. The calibrated coefficients are compared against literature data in Fig. 4.13.

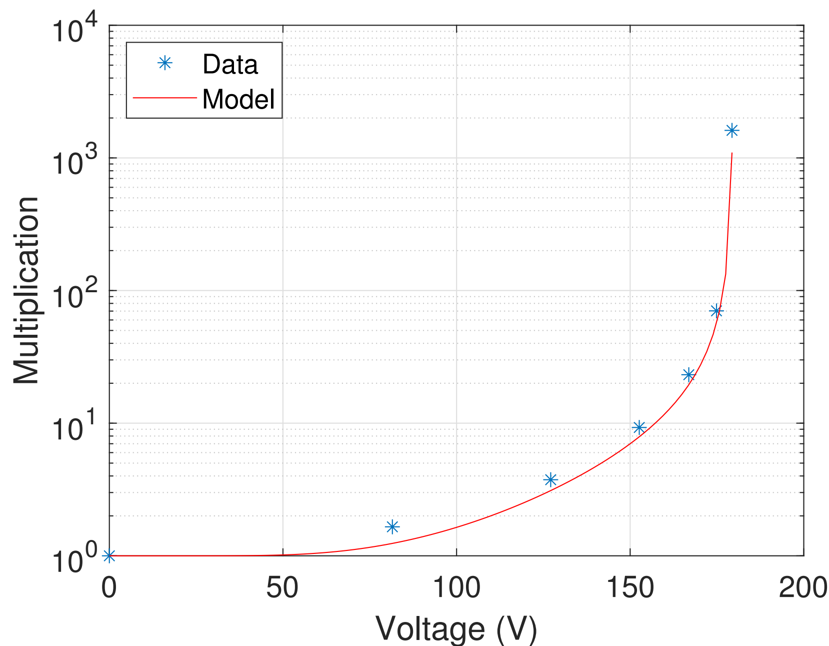

Figure 4.15: Modeled multiplication using calibrated impact ionization coefficients.

For each material, the parameters of the revised Thornber model are summarized in Ta-

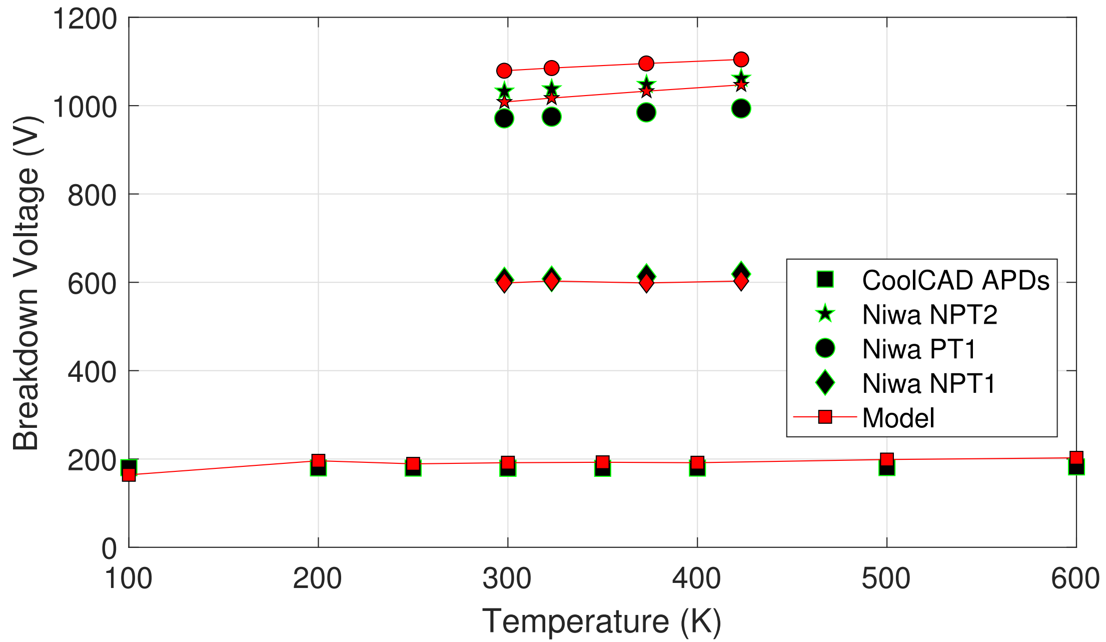

Figure 4.16: Measured and modeled temperature dependence of the breakdown voltage in 4H-SiC.

ble 4.2. The table has missing entries. In the case of GaN, the fit shows that the Raman phonon energy for holes is very large such that the quadratic term in the denominator of the expression in the exponential vanishes. The Raman phonon energy is also large for electrons in gallium oxide. For aluminum gallium nitride, no report was found on the value of holes impact ionization coefficients.

Table 4.2: Calibrated parameters for the impact ionization coefficients of wide- and ultrawide-bandgap semiconductors.

Parameters		Si	4H-SiC	GaN	β-Ga_2O_3	$Al_{0.6}Ga_{0.4}N$	Diamond	AlN
λ $(10^{-10}$m)	Electron	63.84	9.04	9.54	35.36	21.09	13.01	24.69
	Hole	19.71	13.68	34.83			41.77	
E_i (eV)	Electron	2.54	38.01	1.64	9.30	4.12	71.08	7.83
	Hole	3.11	8.69	4.19			1.68	
E_r (eV)	Electron	0.09	0.06	0.28		2.02	0.01	2.49
	Hole	0.01	0.14				0.79	
E_0 (eV)	Electron	1.65	4.95	5.10	9.43	7.81	8.25	9.02
	Hole	1.65	4.95	5.10			8.25	
E_{k_BT} (meV)	Electron	52.52	113.77	242.44	0.00	1.65	1.92	0.07
	Hole	17.99	156.07	51.63			181.80	

The calibration process described above was applied to 4H-SiC $p-i-n$ diodes given devices and experimental data availability. The fitting process relied mainly on the values of impact ionization coefficients reported in the literature for the other materials. The calibration of the coefficients provided a decent fit of the measured multiplication and breakdown voltages. The breakdown voltage measured and reported by Niwa et al [69] could not be fitted at low doping. The model over-predicts the breakdown voltage at low doping, suggesting that low doped materials may have impact ionization coefficients higher than expected.

Conclusion

This chapter proposed a model for the impact ionization coefficients of semiconductors. Those coefficients are important for modeling the multiplication processes leading to avalanche breakdown. The chapter also discussed the multiplication process in $p-i-n$ and $n-i-p$ diodes. Preliminary calculations showed that the injection process affects the multiplication process but does not impact the breakdown voltage. It was seen that the polarity of the i-layer could be used to set increasing or decreasing electric field profiles. It was also observed that a slightly higher breakdown voltage could be achieved when carriers with dominant impact ionization coefficients travel increasing-electric field profiles. Calibrated ionization coefficients are used in the next chapter to assess the on-resistance versus breakdown voltage limits.

Chapter 5: Using Calibrated Impact Ionization Coefficients to Establish more Accurate On-resistance versus Breakdown Voltage Limits of Wide- and Ultrawide-Bandgap Semiconductors for Power Electronics

5.1 Calculation of the Breakdown Voltage Using Calibrated Impact Ionization Coefficients

Avalanche breakdown tells the maximum voltage that a device can block; it occurs when the multiplication of carriers in the semiconductors grows out of control (multiplication equals infinity), resulting in an abrupt surge of current in reverse bias. The mathematical breakdown condition depends on the type of structure, which can be $p-i-n$ or $n-i-p$. This section used calibrated impact ionization coefficients to study the high voltage blocking capability of materials under investigation.

5.1.1 Proposed Method for the Calculation of the Avalanche Breakdown Voltage in Semiconductors

The process used to solve the breakdown voltage is illustrated in the block diagram shown in Fig. 5.1. The applied bias is adjusted until the ionization integral, also referred to as the reduced multiplication (RM), is within a small error, $e \approx 1\times10^{-8}$ from 1.

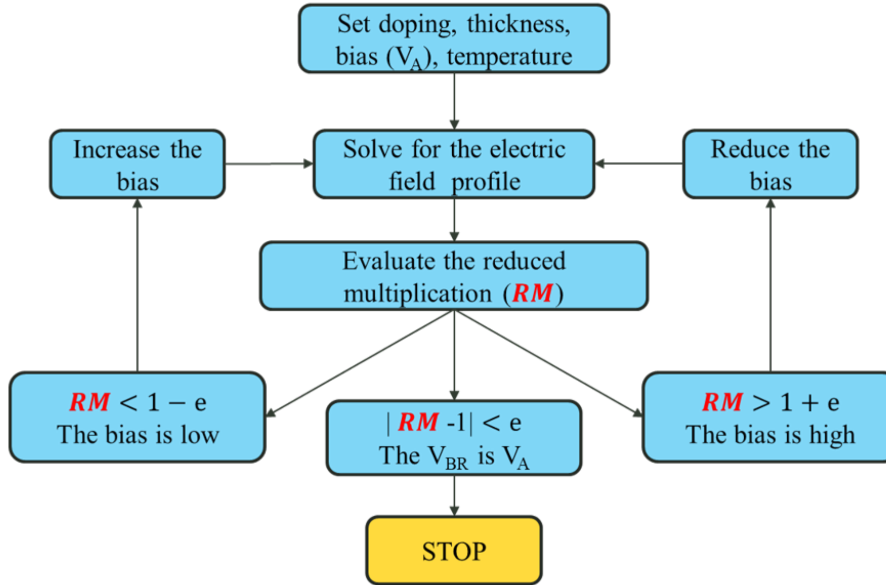

Figure 5.1: Process used for calculating the avalanche breakdown voltage. The voltage is adjusted until the ionization integral is within an error, e, from 1.

The calculation of the breakdown voltage is initiated with the definition of a test structure. For illustration, the characteristics of the test structure simulated are shown in Table 5.1. The temperature and an initial guess of the breakdown voltage are also defined. A good initial guess for the breakdown voltage is 500 V.

Table 5.1: Thicknesses and doping concentrations of the 4H-SiC $p{-}i{-}n$ simulated for theoretical multiplication studies.

	Thickness (μm)	Doping (cm^{-3})
p$^+$-layer	0.2	1×10^{19}
i-layer	1	2×10^{17}
n$^+$-layer	0.2	1×10^{19}

Following the definition of structure, the electric field within the test structure is calculated preferably with the depletion approximation for computational speed. A typical electric field for the device simulated (Table 5.1) is shown in Fig. 5.2 for an applied bias of 199.6 V. The electric field profile is plotted as a function of the position. The p$^+$/n$^-$ interface is at 0 μm, and the n$^-$/n$^+$ interface is located at 1 μm.

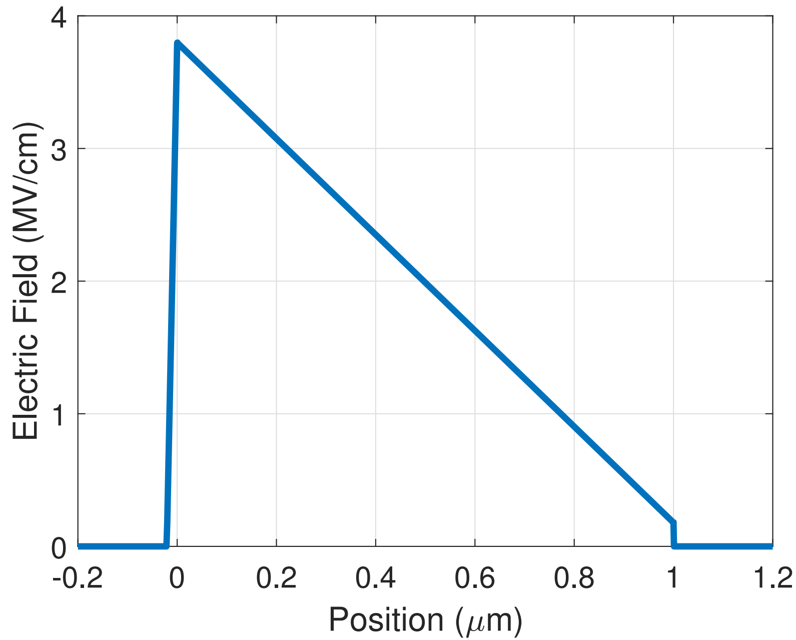

Figure 5.2: Calculated field profile in 4H-SiC $p-i-n$ diode to evaluate the ionization integral. The applied bias is 199.6 V.

The position-dependence of impact ionization coefficients resulting from the electric field profile shown in Fig. 5.2 is plotted in Fig 5.3. The material simulated is 4H-SiC, and the parameters used for calculating the coefficients are given in Table 4.2. The device simulated is a $p-i-n$ diode with an n^- drift layer, adequate for the breakdown voltage limits in 4H-SiC because holes, which are the carriers with the dominant impact ionization coefficients, travel in the increasing direction of the electric field.

The profile of impact ionization coefficients allows evaluating the ionization integral, also referred to as the reduced multiplication. The multiplication can be predicted assuming mixed injection and using (4.21); however, a similar breakdown voltage can be expected considering pure electrons or holes injections. To find the breakdown voltage, (4.18) is used to evaluate the ionization integral. If the ionization integral is less than one, the guessed voltage is small and must be increased. If the ionization integral is greater than one, the guessed voltage needs to be

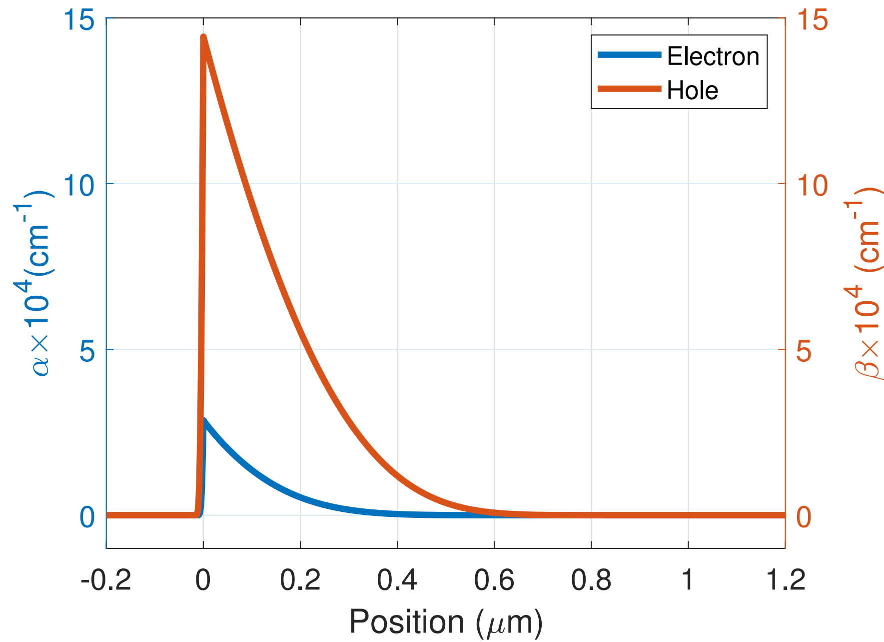

Figure 5.3: Impact ionization coefficients calculated from the electric field profile of 4H-SiC $p-i-n$ diodes. The voltage applied on the diode is 199.6 V.

reduced.

Fig. 5.4 shows the evolution of the guessed breakdown voltage and the evaluated ionization integral in the process of finding the breakdown voltage using the bisection method. For the 4H-SiC $p-i-n$ diode simulated, the initial guess for the breakdown voltage is 500V, and the resulting ionization integral is too large (270480818.6). The next guess for the breakdown voltage is 250 V; however, the ionization integral is still larger than one. The third guess is 125 V; this time, the ionization integral is less than one, suggesting that the breakdown voltage is between 250V and 125V. The bisection method is continued until the ionization integral approach one with a satisfactory metric prescribed by the error e. As seen in Fig. 5.4, the guess voltages converge to the breakdown voltage. The steps used to find the breakdown voltage are applied to many 4H-SiC devices with different geometry and $p-i-n$ devices fabricated with the other materials investigated.

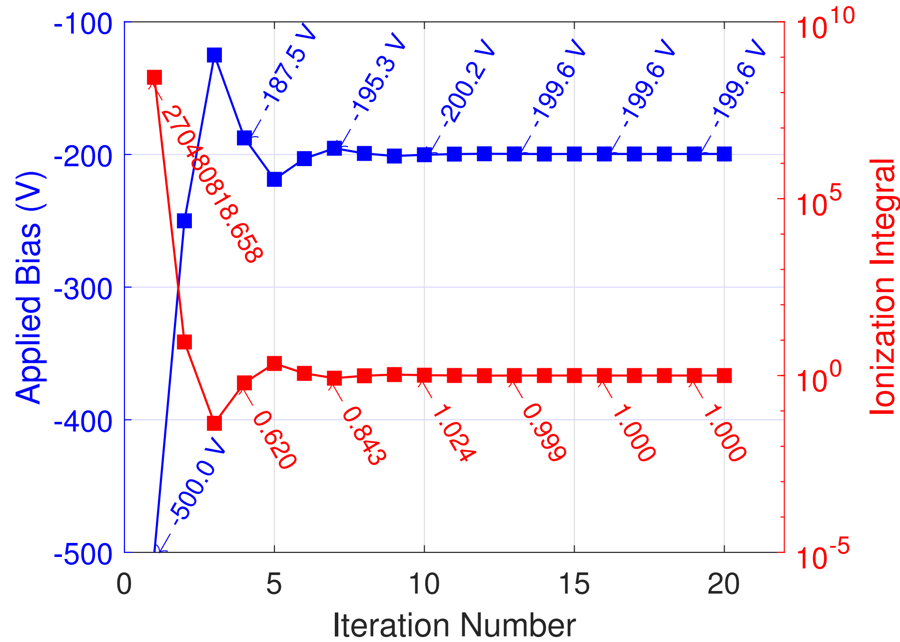

Figure 5.4: Illustration of the iterative approach for solving the ionization integral. The breakdown voltage is found using the bisection method.

5.1.2 The Optimum Structure for the On-resistance Versus Breakdown Voltage Limits

The previous section demonstrated the use of the ionization integral and calibrated impact ionization coefficients to calculate the breakdown voltage. This work is the study of the breakdown limits; the breakdown of various p-i-n structures is calculated as a function of the characteristics of the i-layer. For a $p-i-n$ diodes, the parameters that are very important in terms of breakdown voltage are the thickness and the doping concentration of the i-layer. The cladding layers are usually highly doped, and their primary purpose is to terminate the electric field.

The effect of the i-layer thickness on the breakdown voltage is studied. The breakdown voltage of 4H-SiC $p-i-n$ diodes is calculated based on the i-layer thickness. The other

parameters of the diodes are summarized in Table 5.1. The calculated breakdown voltage is shown in Fig. 5.5; it is seen that the breakdown voltage increases with the thickness of the i-layer.

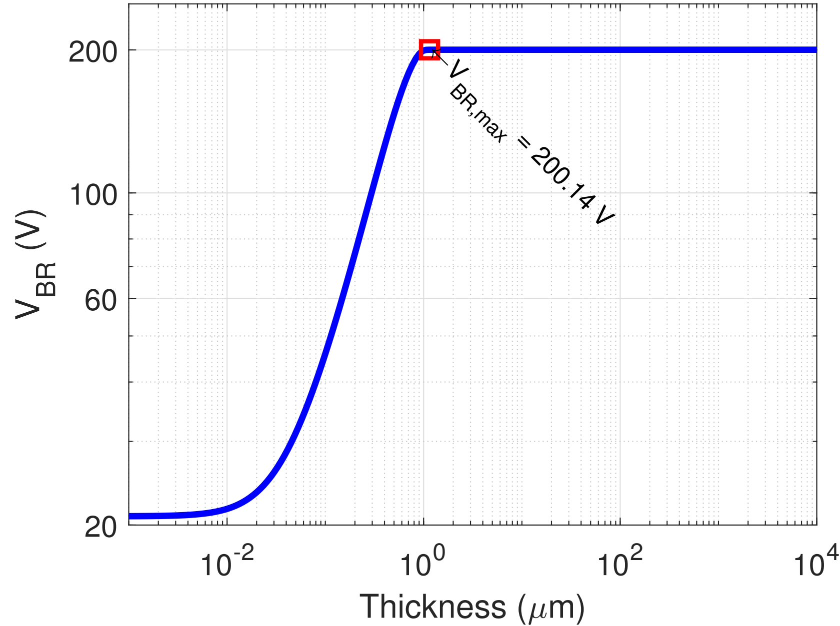

Figure 5.5: Calculated breakdown voltage as a function of the i-layer thickness in 4H-SiC $p{-}i{-}n$ diodes. The doping in the i-layer is set to $2{\times}10^{17}\text{cm}^{-3}$, and the thickness is varied. It is seen that the breakdown voltage stops increasing after a certain thickness, the optimum thickness.

The plot shows three regions. When the thickness is below 10 nm (small), the breakdown voltage appears to be invariant to the thickness of the multiplication layer (thicknesses below 10 nm are unrealistic and should be discarded). Between 10 nm and 1 μm, the breakdown voltage increase significantly with the thickness. Eventually, the breakdown voltage remains constant when the thickness exceeds 1 μm. For this scenario, it is allowed to state that the maximum breakdown voltage achievable with doping of $2{\times}10^{17}\text{cm}^{-3}$ is 200.14 Volts.

Because the breakdown voltage was evaluated as a function of the i-layer thickness, it is convenient to also evaluate the resistance of the diode as a function of the i-layer thickness. Before continuing, it is important to clear the air between the on-resistance and the resistance.

When discussing on-resistance versus breakdown voltage limits in the literature, the on-resistance refers to the resistance of a solid bar, and the breakdown voltage is the maximum voltage that the bar could support when depleted. The i-layer of the $p-i-n$ represents such a bar; because the device has a $p-n$ junction, the depletion is easily achieved, and the being lightly doped, the i-layer carries most (if not all) of the depletion. The literature's on-resistance (from the way it is evaluated) is nothing more than the i-layer resistance. Still, it is not necessarily the diode's actual resistance when it is in the on-state. In the on-state, the conduction mechanism in the diode is dominated by the diffusion of minority, whereas the on-resistance reported in the literature is the unipolar drift resistance. Because this work is interested in the limits, the unipolar resistance of the i-layer is considered the maximum on-resistance. The drift resistance is usually smaller than the diffusion resistance. It is important to note that the drift resistance could be the on-resistance of vertical power MOSFETs. In all, the effective unipolar resistance of the i-layer is considered the on-resistance.

The thickness of the i-layers determines its resistance, which is evaluated using (5.1), where W_{op}, μ_n, μ_p, and N are the thickness of the i-layer, the electron mobility, the hole mobility, and the net concentration of free carriers, respectively. Note that the mobilities μ_n and μ_p can be interchanged if the i-layer is p-doped instead of being n-doped. Once again, the literature is surveyed for the mobility model used to calculate the on-resistance. The models were found for silicon [107], 4H-SiC [108], GaN [109], β-Ga_2O_3 [82], diamond [83], and $Al_xGa_{1-x}N$ [110]. The concentration of minority carriers is very small at large reverse biases and has a negligible effect on the on-resistance; however, at elevated temperature, n_i and the concentration of minority carriers increase significantly and is worth considering mainly for completeness. Bulk incomplete ionization, discussed in Chapter 2, is accounted for in the calculation of the breakdown voltage.

The calculated breakdown voltage is shown in Fig. 5.6 for 4H-SiC. The on-resistance increases with the thickness of the i-layer.

$$R_{on} = \frac{W_{op}}{q\left(\mu_n N + \mu_p \frac{n_i^2}{N}\right)}. \tag{5.1}$$

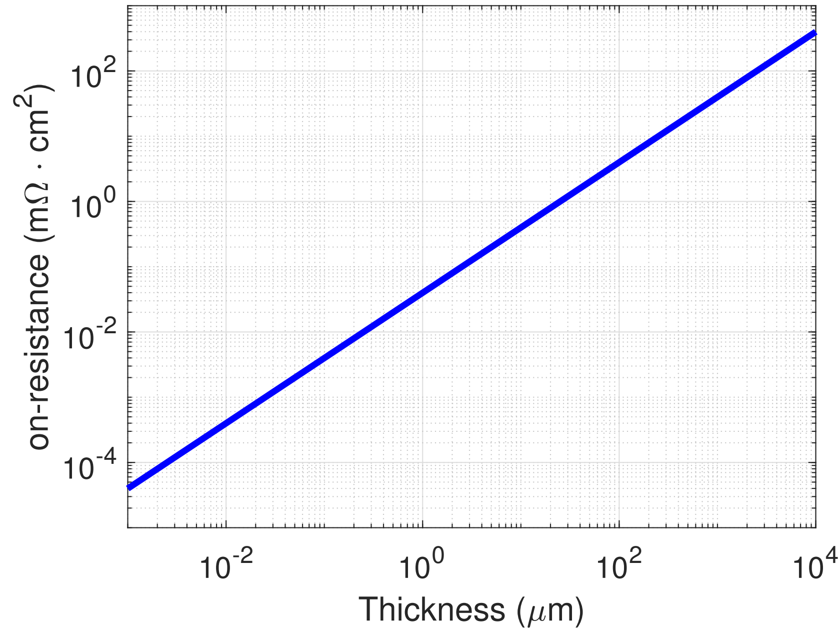

Figure 5.6: Calculated i-layer resistance of a 4H-SiC $p-i-n$ diode as a function of device thickness. The resistance increases with the i-layer thickness.

The past section calculated the breakdown voltage and the on-resistance as a function of the i-layer's thickness. The doping concentration of the i-layer was set at 2×10^{17} cm^{-3}. The two results are combined, and the on-resistance versus the breakdown voltage is plotted in Fig. 5.7.

The plot shows the details of the breakdown voltage and the on-resistance and presents the optimum structure. At 200.14 V, the on-resistance increases vertically because the breakdown voltage has a saturation point with the thickness, while the on-resistance always increases with the thickness.

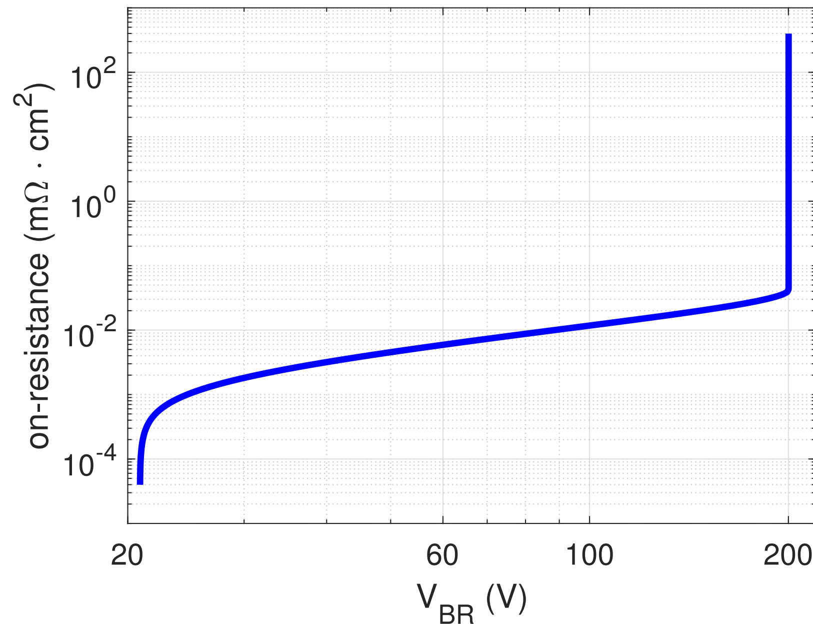

Figure 5.7: On-resistance versus breakdown voltage of a 4H-SiC $p-i-n$ diodes with an i-layer doping concentration of 2×10^{17} cm^{-3}. Past the optimum thickness, the on-resistance increase while the breakdown voltage stops changing.

5.1.3 Breakdown Voltage Calculations in WBG and UWBG Semiconductors

In the past section, the breakdown voltage was studied as a function of the i-layer thickness at a fixed doping concentration. This section investigates the effect of the doping concentration on the optimum structures for a given material. The breakdown voltage is calculated as a function of the i-layer thickness and the i-layer doping concentration as seen in Fig. 5.8 for 4H-SiC and Fig. 5.9 for AlN.

The dashed lines in Fig. 5.8 and Fig. 5.9 indicate devices that are unnecessary thick, as they get more resistive without improvement of the breakdown voltage. For both 4H-SiC and AlN, it is observed that the breakdown voltage saturates after a specific thickness for every doping concentration investigated. The lower the doping concentration, the greater the width of the optimum structure. The electric field changes less rapidly for uniform and low doping concentrations, and

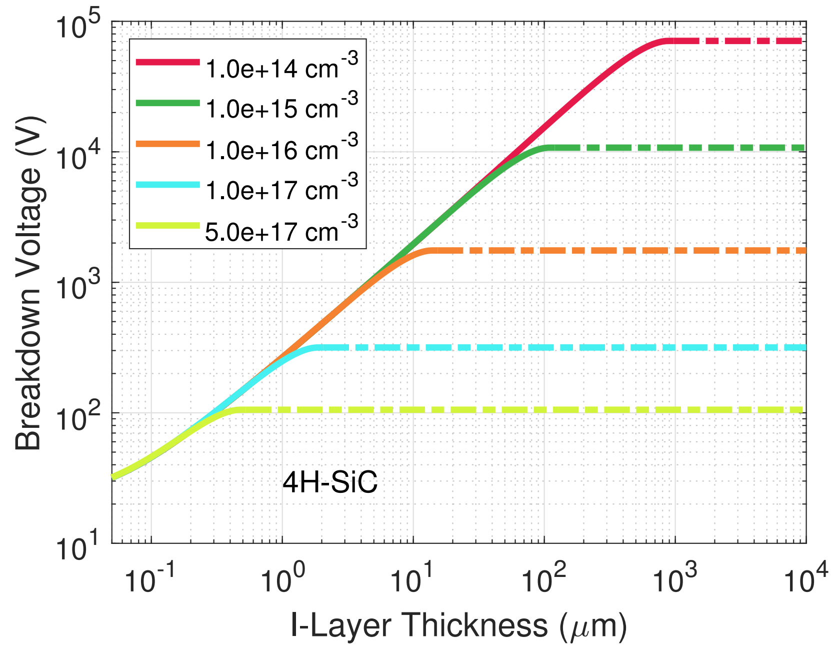

Figure 5.8: Calculated breakdown voltage as a function of the i-layer thickness for several doping concentrations in 4H-SiC.

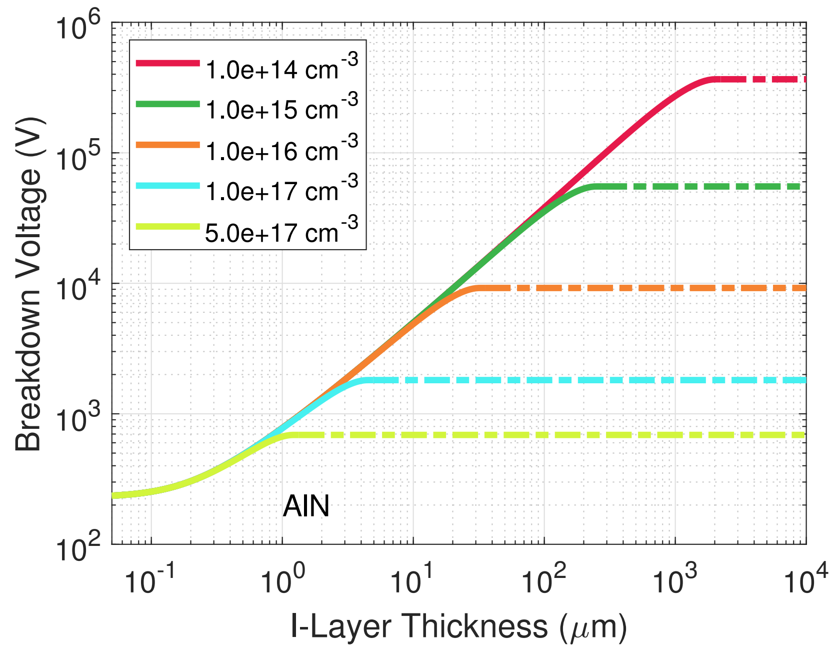

Figure 5.9: Calculated breakdown voltage as a function of the i-layer thickness for several doping concentrations in AlN.

higher depletion widths are achievable. A crucial point to note is that for a given doping concentration, there is a unique optimum thickness leading to a unique optimum breakdown voltage. For the optimized structure, the doping concentration of the i-layer, the thickness of the i-layer, and the breakdown voltage form a unique trio so that knowledge of one leads to the extraction of the other two. For example, knowledge of the doping concentration allows the recovery of the optimum thickness and the breakdown voltage. It is possible to recover the optimum doping and the optimum thickness from the breakdown voltage. It is possible to find the optimum doping and breakdown voltage from a given thickness.

It is convenient to design p-i-n structures with targeted breakdown voltages. Here, the goal is to find the combination of doping and i-layer thickness resulting in a specific breakdown voltage. Fig. 5.10 shows the design for specifically targeted voltages from 100 V up to 50 kV.

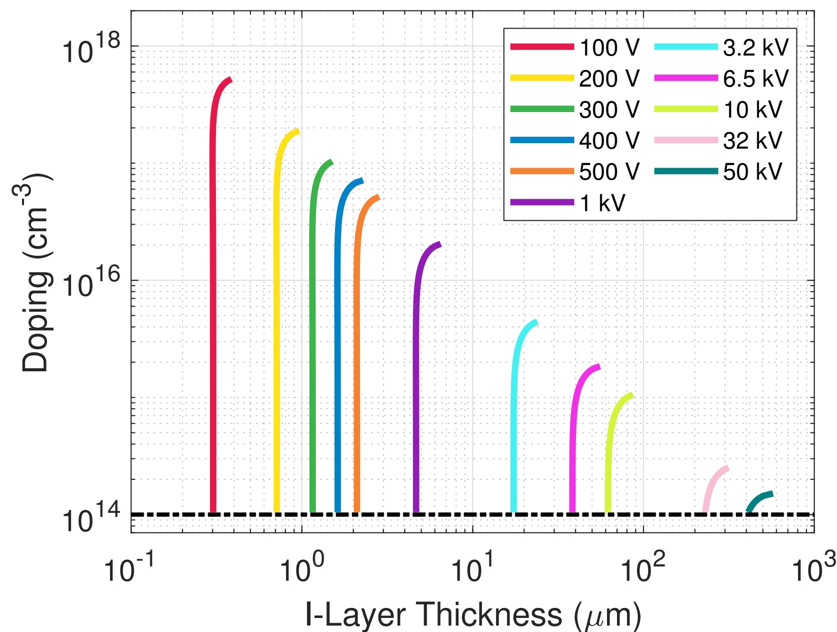

Figure 5.10: Designing 4H-SiC $p-i-n$ diodes for a specific breakdown voltage. Doping levels and i-layer thicknesses are carefully selected so that the $p-i-n$ structure breaks at the targeted voltage.

For each targeted voltage, the design choices are fundamentally limited by the minimum achievable doping. Achieving a higher blocking voltage requires a decrease in the doping concentration and an increase of the minimum i-layer thickness. Beyond the optimum thickness, no increase in the doping is necessary to maintain the breakdown voltage (if the doping is increased, the breakdown voltage will decrease, thus deviating from the targeted voltage). Consequently, after the saturation thickness, the solutions are such that the doping remains constant for all i-layer thicknesses; in other words, the solutions become horizontal flat lines. These observations are explained by picturing the total electric field within the structure.

It is common to think about the reverse bias; what should be considered with more attention is the reverse field, which has a component due to doping (built-in field) and another component due to the reverse bias (the external field). The field is what triggers the breakdown. At low i-layer thicknesses, the larger component of the field comes from the applied bias, so the breakdown becomes very sensitive to the i-layer thickness and less sensitive to the doping. High voltage devices have larger thicknesses and tend to reach their saturation thickness at lower doping levels. For high voltage devices, the breakdown is less sensitive to the i-layer thickness and is highly affected by the doping of the i-layer. It is also observed that, as the targeted breakdown voltage increases, the solution space for its design becomes narrower due to the limits imposed by the doping floor of the material. With 4H-SiC, 50 kV can only be theoretically achieved if the doping is less than 1.2×10^{14} cm^{-3}. The doping floor of 4H-SiC is 1×10^{14} cm^{-3} [111], so the range of doping capable of achieving 50 kV is very small.

5.2 The Critical Field: a By-product of Breakdown Voltage Calculations

5.2.1 Extraction of the Critical Field from Breakdown Voltage Calculations

One of the main contributions of this work is that the critical field, which is used to evaluate the Baliga figure-of-merit, is not assumed to be a constant value. The critical is defined as the peak electric field at breakdown. The critical field is extracted by simply calculating the electric profile at the breakdown voltage and finding its peak. For illustration, Fig. 5.11 shows the electric field profile for several devices that have the same i-layer doping concentration but different thickness.

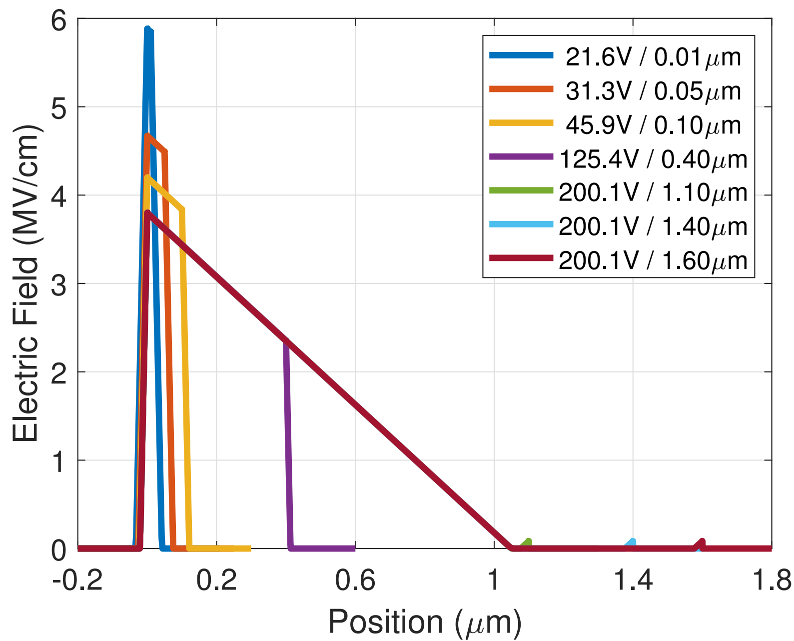

Figure 5.11: Calculated field profile at breakdown voltage for 4H-SiC $p - i - n$ diodes with different i-layer thicknesses. The breakdown voltage and the thickness of the i-layer are indicated in the legend. The breakdown voltage remains constant after the optimum thickness because the electric field profile stops changing.

The critical field is plotted as a function of the i-layer thickness in Fig. 5.12. For more details, the critical field is calculated as a function of the i-layer thickness for several doping

concentrations. The calculated critical values are plotted in Fig. 5.13 for 4H-SiC and Fig. 5.14 for AlN.

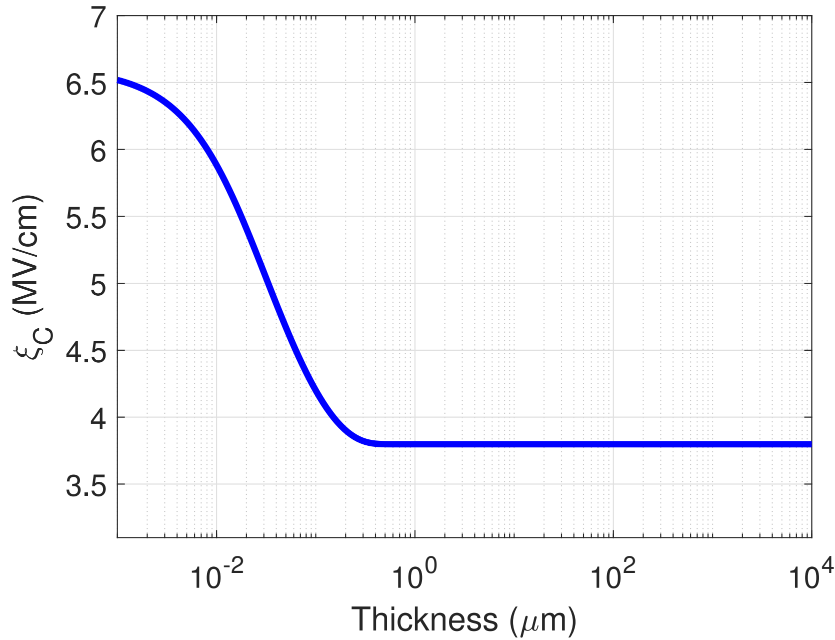

Figure 5.12: Thickness dependence of the critical field in 4H-SiC $p-i-n$ diode at room temperature. The i-layer doping concentration is 2×10^{17} cm^{-3}.

The critical field decreases with the i-layer doping. It is also seen that the critical field becomes doping-dependent at large thickness. Low values of the critical field are obtained at low doping concentrations. The critical field of 4H-SiC ranges from 1.6 MV/cm to 6 MV/cm. In AlN, an ultrawide-bandgap semiconductor, the critical field ranges from about 3.8 MV/cm to 18 MV/cm. The calculations agree with reports that materials with a larger bandgap have a higher critical field. This work presents the thickness and doping dependence of the critical field, which is usually specified as a constant for each material. This work also allows the modeling of the critical field. It is more convenient to model the critical field as a function of the doping concentration. When assessing power devices' on-resistance versus breakdown limits, the critical field considered is that of an optimum structure. Similarly, optimum devices are evaluated for

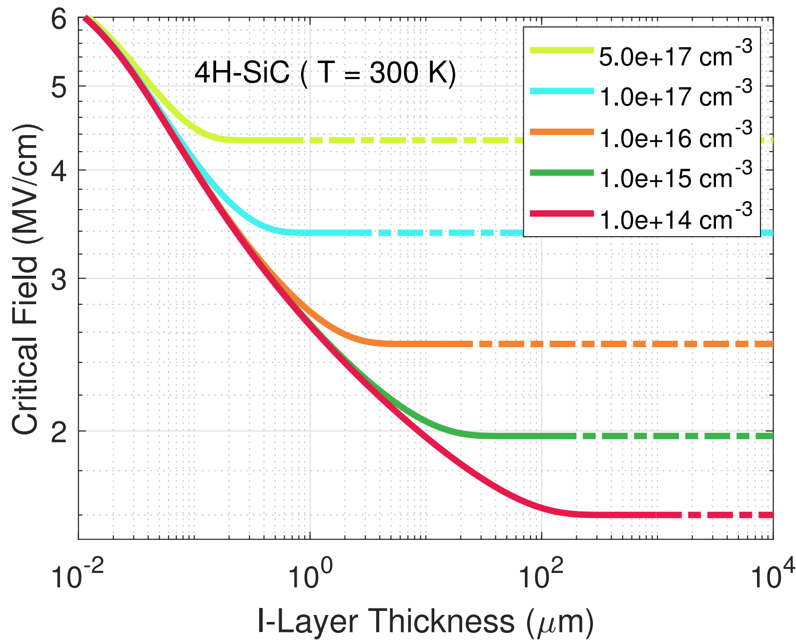

Figure 5.13: Calculated critical field in 4H-SiC $p-i-n$ diodes as a function of the i-layer thickness for several doping concentrations. Each doping level shows a saturation of the critical field at different i-layer thicknesses.

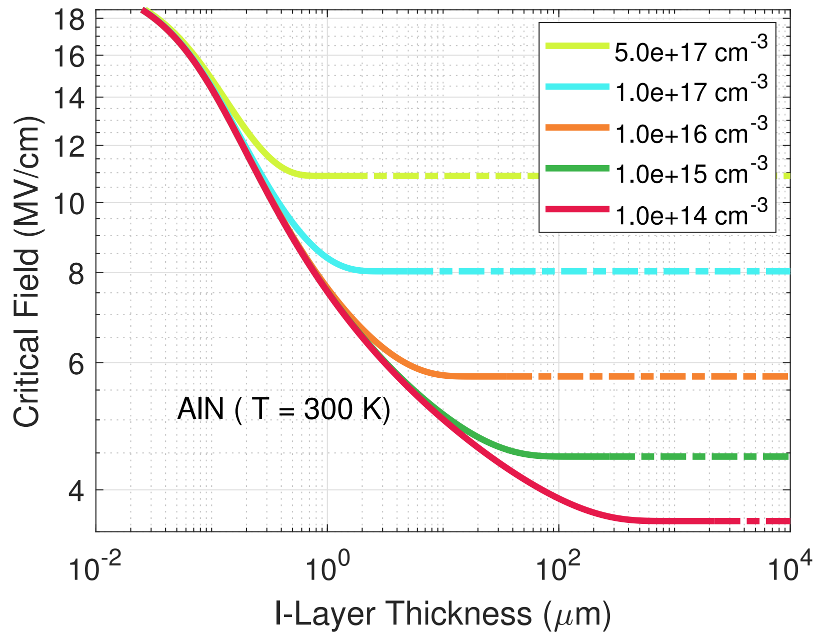

Figure 5.14: Calculated critical field in AlN as a function of the i-layer thickness for several doping concentrations. The calculated critical field of AlN is much higher compared to that of 4H-SiC.

each doping concentration to model the critical field.

5.2.2 Modeling of the Critical Field Calculated Using Impact Ionization Coefficients

In the previous section, the breakdown voltage and the critical field were evaluated as a function of the i-layer thickness for several $p-i-n$ structures. It was found that the breakdown voltage increases and the critical field decreases with increasing i-layer thickness. For each doping, there is a threshold thickness at which the breakdown voltage ceases to increase. The calculations showed a saturation of the breakdown voltage and the critical field. Though materials with a large bandgap are advantageous because they have large critical fields, the calculations show that large critical fields are associated with small breakdown voltages. Low critical fields result in large breakdown voltages.

Modeling of the critical is important for an easy evaluation of the Baliga figure of merit as given by (1.5). Note that in (1.5) the breakdown voltage is indirectly a function of the optimum doping, which is uniquely associated with the optimum thickness. Because the optimum structure is associated with the onset of breakdown voltage saturation, the critical field needed for the limit of a material is the minimum critical field for a given doping concentration. As seen in Fig. 5.13 and Fig. 5.14, for each doping concentration, there is a minimum critical field. The minimum critical field is plotted as a function of the doping concentration in Fig. 5.15.

The symbols indicate the minimum critical field for a given doping concentration. The solid lines represent fits using (5.2), where A, B, and P are fitting parameters.

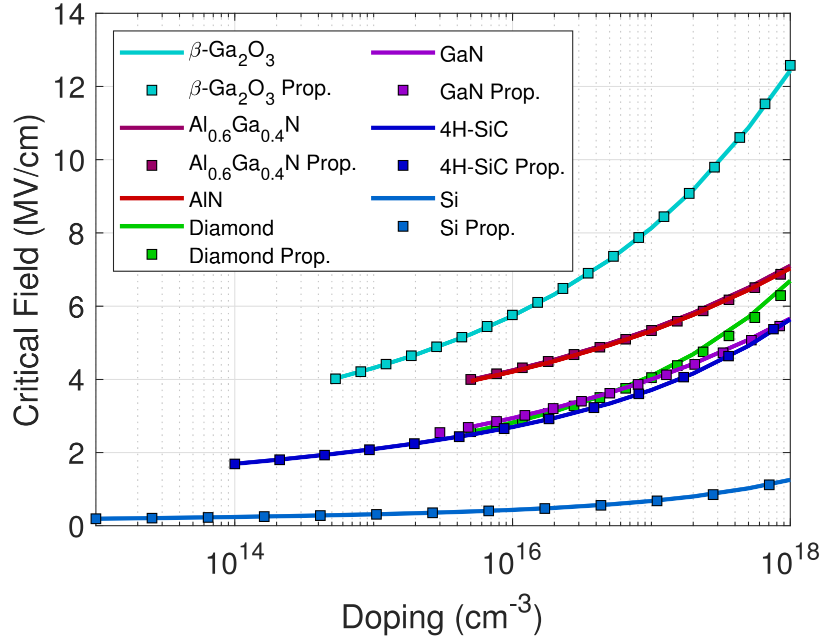

Figure 5.15: Extracted doping dependence of the critical field in wide- and ultrawide-bandgap semiconductors.

$$\xi_C = \frac{B}{\left[1 - A \cdot \log_{10}\left(\frac{N}{10^{16}}\right)\right]^P} (\mathrm{V/cm}) \tag{5.2}$$

Table 5.2: Critical electric field parameters.

Materials	B (MV/cm)	A	P
Si	0.43	0.27	1.38
4H-SiC	2.70	0.22	1.29
GaN	2.94	0.11	2.60
β-Ga_2O_3	5.76	0.18	1.75
$Al_{0.6}Ga_{0.4}N$	4.25	0.16	1.29
Diamond	2.82	0.22	1.45
AlN	4.21	0.16	1.28

The parameters for each of the investigated materials are summarized in Table 5.2. The critical field results obtained in this work are in close agreement with the results obtained in our previous study [112]. For Si and 4H-SiC, which are considered mature materials, the breakdown

voltage results also agree with the results seen in Baliga's work [10], indicating the effectiveness of this study. For diamond, it is seen that the critical field is much lower compared to what one would have expected for materials with such a high bandgap. It is also observed that $Al_{0.6}Ga_{0.4}N$ and AlN have similar critical-field trends (The fit for AlN is omitted because it is too close to that of $Al_{0.6}Ga_{0.4}N$).

5.3 Improved On-resistance versus Breakdown Voltage Figure-of-Merit for Wide- and Ultrawide-Bandgap Semiconductors as a Function of the Temperature

The previous section set a framework to evaluate the on-resistance and the breakdown voltage of $p - i - n$ as a function of the thickness and doping concentration of the i-layer. This section investigates the temperature dependence of the on-resistance versus breakdown voltage limits.

5.3.1 Impact of the Temperature on the Breakdown Voltage

The temperature dependence of the breakdown voltage is accounted for with the temperature dependence of impact ionization discussed in Section 4.3.2 and is shown in Fig. 5.16 for 4H-SiC.

The characteristics of the device simulated are summarized in Table 5.1. Just as observed experimentally, the temperature has a limited effect on the breakdown voltage. The drift of the breakdown due to temperature changes is less than 5%.

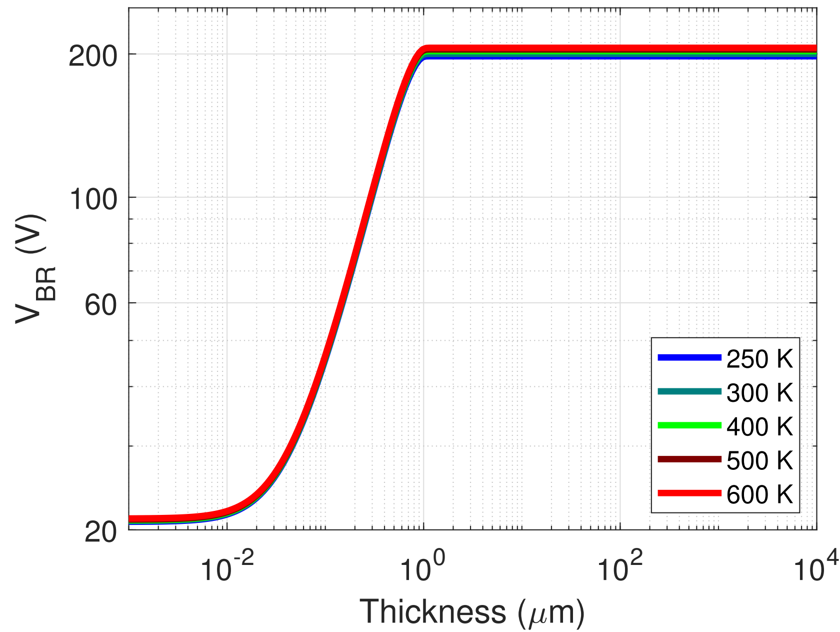

Figure 5.16: Calculated temperature dependence of the breakdown voltage in 4H-SiC. The effects of the temperature on the breakdown voltage are not drastic.

5.3.2 Impact of the Temperature on the On-Resistance

The temperature dependence of the on-resistance is accounted for with the temperature dependence of the mobility and of incomplete ionization. The on-resistance is calculated as a function of the i-layer thickness for several temperatures for an n-type doped substrate (2×10^{17} cm^{-3}) and is plotted in Fig. 5.17 for 4H-SiC and Fig. 5.18 for diamond.

At elevated temperatures, two phenomena compete for the values of the resistance. The deterioration of mobility with the temperature increases the on-resistance, while the enhanced ionization of dopants decreases the on-resistance. In the case of SiC, where the ionization energy of dopants is not very large (compared to diamond), it is observed that the temperature tends to increase the on-resistance. In the case of diamond, where the ionization energy of dopants is significant, the temperature has a more substantial effect on the ionization of dopants. It is seen

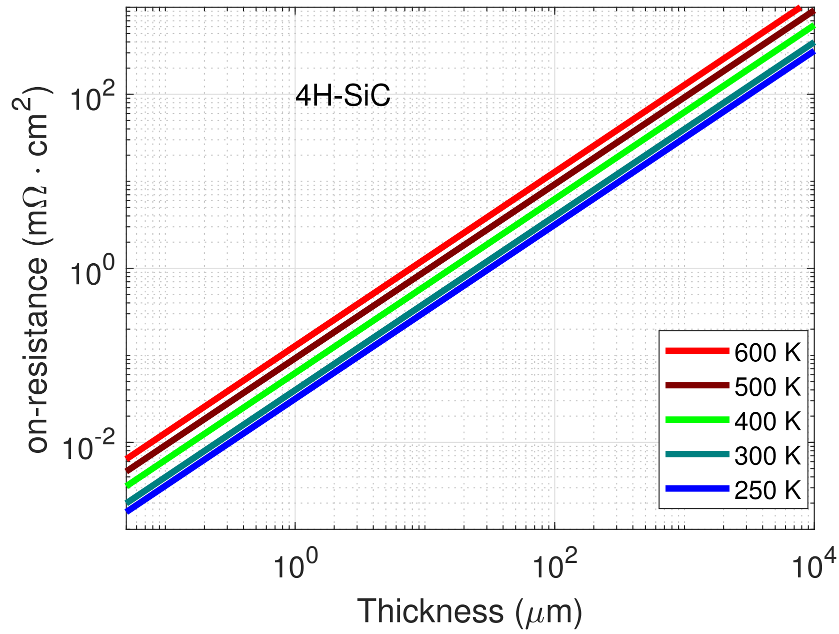

Figure 5.17: Temperature dependence of the i-layer resistance of 4H-SiC (calculated with (5.1)). The resistance is observed to increase with the temperature.

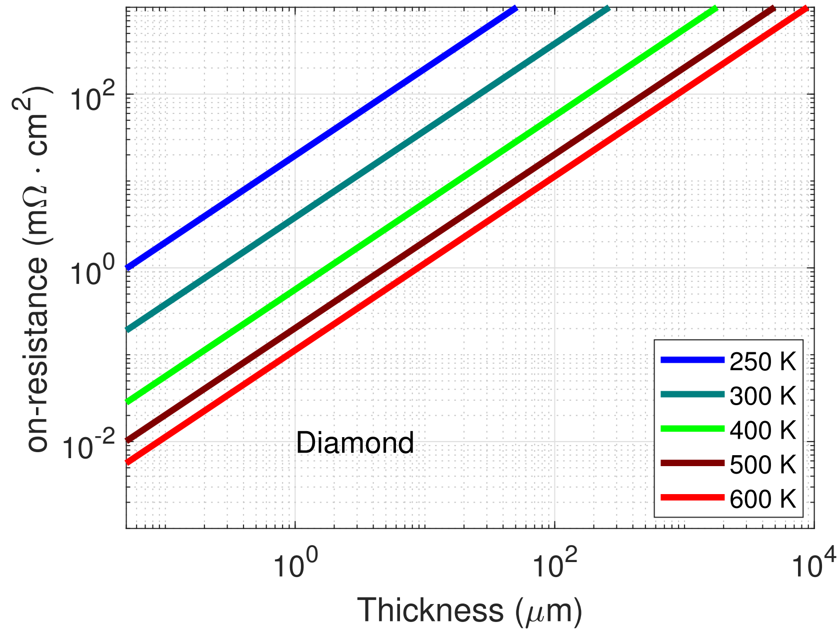

Figure 5.18: Temperature dependence of the i-layer resistance in an n-type doped diamond. The i-layer resistance decreases significantly when the temperature rises.

that the temperature significantly reduces the on-resistance.

5.3.3 Improved On-Resistance Versus Breakdown Voltage of Wide- and Ultrawide-Bandgap Semiconductors

The previous section of this work discussed breakdown voltage calculations from impact ionization coefficients; it also considered the assessment of the on-resistance using existing mobility models and accounting for the incomplete ionization of dopants. From the thickness of the $p-i-n$ diode's i-layer, it is possible to compute the breakdown voltage and the on-resistance of multiple $p-i-n$ structures and create a plot of the on-resistance versus breakdown voltage as previously shown in Fig. 5.7. The plot of Fig. 5.7 is reproduced for several doping concentration and the results are shown in Fig. 5.19. Just as previously observed, the on-resistance and the breakdown voltage both increase with the thickness of the i-layer. There is a threshold thickness at which the breakdown voltage remains constant while the resistance continues to increase, resulting in unnecessarily thick devices.

The plot of the on-resistance versus breakdown voltages shown in Fig. 5.19 omits devices that are unnecessary thick. The breakdown voltage and the on-resistance are evaluated up to the optimum thickness. The set of curves shown in Fig. 5.19 highlights the on-resistance versus breakdown voltage limits of 4H-SiC, and the process is repeated for other materials. Fig. 5.19 shows that each doping level considered is associated with a unique optimum breakdown voltage and an optimum on-resistance. The higher the doping concentration, the lower the optimum breakdown voltages and optimum on-resistance.

The on-resistance versus breakdown voltage limits line is established by connecting the

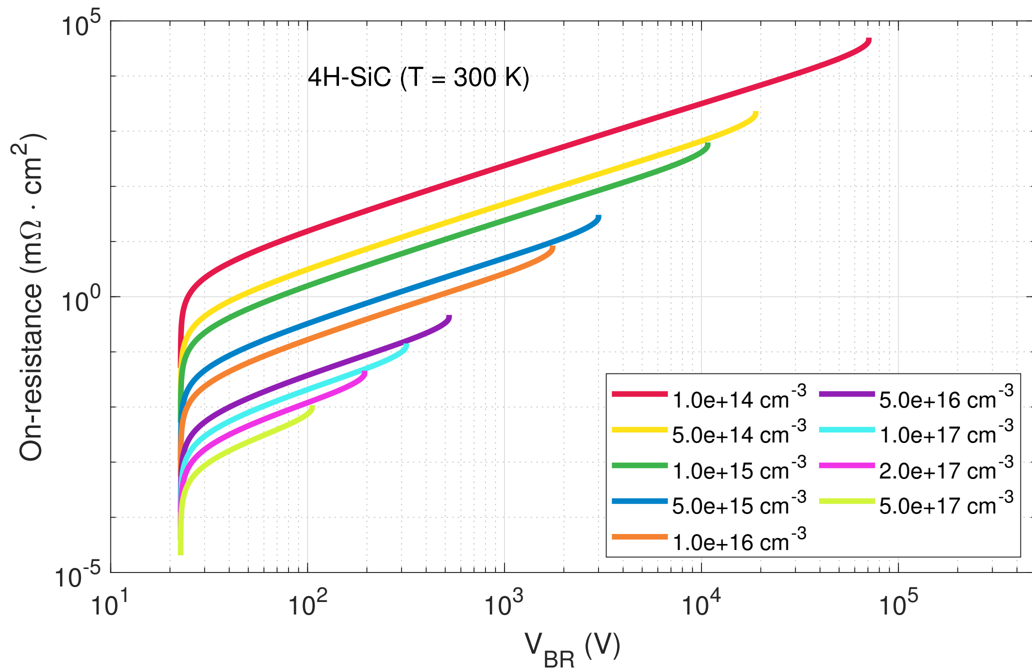

Figure 5.19: On-resistance versus breakdown voltage calculated as a function of drift-layer doping.

optimum breakdown voltage and on-resistance associated with each doping concentration as seen in Fig. 5.21.

This work investigated two aspects of the optimum breakdown voltage. For a given doping concentration, the optimum breakdown voltage can first be considered as the maximum achievable voltage at that doping level. However, it is also worth noticing that the on-resistance increases much faster before reaching the maximum breakdown voltage (The curves curl upward just before the end). Getting the maximum breakdown voltage becomes very costly in terms of the on-resistance. As such, the on-resistance versus breakdown voltage limits can be extracted slightly before the maximum breakdown voltage, as presented in Fig. 5.21. The points at which the change in curvature observed in Fig. 5.19 occur can be made evident by rotating the calculated on-resistance versus breakdown voltage anti-clockwise by about an angle of about $5\pi/8$ as

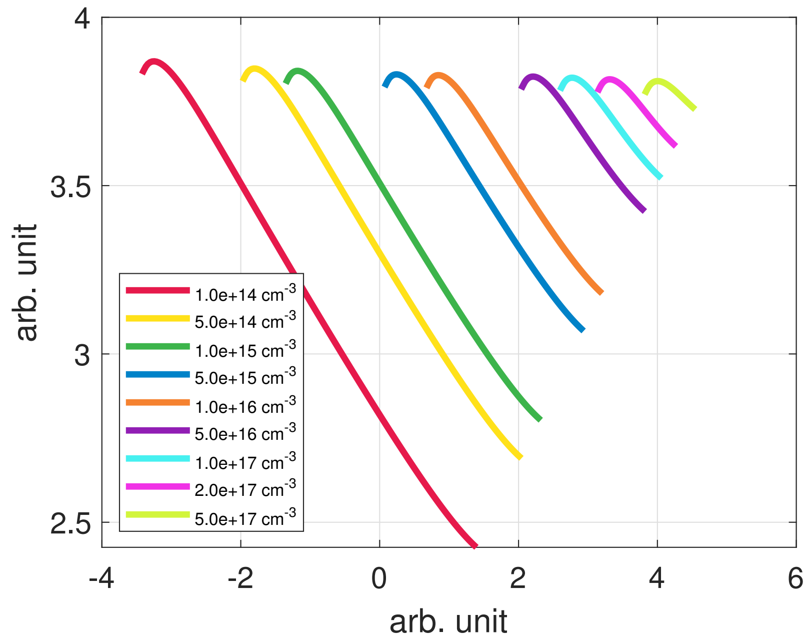

Figure 5.20: Rotating the R_{ON} versus V_{BR} curves to obtain the optimum limits. Rotating by an angle of $5\pi/8$ radians makes the optimum points maximums easily extractable.

shown in Fig. 5.20. The optimum points are then matched with the peaks of the curves shown in Fig. 5.20.

There is only a slight difference between the limits extracted at the maximum breakdown voltage and those obtained at curvature change. It is essential to correlate the optimum device with the devices used in the literature to derive the on-resistance versus breakdown voltage figure of merit. As seen in Fig. 1.5, the substrate considered is just fully depleted, and the electric field profile is shaped like a right triangle. The optimum structure also has an almost right rectangular electric field profile at the breakdown voltage. The ideality of the right rectangle is slightly compromised with the punch-through in the cladding layers, and the punch-through effects are insignificant, especially when the doping concentration in the cladding layers is high.

Fig. 5.21 shows how different doping concentrations lead to the on-resistance versus breakdown voltage limit of 4H-SiC at room temperature. Starting from several doping concentrations

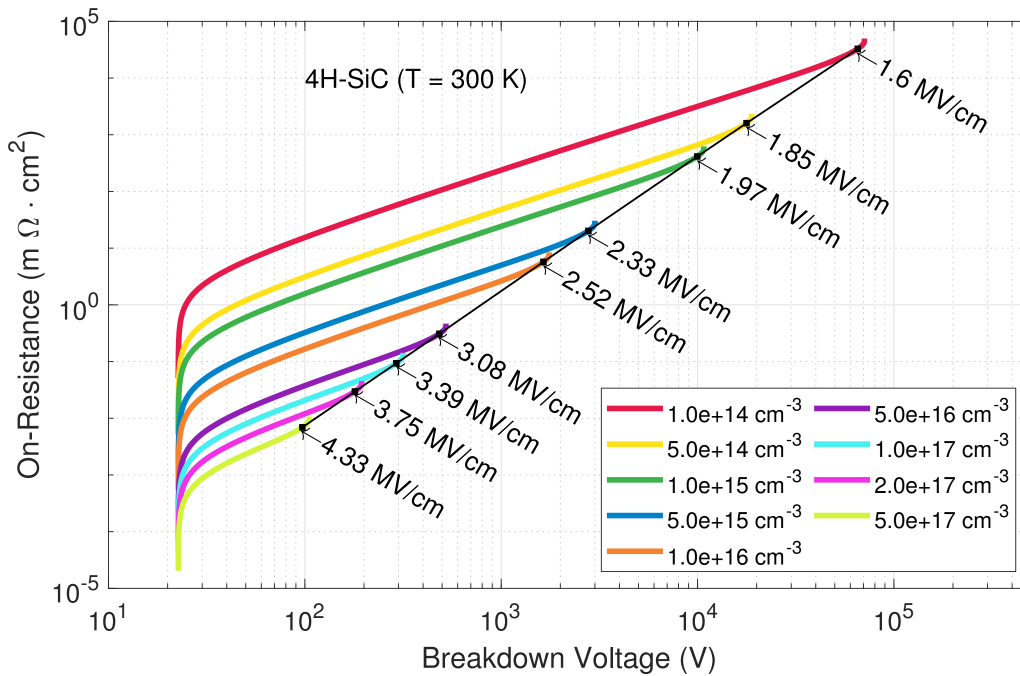

Figure 5.21: Calculated on-resistance versus breakdown voltage along with the limits given by the optimized structures (black line).

(from the minimum achievable doping to 10^{18} cm^{-3}), the optimum thickness is found, and the corresponding optimum on-resistance and breakdown voltages are calculated. The breakdown voltage and the on-resistance are also evaluated as a function of the temperature. The temperature affects the breakdown voltage through impact ionization coefficients and the on-resistance through the mobility and the incomplete ionization of dopants. The calculations are performed for several temperatures and the different materials investigated. The on-resistance versus breakdown voltage limits for the material studied are shown in Fig. 5.22 for 300 K, in Fig. 5.23 for 400 K, and in Fig. 5.24 at 800 K.

For each material, the simulated doping range is adjusted to reflect the minimum achievable doping levels reported in the literature. Those minimum doping levels are on the order of 2.5×10^{14} cm^{-3} for β-Ga_2O_3 [113], 1 to 5×10^{15} cm^{-3} for GaN [114], 1×10^{14} cm^{-3} for

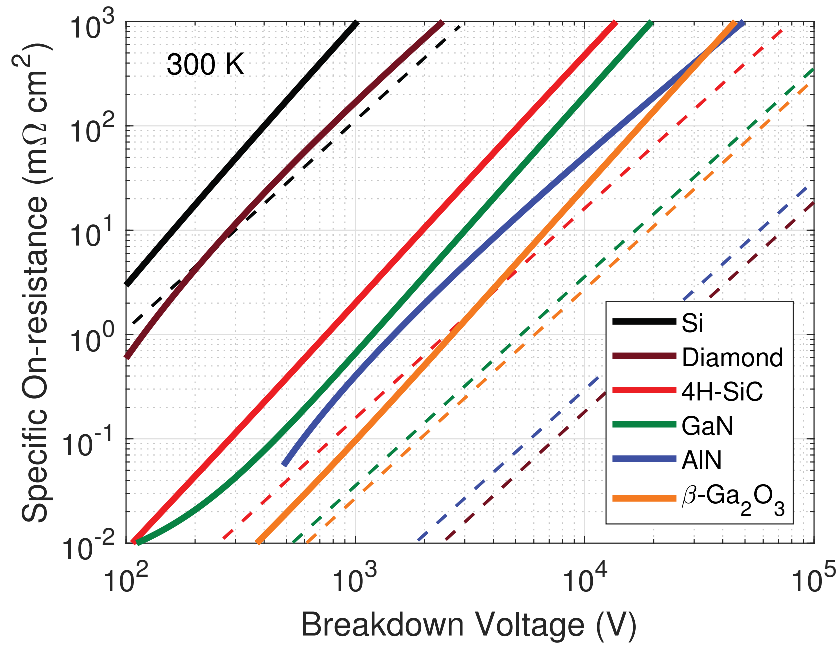

Figure 5.22: Calculated on-resistance versus breakdown voltage limits of si, WBG- and UWBG-semiconductors at 300 K. The solid lines represent limits obtained in this work; the dashed lines represent limits reported by Tsao et al. [11].

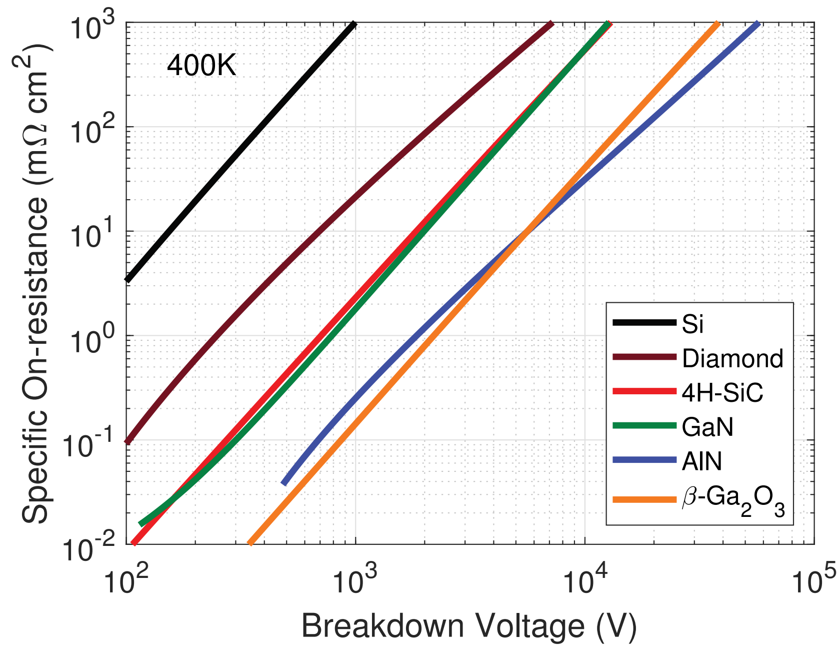

Figure 5.23: Calculated on-resistance versus breakdown voltage limits of si, WBG- and UWBG-semiconductors at 400 K.

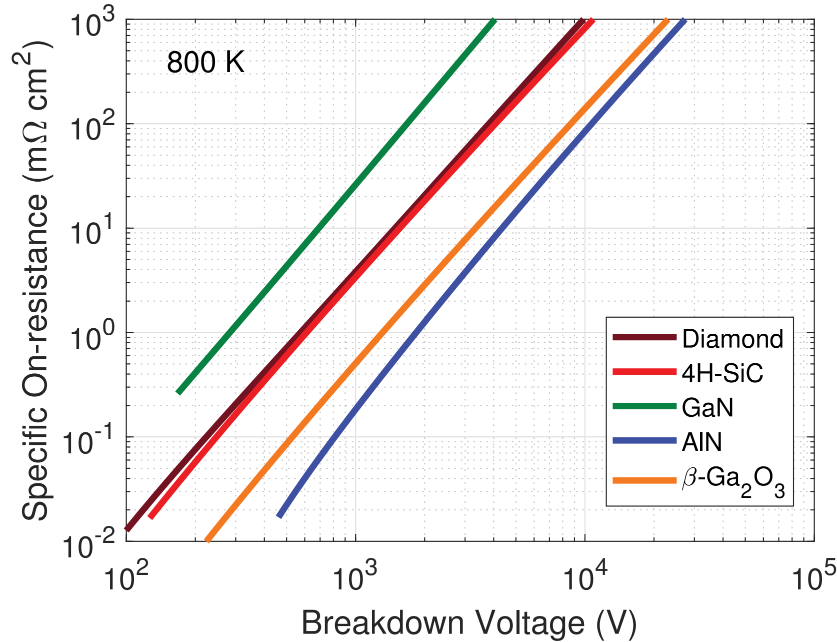

Figure 5.24: Calculated on-resistance versus breakdown voltage limits of si, WBG- and UWBG-semiconductors at 800 K.

4H-SiC [111], and 1×10^{13} cm^{-3} for Si. The calculations show that the power performance of ultrawide-bandgap semiconductors improves with the temperature; despite the reduction of the mobility at elevated temperature, the enhanced ionization of dopants is more pronounced, resulting in the lowering of the on-resistance. The performance of β-Ga_2O_3 and wide bandgap materials seems to deteriorate with temperature. At room temperature, the proposed limits improve on existing limits that overestimate device performance.

Conclusion

This chapter demonstrated the use of impact ionization coefficients for breakdown voltage calculations. Breakdown voltages calculated as a function of the i-layer thickness for a fixed doping concentration showed the existence of a threshold thickness (critical thickness or optimum thickness) at which the breakdown voltage ceases to increase with the thickness. Devices with

an optimum thickness are such that their electric field profile at breakdown is shaped like a right triangle, just as the field profile used for deriving the unipolar Baliga figure-of-merit. Calculating the breakdown voltage as a function of the i-layer thickness for various doping concentrations highlighted that the optimum thickness is unique for a given doping concentration. The work showed that each limiting breakdown voltage is associated with a unique optimum thickness and optimum doping. The calculated critical field decreases with thickness and increases with doping concentration. Calculations also showed that each doping level is associated with a minimum critical field, and high breakdown voltages are achieved at low critical field values. The chapter discussed critical field models for wide- and ultrawide-bandgap semiconductors. The chapter also investigated the effects of the temperature on the device's performance. The temperature is observed to have a negligible impact on the breakdown voltage (seen experimentally for 4H-SiC); however, for semiconductors with high ionization energies, the temperature significantly lowers the on-resistance. Calculated breakdown voltages and on-resistance were merged, and improved on-resistance versus breakdown voltage limits were obtained. It is seen that the high voltage performance of a semiconductor is limited by the minimum achievable doping, which tends to be high for large gap materials. The temperature is seen to improve the power performance of ultrawide-bandgap materials, suggesting that they are suitable and convenient for high-temperature applications.

Chapter 6: Application and Conclusion

Using impact ionization coefficients for multiplication and breakdown voltage calculations provided a more fundamental approach to evaluating the power performance of wide and ultrawide bandgap semiconductors. This chapter discusses how breakdown voltages and on-resistances calculated using impact ionization coefficients are used to assess the efficiency and the power density of power electronics devices depending on the material used for their fabrication. In addition to efficiency studies, the chapter discusses avalanche photodiodes and how impact ionization coefficients affect some aspects of their operations. The incorporation of impact ionization coefficients in the drift-diffusion model for simulating breakdown characteristics of devices is discussed. The second part of this chapter presents the main findings of the dissertation and ideas worth pursuing to expand on them.

6.1 Use of Calculated Breakdown Voltage and On-Resistance to Assess the Efficiency of Power Electronics Devices

In the past chapters, the primary concern was the trade-offs between the on-state resistance and the breakdown voltage of power devices. Another important trade-off for power electronics platforms (namely converter systems) is that of power density versus efficiency. Calculated breakdown voltages and on-resistance are essential for comparing studied materials for their efficiency

and power density. During operations, the total power loss has two components: the switching loss and the conduction loss. The switching loss is due to leakage through the output capacitance, and the conduction loss is due to the ohmic joule heating through the on-resistance. For an illustration of the power loss during operation, a vertical power MOSFET subject to switching cycles of an electrical platform (boost or buck converter) is considered. The energy loss during switching is

$$E_{C_{oss}} = \int_0^{t(V_{DS})} v_{DS}(t) i(t) dt, \tag{6.1}$$

where $t(V_{DS})$ is the time it takes to switch from 0 to V_{DS}. $v_{DS}(t)$ and $i(t)$ are the time dependent drain to source voltage and current during switching, respectively. Using $i(t) = C_{oss}(v_{DS}) \frac{dv_{DS}(t)}{dt}$ leads to

$$E_{C_{oss}} = \int_0^{t(V_{DS})} v_{DS}(t) C_{oss}(v_{DS}) dv_{DS} \tag{6.2}$$

The output capacitance for the case of a vertical power MOSFET is just the depletion capacitance. The depletion capacitance is inversely proportional to the square root of the applied bias. It is convenient to express the bias dependence of the depletion capacitance using the breakdown voltage depletion as a reference. the output capacitance, which is the drain to source capacitance for the case of a power MOSFET (see Fig. 3.2) can be expressed as

$$\begin{aligned} C_{oss}(v_{DS}) &= \epsilon_0 \epsilon_r \frac{A}{W(v_{DS})} \\ &= \epsilon_0 \epsilon_r \frac{A}{W(V_{BR})} \sqrt{\frac{V_{BR}}{v_{DS}}}. \end{aligned} \tag{6.3}$$

A is the area of the power semiconductors. $W_{v_{DS}}$ is the depletion width at a voltage v_{DS} during the switching process, and $W_{V_{BR}}$ is the depletion width at the breakdown voltage, ideally the maximum depletion width or the thickness of the drift region for an optimized device. The energy loss due to switching becomes

$$E_{C_{oss}} = \int_0^{t(V_{DS})} \epsilon_0 \epsilon_r \frac{A}{W(BR)} \sqrt{\frac{V_{BR}}{v_{DS}}} v_{DS} dv_{DS}. \tag{6.4}$$

Performing the integral and using 0 and V_{DS} for the boundary of v_{DS} yields the following equation for the energy loss due to switching through the output capacitor.

$$E_{C_{oss}} = \frac{2}{3} \epsilon_0 \epsilon_r \frac{A}{W(V_{BR})} \sqrt{V_{BR}} V_{DS}^{3/2} \tag{6.5}$$

The power loss due to switching is obtained by multiplying the derived energy by the converter's switching frequency, $f_s w$. The ohmic is calculated from the on-resistance R_{ON}, and the on-state current I_{ON} and is modulated using the duty cycle, σ. The total power loss, $P_L oss$ is the sum of the switching loss and the ohmic loss and can be expressed as

$$P_{Loss} = \frac{2}{3} \epsilon_0 \epsilon_r \frac{A}{W(V_{BR})} \sqrt{V_{BR}} V_{DS}^{3/2} f_{sw} + \frac{\delta R_{ON} I_{ON}^2}{A} \tag{6.6}$$

The switching, ohmic, and total switching were assessed for 4H-SiC. The thickness and the on-resistance used for calculating the losses were obtained using the procedure explained in Chapter 5 and are summarized in Table 6.1. For the calculation, the Power MOSFET was designed to have a breakdown voltage of 6.5 kV, block 6 kV in the off-state, and run 10 A of current in the on-state.

Table 6.1: Calculated optimum thickness ($W(V_{BR})$) and on-resistance (R_{ON}) for a targeted breakdown voltage of 6.5 kV in wide- and ultrawide-bandgap semiconductors.

Materials	Temperature [K]	$W(V_{BR})$ [μm]	R_{ON} [m$\Omega \cdot cm^2$]
4H-SiC	300	54.03	20.73
	500	54.03	60.38
	700	54.00	124.12
GaN	300	48.36	12.73
	500	48.36	34.97
	700	48.6	68.37
β-Ga_2O_3	300	19.54	3.56
	500	19.54	8.71
	700	19.54	14.34
$Al_{0.4}Ga_{0.6}N$	300	29.09	6.95
	500	29.08	8.51
	700	29.08	15.36
Diamond	300	54.15	11540.05
	500	54.15	115.41
	700	54.15	38.18
AlN	300	27.98	31.62
	500	28.01	11.07
	700	28.01	14.78

The calculated power loss are shown in Fig. 6.1 as a function of the device area A. While the conduction losses decrease with increasing the device's area, the switching losses increase with the device's area. The plot displays a minimum corresponding to the minimum total power loss.

The optimum area can be found by finding the zero of $\frac{dP_{Loss}}{dA}$. The optimum area A_{op} that minimizes the switching loss is given by

$$A_{op} = \sqrt{\frac{\delta R_{ON} I_{ON}^2 3W(V_{DS})}{2\epsilon_0\epsilon\sqrt{V_{BR}}V_{DS}^{3/2} f_{sw}}}. \tag{6.7}$$

The corresponding optimum power (The minimum power loss as a function of the area) is given by

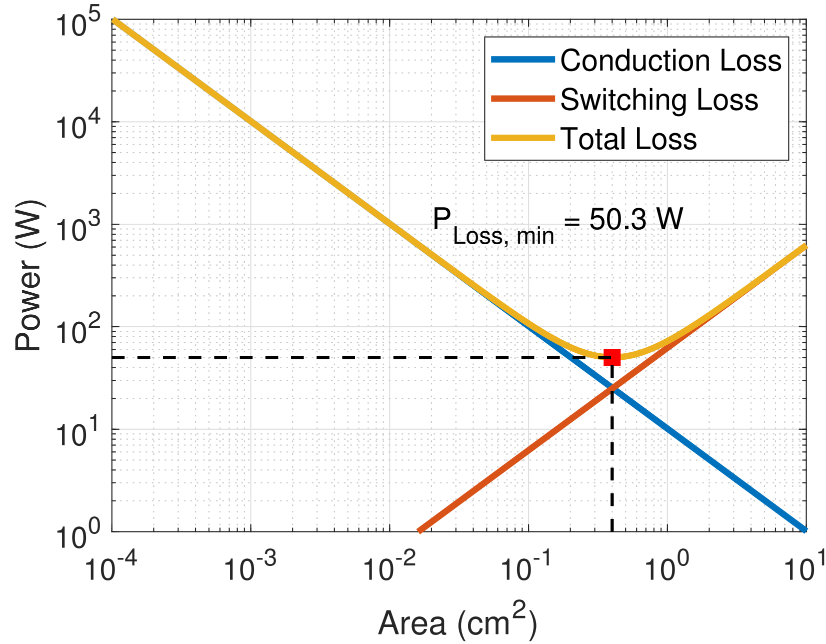

Figure 6.1: Calculated area dependence of the conduction, switching, and total loss for a 4H-SiC in a switching application. The calculations are performed at room-temperature. It is assumed that the device's breakdown voltage is 6.5 kV and that it is operating at 6 kV with a current of 10 A in the on-state.

$$P_{Loss,min} = 2\sqrt{\frac{2\epsilon_0\epsilon_r\sqrt{V_{BR}}V_{DS}^{3/2}f_{sw}\delta R_{ON}I_{ON}^2}{3W(V_{DS})}}. \quad (6.8)$$

The calculations were repeated for the other materials under investigation; Fig. 6.2 shows the total loss in wide- and ultrawide-bandgap semiconductors as a function of the area. The parameters used for the calculation are summarized in Table 6.1, and the operating conditions are 6.5 kV for the breakdown voltage, 6 kV for the reverse voltage, and 10 A for the forward current. The calculations show that β-Ga_2O_3 offers the best efficiency and power density. β-Ga_2O_3 is the ultrawide-bandgap material studied with the least ionization energy for n-type doping. β-Ga_2O_3 also benefits from low values of impact ionization coefficients, likely due to the poor mobility of electrons, resulting in low impact ionization coefficients and large breakdown voltages.

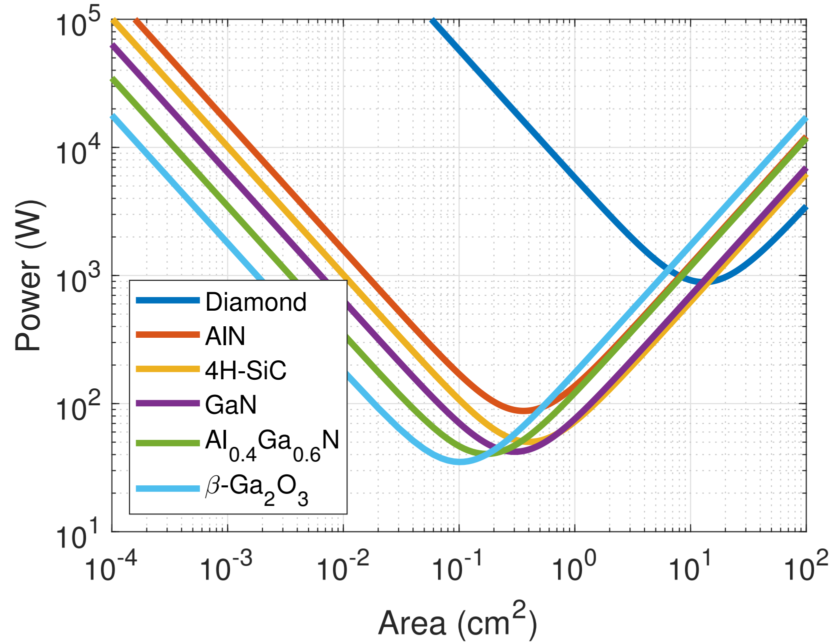

Figure 6.2: Calculated switching loss in wide- and ultra-wide bandgap semiconductors devices during switching. The calculations are perform using (6.6) along with the parameters indicated in Table 6.1.

The total power loss is investigated as a function of the temperature. Fig. 6.3 and Fig. 6.4 shows the calculated total power loss at 300 K, 500 K, and 700 K in 4H-SiC and diamond, respectively.

For 4H-SiC, it is observed that the optimal power density and efficiency are degraded at elevated temperatures, for the overall effect of the temperature is an increase of the on-resistance. In diamond, improvements in power density and efficiency are observed when the temperature increases. The high ionization energy of dopants in diamond results in high resistances at room temperature; As the temperature increases, the ionization of dopants is enhanced, resulting in better performance.

It is important to note that the on-resistance considered in this work is that of a solid bar. Because of the high ionization energy of dopants in diamond, the on-resistance versus breakdown

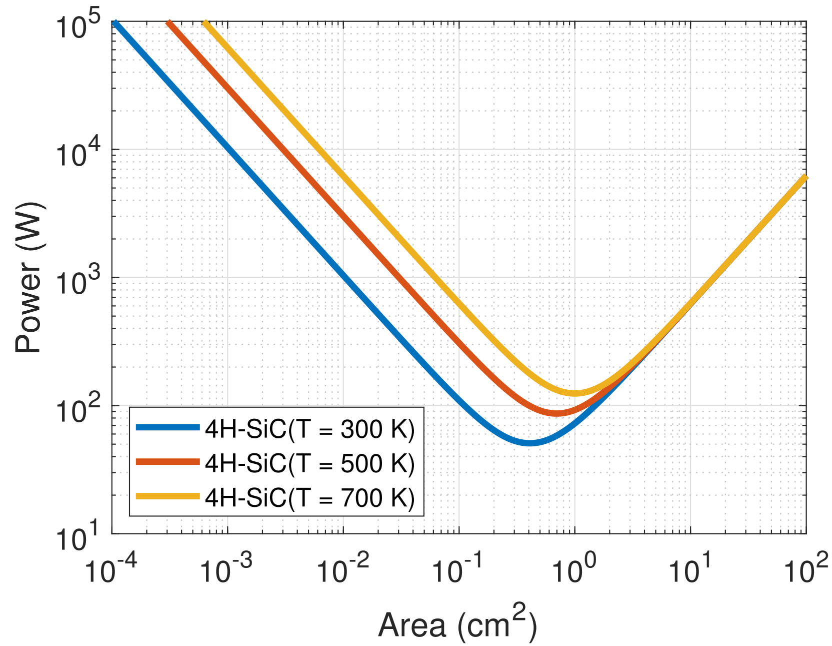

Figure 6.3: Effect of the temperature on the power losses of 4H-SiC power switches. The increase in temperature results in higher resistance and deterioration of efficiency and power density.

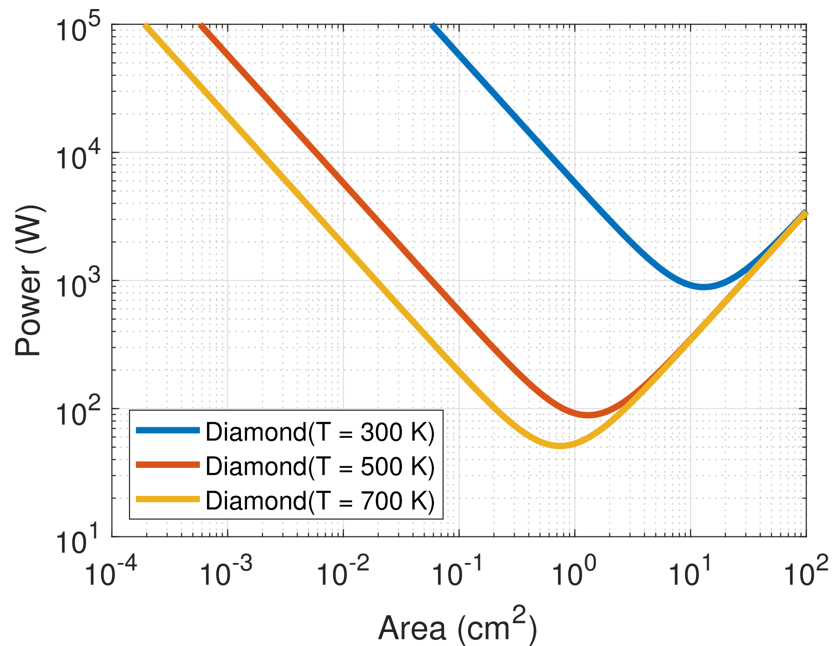

Figure 6.4: Effects of the temperature on the power losses in diamond. The temperature improves the performance by augmenting the power density and reducing the optimum power loss.

voltage limits, the efficiency, and the power density of diamond is observed to be poor. The observation does not necessarily mean that diamond is not a valuable semiconductor. Diamond is an excellent material for RF electronics, where achieving a high breakdown voltage is not a top priority. for power electronics, p-type diamond is preferred for the lower ionization energy of acceptors. Multiple doping alternatives, such as surface transfer doping, are viable paths for improving the concentration of active dopants in diamond, which already exhibits high carrier mobility. Conduction doesn't have to happen through the bulk as studied in this chapter; in fact, there is a significant difference between the power figure-of-merit for vertical and lateral devices [115]. A lateral power device that exploits surface transfer doping could project diamond as one of the highly desired materials for power electronics.

6.2 Impact Ionization Coefficients and the Performance of Avalanche Photodiodes

Avalanche photodiodes are similar to $p-i-n$ structures because their architecture consists of an intrinsic layer (or lowly doped layer) sandwiched between two heavily doped layers of opposite polarity. This work measured $p-i-n$ structures to backtrack impact ionization coefficients from their reverse current-voltage characteristics. This section provides more insight into the operation of avalanche photodiodes in linear and Geiger modes.

6.2.1 Characterization of Avalanche Photodiodes in Linear Mode

In linear mode operation, the diodes are illuminated with an optical source, and the photocurrent is measured as a function of the applied bias. Figure 6.5 shows the test setup for linear

mode testing. The lamp emits a monochromatic beam of light; the wavelength of the light emitted can be set from 200 nm to 700 nm. A filter adjusts the intensity of the light emitted, which is projected on the device through an optical fiber. The diameter of the fiber is 200 μn.

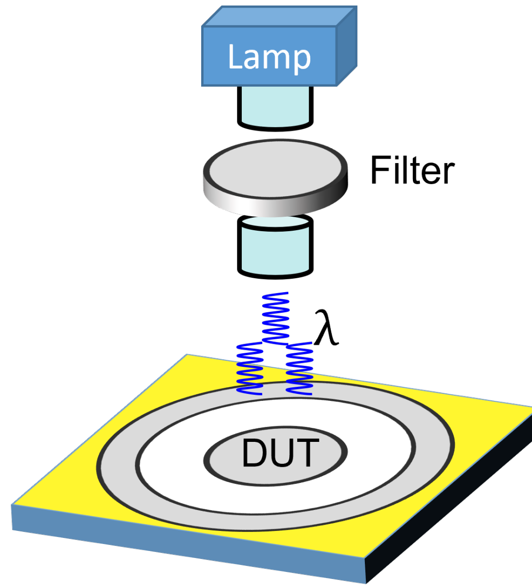

Figure 6.5: Setup for linear mode testing.

4H-SiC avalanche photodiodes were characterized in the linear mode setup. Current-voltage characteristics measured as a function of the light source's wavelength are shown in Fig. 6.6. The figure (6.6(a)) also shows the reversed current-voltage characteristic measured in the dark.

Figure 6.6 highlights the effect of the optical wavelength on the measured current-voltage characteristics. Measurements in the dark to up to 280 nm show an increase in the unity gain (low biases) current with increasing wavelength. Measurements at high wavelength, from 290 nm to 390 nm, show a decrease of unity gain current with increasing wavelength. The diode's response (at zero bias) to various optical wavelengths is shown in Fig. 6.7. The observed trend conforms to existing rules about the absorption of carriers in semiconductors. Light sources with high energy

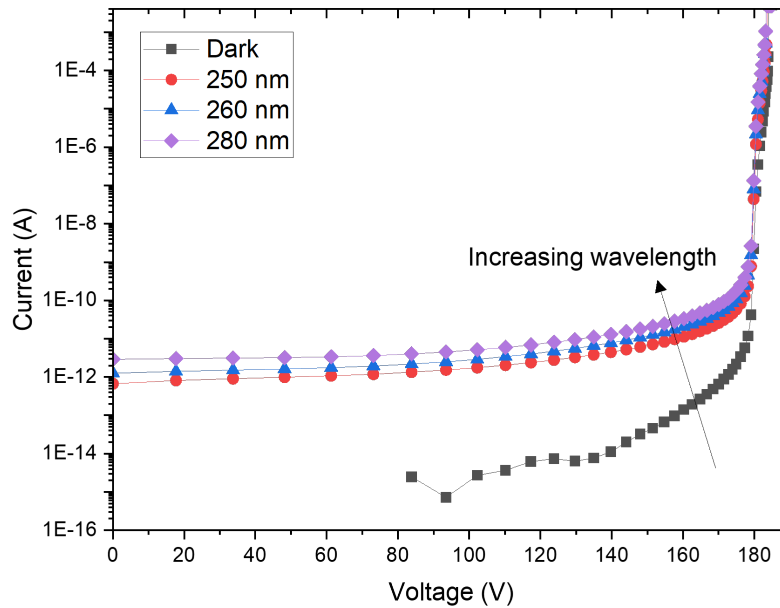

(a)

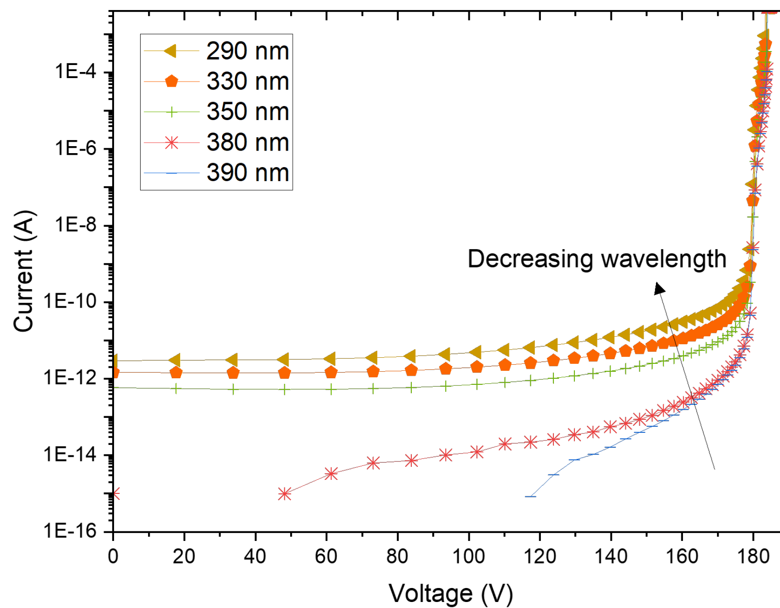

(b)

Figure 6.6: Measured photo-current as a function of the optical wavelength. In (a), the photo-current increases as the wavelength increases. In (b) the photo-current decreases with increasing wavelength. The calculated cut-off wavelength of 4H-SIC is 380.6 nm; this cut-off wavelength is observed experimentally.

(low wavelengths are absorbed close to the surface). As the light goes through the material, its intensity is attenuated according to the following equation

$$I_n(x) = I_{n0} \exp^{-\alpha_{op} x}, \tag{6.9}$$

where, the absorption coefficient α_{op} is given by

$$\alpha_{op} = \frac{4\pi k_{op}}{\lambda_{op}}. \tag{6.10}$$

The parameter λ_{op} denotes the wavelength of the light, and k_{op} is called the extinction coefficient.

The diode measured is n-illuminated; the top layer is n-type doped, and excess holes are created when illuminated at a low wavelength. When the wavelength is too small, the excess holes can recombine before entering the high field region where they can drift. While impact ionization coefficients are not relevant for operation at unity gain, higher voltages result in larger punch-through depletion width toward the surface and improve carriers' collection and gain [116].

When the wavelength increases, the optical energy decreases. To be absorbed, the energy of the incident photon should be higher than the material's bandgap. The relationship between the wavelength and the energy is given by

$$E = \frac{hc}{\lambda_{op}}. \tag{6.11}$$

For 4H-SiC, which has a bandgap of 3.26 eV, the cut-off wavelength (maximum wavelength) of a photon that can be absorbed is

$$\lambda_{op} = \frac{1.2408}{3.26} \times 10^{-6} = 380.6 \text{ nm}. \tag{6.12}$$

As seen in Fig. 6.6, at 390 nm, the diode behaves as if it was in the dark.

6.2.1.1 The Quantum Efficiency

Another important characteristic of avalanche photodiodes is the quantum efficiency, which is the number of charges collected per incident photon. The number of electrons emitted, n_e, in a period t is given by

$$n_e = \frac{I_{ph} t}{q}, \tag{6.13}$$

where I_{ph} is the measured photo-current at unity gain. The number of photons incident in a time t is given by

$$n_{ph} = \frac{P_{op} t}{h\nu} \tag{6.14}$$

The quantum efficiency is

$$\aleph = \frac{n_e}{n_{ph}} = \frac{I_{ph}}{P_{ot}} \frac{h\nu}{q} = \Re \frac{h\nu}{q}. \tag{6.15}$$

6.2.1.2 The Responsivity

In addition to the quantum efficiency, the responsivity, $\Re$ is another metric of high interest for avalanche photodiodes. The responsivity is the ratio of the photo-generated current to the incident optical power. The responsivity can also be expressed as a function of the quantum efficiency; it results that

$$\Re = \frac{I_{ph}}{P_{op}} = \frac{\aleph q}{hc}\lambda. \tag{6.16}$$

The plot of the responsivity is shown in Fig. 6.7 as a function of the illumination wavelength for a 4H-SiC avalanche photodiode. If the quantum efficiency remains constant and invariant to the wavelength, the responsivity becomes a straight line. Responsivity for constant efficiency of 25 %, 50%, 75 % and 100 % are shown in Fig.6.7 for reference.

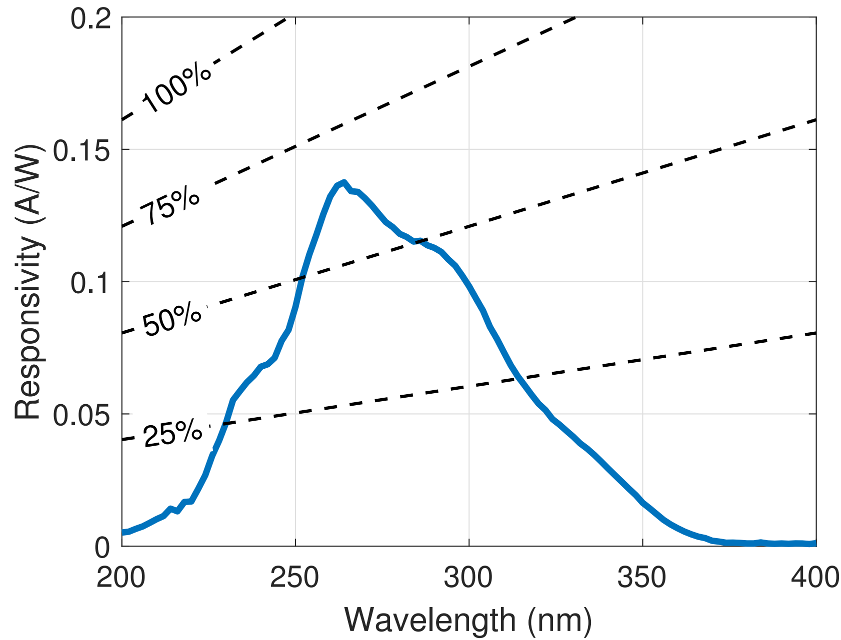

Figure 6.7: Measured responsivity in 4H-SiC avalanche photodiodes. Reference lines are added for quantum efficiency of 25 %, 50%, 75 % and 100 %.

The characterization of diodes in linear mode allows the extraction of the responsivity; however, extracting the quantum efficiency is challenging because of underfilling problems. If the diode's surface is smaller than the area of the incident optical beam, not all the sourced light is incident on the device, and finding the effective power incident on the device becomes challenging.

6.2.2 Characterization of Opto-electronics Devices with Impact Ionization Coefficients: Geiger Mode Operation

While in linear mode setup, the wavelength of the light can be changed by adjusting the lamp, in Geiger mode operation, the optical source has only one wavelength. However, the bean size is much smaller and can be calibrated to determine the number of photons incident on the measured sample. The setup for Geiger mode testing is shown on Fig. 6.8.

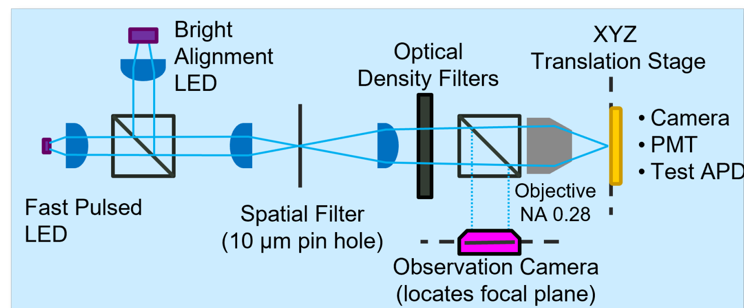

Figure 6.8: Illustrative diagram for scanning Geiger mode experiments.

The evaluation of $p - i - n$ diodes in the Geiger mode setup was performed with a 285 nm fast pulsed LED source. The setup was calibrated for about a half-million (438709) incident photons per second. In Geiger mode testing, the avalanche photodiode is biased close to breakdown, and incident photons trigger the breakdown process. Photons that trigger breakdown are successfully detected. When a breakdown occurs, the current surge leads to a significant voltage drop across the quenching resistor connected in series with the diodes. As the quenching resistor steals the voltage across the diode, the current lowers, and the diode, now acting as a photon detector, awaits the next quenching cycle. More on Geiger mode operation can be found in [117]. In Geiger mode operation, the avalanche photodiode works as a single-photon detector, and the single-photon detection efficiency (SPDE) is one of its essential characteristics.

Using a discriminator at the cathode of the avalanche photodiodes allows the counting of quenching cycles. In the dark, no incident photon triggers an avalanche; however, quenching cycles are still observed, likely triggered by carriers emanating from defect centers. The dark and total counts of the detector are shown in Fig. 6.9 for a pulsed light source of 285 nm. The single-photon detection efficiency is obtained by dividing the photo counts by the number of incident photons. The photo count is obtained by subtracting the dark count from the total count. The plot of the single-photon detection efficiency is shown in Fig. 6.10 for the 4H-SiC diodes investigated.

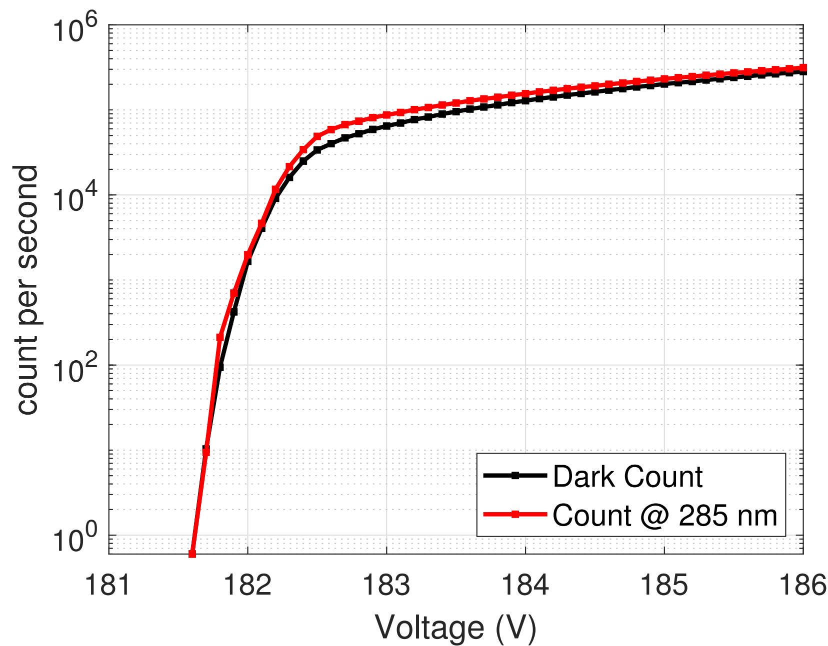

Figure 6.9: Dark and photo counts measured on 4H-SiC avalanche photodiodes as a function of the applied bias.

The measured single detection efficiency (SPDE) saturates at about 7%. Several factors may influence the SPDE; the low response time of the diode due to a large RC constant could result in long quenching cycles receiving more than two photons. The measured SPDE can be improved if the number of photons incident per second is reduced, but one runs the risk of blocking all the light. The dark count also contributes to low SPDE. DLTS analysis performed in

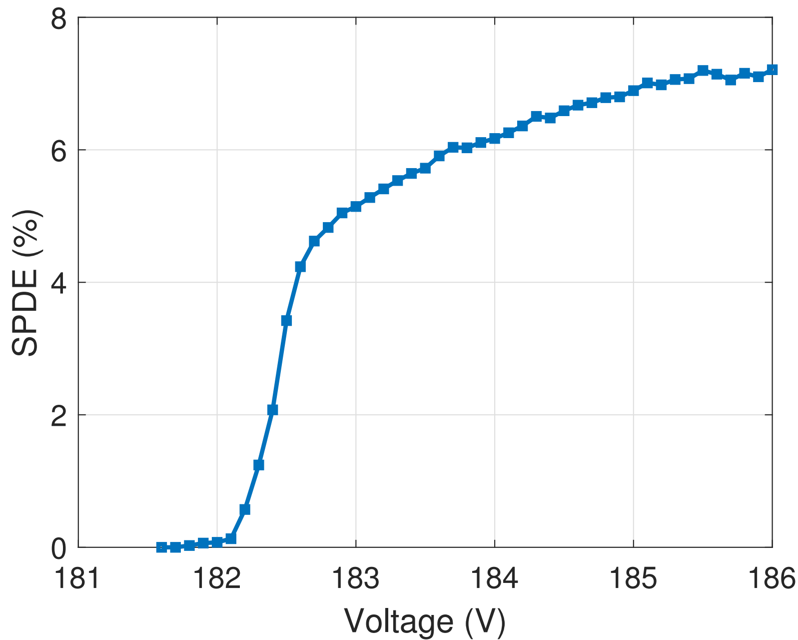

Figure 6.10: Calculated single-photon detection efficiency of a 4H-SiC avalanche photodiode.

this work revealed the presence of deep traps in 4H-SiC substrates. Emissions from those deep traps also alter the SPDE of devices.

As captured by the equation below, the SPDE is the product of the quantum efficiency by the avalanche probability as given by (6.17). The avalanche probability increases with the applied bias. The problem with high biases is that the dark count catches up with the total count (the total count is the sum of the dark and photo counts). Though there is little to no report on the empirical formula for the avalanche probability, impact ionization coefficients allow the determination of the avalanche probability through Monte Carlo simulations [118]. The random motion of carriers within the drift region can be repeatedly emulated; the avalanche probability is the fraction of emulations resulting in a breakdown. In this case, the breakdown voltage is dependent upon the reverse current reaching a set threshold point.

Another important aspect of the operation of avalanche photodiodes is the detection uni-

formity of devices. When a diode is non-uniform, the probability that a photon gets detected will depend on where it impinges on the surface of the device. Fig. 6.11 shows the spatial uniformity of the measured diode with a reverse bias of 20 V.

$$\text{SPDE} = \text{QE} \times \text{AP} \tag{6.17}$$

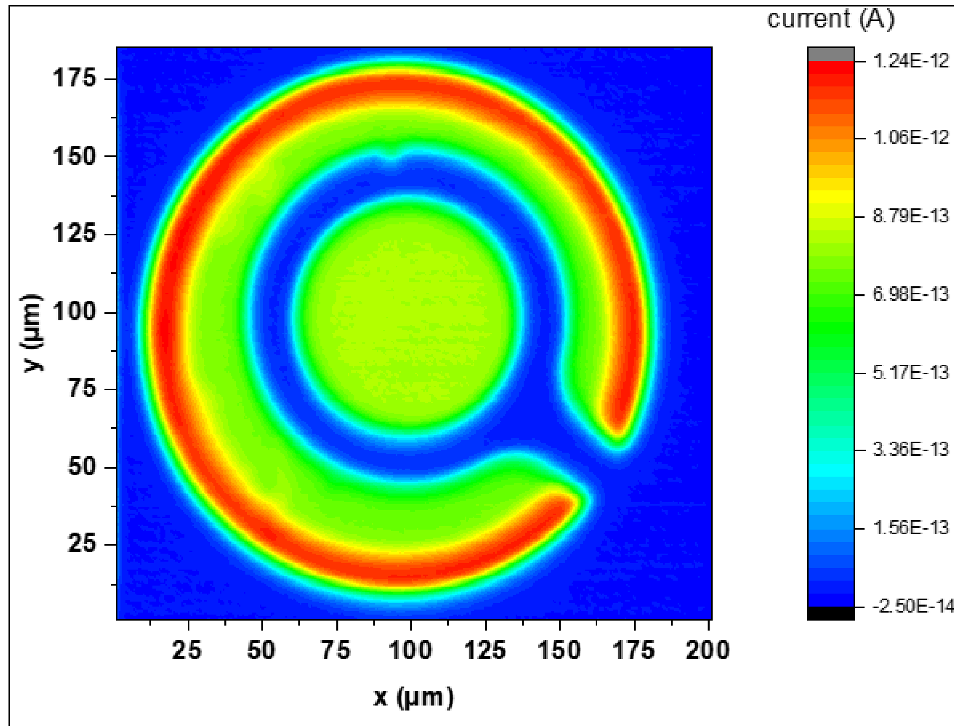

Figure 6.11: Spatial dependence of the photo-current in 4H-SiC avalanche photodiodes biased at 20 V. The diameter of the diode is 200 μm, and the surface is scanned with a 10 μm spot size pulsed LED at 285 nm.

The diode measured is shown in Fig. 2.27. It is observed that the diode becomes more non-uniform as the reverse bias increases. The reasons behind the non-uniformity are still under investigation. It has been suggested that the non-uniformity problem results from poor field spreading on the surface of the device. More efforts to are needed to fully understand non-uniformity.

6.3 Impact Ionization Coefficients and the Drift-Diffusion Equations

Impact ionization coefficients are also crucial for their use in the drift-diffusion model to simulate the reverse current-voltage characteristics of semiconductors devices. The equations commonly used in the drift-diffusion model are the Poisson, the continuity, and the current equations. The Poisson equation is expressed as

$$\nabla^2\phi = -\frac{q}{\epsilon}\left(p - n + N_D^+ - N_A^-\right) \tag{6.18}$$

The continuity equation for electrons is

$$\frac{dn}{dt} = \frac{1}{q}\nabla J_n + G_n - R_n, \tag{6.19}$$

where G_n is the generation rate, and R_n is the recombination rate. Similarly, the hole's continuity equation is

$$\frac{dp}{dt} = \frac{1}{q}\nabla J_p + G_p - R_p, \tag{6.20}$$

where G_p and R_p are the generation and recombination rate for electrons and holes, respectively. The electron current is given by (6.21) and (6.22), where μ_n and μ_p are the mobility for electrons and holes respectively. The parameters D_n and D_p are the diffusion constant for electrons and holes, respectively.

$$J_n = -q\mu_n n\nabla\phi + qD_n\nabla n. \tag{6.21}$$

$$J_p = -q\mu_p p \nabla \phi - qD_p \nabla p. \tag{6.22}$$

The generation rate due to the impact ionization collisions is

$$G = \frac{\left|\overrightarrow{J_n}\right| \alpha_n + \left|\overrightarrow{J_p}\right| \alpha_p}{q}. \tag{6.23}$$

When impact ionization collisions are dominants, $G = G_n = G_p$. The calibrated impact ionization coefficients reported in Table 4.2 was use to simulated a $p-i-n$ structure with an i-layer doping of 5×10^{15} cm^{-3} with a thickness of 0.48 μm. The current-voltage characteristic of the avalanche photodiodes measured and modeled with calibrated impact ionization coefficients are shown in Fig. 6.12. The simulation is done by incorporating calibrated impact ionization coefficients into a commercial simulator, Sentaurus Device [119]. While modeling results and measured data agree well at low gains, discrepancies are observed at larger multiplications. At large gains, the series resistance lowers the effective voltage across the diode, resulting in experimental currents lower than that predicted by theory.

The results shown in Fig. 6.12 are representative of a single device. It is challenging to model the current-voltage characteristics accurately because of fabrication reproducibility. Though processed on the same wafer, the 4H-SiC diodes studied for the multiplication data performed differently, mainly in their off-state leakage. The variation of breakdown voltage observed between the measures devices was up to 7 V, resulting in slight inaccuracies in the ability to predict the breakdown voltage. The gain is even more challenging to model because it is susceptible to the voltage across the multiplication layer, which is highly affected by the series resistance. It is worth accounting for the fraction of generated carriers lost to recombination processes for

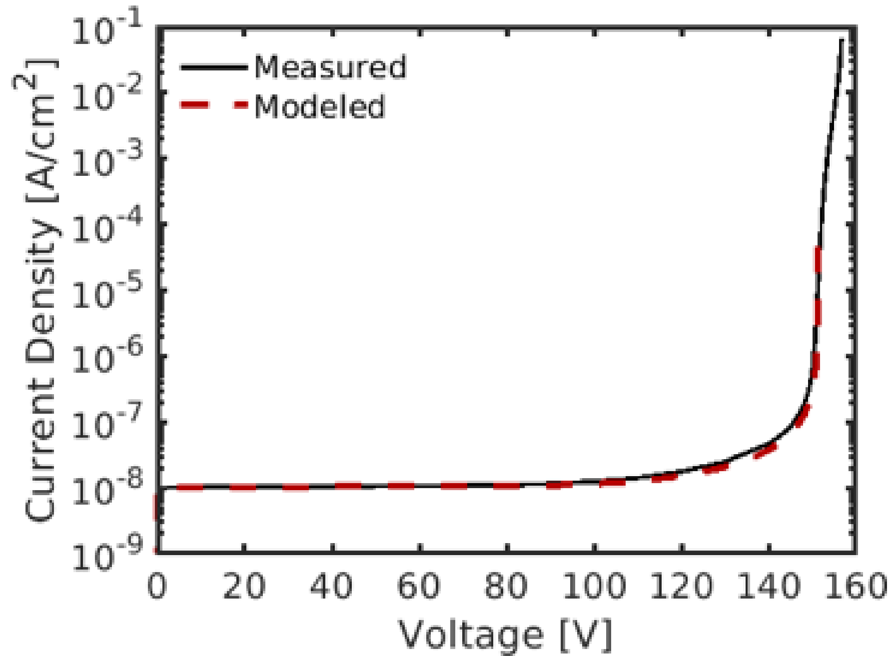

Figure 6.12: Measured and modeled with impact ionization coefficients current-voltage characteristic of a 4H-SiC $p-i-n$ diode. The simulation was performed with Synopsys TCAD, a commercial simulator into which was incorporated impact ionization coefficients celebrated in this work.

improved modeling.

6.4 Conclusion, Key Contributions and Future Work

The advances in electronics observed in the 20th century have changed how humans interact with themselves and the world. The use of electrical systems in conjunction with mechanical machines has tremendously improved human living standards and productivity. Initially conceived for radios and televisions, electronics devices have perfected over time and are present across the spectrum from low- to high-energy systems. The use of machinery for meeting the increasing needs of a growing population has resulted in problems of energy shortage and environmental concerns. Developing efficient electronics systems with high power density is a viable solution for reducing greenhouse gas emissions and the efficient use of available resources of

energy. Because of their properties, wide- and ultrawide-bandgap semiconductors have gained a lot of attention from the research community for the past decades as great candidates for the fabrication of power electronic devices. Compared to silicon, materials with a large bandgap can operate at much higher temperatures, reducing the need for cooling requirements. Their critical field and saturation velocity are much higher, enabling high-speed operations. Also, large bandgap materials allow the fabrication of devices with a high power density and more efficiency.

6.4.1 Contributions

Compared to silicon, however, wide- and ultrawide-bandgap materials are not well matured, and the understanding of those materials is still limited by several factors such as the ability to grow good quality materials, doping-related challenges, and fabrication challenges. To better understand the power performance of wide- and ultrawide-bandgap semiconductors, this work investigated the on-resistance versus breakdown voltage limits of WBG and UWBG materials for power electronics application as a function of the temperature. Instead of using an empirical formula for the trade-offs between the on-resistance and the breakdown voltage, the calculations considered the incomplete activation and ionization of dopants for an improved evaluation of the on-resistance and impact ionization coefficients for breakdown voltage calculations.

Investigation results for p-type doped 4H-SiC substrates showed that ion implantation (as opposed to epitaxial growth) could increase the substrate resistivity by a factor of ten, resulting in deteriorated on-resistance limits. The incomplete ionization of dopants was investigated in substrates, junctions at zero bias, and junctions subjected to reverse biases using the Poisson equation. For Uniformly doped substrates in equilibrium, the Poisson equation simplifies to the

charge neutrality equation, and the temperature dependence of dopant ionization was investigated. The ionization energy of dopants was modeled as a function of the doping concentration, and results showed that materials with high ionization energy, such as diamond, could have their on-resistance three order of magnitude larger than that expected if dopants were fully ionized. For junctions, the electric profile was calculated as a function of the temperature, and it was observed that because of field-assisted ionization, the incomplete ionization of dopant was less severe in the space charge regions and more prominent quasi-neutral regions. Also, because of field-assisted ionization, electric field profiles calculated with the depletion approximation and the assumption of 100% ionization were similar to electric field profiles calculated with an account of incomplete ionization.

The concentration of free carriers was obtained with the study of incomplete ionization. It was found that because of their large bandgap, in reverse bias, carriers are less likely to gain enough energy via lucky drift to initiate avalanche breakdown, prompting questions on the origin of carriers for avalanche breakdown in the dark. Deep level transient spectroscopy was employed to study deep traps in 4H-SiC $p-i-n$ structures. The extracted density of deep levels and the extracted temperature dependence of their emission time constant suggested that generation-recombination centers in materials contribute to background currents through a succession of emission and capture processes. The series resistance, the total resistance, and the non-ideality factors extracted from forward I-V characteristics measured on 4H-SiC $p-i-n$ diodes as a function of the temperature showed the effects of incomplete ionization. Also, the measured capacitance was modeled, and the extracted effective doping concentrations in the depletion region were similar to that obtained theoretically.

The calculated electric field profile was essential for evaluating the temperature depen-

dence of impact ionization coefficients modeled with a modified Thornber expression. This work calibrated impact ionization coefficients based on measured coefficients reported in the literature and measured multiplication and breakdown voltages. Theoretical breakdown voltages were calculated for $p - i - n$ diodes as a function of the i-layer thickness and doping concentration. The calculation showed the existence of optimum structures suitable for assessing the breakdown voltage versus on-resistance limits.

Breakdown voltage calculation using impact ionization coefficients showed that materials with a larger bandgap have higher ionization threshold energy and consequently lower impact ionization coefficients at a given electric field. Materials with low impact ionization coefficients can block larger voltages with thinner thickness. For $p - i - n$ diodes, it was found that the breakdown voltage increases with the i-layer thickness and reduces with the i-layer doping concentration. Studies of the breakdown voltage as a function of the i-layer thickness revealed the existence of an optimum thickness at which the breakdown voltage ceases to increase with the i-layer thickness. It was found that the optimum thickness and the corresponding optimum doping and breakdown voltage form a unique trio, and the set of such trio defines the on-resistance versus breakdown voltage limits of a material. The ability of a material to block large voltages also depends on the minimum achievable doping concentration (the doping floor), which limits the maximum breakdown voltage.

Temperature studies have indicated that the on-resistance results from trade-offs between the enhanced ionization of dopants and mobility deterioration. For wide bandgap semiconductors with reasonable ionization energy, the temperature degrades the material's performance; however, for some of the ultrawide-bandgap semiconductors with high ionization energy (Diamond, for example), the on-resistance was found to decrease with the temperature. Experimental studies

revealed that at low temperatures, the breakdown voltage decreases with the increase of temperature because the incomplete ionization of the dopants results in lower internal fields. It was also observed that at elevated temperature, the breakdown voltage increases with the temperature due to the growing population of phonons which enhances carriers' scattering, reduces their carriers' energy, and decreases the practical values of impact ionization coefficients.

Previous reports have shown that accounting for incomplete ionization is crucial for improving the accuracy of semiconductors' power limits. In addition to the study of incomplete ionization, this work has not assumed a constant value for the critical field. Instead, the critical field was obtained as a by-product of breakdown voltage calculations and was modeled as a function of the doping concentration and drift layer thickness. The main findings of this work rely on existing values of impact ionization coefficients. As demonstrated in this work, knowledge of those coefficients is paramount for the performance predictions of power devices. It can be said that the maturity of a given material relies upon the accuracy of its impact ionization coefficients. Those coefficients are paramount because they are the products of micro-scale quantum phenomena happening at the device physics level, and they are also the primary source driving the devices' performance observed at the macro-scale. As important as they are, there are numerous challenges related to establishing accurate values of impact ionization coefficients.

Impact ionization coefficients are commonly modeled as a function of the electric field, but the ability of a carrier to engage in an impact ionization collision depends on its energy. A low energy carrier in a high electric field region cannot trigger an impact ionization collision at the observed location; however, with sufficiently high energy, carriers can impact ionize even in low electric field regions. It would be more accurate to model impact ionization coefficients as a function of carriers' energy; however, this is hardly achievable because, unlike the electric

field, carriers' energy is not a local property of the material and constantly change depending on carriers' history. While for small-scale systems, the problem of electric field and carrier's energy needs to be addressed, for thicker devices (power electronics) that do not suffer from the dark space problem, it is convenient and reasonable to model impact ionization coefficients as a function of the local electric field because those coefficients are a statistical average of how many impact ionization collisions are encountered when a carrier travel one centimeter of the material.

6.4.2 Future Work

New considerations are likely necessary for modeling impact ionization coefficients for microelectronics and low-power systems. For power electronics, modeling impact ionization coefficients as a function of the local field is acceptable; however, results from this work suggest that it could be more accurate to include a doping dependence in the modeling of impact ionization coefficients, i.e., $\alpha(\xi, T, N)$. For $Al_xGa_{1-x}N$ there are additional challenges because coefficients should account for both doping and alloy composition variations. The results obtained in this work relied closely on impact ionization coefficients existing in the literature, and the need to get more accurate values of impact ionization coefficients has been demonstrated. Though it may require a lot of computational and experimental resources, it is worth converging efforts for more detailed studies of impact ionization coefficients because they inform on device performance and reinforce understanding of materials. As demonstrated in this work, impact ionization coefficients are essential for calculating the critical field and the breakdown voltage, which in turn helps captures the power density of materials. They are also crucial for the simulation of the current-voltage characteristics of devices. Efforts to predict impact ionization coefficients from ab-initio

studies, such as solving the Boltzmann transport equation or Monte Carlo simulations, require in-depth studies of fundamental material properties. Such exercise requires accurate knowledge of the energy band diagram to extract the dispersion relation, the effective masses, and other parameters necessary to describe carrier-lattice interactions.

Chapter A: Equations for Trapezoidal Field Profile of Punch Through $p-i-n$ Diodes

When the doping concentration in the i-layer or its the thickness are sufficiently small, the electric field profile in the $p-i-n$ diode is trapezoidal as seen below.

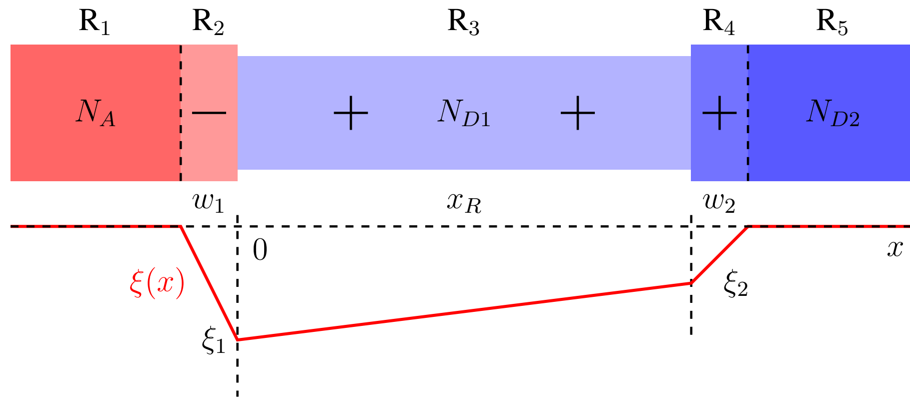

Figure A.1: Trapezoidal field profile (not drawn to scale) in a $p-i-n$ diode.

The slope of the electric field in the p^+, n^-, and n^+ regions are given by m_1, m_2, and m_3, respectively; those slopes can be expressed as

$$m_1 = \frac{qN_A}{\epsilon}, m_2 = \frac{qN_{D1}}{\epsilon}, \text{ and } m_3 \approx \frac{qN_{D2}}{\epsilon} \tag{A.1}$$

The charge neutrality equation is

$$w_1 N_A \approx x_R N_{D1} + x_2 N_{D2} \longrightarrow w_1 \approx x_R \frac{N_{D1}}{N_A} + w_2 \frac{N_{D2}}{N_A}. \tag{A.2}$$

The total built-in potential with an applied bias V_A, a $p^+ - n^-$ built-in potential V_{bi1}, and a $n^- - n^+$ built in potential V_{bi2} is

$$V_T = V_A + V_{bi1} + V_{bi2} \approx \frac{1}{2}\xi_1(w_1 + x_R) + \frac{1}{2}\xi_2(w_2 + x_R), \tag{A.3}$$

where ξ_1 and ξ_2 are the peak electric field at the $p^+ - n^-$ and $n^- - n^+$ interfaces, respectively; those peaks field are expressed as $\xi_1 = m_1 w_1$ and $\xi_2 = m_3 w_2$. The total built-in potential, V_T, is such that

$$\begin{aligned}
2V_T &\approx m_1 w_1^2 + m_1 w_1 x_R + m_3 w_2^2 + m_3 w_2 x_R \\
&\approx m_1 \left(x_R \frac{N_{D1}}{N_A} + w_2 \frac{N_{D2}}{N_A} \right)^2 + m_1 \left(x_R \frac{N_{D1}}{N_A} + w_2 \frac{N_{D2}}{N_A} \right) x_R + m_3 w_2^2 + m_3 w_2 x_R \\
&\approx m_1 x_R^2 \left(\frac{N_{D1}}{N_A} \right)^2 + 2 m_1 x_R \left(\frac{N_{D1}}{N_A} \right) w_2 \left(\frac{N_{D2}}{N_A} \right) + m_1 w_2^2 \left(\frac{N_{D2}}{N_A} \right)^2 \\
&+ m_1 x_R^2 \left(\frac{N_{D1}}{N_A} \right) + m_1 x_R w_2 \left(\frac{N_{D2}}{N_A} \right) + m_3 w_2^2 + m_3 w_2 x_R
\end{aligned} \tag{A.4}$$

Therefore, the quadratic equation in w_2 is

$$\begin{aligned}
&w_2^2 \left[m_1 \left(\frac{N_{D1}}{N_A} \right)^2 + m_3 \right] + w_2 \left[2 m_1 x_R \frac{N_{D1}}{N_A} \frac{N_{D2}}{N_A} + m_1 x_R \frac{N_{D2}}{N_A} + m_3 x_R \right] \\
&\left[m_1 x_R^2 \left(\frac{N_{D1}}{N_A} \right)^2 + m_1 x_R^2 \frac{N_{D1}}{N_A} - 2V_T \right] \approx 0
\end{aligned} \tag{A.5}$$

Substituting for the slopes, The three parameters for the quadratic are

$$A = \frac{qN_A}{\epsilon}\left(\frac{N_{D2}}{N_A}\right)^2 + \frac{qN_{D2}}{\epsilon} = \frac{qN_{D2}}{\epsilon}\left(\frac{N_{D2}+N_A}{N_A}\right) \tag{A.6}$$

$$B = x_R\left(2\frac{qN_A}{\epsilon}\frac{N_{D1}}{N_A}\frac{N_{D2}}{N_A} + \frac{qN_A}{\epsilon}\frac{N_{D2}}{N_A} + \frac{qN_{D2}}{\epsilon}\right) = 2x_R\frac{qN_{D2}}{\epsilon}\left(\frac{N_{D1}+N_A}{N_A}\right) \tag{A.7}$$

$$C = \frac{qN_A}{\epsilon}x_R^2\frac{N_{D1}}{N_A}\left(\frac{N_{D1}+N_A}{N_A}\right) - 2V_T = \frac{qN_{D1}}{\epsilon}x_R\left(\frac{N_{D1}+N_A}{NA}\right) - 2V_T \tag{A.8}$$

Note that this derivation applies to trapezoidal field profiles with the punch-throughs terminating in the cladding layers. There are cases where the punch-throughs extend to the contact; one or both of the cladding layers are fully depleted. The charge neutrality equation still applies and leads to quadratic equations like the one derived above.

Bibliography

[1] The nobel prize in physics 1956.

[2] Lillian Hoddeson. The discovery of the point-contact transistor. *Historical Studies in the Physical Sciences*, 12(1):41–76, 1981. doi:10.2307/27757489.

[3] 1948: Conception of the junction transistor.

[4] U.S. Department of Energy: Energy Efficiency and Renewable Energy. How do all-electric cars work. Accessed on May 14th[Online], 2018.

[5] G. Pennington and N. Goldsman. Simulation of electron transport in (0001) and $(11\bar{2}0)$ 4H-SiC inversion layers. *Journal of Applied Physics*, 106(6):1063, July 2009. doi:10.1063/1.3212970.

[6] G. Pennington and N. Goldsman. Self-consistent calculations for n-type hexagonal SiC inversion layers. *Journal of Applied Physics*, 95(8):4223–4234, March 1998.

[7] R. Mickevičius and J. H. Zhao. Monte carlo study of electron transport in SiC. *Journal of Applied Physics*, 83(6):3161, June 2004. doi:10.1063/1.367073.

[8] Ke Zeng and Srabanti Chowdhury. Designing beveled edge termination in GaN vertical p-i-n diode-bevel angle, doping, and passivation. *IEEE Transactions on Electron Devices*, 67(6):2457–2462, 2020. doi:10.1109/TED.2020.2987040.

[9] B. McEwen, I. Mahaboob, E. Rocco, K. Hogan, V. Meyers, R. Green, F. Nouketcha, T. Murray, V. Kaushik, A. Lelis, et al. Investigation of the effects of forming gas annealing on Al_2O_3/GaN interface. *Journal of Electronic Materials*, 50(1):80–84, 2021.

[10] B Jayant Baliga. *Gallium nitride and silicon carbide power devices*. World Scientific, 2017.

[11] J. Y. Tsao, S. Chowdhury, M. A. Hollis, D. Jena, N. M. Johnson, K. A. Jones, R. J. Kaplar, S. Rajan, C. G. Van de Walle, E. Bellotti, C. L. Chua, R. Collazo, M. E. Coltrin, et al. Ultrawide-bandgap semiconductors: Research opportunities and challenges. *Advanced Electronic Materials*, 4(1):1600501, 2018. doi:10.1002/aelm.201600501.

[12] Ogyun Seok and Min-Woo Ha. Effects of incomplete ionization on forward current–voltage characteristics of p-type diamond schottky barrier diodes based on numerical simulation. *Japanese Journal of Applied Physics*, 60(SC):SCCE08, 2021. doi:10.35848/1347-4065/abf2a7.

[13] Nikolai Teofilov. *Optical investigations on the wide bandgap semiconductors diamond and aluminumnitride*. PhD thesis, Universität Ulm, 2007.

[14] Y. Katamune, D. Mori, D. Arikawa, A. Izumi, T. Shimaoka, K. Ichikawa, and S. Koizumi. n-type doping of diamond by hot-filament chemical vapor deposition growth with phosphorus incorporation. *Applied Physics A*, 126(11):1–6, 2020. doi:10.1007/s00339-020-04060-w.

[15] H. Aida, K. Nishiguchi, H. Takeda, N. Aota, K. Sunakawa, and Y. Yaguchi. Growth of β-Ga_2O_3 single crystals by the edge-defined, film fed growth method. *Japanese Journal of Applied Physics*, 47(11R):8506, 2008. doi:10.1109/TED.2007.906966.

[16] M. Higashiwaki, A. Kuramata, H. Murakami, and Y. Kumagai. State-of-the-art technologies of gallium oxide power devices. *Journal of Physics D: Applied Physics*, 50(33):333002, 2017. doi:10.1088/1361-6463/aa7aff.

[17] Jiancheng Yang, Fan Ren, Marko Tadjer, S. J. Pearton, and A. Kuramata. 2300v reverse breakdown voltage Ga_2O_3 schottky rectifiers. *ECS Journal of Solid State Science and Technology*, 7(5):Q92, 2018. doi:10.1149/2.0241805jss.

[18] Yuichi Oshima, Encarnación G Víllora, and Kiyoshi Shimamura. Halide vapor phase epitaxy of twin-free α-Ga_2O_3 on sapphire (0001) substrates. *Applied Physics Express*, 8(5):055501, 2015. doi:10.7567/apex.8.055501.

[19] Yuichi Oshima, Encarnación G V$\acute{\ell}$llora, and Kiyoshi Shimamura. Quasi-heteroepitaxial growth of β-Ga_2O_3 on off-angled sapphire (0 0 0 1) substrates by halide vapor phase epitaxy. *Journal of Crystal Growth*, 410:53–58, 2015. doi:10.1016/j.jcrysgro.2014.10.038.

[20] H. Murakami, K. Nomura, K. Goto, K. Sasaki, K. Kawara, Q. T. Thieu, R. Togashi, Y. Kumagai, M. Higashiwaki, A. Kuramata, et al. Homoepitaxial growth of β-Ga_2O_3 layers by halide vapor phase epitaxy. *Applied Physics Express*, 8(1):015503, 2014. doi:10.7567/apex.8.015503.

[21] K. Goto, K. Konishi, H. Murakami, Y. Kumagai, B. Monemar, M. Higashiwaki, A. Kuramata, and S. Yamakoshi. Halide vapor phase epitaxy of Si doped β-Ga_2O_3 and its electrical properties. *Thin Solid Films*, 666:182–184, 2018. doi:10.1016/j.tsf.2018.09.006.

[22] Kazushiro Nomura, Ken Goto, Rie Togashi, Hisashi Murakami, Yoshinao Kumagai, Akito Kuramata, Shigenobu Yamakoshi, and Akinori Koukitu. Thermodynamic study of β-Ga_2O_3 growth by halide vapor phase epitaxy. *Journal of crystal growth*, 405:19–22, 2014. doi:10.1016/j.jcrysgro.2014.06.051.

[23] Keita Konishi, Ken Goto, Rie Togashi, Hisashi Murakami, Masataka Higashiwaki, Akito Kuramata, Shigenobu Yamakoshi, Bo Monemar, and Yoshinao Kumagai. Comparison of O_2 and H_2O as oxygen source for homoepitaxial growth of β-Ga_2O_3 layers by halide vapor phase epitaxy. *Journal of Crystal Growth*, 492:39–44, 2018. doi:10.1016/j.jcrysgro.2018.04.009.

[24] M. Higashiwaki, K. Konishi, K.and Sasaki, K. Goto, K. Nomura, Q. T. Thieu, R. Togashi, H. Murakami, Y. Kumagai, B. Monemar, et al. Temperature-dependent capacitance-voltage and current-voltage characteristics of Pt/Ga_2O_3 (001) schottky barrier diodes fabricated on n^--Ga_2O_3 drift layers grown by halide vapor phase epitaxy. *Applied Physics Letters*, 108(13):133503, 2016. doi:10.1063/1.4945267.

[25] Hiu Yung Wong and Armand C. Fossito Tenkeu. Advance TCAD simulation and calibration of gallium oxide vertical transistors. *ECS Journal of Solid State Science and Technology*, 9(3):035003, Feb 2020. doi:10.1149/2162-8777/ab7673.

[26] Wesley Ooi Tat Lung, Cheang Pei Ling, You Ah Heng, and Chan Yee Kit. High field carrier transport properties of $Al_{0.45}Ga_{0.55}N$. *Malaysian Journal of Fundamental and Applied Sciences*, 16(5):519–523, 2020. doi:10.11113/mjfas.v16n5.1753.

[27] H. He, R. Orlando, M. A. Blanco, R. Pandey, E. Amzallag, I. Baraille, and Michel Rérat. First-principles study of the structural, electronic, and optical properties of Ga_2O_3in its monoclinic and hexagonal phases. *Physical Review B*, 74(19):195123, 2006. doi:10.1103/PhysRevB.74.195123.

[28] Cong-Cong Li, Ming Gong, Xiang-Don Chen, Shen Li, Bo-Wen Zhao, Yang Dong, Guang-Can Guo, and Fang-Wen Sun. Temperature dependent energy gap shifts of single color center in diamond based on modified varshni equation. *Diamond and Related Materials*, 74:119–124, 2017. doi:10.1016/j.diamond.2017.03.002.

[29] Yuan Taur and Tak H. Ning. *Fundamentals of modern VLSI devices*. Cambridge university press, 2013.

[30] Yuewei Zhang and James S. Speck. Importance of shallow hydrogenic dopants and material purity of ultra-wide bandgap semiconductors for vertical power electron devices. *Semiconductor Science and Technology*, 35(12):125018, 2020. doi:10.1088/1361-6641/abbba6.

[31] C. Darmody and N. Goldsman. Incomplete ionization in aluminum-doped 4H-silicon carbide. *Journal of Applied Physics*, 126(14):145701, oct 2019. doi:10.1063/1.5120707.

[32] Heiko Steinkemper, Michael Rauer, Pietro Altermatt, Friedemann D Heinz, Christian Schmiga, and Martin Hermle. Adapted parameterization of incomplete ionization in aluminum-doped silicon and impact on numerical device simulation. *Journal of Applied Physics*, 117(7):074504, 2015. doi:10.1063/1.4913255.

[33] N. Donato and F. Udrea. Static and dynamic effects of the incomplete ionization in superjunction devices. *IEEE Transactions on Electron Devices*, 65(10):4469–4475, 2018. doi:10.1109/TED.2018.2867058.

[34] Y. Arakawa, K. Ueno, H. Imabeppu, A. Kobayashi, J. Ohta, and H. Fujioka. Electrical properties of Si-doped GaN prepared using pulsed sputtering. *Applied Physics Letters*, 110(4):042103, 2017. doi:10.1063/1.4975056.

[35] Aurélien Maréchal, Nicolas Rouger, J-C Crebier, Julien Pernot, Satoshi Koizumi, Tokuyuki Teraji, and Etienne Gheeraert. Model implementation towards the prediction of j (v) characteristics in diamond bipolar device simulations. *Diamond and related materials*, 43:34–42, 2014. doi:10.1016/j.diamond.2014.01.009.

[36] Yoshitaka Taniyasu, Makoto Kasu, and Toshiki Makimoto. Electrical conduction properties of n-type Si-doped AlN with high electron mobility (>100 $cm^2v^{-1}s^{-1}$). *Applied physics letters*, 85(20):4672–4674, 2004. doi:10.1063/1.1824181.

[37] H. Katayama-Yoshida, T. Nishimatsu, T. Yamamoto, and N. Orita. Codoping method for the fabrication of low-resistivity wide band-gap semiconductors in p-type GaN, p-type AlN and n-type diamond: prediction versus experiment. *Journal of Physics: Condensed Matter*, 13(40):8901, 2001. doi:10.1088/0953-8984/13/40/304.

[38] Richard S. Muller, Theodore I. Kamins, and Mansun Chan. *Device electronics for integrated circuits*. John Wiley and Sons, 2003.

[39] Hiroki Wakimoto, Takashi Matsumoto, Koji Yano, and Tsutomu Muranaka. Leakage current analysis of silicon diode with anode activated by furnace annealing or laser annealing using deep level transient spectroscopy. *AIP Advances*, 10(12):125301, 2020. doi:10.1063/5.0024744.

[40] Ioffe Institute. Silicon carbide: Recombination parameters. Accessed on June 20th[Online].

[41] M. Simon Sze and K. Kwok Ng. *Physics of semiconductor devices*. John wiley & sons, 2006.

[42] A. V. Kuchuk, P. Borowicz, M. Wzorek, M. Borysiewicz, R. Ratajczak, K. Golaszewska, E. Kaminska, V. Kladko, and A. Piotrowska. Ni-based ohmic contacts to n-type 4H-SiC: The formation mechanism and thermal stability. *Advances in Condensed Matter Physics*, 2016, 2016. doi:10.1155/2016/9273702.

[43] Ziwei Zhou, Weiwei He, Zhenzhong Zhang, Jun Sun, Adolf Schöner, and Zedong Zheng. Characteristics of Ni-based ohmic contacts on n-type 4H-SiC using different annealing methods. *Nanotechnology and Precision Engineering*, 4(1):013006, 2021. doi:10.1063/10.0003763.

[44] COOLCAD ELECTRONICS. UV Avalanche Photodiodes (APD) and Avalanche Photodetectors. Accessed on June 24th[Online].

[45] J. F. Barbot, C. Blanchard, E. Ntsoenzok, and J. Vernois. Defect levels in n-silicon after high energy and high dose implantation of proton. *Materials Science and Engineering: B*, 36(1-3):81–84, 1996. doi:10.1016/0921-5107(95)01281-8.

[46] W. Götz and N. M Johnson. Characterization of dopants and deep level defects in gallium nitride. In *Semiconductors and Semimetals*, volume 57, pages 185–207. Elsevier, 1999. doi:10.1016/S0080-8784(08)62618-6.

[47] D. K. Schroder. *Semiconductor Material and Device Characterization*. Wiley, New York, 1990.

[48] T. A. G. Eberlein, R. Jones, and P. R. Briddon. Z_1/Z_2 defects in 4H-SiC. *Physical review letters*, 90(22):225502, 2003. doi:10.1103/PhysRevLett.90.225502.

[49] Koutarou Kawahara, Xuan Thang Trinh, Nguyen Tien Son, Erik JanzÈn, Jun Suda, and Tsunenobu Kimoto. Quantitative comparison between $Z_{1/2}$ center and carbon vacancy in 4H-SiC. *Journal of Applied Physics*, 115(14):143705, 2014. doi:10.1063/1.4871076.

[50] T. Umeda, Y. Ishitsuka, J. Isoya, N. T. Son, Erik Janzén, N. Morishita, T. Ohshima, H. Itoh, and A. Gali. EPR and theoretical studies of negatively charged carbon vacancy in 4H-SiC. *Physical review B*, 71(19):193202, 2005. doi:10.1103/PhysRevB.71.193202.

[51] C. G. Hemmingsson, N. T. Son, .A Ellison, J. Zhang, and E Janzén. Negative-U centers in 4H silicon carbide. *Physical Review B*, 58(16):R10119, 1998. doi:10.1103/PhysRevB.58.R10119.

[52] S. Sasaki, K. Kawahara, G. Feng, G. Alfieri, and T. Kimoto. Major deep levels with the same microstructures observed in n-type 4H-SiC and 6H-SiC. *Journal of Applied Physics*, 109(1):013705, 2011. doi:10.1063/1.3528124.

[53] F. C. Beyer, C. G. Hemmingsson, Stefano Leone, Y-C Lin, A. Gällström, Anne Henry, and Erik Janzén. Deep levels in iron doped n-and p-type 4H-SiC. *Journal of Applied Physics*, 110(12):123701, 2011. doi:10.1063/1.3669401.

[54] Nguyen Tien Son, Xuan Thang Trinh, Lars Sundnes Løvlie, Bengt Gunnar Svensson, K Kawahara, J Suda, T Kimoto, T Umeda, J Isoya, T Makino, et al. Negative-U system of carbon vacancy in 4H-SiC. *Physical review letters*, 109(18):187603, 2012. doi:10.1103/PhysRevLett.109.187603.

[55] Aurangzeb K. and Yamaguchi M. Deep Level Transient Spectroscopy: A Powerful Experimental Technique for Understanding the Physics and Engineering of Photo-Carrier Generation, Escape, Loss and Collection Processes in Photovoltaic Materials. In Leonid A. Kosyachenko, editor, *Solar Cells*, chapter 7. IntechOpen, Rijeka, 2015. doi:10.5772/59419.

[56] SEMETROL LLC. Deep Level Transcient Spectroscopy. Accessed on June 20th[Online].

[57] F. Nouketcha, Y. Cui, A. Lelis, R. Green, C. Darmody, J. Schuster, and N. Goldsman. Investigation of wide-and ultrawide-bandgap semiconductors from impact-ionization coefficients. *IEEE Transactions on Electron Devices*, 67(10):3999–4005, 2020. doi:10.1109/TED.2020.3009622.

[58] Gary Wayne Pennington. *Electron Transport Simulations and Band Structure Calculations of New Materials for Electronics: Silicon Carbide and Carbon Nanotubes.* PhD thesis, University of Maryland, Department of Electrical and Computer Engineering, College Park, 2003.

[59] N. Goldsman and C. Darmody. *Semiconductor and Device Physics: A Concise Introduction*. n.p., 2001.

[60] G. E. Stillman and C. M. Wolfe. Avalanche photodiodes. In *Semiconductors and semimetals*, volume 12, pages 291–393. Elsevier, 1977. doi:10.1016/S0080-8784(08)60150-7.

[61] M. H. Woods, W. C. Johnson, and M. A. Lampert. Use of a schottky barrier to measure impact ionization coefficients in semiconductors. *Solid-State Electronics*, 16(3):381–394, 1973. doi:10.1016/0038-1101(73)90013-0.

[62] A. G. Chynoweth. Chapter 4 Charge Multiplication Phenomena. In R.K. Willardson and Albert C. Beer, editors, *Semiconductors and semimetals*, volume 4, pages 263–325. Elsevier, 1968. doi:10.1016/S0080-8784(08)60345-2.

[63] G. Beni and F. Capasso. Effect of carrier drift velocities on measured ionization coefficients in avalanching semiconductors. *Physical Review B*, 19(4):2197–2203, 1979. doi:10.1103/PhysRevB.19.2197.

[64] Y. Okuto and C. R. Crowell. Ionization coefficients in semiconductors: A nonlocalized property. *Physical review B*, 10(10):4284, 1974. doi:10.1103/PhysRevB.10.4284.

[65] C. A. Lee, R. A. Logan, R. L. Batdorf, J. J. Kleimack, and W. Wiegmann. Ionization rates of holes and electrons in silicon. *Physical Review*, 134(3A):A761–A773, May 1964. doi:10.1103/PhysRev.134.A761.

[66] C. A. Lee, R. L. Batdorf, W. Wiegmann, and G. Kaminsky. Time dependence of avalanche processes in silicon. *Journal of Applied Physics*, 38(7):2787–2796, 1967. doi:10.1063/1.1710004.

[67] S. Nida and U. Grossner. High-temperature impact-ionization model for 4H-SiC. *IEEE Transactions on Electron Devices*, 66(4):1899–1903, apr 2019. doi:10.1109/TED.2019.2899285.

[68] T. Hatakeyama, T. Watanabe, T. Shinohe, K. Kojima, K. Arai, and N. Sano. Impact ionization coefficients of 4H silicon carbide. *Applied Physics Letters*, 85(8):1380–1382, 2004. doi:10.1063/1.1784520.

[69] Hiroki Niwa, Jun Suda, and Tsunenobu Kimoto. Impact ionization coefficients in 4H-SiC toward ultrahigh-voltage power devices. *IEEE Transactions on Electron Devices*, 62(10):3326–3333, 2015. doi:10.1109/TED.2015.2466445.

[70] Sealy John Townsend. *Electricity in gases*. Ripol Klassik, 1915.

[71] Gene A. Baraff. Distribution functions and ionization rates for hot electrons in semiconductors. *Physical Review*, 128(6):2507–2517, Dec 1962. doi:10.1103/PhysRev.128.2507.

[72] Y. Okuto and C. R. Crowell. Threshold energy effect on avalanche breakdown voltage in semiconductor junctions. *Solid-State Electronics*, 18(2):161–168, 1975. doi:10.1016/0038-1101(75)90099-4.

[73] Y. Okuto and C. R. Crowell. Energy-conservation considerations in the characterization of impact ionization in semiconductors. *Physical Review B*, 6(8):3076–3081, Oct 1972. doi:10.1103/PhysRevB.6.3076.

[74] N. Goldsman, Y. Wu, and J. Frey. Efficient calculation of ionization coefficients in silicon from the energy distribution function. *Journal of Applied Physics*, 68(3):1075–1081, April 1990. doi:10.1063/1.346747.

[75] A. Hiraiwa and H. Kawarada. Figure of merit of diamond power devices based on accurately estimated impact ionization processes. *Applied Physics Letters*, 114(3):034506, July 2013. doi:10.1063/1.4816312.

[76] Krishnendu Ghosh and Uttam Singisetti. Impact ionization in β-Ga_2O_3. *Journal of Applied Physics*, 124(8):085707, 2018. doi:10.1063/1.5034120.

[77] C. Bulutay. Electron initiated impact ionization in AlGaN alloys. *Semiconductor Science and Technology*, 17(10):L59–L62, 2002. doi:10.1088/0268-1242/17/10/102.

[78] C. L. Anderson and C. R. Crowell. Threshold energies for electron-hole pair production by impact ionization in semiconductors. *Phys. Rev. B*, 5:2267–2272, Mar 1972. doi:10.1103/PhysRevB.5.2267.

[79] W. N. Grant. Electron and hole ionization rates in epitaxial silicon at high electric fields. *Solid-State Electronics*, 16(10):1189–1203, 1973. doi:10.1016/0038-1101(73)90147-0.

[80] K. K. Thornber. Applications of scaling to problems in high-field electronic transport. *Journal of Applied Physics*, 52(1):279–290, 1981. doi:10.1063/1.328490.

[81] Josef Lutz, Heinrich Schlangenotto, Uwe Scheuermann, and Rik De Doncker. *Semiconductor power devices, Physics Characteristics, Reliability*, volume 2. Springer, Berlin, Heidelberg, 2011. doi:10.1007/978-3-642-11125-9.

[82] Nan Ma, Nicholas Tanen, Amit Verma, Zhi Guo, Tengfei Luo, Huili Xing, and Debdeep Jena. Intrinsic electron mobility limits in β-Ga_2O_3. *Applied Physics Letters*, 109(21):212101, 2016. doi:10.1063/1.4968550.

[83] Nazareno Donato. *Modeling and Design of Diamond Power Semiconductor Devices*. PhD thesis, St Edmund's College, University of Cambridge, Department of Engineering, jul 2019.

[84] I. Silvaco. Atlas user's manual device simulation software. *Santa Clara, CA*, 2010.

[85] S. Wang, N. Goldsman, and K. Hennacy. Calculation of impact ionization coefficients with a third-order legendre polynomial expansion of the distribution function. *Journal of Applied Physics*, 71(4):1815–1822, Nov 1991. doi:10.1063/1.351188.

[86] E. Bellotti and F. Bertazzi. A numerical study of carrier impact ionization in $Al_xGa_{1-x}N$. *Journal of Applied Physics*, 111(10):103711, 2012. doi:10.1063/1.4719967.

[87] A. Akturk, N. Goldsman, S. Potbhare, and A. Lelis. High field density-functional-theory based monte carlo: 4H-SiC impact ionization and velocity saturation. *Journal of Applied Physics*, 105(3):033703, 2009. doi:10.1063/1.3074107.

[88] A. Merve. *Measurement of Impact Ionization Coefficients in GaN*. PhD thesis, Raleigh, North Carolina, 2012.

[89] Dong Ji, Burcu Ercan, and Srabanti Chowdhury. Experimental determination of impact ionization coefficients of electrons and holes in gallium nitride using homojunction structures. *Applied Physics Letters*, 115(7):073503, 2019. doi:10.1063/1.5099245.

[90] K. Roze, N. A. Bannov, K. W. Kim, W. C. Holton, and M. A. Littlejohn. Temperature dependence of impact ionization coefficients in p-Si. *Journal of Applied Physics*, 83(9):4988–4990, 1998. doi:10.1063/1.367303.

[91] M. Ershov and V. Ryzhii. Temperature dependence of the electron impact ionization coefficient in silicon. *Semiconductor Science and Technology*, 10(2):138–142, Feb 1995. doi:10.1088/0268-1242/10/2/003.

[92] D. J. Massey, J. P. R. David, and G. J. Rees. Temperature dependence of impact ionization in submicrometer silicon devices. *IEEE Transactions on Electron Devices*, 53(9):2328–2334, 2006. doi:10.1109/TED.2006.881010.

[93] D. R. Decker and C. N. Dunn. Temperature dependence of carrier ionization rates and saturated velocities in silicon. *Journal of Electronic Materials*, 4(3):527–547, 1975. doi:10.1007/BF02666234.

[94] R. Van Overstraeten and H. De Man. Measurement of the ionization rates in diffused silicon p-n junctions. *Solid-State Electronics*, 13(5):583–608, May 1970. doi:10.1016/0038-1101(70)90139-5.

[95] R. Raghunathan and B. J. Baliga. Temperature dependence of hole impact ionization coefficients in 4H and 6H-SiC. *Solid-State Electronics*, 43(2):199–211, 1999. doi:10.1016/S0038-1101(98)00248-2.

[96] Y. Zhao, H. Niwa, and T. Kimoto. Impact ionization coefficients in 4H-SiC in a wide temperature range. *Japanese Journal of Applied Physics*, 58:018001, Nov 2019. doi:10.7567/1347-4065/aae985.

[97] T. Hatakeyama. Measurements of impact ionization coefficients of electrons and holes in 4H-SiC and their application to device simulation. *Physica Status Solidi (a)*, 206(10):2284–2294, 2009. doi:10.1002/pssa.200925213.

[98] A. O. Konstantinov, Q. Wahab, N. Nordell, and U. Lindefelt. Study of avalanche breakdown and impact ionization in 4H silicon carbide. *Journal of Electronic Materials*, 27(4):335–341, 1998. doi:10.1007/s11664-998-0411-x.

[99] B. K. Ng, John P. R. David, Richard C. Tozer, Graham J. Rees, Feng Yan, Jian H. Zhao, and Maurice Weiner. Nonlocal effects in thin 4H-SiC UV avalanche photodiodes. *IEEE Transactions on Electron Devices*, 50(8):1724–1732, 2003. doi:10.1109/TED.2003.815144.

[100] J. E. Green, W. S. Loh, A. R. J. Marshall, B. K. Ng, R. C. Tozer, J. P. R. David, S. I. Soloviev, and P. M. Sandvik. Impact ionization coefficients in 4H-SiC by ultralow excess noise measurement. *IEEE Transactions on Electron Devices*, 59(4):1030–1036, 2012. doi:10.1109/TED.2012.2185499.

[101] W. S. Loh, B. K. Ng, J. S. Ng, Stanislav I Soloviev, Ho-Young Cha, Peter M. Sandvik, C. Mark Johnson, and P. R. David. Impact ionization coefficients in 4H-SiC. *IEEE Transactions on Electron Devices*, 55(8):1984–1990, 2008. doi:10.1109/TED.2008.926679.

[102] Ayse zbek Merve. *Measurement of Impact Ionization Coefficients in GaN*. PhD thesis, North Carolina State University, 2012.

[103] S. J. Pearton, F. Ren, M. Tadjer, and J. Kim. Perspective: Ga_2O_3 for ultra-high power rectifiers and MOSFETS. *Journal of Applied Physics*, 124(22):220901, 2018. doi:10.1063/1.5062841.

[104] S. J. Rashid, A. Tajani, D. J. Twitchen, L. Coulbeck, F. Udrea, T. Butler, N. L. Rupesinghe, M. Brezeanu, Jan Isberg, A. Garraway, et al. Numerical parameterization of chemical-vapor-deposited (CVD) single-crystal diamond for device simulation and analysis. *IEEE Transactions on Electron Devices*, 55(10):2744–2756, 2008. doi:10.1109/TED.2008.2003225.

[105] E. Bellotti, F. Bertazzi, S. Shishehchi, M. Matsubara, and M. Goano. Theory of carriers transport in III-nitride materials: State of the art and future outlook. *IEEE Transactions on Electron Devices*, 60(10):3204–3215, 2013. doi:10.1109/TED.2013.2266577.

[106] Turgut Tut, Mutlu Gokkavas, Bayram Butun, Serkan Butun, Erkin Ulker, and Ekmel Ozbay. Experimental evaluation of impact ionization coefficients in $Al_xGa_{1-x}N$ based avalanche photodiodes. *Applied Physics Letters*, 89(18):183524, 2006. doi:10.1063/1.2385216.

[107] Narain D. Arora, John R. Hauser, and David J. Roulston. Electron and hole mobilities in silicon as a function of concentration and temperature. *IEEE Transactions on Electron Devices*, 29(2):292–295, Feb 1982. doi:10.1109/T-ED.1982.20698.

[108] Dionysios Stefanakis and Konstantinos Zekentes. TCAD models of the temperature and doping dependence of the bandgap and low field carrier mobility in 4H-SiC. *Microelectronic Engineering*, 116:65–71, 2014. doi:10.1016/j.mee.2013.10.002.

[109] T. T. Mnatsakanov, M. E. Levinshtein, L. I. Pomortseva, S. N. Yurkov, G. S. Simin, and M. A. Khan. Carrier mobility model for GaN. *Solid-State Electronics*, 47(1):111–115, 2003. doi:10.1016/S0038-1101(02)00256-3.

[110] Stanislav Vitanov. *Simulation of High Electron Mobility Transistors*. PhD thesis, Eingereicht an der Technischen Universität Wien Fakultät für Elektrotechnik und Informationstechnik, Celestijnenlaan 200d-bus 2417 3001 Leuven België, 12 2010.

[111] T. Kimoto and Y. Yonezawa. Current status and perspectives of ultrahigh-voltage SiC power devices. *Materials Science in Semiconductor Processing*, 78:43–56, May 2018. doi:10.1016/j.mssp.2017.10.010.

[112] F. Nouketcha, A. Lelis, R. Green, Y. Cui, C. Darmody, and N. Goldsman. Detailed study of breakdown voltage and critical field in wide bandgap semiconductors. In *2019 IEEE 7th Workshop on Wide Bandgap Power Devices and Applications (WiPDA)*, pages 200–207, 2019. doi:10.1109/WiPDA46397.2019.8998828.

[113] M. Higashiwaki, K. Sasaki, A. Kuramata, T. Masui, and S. Yamakoshi. Gallium oxide (Ga_2O_3) metal-semiconductor field-effect transistors on single-crystal β-Ga_2O_3 (010) substrates. *Applied Physics Letters*, 100(1):013504, 2012. doi:10.1063/1.3674287.

[114] M. Xiao, R. Zhang, D. Dong, H. Wang, and Y. Zhang. Design and simulation of GaN superjunction transistors with 2DEG channels and fin channels. *IEEE Journal of Emerging and Selected Topics in Power Electronics*, 7(3):1475–1484, 2019. doi:10.1109/JESTPE.2019.2912978.

[115] A. G. Baca, A. M. Armstrong, B. A. Klein, A. A. Allerman, E. A. Douglas, and R. J. Kaplar. Al-rich AlGaN based transistors. *Journal of Vacuum Science & Technology A: Vacuum, Surfaces, and Films*, 38(2):020803, 2020. doi:10.1116/1.5129803.

[116] A. V. Sampath, Y. Chen, A. Llopis, H. Shen, J. Smith, S. Kelley, J. Schuster, F. Nouketcha, J. C. Campbell, and M. Wraback. Enhanced far ultraviolet spectral response and gain in SiC avalanche photodiodes. *Applied Physics Letters*, 118(22):221102, 2021. doi:10.1063/5.0050046.

[117] Ariane Laura Beck. *Wide band gap avalanche photodiodes for ultraviolet single photon detection*. PhD thesis, The University of Texas at Austin, may 2006.

[118] J. D. Petticrew, S. J. Dimler, X. Zhou, A. P. Morrison, C. H. Tan, and J. S. Ng. Avalanche breakdown timing statistics for silicon single photon avalanche diodes. *IEEE Journal of Selected Topics in Quantum Electronics*, 24(2):1–6, 2017. doi:10.1109/JSTQE.2017.2779834.

[119] Synopsys. Sentaurus Device: An advanced multidimensional (1D/2D/3D) device simulator . Accessed on June 20th[Online].